Antiprotons in a Penning Trap: A New Measurement of the Inertial Mass

A thesis presented

by

Robert Lee Tjoelker

to

The Department of Physics

in partial fulfillment of the requirements

for the degree of

Doctor of Philosophy

in the subject of

Physics

Harvard University

Cambridge, Massachusetts

September 1990

Abstract

Antiprotons from the Low Energy Antiproton Ring (LEAR) at CERN with a kinetic energy of 5.9 MeV are passed through matter and captured in a cylindrical Penning trap. Using electron cooling, they are brought into thermal equilibrium with the 4 K trapping environment and have been stored for up to 2 months directly establishing the antiproton lifetime to be greater than 103 days.

The inertial masses of the antiproton and proton are compared by direct non-destructive measurments of their oscillatory motions in a Penning trap. An open endcap cylindrical trap produces a high purity quadrupole potential and allows antiprotons to be trapped and cooled. A self-shielding superconducting solenoid compensates the fluctuating magnetic field in the accelerator hall.

The measured mass ratio is $m_{\bar{p}}/m_p = 0.999\,999\,977(42)$. The achieved accuracy of 4.2×10^{-8} is one thousand times more precise than obtained with previous techniques, and is the most stringent test of CPT invariance with baryons. As part of a thorough systematic study, independent comparisons to electrons yield the mass ratios $m_{\bar{p}}/m_{e^-}$=1836.152 648(89) and m_p/m_{e^-}=1836.152693(88).

Contents

To the Memory of My Father,

Lawrence Earle Tjoelker

Acknowledgements

I am grateful to all the members of the TRAP collaboration who have contributed in many ways to the success of this work. I would like to thank my advisor Jerry Gabrielse for making possible this challenging research opportunity and for his support. My thanks to Luis Orozco, Steve Rolston, Xiang Fei, Hartmut Kalinowsky, Johannes Haas, Tom Trainor, Kris Helmerson, and Bill Kells.

I also wish to thank Ching-Hua Tseng, Loren Haarsma, Joseph Tan, Ben Brown, Won Ho Jhe, and David Phillips for their contributions. Dan Skow, Ron Musgrave, and Heinz Guldenmann constructed many of the components for the cryogenic system, and L.R. DeFeo and E. Sefner machined the traps. I would also like thank Oscar Vilches for his help and enthusiasm. This work would not have been possible without the assistance of many others at Harvard University, the University of Washington, and the LEAR facility at CERN. I thank you all.

Most of all I thank Delinda for her love and patience, and Benjamin and Melissa for reminding me that there are many wonderful things in life other than physics!

List of Figures

Chapter 1

Introduction

Antiprotons were first observed in 1955 at the Berkeley Bevatron in what can be considered the first mass comparison between antiprotons and protons (accuracy $\approx 5\%$)[18]. Antiprotons are extremely rare in cosmic rays and for most practical purposes are only available for experimentation as products of high energy collisions at large particle accelerators. The relative scarcity and high energy nature of antiprotons make it difficult to achieve high precision measurements of their fundamental properties. Unprecedented accuracies would be possible if only a small number of antiprotons could be studied in the low energy environment of an ion trap [24,61,36].

In this thesis, a measurement of the antiproton inertial mass 1000 times more accurate than previously obtained is described. This substantial improvement is the result of slowing, trapping, and cooling antiprotons into the low energy environment of a Penning trap [37,45] and the application of high precision mass spectroscopy techniques [48].

Measurements of the antiproton inertial mass are made by comparing their confinement eigenfrequencies in a new open endcap cylindrical Penning trap to those of protons. The antiproton to proton mass ratio is measured to be

$$m_{\bar{p}}/m_p = 0.999\ 999\ 977(42). \tag{1.1}$$

The fractional uncertainty is determined to be 4.2×10^{-8} after a thorough investigation of possible systematic effects. This measurement becomes the most sensitive test of CPT invariance on a baryon system.

1.1 Motivation

During the later half of this century, tests of symmetry principles in physics have resulted in most unexpected and fundamentally important surprises. In 1956, the weak interactions were shown to be parity violating [67,118]. In 1964, observations showed that the results of interactions involving the K meson and its antiparticle were different under a combined transformation of parity and a change in sign of electric charge [19]. This phenomena, known as charge-parity (CP) violation, remains one of the most stimulating problems of particle physics.

A fundamental symmetry in our description of nature is CPT symmetry. CPT symmetry implies that the physical interactions in our world are identical to those in a world where you simultaneously change the sign of baryon number, strangeness, lepton number, muon number, and electric charge (Charge conjugation C), change sign of the spatial coordinates (Parity P), and change the direction of time (Time reversal T). Invariance under such a transformation is required by general principles of relativistic field theory [80,112]. Some of the consequences of CPT invariance which can be experimentally tested are the equality of the masses, mean lifetime, and magnetic moment (with opposite sign) of a particle with its antiparticle.

The most precise tests of CPT invariance to date are summarized in Fig. 1.1. Only two tests have an accuracy significantly higher than the the work reported in this thesis comparing the antiproton and proton masses. The electron and positron magnetic moments have been compared to an accuracy of 4×10^{-12} [102]. Of particles that participate in the strong interactions, the only high precision test of CPT invariance results from the K_L and K_S mass oscillation, providing an extremely sensitive test of the mass difference of the eigenstates, K_0 and $\overline{K}_0$. This measurement implies a fractional mass difference of $\Delta m_{K^0}/m_{K^0} < 10^{-18}$. Previous measurements of the $p - \overline{p}$ mass difference of 5×10^{-5} provide the best limit on CPT invariance in a baryon system. Reaching a proposed goal of measuring the antiproton-proton mass difference to an accuracy of 10^{-9} will improve this limit by more than four orders of magnitude [92,36].

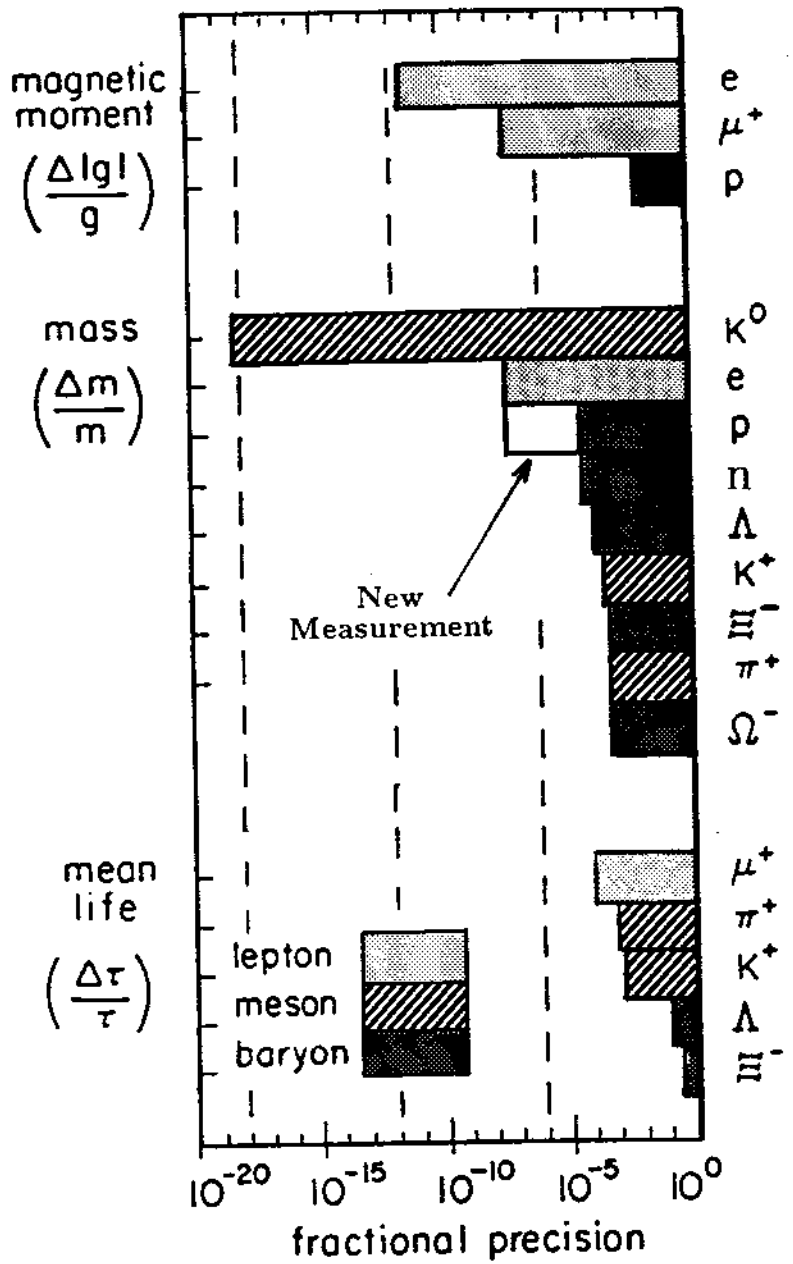

Figure 1.1: Tests of CPT Invariance using baryons, mesons, and leptons. (Data from **Review of Particle Properties**; Physics Letters **B204**, April 1988)

There have been four previous determinations of the antiproton inertial mass [3,56,81,82] as shown in Fig. 1.2 and compared with the measured proton mass which is known to much higher precision. All of the previous mass determinations used exotic atoms formed when an incident high energy antiproton is slowed in a target and captured by a nucleus. Measurements of the exotic atom are made on antiprotons which occupy orbits within the lowest electron orbit, yet are still still outside of the range of nuclear strong interactions. To first approximation, the exotic atom can then be treated as an hydrogenic atom. De-excitation X-rays are measured and the transition identified. The transition energy is nearly proportional to the reduced mass and the antiproton mass can be deduced by comparing the measured values with theoretical values. Corrections to the measured energy eigenvalues taken into account include vacuum polarization, higher order radiative terms, electron screening, finite nuclear size, and nuclear polarization. The most precise measurement from these techniques puts a limit on a possible difference between the antiproton and proton masses of 5×10^{-5} [81].

It has been proposed to put a limit on the antiproton-proton mass difference by comparing the antiproton and proton radii while circulating in a large accelerator ring [94]. This method may be feasible in a ring such as the Super Proton Synchrotron (SPS) at the European Center for Particle Physics (CERN), though it has not been demonstrated that improvements over the accuracy achievable using exotic atom methods are obtainable with present machine parameters.

1.2 Mass Spectroscopy in a Penning Trap

The use of static electric and magnetic fields to increase the containment times of electrons was first documented by F.M. Penning in 1936 [77]. In 1949, a device called the omegatron was developed by H. Sommer, H.A. Thomas and J.A. Hipple at the National Bureau of Standards which was subsequently used to measure the charge to mass ratio of the proton by a cyclotron resonance technique [87]. In the 1960's and early 1970's, H. Dehmelt and associates at the University of Washington highly refined the use of static electric and magnetic fields into what

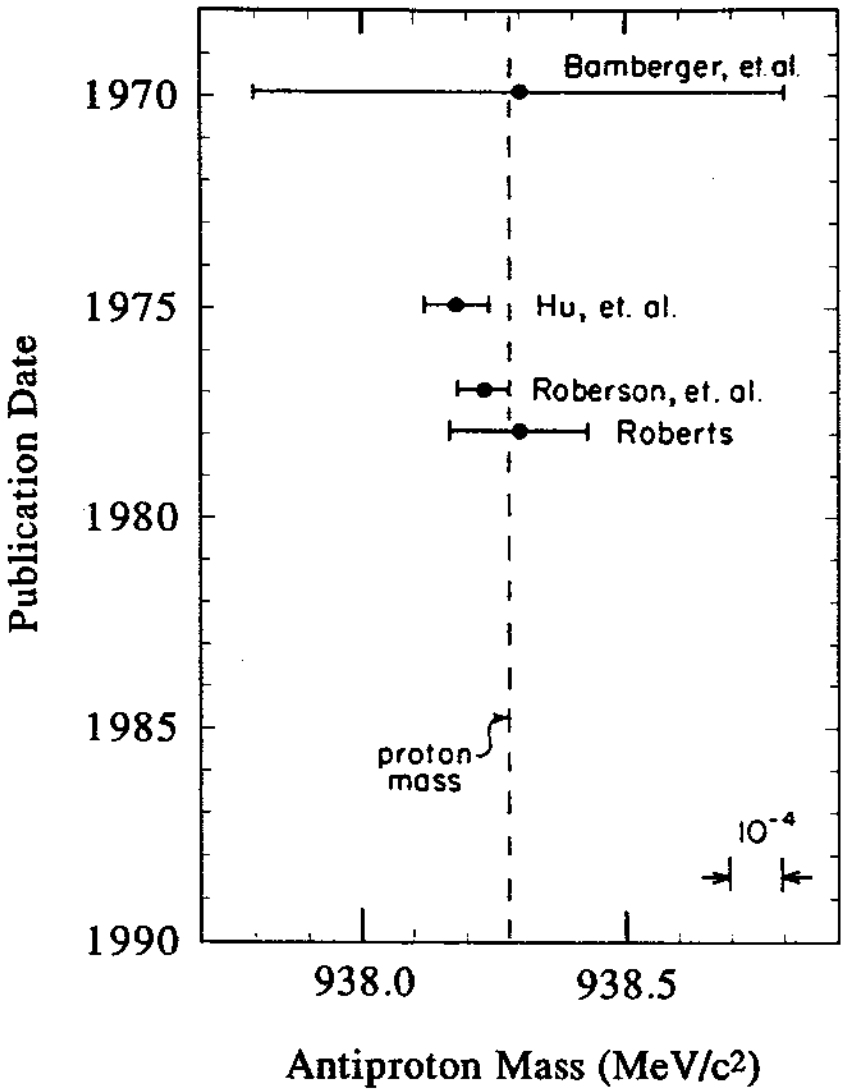

Figure 1.2: Previous measurements of the antiproton inertial mass compared to the proton mass. The uncertainty of the new measurement reported in this thesis is approximately 30 times narrower than the dashed line.

has become known as the Penning trap.

The Penning trap consists of a uniform static magnetic field superimposed on an electrostatic quadrupole potential. Such a device can hold charged particle(s) nearly at rest in free space essentially indefinitely. In 1973, Wineland, Ekstrom, and Dehmelt succeeded in isolating a single electron in such a trap [113] which led to a greatly improved measurement of the electron g-factor [25]. Since then, the use of such traps has greatly expanded and the Penning trap has become an important tool in the field of precision measurements. One such use is as a technique for high precision mass spectroscopy.

The trap technique has a number of advantages over other techniques for performing mass spectroscopy measurements. If the trap environment is cryogenically cooled, an extremely good vacuum can be obtained. This makes possible very long confinement times and the achievement of good signal-to-noise with even a single particle. Another advantage is that very different masses can be compared unlike, for example the Smith-Wabstra RF spectrometer, which is limited to comparing mass doublets. (Such a spectrometer has also been proposed as a method to determine the antiproton inertial mass to higher precision [92]). A final advantage is that detection schemes can be employed with Penning traps that yield very narrow lineshapes (presently $\Delta\nu/\nu \approx 4 \times 10^{-10}$ for RF detection schemes). Narrow lines and long containment times provide the possibility of a thorough quantification of perturbations and systematic effects.

One of the first high precision mass comparisons using a Penning trap was the direct determination of the fundamental mass ratio m_p/m_e. A group at Mainz University determined m_p/m_e with a detection scheme that relied on a destructive time-of-flight technique [50,53]. Another group, from the University of Washington performed the measurement also using a Penning Trap, but instead used non-destructive RF detection techniques [98,99,100]. Both techniques have their merits and have been highly refined in recent years. In addition to the proton and electron, the positron has also been studied in a Penning trap [86,102]. The positron magnetic moment and inertial mass has been compared to that of the electrons with high precision resulting in the most precise test of CPT invariance

using leptons (Fig. 1.1).

Recent high precison measurements with Penning traps demonstrate the promise of this technique in the field of mass spectroscopy. The Washington group, led by R. VanDyck, have made several different measurments and have claimed a resolution approaching 10^{-10} [72]. Their most precise published measurement has a fractional uncertainty of 3.4×10^{-9}, limited by the stability of their magnetic field. They have also compared other ions to the $^{12}C^{+4}$ ion, which yields a direct comparison to the defined atomic mass unit (amu) [72] .

Recently, use of a superconducting resonant detection circuit coupled to an RF squid [110] have resulted in a measurement by an MIT group of $m(CO^+)/m(N_2^+)$ with a reported fractional uncertainty of 4×10^{-10} [21]. This measurement is also limited by the temporal stability of the magnetic field [47,23].

Finally, the time-of-flight ejection method pioneered at Mainz University is continued today G. Werth [111] and is also used at ISOLDE at CERN to perform mass comparisons of relatively short lived radioactive ions at the 10^{-7} level [5].

Over just a few years, spectroscopy in a Penning trap has become the standard for high precision mass determinations of charged particles with long lifetimes.

1.3 Antiprotons: Challenges and Solutions

The Penning trap is an ideal environment for studying stable low energy charged particles. Our goal has been to compare the antiproton and proton inertial masses by measuring their cyclotron frequencies in a Penning trap [36]. Because antiprotons are presently only available from a high energy accelerator, the prospect of putting antiprotons into the low energy (typically 4 K) environment has presented us with several major challenges. In this thesis, solutions to these major challenges and the resulting improved measurement of the antiproton inertial mass are described in detail.

We start in Chapter 2 with a brief review of the particle motions and the mass spectroscopy technique in a Penning trap.

In Chapters 3 and 4, we describe how we resolve the challenges imposed by

working with antiprotons. In Chapter 3, we discuss the development of a new cylindrical open endcap trap and the cryogenic and support system that allows for interfacing the trap to an accelerator complex while maintaining the trap at 4 K. We also address concerns with large magnetic fluctuations in the accelerator environment and describe a custom built superconducting solenoid capable of producing a strong, highly uniform, and stable magnetic field. This solenoid is unique in that it also is capable of shielding the trap from external magnetic fluctuations by a factor as much as 156.

Chapter 4 presents our techniques for reducing the incoming antiproton energy by more than ten orders of magnitude. We summarize the slowing and capture of antiprotons into the new trap and subsequent cooling to 4.2 K using a novel form of electron cooling. We also measure the antiproton containment lifetime, an important observation that signifies the appropriateness of using non-destructive RF techniques to perform the mass measurement.

In Chapters 5 through 9 we turn our attention to using RF detection in the open access trap. In Chapter 5, we cover the experimental details of detecting the particle motions outlined in Chapter 2. In Chapter 6 and 7, we present experimental results in the new trap using electrons and protons. Chapter 8 and 9 present indirect and direct observations of the antiproton cyclotron motion.

In Chapter 10 we provide a comprehensive discussion of systematic checks and quantify the magnetic and electric perturbations to the trapping field at our present level of accuracy. Chapter 11 describes the mass comparison from a series of frequency measurements using antiprotons, protons, and electrons. In Chapter 12 we conclude this thesis by presenting mass comparisons for $m_{\bar{p}}/m_p$, $m_{\bar{p}}/m_{e^-}$, and m_p/m_{e^-}. We compare to previous measurements and discuss possible future research as a result of this work.

Chapter 2

Particle Motions in a Penning Trap

A single charged particle in a Penning trap is a bound system that has many analogies to the hydrogen atom except that the atomic nucleus has been replaced by an external electrostatic quadrupole potential superimposed on a spatially uniform, stable magnetic field.

In this chapter, the essential elements of particle motions in the Penning trap are summarized. Detailed accounts are reviewed elsewhere [13].

2.1 Perfect Trap

If a particle of charge e and mass m is placed in a uniform magnetic field $\mathbf{B} = B_0\hat{z}$, the particle travels around the field line in a cyclotron orbit, with the free space cyclotron frequency

$$\omega_{\mathbf{c}} = \frac{|eB|}{mc}\hat{z} = \omega_c\hat{z}. \tag{2.1}$$

The motion of the particle is bound in a Penning trap by superimposing an electric quadrupole potential

$$V(\mathbf{r}) = \frac{V_0}{2}\frac{z^2 - \rho^2/2}{d^2}. \tag{2.2}$$

The variables z and ρ are cylindrical coordinates and d is a characteristic trap dimension.

The quadrupole potential has traditionally been produced by placing electrodes along equipotentials of V(r). Two 'endcaps' follow the hyperbola of revolution

$$z = \pm\sqrt{z_0^2 + \rho^2/2}, \tag{2.3}$$

and one 'ring' electrode is along the hyperbola of revolution

$$z^2 = \frac{1}{2}(\rho^2 - \rho_0^2). \tag{2.4}$$

The characteristic trap dimension is defined by

$$d^2 \equiv \frac{1}{2}(z_0^2 + \frac{\rho_0^2}{2}) \tag{2.5}$$

in terms of the minimum axial and radial distances to the trap electrodes, z_0 and ρ_0.

The equations of motion result from the Lorentz force on the charged particle

$$\mathbf{F} = -e\nabla V + \frac{e}{c}\mathbf{v} \times \mathbf{B}. \tag{2.6}$$

The axial motion along $\hat{z}$ decouples since $v_z\hat{\mathbf{z}} \times \mathbf{B} = 0$. The resulting equation of motion is that of a simple harmonic oscillator

$$\ddot{z} + \omega_z^2 z = 0, \tag{2.7}$$

with angular [1] axial frequency

$$\omega_z^2 = \frac{eV_0}{md^2}. \tag{2.8}$$

The radial equation of motion is

$$m\ddot{\boldsymbol{\rho}} = e[\mathbf{E}_\rho + (\frac{\dot{\boldsymbol{\rho}}}{c}) \times \mathbf{B}] \tag{2.9}$$

where E_ρ is the radial component of the quadrupole electric field which we can express in terms of the axial frequency

$$E_\rho = -\frac{\partial V}{\partial \rho} = \frac{V_0}{2d^2}\rho = \frac{1}{2}\frac{m}{e}\omega_z^2\rho. \tag{2.10}$$

[1] Throughout this thesis, either the frequency ν or the equivalent angular frequency $\omega = 2\pi\nu$ is used depending upon which is more convenient in the immediate context.

Thus the radial equation of motion in terms of the free space cyclotron and axial frequencies ω_c and ω_z, in a Penning trap is

$$\ddot{\boldsymbol{\rho}} - \omega_c \times \dot{\boldsymbol{\rho}} - \frac{1}{2}\omega_z^2 \boldsymbol{\rho} = 0. \tag{2.11}$$

When $\omega_z \rightarrow 0$ (i.e. the voltage $V_0 \rightarrow 0$), we recover the equation of motion describing uniform circular motion at the free space cyclotron frequency ω_c.

Solving Eq. 2.11 yields two eigenfrequencies given by

$$\omega_c' = \omega_c - \frac{\omega_z^2}{2\omega_c'} = \omega_c - \omega_m \tag{2.12}$$

and

$$\omega_m = \frac{\omega_z^2}{2\omega_c'}. \tag{2.13}$$

The frequency ω_c' is the modified cyclotron frequency, and it reflects the deviation from the free space cyclotron frequency ω_c resulting from the presence of the electric quadrupole field. The magnetron frequency ω_m describes the slow circular motion that results from a balance between the radially inward motional electric field and the radially outward electric field. The magnetron motion is unstable in that removing energy from it increases the orbit size. Fortunately, the radiation damping is usually so small that the motion is stable for many years.

The condition for which a charged particle will be bound in the Penning trap is

$$\omega_z \leq \frac{\omega_c}{\sqrt{2}}. \tag{2.14}$$

which requires that the inward motional field be larger than the outward motional field. For typical trap sizes and field strengths

$$\omega_m \ll \omega_z \ll \omega_c'. \tag{2.15}$$

describes the hierarchy in the trap eigenfrequencies.

In a perfect Penning trap the free space cyclotron frequency is given exactly by Eq. 2.12 and 2.13 so that a measurement of ν_c' and ν_z is sufficient to measure ν_c . A comparison of charge to inertial mass ratios can be made in a Penning trap by measuring the free space cyclotron frequency of two different particles.

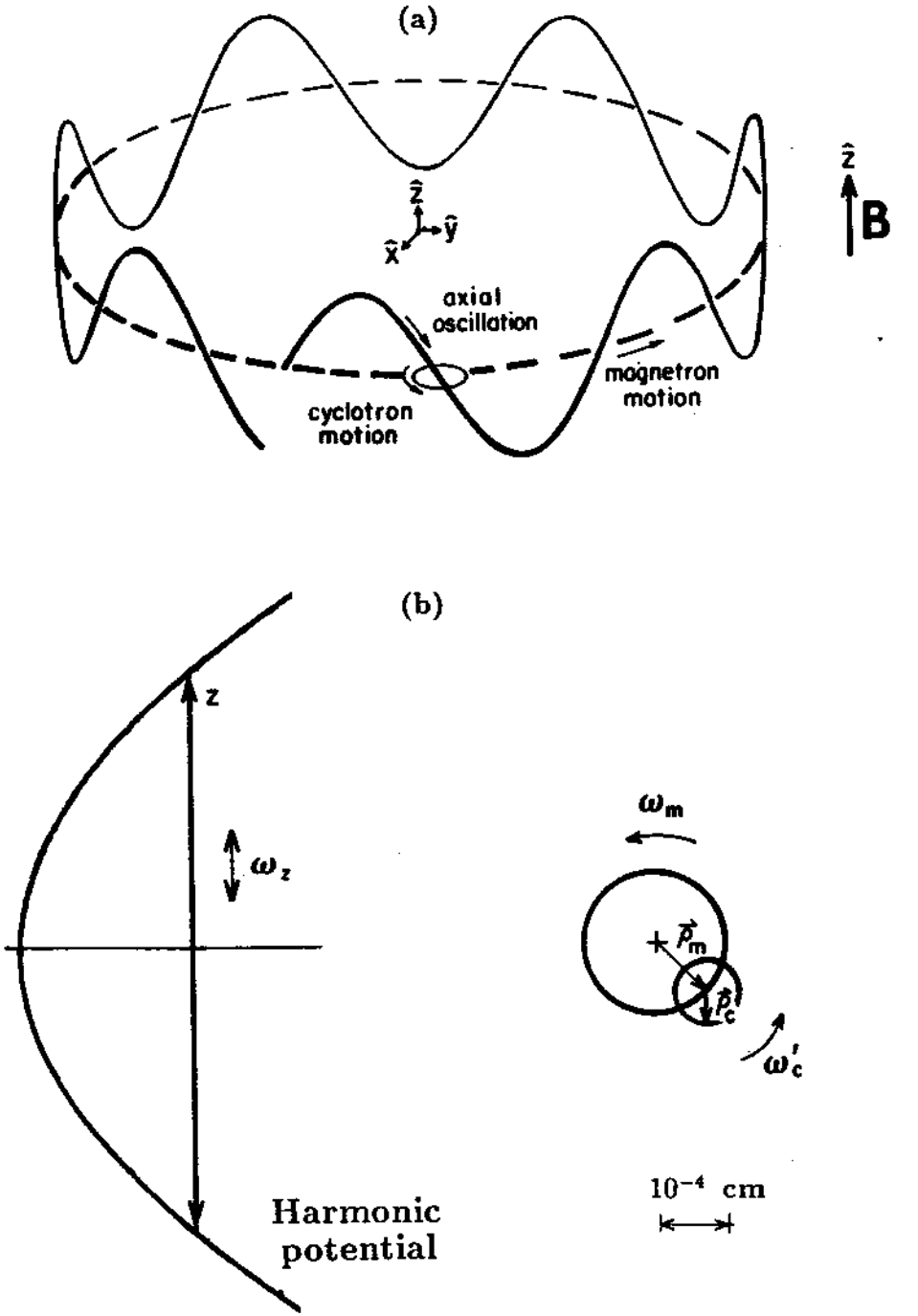

Figure 2.1: (a) Schematic representation of the orbit of a charged particle confined in a Penning trap. (b) A scaled representation of the three oscillatory motions for a confined antiproton ($T_z = T_c$ =4K, $T_m = (\omega_m/\omega_c)4$ K).

For example, the ratio of the cyclotron frequencies for a proton with mass m_p and charge q_p, to that of an antiproton with mass $m_{\overline{p}}$ and $q_{\overline{p}}$ is

$$\frac{\nu_c(p)}{\nu_c(\overline{p})} = \frac{q_p B/m_p c}{q_{\overline{p}} B/m_{\overline{p}} c} = \frac{q_p}{m_p}\frac{m_{\overline{p}}}{q_{\overline{p}}} \tag{2.16}$$

This last equality requires the magnetic field to be the same for both species over the duration of the comparison, a topic we return to in Chapter 10.

A comparison of cyclotron frequencies is a often referred to as a comparison of the inertial masses. For matter ions, reference to a cyclotron frequency being a mass comparison is justified by charge quantization and the stringent experimental limits put on charge neutrality between the proton and electron of $(q_{p^+} + q_{e^-}) < 10^{-19}e$ [62]. Strictly speaking, the measurements reported in this thesis are a comparison of the charge to mass ratio of the antiproton and the proton.

2.2 Imperfect Traps: The Invariance Theorem

Real traps have physical imperfections. For example, the trap electrodes can be slightly distorted and the quadrupole electrostatic field is not perfectly aligned along the uniform magnetic field.

Imperfections in the quadrupole potential field introduce anharmonic terms to the axial equation of motion expressed in Eq. 2.7. For this reason, the three electrode Penning trap is often modified by adding two 'compensation' electrodes [95,30]. The purpose of such electrodes is to tune out possible higher order anharmonic contributions to the potential. Nevertheless, the degree to which a perfect quadrupole can be produced is limited by the asymmetries and misalignment which exist.

The degree to which leading imperfections affect the achievable precision in a cyclotron frequency measurement has been discussed by Brown and Gabrielse [8,13]. Let $\overline{\omega}_c'$, $\overline{\omega}_z$, and $\overline{\omega}_m$ be the measured cyclotron, axial, and magnetron frequencies in a non-ideal trap with an asymmetry parameter ϵ representing deviations from the ideal quadrupole potential by

$$U = \frac{1}{2}m\omega_z^2[z^2 - \frac{1}{2}(x^2+y^2) - \frac{1}{2}\epsilon(x^2-y^2)], \tag{2.17}$$

and angles (θ, ϕ) representing a misaligned magnetic field given by

$$\mathbf{B} = B(\sin\theta\cos\phi\hat{i} + \sin\theta\sin\phi\hat{j} + \sin\theta\sin\phi\hat{k}). \tag{2.18}$$

Brown and Gabrielse [8,13] have derived an invariance theorem

$$\omega_c^2 = \overline{\omega}_c'^2 + \overline{\omega}_z^2 + \overline{\omega}_m^2. \tag{2.19}$$

This theorem provides a means of obtaining the free space cyclotron frequency (the one of interest for mass comparisons) from the measured trap eigenfrequencies.

The measured eigenfrequencies $\overline{\omega}_c'$, $\overline{\omega}_z$, and $\overline{\omega}_m$ can be expanded in terms of the distortion parameter ϵ and the tilting angles (θ, ϕ) by the following expressions:

$$\overline{\omega}_z^2 \approx \omega_z^2[1 - \frac{3}{2}\sin^2\theta(1 + \frac{1}{3}\epsilon\cos 2\phi)] \tag{2.20}$$

$$\overline{\omega}_m \approx \frac{\overline{\omega}_z^2}{2\overline{\omega}_c'}(1-\epsilon)^{1/2}[1 - \frac{3}{2}\sin^2\theta(1 + \frac{1}{3}\epsilon\cos 2\phi]^{-3/2} \tag{2.21}$$

Eliminating $\overline{\omega}_m$ from the invariance theorem, we obtain an expression for the free space cyclotron frequency in terms of the asymmetry parameter ϵ and tilt angle θ as

$$\frac{\omega_c}{\overline{\omega}_c'} = 1 + \frac{1}{2}\left(\frac{\overline{\omega}_z}{\overline{\omega}_c'}\right)^2 + \frac{9}{16}\left(\frac{\overline{\omega}_z}{\overline{\omega}_c'}\right)^4(\theta^2 - \frac{2}{9}\epsilon^2) + \ldots \ . \tag{2.22}$$

From Eq. 2.15, terms proportional to $(\omega_z/\omega_c)^6$ and higher order terms are small and can be neglected. For vanishing θ and ϵ, we recover Eq. (2.12) for an ideal trap.

As an example, assuming that θ =1° or $|\epsilon| = 1\%$, the correction term for electrons in a typical trap in $(\overline{\nu}_z(e^-)/\overline{\nu}_c'(e^-))^4 \approx 10^{-14}$. Using protons, such imperfections can become significant. For the small trap (d=0.112 cm) used by VanDyck and Schwinberg [98] to measure the proton to electron mass, $(\overline{\nu}_z(p)/\overline{\nu}_c'(p))^4 \approx 3\times10^{-4}$ and the correction term in Eq. 2.22 is about 5×10^{-8}. Therefore trap imperfections and misalignments can play an important role when measuring protons or antiprotons. However, our use of a much larger trap (Chapter 3) makes the third term negligible at the precison reported in this thesis.

2.3 Extension to Many Particles

The equations in Sections 2.1 and 2.2 are derived only for the case of a single particle. For the comparisons reported here, we have always used more than one.

Wineland and Dehmelt generalized the equations of motion to the case of n harmonically bound particles of a single species [115]. They model the particles each of mass m and bound with a spring constant k, and driven by the potential between capacitor plates separated by a distance d. The equation of motion including mutual interactions (for simplicity assumed to be in the z direction only) is for the i^{th} particle

$$m\ddot{z}_i = -kz_i + \sum_{j\neq i}^{n} F_{ij} + F'_{ei}. \tag{2.23}$$

The term F_{ij} is the Coulomb force on the i^{th} particle due to the j^th particle. F'_{ei} is the external force on the i^{th} particle given by

$$F_{ei} = \frac{eV}{d} + \sum_{j}^{n} F_{ind}(i,j). \tag{2.24}$$

F'_{ind}(i,j) is the force on the i^{th} particle from the induced image charge in the capacitor plates (in actuality the trap electrodes) of the j^{th} particle. The spring constant k in Eq. 2.23 is a function of $F_{ind}(i,j)$, thus there is an n dependence.

For large particle numbers, such a force will yield a number dependent shift in the oscillation frequency (ref. [115] and Chapter 4). Assuming the numbers are kept small or the trap is sufficiently large, $F'_{ind} \approx 0$ we sum Eq. (2.23) over n particles giving

$$m\ddot{Z} = -kZ + \frac{eV}{d} + \sum_{i}^{n}\sum_{i\neq j}^{n} F_{ij} \tag{2.25}$$

where $Z = \sum_j^n Z_j/n$ is the center of mass coordinate for the n particle system. Newton's third law implies $F_{ij} = -F_{ji}$ so the sum vanishes. In the small number approximation, (2.25) becomes

$$m\ddot{Z} + -kZ = \frac{eV}{d}. \tag{2.26}$$

This equation for n particles also describes the motion of a harmonic oscillator with a center of mass oscillation at the frequency of a single particle of mass m

and charge q. Analogously, the cyclotron and magnetron center of mass motions are also similar to those of a single particle.

Chapter 3

The Antiproton Trap

Antiprotons are created, collected, and decelerated at CERN. The lowest energies available for experimentation are still around 5.9 MeV. A major challenge of the mass comparison experiment in a Penning trap is to load antiprotons, only available from an external high energy source. This places new constraints on the trapping apparatus not previously required for earlier studies using electrons, protons, and other common ions. In this chapter, we cover some of the major apparatus requirements, design criteria, and solutions so that the trap can be interfaced to the CERN accelerator complex which serves as an antiproton source.

3.1 Open Endcap Trap

Previous high precison measurements of charged particles such as electrons and protons, have been done in traps with electrodes shaped along equipotentials of the desired quadrupole potential. Protons and electrons are typically loaded by passing an electron beam through the trap where neutral atoms in the trap region are ionized, and then confined in the properly biased harmonic potential well. Since antiprotons must be obtained from an external high energy source, with a FWHM beam diameter often on the order of 1 cm, it is necessary to provide larger access to the trap than the small holes and slits often used in hyperbolic traps. In addition, the antiproton capture efficiency (Chapter 4) is proportional to the length of the trapping region making a very long trap advantageous.

For the purpose of access and particle confinement, cylindrical Penning traps

with long, open endcap electrodes have been previously used. In 1965 such a device was used to produce polarized electron beams [15]. Long cylindrical traps have also been used for the containment and study of cold electron plasmas [70]. In 1986, for an earlier version of our present work, we used a simple three electrode cylindrical trap to capture antiprotons in an ion trap for the first time [37]. Recently, cylindrical style traps have also been used for experiments requiring access for lasers [51] and cold neutron beams [16].

A much purer electric quadrupole potential is required for precise studies of elementary particles when the trap is an important part of the bound system. For purposes of access to an antiproton source and the requirements for mass spectroscopy, we have developed an open endcap consisting of a series of cylindrical electrodes shown in Fig. 3.1. This trap is unique in that it allows for adjusting the purity of the quadrupole potential without affecting the depth of the harmonic well [43].

3.1.1 A Tunable Quadrupole From Cylindrical Electrodes

By careful selection of the trap electrode dimensions and with appropriate biasing, we have designed and constructed an orthogonalized, tunable cylindrical trap. The cylindrical trap scheme can thereby produce an extremely good quadrupole potential over a small region in the trap center where the contained particles reside 3.2.

The electric potential at the center of the trap can be described by an expansion of Legendre polynomials

$$V = \frac{1}{2} V_0 \sum_{k=0}^{\infty} C_k \left(\frac{r}{d}\right)^k P_k(cos\theta) \tag{3.1}$$

where V_0 is the potential difference applied between the ring and endcap electrodes of the ideal three electrode trap. The variable d is the characteristic size of the trap defined in Eq. 2.5, $P_k(\cos\theta)$ is the k^{th} Legendre polynomial, and C_k is a dimensionless weighting coefficient.

For a perfect electric quadrupole, all coefficients other than C_0 and C_2 in the expansion 3.1 are zero. For the cylindrical trap, C_2 is less than unity reflecting

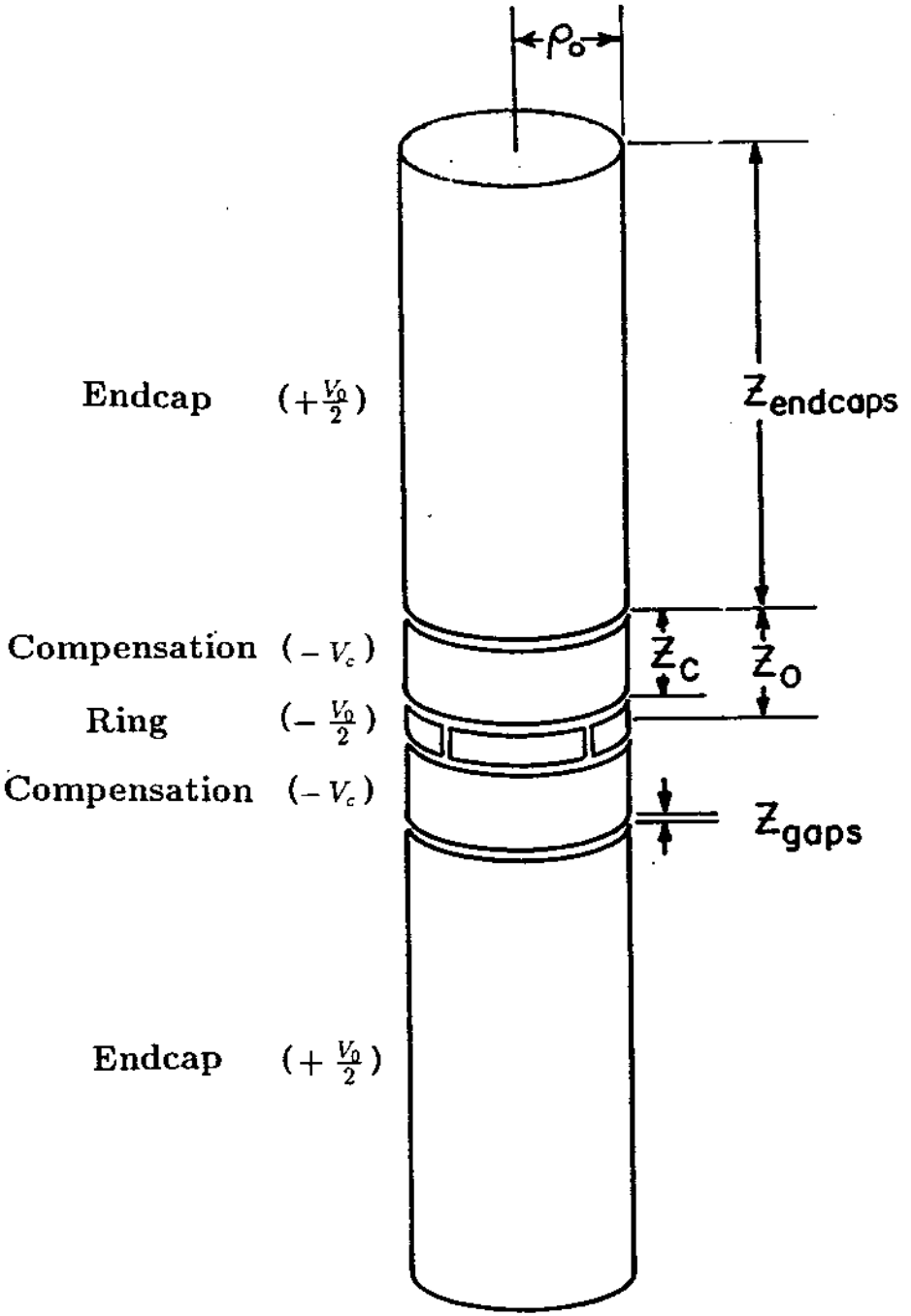

Figure 3.1: The open-endcap compensated cylindrical Penning trap.

a deviation from the hyperbolic electrode geometry (with $C_2 = 1$ resulting from electrodes along the hyperbolic surface $r^2 P_2(\cos\theta)$=constant). In the more general case the axial oscillation frequency of a particle of mass m, and electric charge q, resulting from the quadrupole field weighted by C_2 is

$$\omega_z^2 = \frac{qV_0}{md^2} C_2. \tag{3.2}$$

Cylindrical 'compensation' electrodes shown in Fig. 3.1 provide for tunability. Since the trap has reflection symmetry about the plane z=0, higher order terms that contribute to anharmonicity are the next even order terms C_4 and C_6. These terms can be compensated by adjusting the potential V_c applied to the two compensation electrodes.

It is most convenient to analyze the potential near the trap center (defined as the origin) as the superposition of two separate boundary value problems [30]. The superimposed potential resulting from the two boundary conditions is

$$V = V_0\phi_0 + V_c\phi_c = \frac{1}{2}V_0 \sum_{k=0}^{\infty} C_k \left(\frac{r}{d}\right)^k P_k(cos\theta) \tag{3.3}$$

where

$$\phi_0 \equiv \frac{1}{2}\sum_{k=0}^{\infty} C_k^{(0)} \left(\frac{r}{d}\right)^k P_k(cos\theta), \tag{3.4}$$

and

$$\phi_c \equiv \frac{1}{2}\sum_{k=0}^{\infty} D_k^{(0)} \left(\frac{r}{d}\right)^k P_k(cos\theta). \tag{3.5}$$

The potential ϕ_0 is due to a potential of -1/2 applied to the ring and +1/2 applied to the endcaps, with the compensation electrodes grounded. The potential ϕ_c is due to a potential of 1 applied to the compensation electrodes with all other electrodes grounded. The coefficients $C_k^{(0)}$ and $D_k^{(0)}$ are solved in the standard way by equating the above expansions to the applied potential along the appropriate boundary and integrating over the orthonormal set of Legendre polynomials and the small term $(r/d)^k$.

From 3.3, the expansion coefficients C_k can be expressed in terms of the others by

$$C_k = C_k^{(0)} + D_k \frac{V_c}{V_0}. \tag{3.6}$$

Adjusting V_c thus offers the possibility to make C_4 to improve the trap harmonicity. From Eq. 3.6 the optimum tuning ratio is

$$\left(\frac{V_c}{V_0}\right)_{C_4=0} = \frac{-C_4^{(0)}}{D_4}. \tag{3.7}$$

This is it is highly desirable that the leading order anharmonic coefficient C_4=0, since this along with higher order coefficients is responsible for amplitude (energy) dependent shifts of the particle axial frequency. The shift is approximately

$$\frac{\Delta\omega_z}{\omega_z} = \frac{3}{2}\frac{\widetilde{C_4}}{C_2}\frac{E_z}{qV_0C_2} \tag{3.8}$$

where E_z is the energy in the axial motion and

$$\widetilde{C_4} = C_4 + \frac{5}{2}C_6\frac{E_z}{qV_0C_2} \tag{3.9}$$

takes into account C_4 and the next higher order term C_6 [30].

Another useful potential scheme applied to the trap is an antisymmetric potential $\pm V_A/2$ to either the endcaps or the compensation electrodes [31]. Under such boundary conditions, expansion 3.1 will only consist of odd terms. The leading order odd term k=1 has the effect of applying a linear electric field across the center. This has applications for deliberately displacing the confined particles, and is relevant for particle detection (discussed in Chapter 5). The potential within the trap is given by

$$V = V_A\phi_A. \tag{3.10}$$

The solutions to Laplace's equation ϕ_A which satisfies the antisymmetric boundary condition $\pm V_A/2$ to the endcap or compensation electrodes respectively are

$$\phi(\mathbf{r})_{A,c} = \frac{1}{2}\sum_{k_{odd}=1}^{\infty} c_k\left(\frac{r}{z_0}\right)^k P_k(cos\theta) \tag{3.11}$$

and

$$\phi(\mathbf{r})_{A,d} = \frac{1}{2}\sum_{k_{odd}=1}^{\infty} d_k\left(\frac{r}{z_0}\right)^k P_k(cos\theta). \tag{3.12}$$

The size of the lowest order coefficients c_1 and d_1 are very useful for issues regarding particle detection and damping.

The computation for our open endcap trap was carried out by Gabrielse, Haarsma, and Rolston [43] following an earlier analysis by Gabrielse and MacKintosh on a related cylindrical geometry but with flat endcaps[32].

The relative dimensions ρ_0/z_0 and z_c/z_0 are chosen such that D_2=0 so that the trap is orthogonalized. Equation 3.6 implies that $C_2 = C_2^{(0)}$. Detailed figures, showing critical trap coefficients as a function to the relative trap dimensions ρ_0/z_0 and z_c/z_0 are found in reference [43].

The relative dimensions chosen for the antiproton trap, and the calculated coefficients corresponding to the multipole expansion about the trap center are shown in Table 3.1. We note D_4 is sufficiently large so that C_4 can be tuned using reasonable potentials. For a given trap, it is desirable to minimize the quality factor $\gamma \equiv D_2/D_4$ [13]. From 3.6, C_4 is calculated to be minimized with a potential applied to the compensation electrodes of $V_c = -0.381V_0$ where $V_0/2$ is applied to the endcap, and $V_0/2$ is applied to the ring (for V_0 applied to the ring with the endcaps held at ground, the compensation potential is expressed by $V_c = 0.8809V_0$). . In addition, the selected relative dimensions also have the feature that at the optimal tuning point V_c/V_0 to make C_4=0, then $C_6 = C_6^{(0)} + (0.3811)D_6 = 0$. From 3.8 and 3.9, the advantages of this scheme are evident.

The potential in the cylindrical trap resulting from the chosen relative dimensions is shown in Fig. 3.2. The quadrupole field resulting from a hyperbolic shaped trap with the same effective dimension $\tilde{d} = d/\sqrt{C_2}$ is superimposed in the dashed lines to illustrate the effectiveness of this scheme for producing a quadrupole region in the trap center.

There are several competing criteria for choosing the absolute trap size. First, access is needed to obtain a good antiproton trapping efficiency requiring a reasonable size for ρ_0 and as long as trap as practical. The antiproton beam when optimally focussed can have a FWHM diameter of 2 mm, though the beam diameter can often be on the order of 1 cm. Second, the effectiveness of particle resistive detection and damping (Chapter 5) depends on the trap dimensions. For the axial motion, the detected signal is proportional to $(d_1/z_0)^2$ if the detection is on the compensation electrode, and $(c_1/z_0)^2$ if the detection is on the endcap

Table 3.1: (a) The relative trap electrode size to produce an compensated cylindrical Penning trap. (b) Expansion coefficients calculated for several useful boundary conditions. (c) Measured trap coefficients.

(a) Relative Electrode Sizes to Produce $D_2 = 0$ and $C_6 = 0$

Radius	ρ_0/z_0	$= 1.0239$
Compensation Electrodes	z_c/z_0	$= 0.8351$
Endcap Electrodes	$z_{endcaps}/z_0$	$= 4.312$
Gaps Between Electrodes	z_{gaps}/z_0	$= 0.0303$
Tuning Ratio for Minimal C_4	V_c/V_0	$= 0.3811$

(b) Expansion Coefficients

$C_2^{(0)} = 0.5449$
$C_4^{(0)} = -0.2119$
$C_6^{(0)} = 0.1638$
$C_8^{(0)} = -0.1359$

$D_2 = 0$
$D_4 = -0.5560$
$D_6 = 0.4300$
$D_8 = 0.2609$

$C_2 = 0.5449$
$C_4 = 0$
$C_6 = 0$
$C_8 = -0.0365$
$C_0 = 0.775$

$c_1 = 0.3346$
$c_3 = 0.2202$
$c_5 = -0.0385$

$d_1 = 0.8994$
$d_3 = -0.8439$
$d_5 = 0.3915$

(c) Measured Coefficients

$C_2 = 0.551$
$D_2 \leq 0.005$
$C_4 << 0.0008$

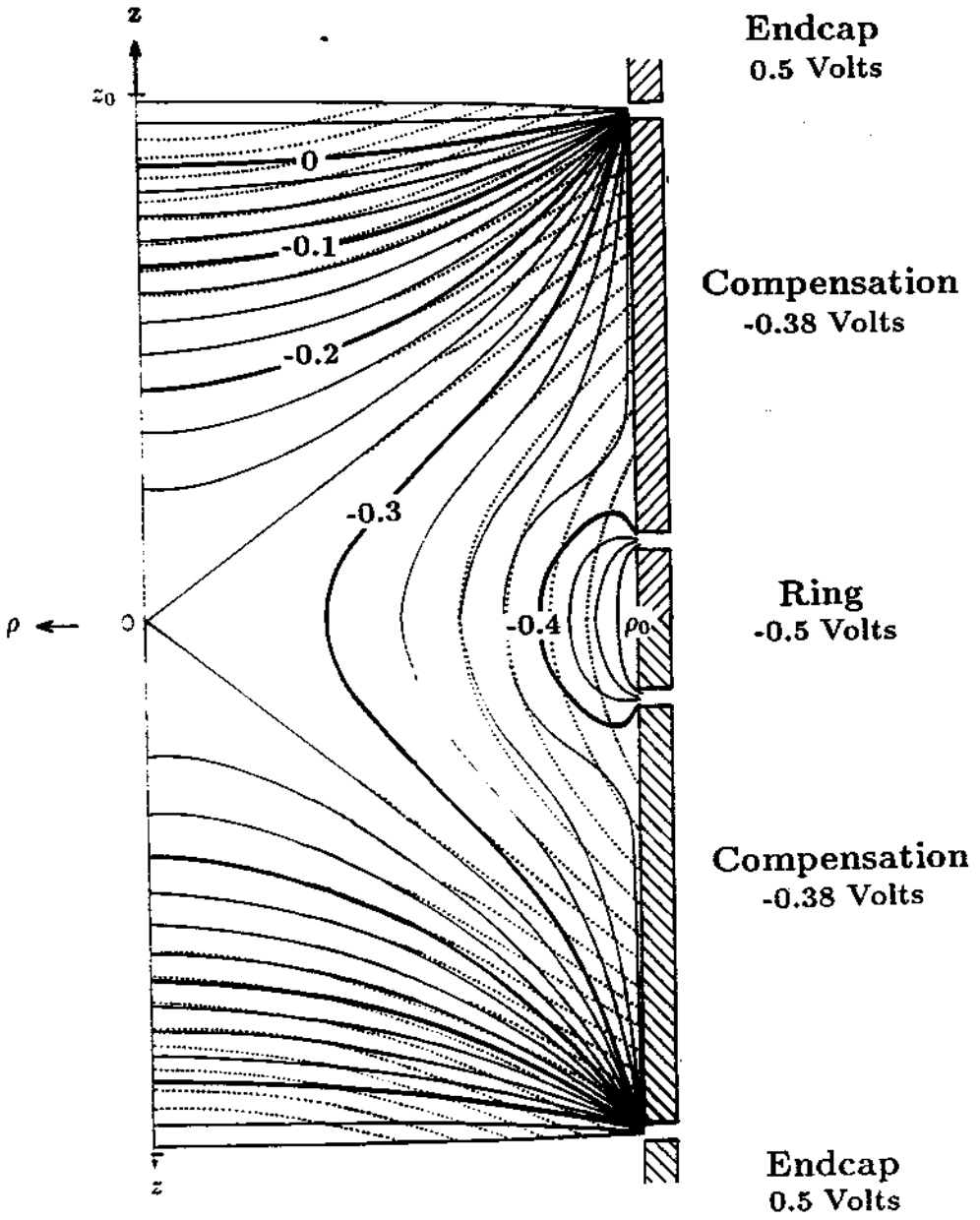

Figure 3.2: Electrostatic equipotential field lines in the compensated, open-endcap trap (solid) compared with the field lines for an ideal quadrupole potential (dotted).

electrode. For detection and damping a small z_0 (and ρ_0) is desirable. Finally, perturbations of the uniform magnetic field and the ideal quadrupole potential in the center of the trap where the confined particles reside become smaller the farther away the trap electrodes are. In addition, measurements in a larger trap will be much less sensitive to trap asymmetries and misalignment as shown in 2.22 a large trap makes the frequency hierarchy in Eq. 2.15 more pronounced.

With emphasis on loading and cooling antiprotons, we constructed a trap with the dimensions and resonant frequencies given in Table 3.2 and shown in Fig. 3.1. (If needed, we could later transfer the cooled antiprotons to a traditional hyperbolic trap with a small access hole). This trap has a characteristic dimension of $d/\sqrt{C_2}$=0.693 cm which for typical fields and trapping potentials results in $(\overline{\nu}_z\ /\overline{\nu}_c')^4 \approx 2\times 10^{-7}$ for antiprotons. The tradeoffs in the selected trap size will become more apparent when we discuss particle detection and damping (Chapter 5), and systematic perturbations due to the location and condition of the trap electrodes (Chapter 10).

3.1.2 Construction Issues

In practice our trap is slightly more complicated than the five electrodes discussed above. To allow direct detection and damping of ν_c' the ring electrode is divided into quadrants [97]. To allow sideband cooling of the magnetron motion [114], the compensation electrodes are each split into 2 segments. These vertical slits have not been taken into account in the coefficient calculations [43].

To minimize distortion of the magnetic field, the trap electrodes are constructed of OFHC copper. The electrodes are spaced, interlocked, and self aligned using small MACOR rings, all of these pieces are machined to tolerances of 0.005 mm (0.0002") [1]. The gaps between the electrodes are 0.18 mm and the depth to width of the gap is 9.2 so that any exposed MACOR or sapphire is sufficiently screened electrostatically. The ring and compensation electrodes were sectioned with electric discharge machining (EDM) and have sectioned gap widths of 0.15

[1]Throughout the remainder of this chapter, dimensions are ocassionally reported in inches (1"=2.54 cm) if it better describes a standard material size or machining dimension.

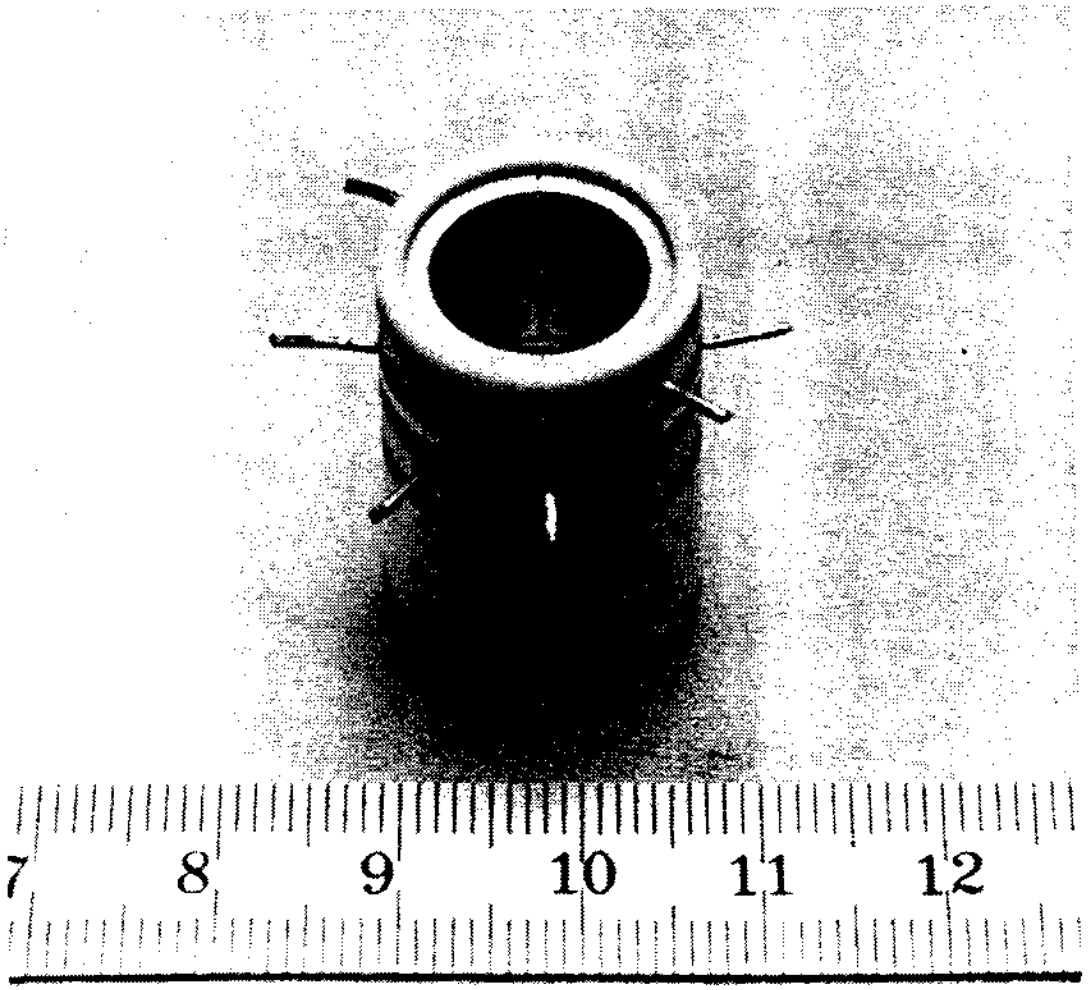

Radius	$\rho_0 = 0.6000$ cm.
Length	$z_0 = 0.5860$ cm.
Characteristic Dimension	$d = 0.5116$ cm.
Effective Dimension	$d/\sqrt{C_2} = 0.6931$ cm.

Figure 3.3: The open endcap trap showing the assembled split compensation and quad ring electrodes (scale in cm).

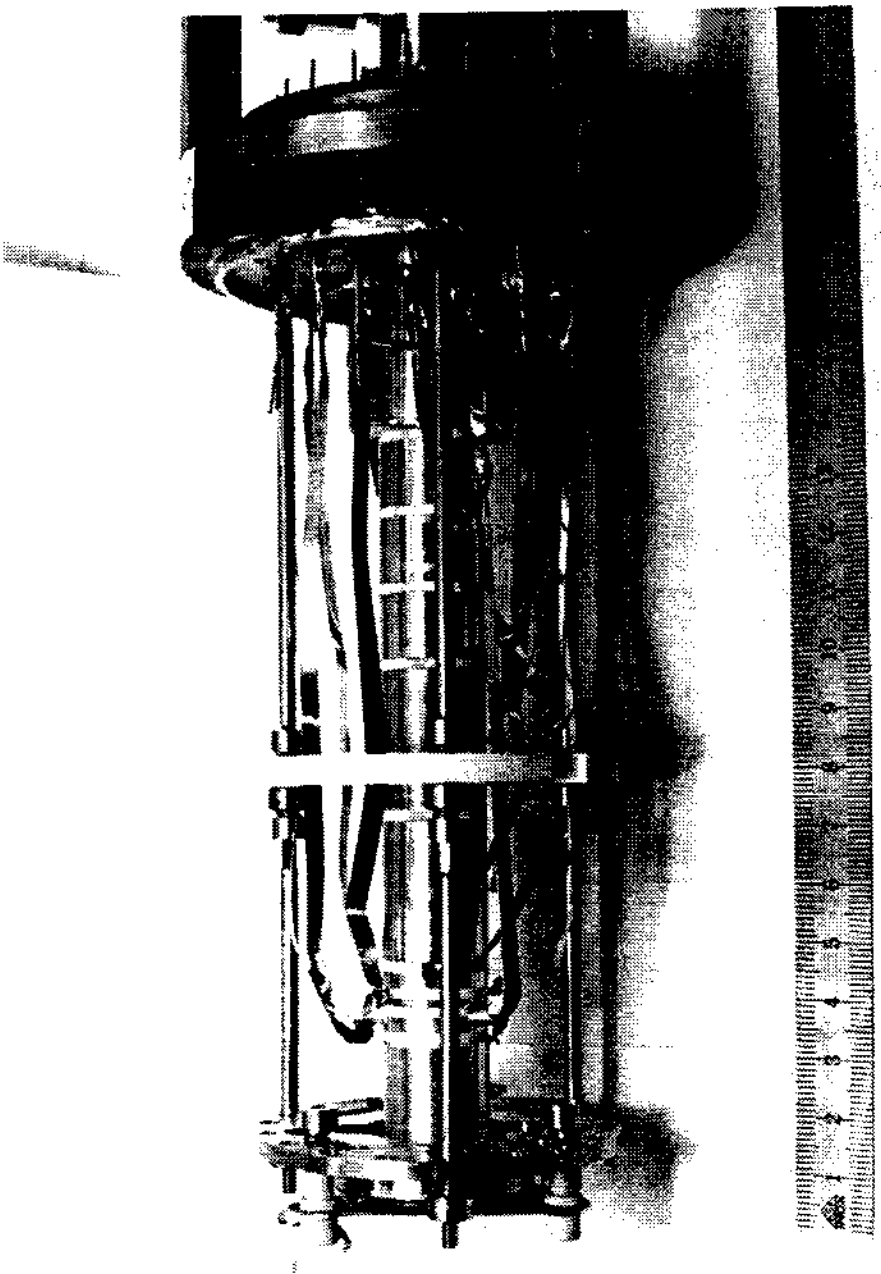

Figure 3.4: The extended cylindrical trap mounted from the upper flange of the trap vacuum enclosure (scale in cm).

Table 3.2: Typical eigenfrequencies for chosen trap dimensions and field strengths.

Electrons:	**Antiprotons (Protons):**
$\nu_z(e^-)$=9.63152 $V_0^{1/2}$ MHz/$\sqrt{Volt}$	$\nu_z(\overline{p})$ =0.22477 $V_0^{1/2}$ MHz/$\sqrt{Volt}$
$\nu_c\ (e^-)$=27.99225 B_0 GHz/Tesla	$\nu_c\ (\overline{p})$ =15.24507 B_0 MHz/Tesla
V_0=+32 V, B_0 ≈5.86 T	$V_0 = \pm 71$ V, B_0 ≈5.86 T
$\nu_z\ (e^-) = 54$ MHz	$\nu_z\ (\overline{p}) = 1.9$ MHz
$\nu_c\ (e^-) = 164$ GHz	$\nu_c\ (\overline{p}) = 89.3$ MHz
$\nu_m\ (e^-) = 9.1$ kHz	$\nu_m\ (\overline{p}) = 20$ kHz

mm. The segments are azimuthally separated and aligned with 1 ± 0.005 mm diameter sapphire spheres. The copper electrodes have been plated with a 0.2 μm diffusion barrier of rhodium and a 2 μm layer of gold to avoid oxidation and minimize possible surface charge accumulation. surface charge. The harmonic region of the constructed trap is shown in Fig. 3.3 and Fig. 3.5 shows the location of the sapphire spheres.

For purposes of containing high energy antiprotons, the trap is lengthened by additional cylindrical segments as shown in Fig. 3.4 to increase the trapping efficiency during the loading process (Chapter 4). This long trap is sufficient for confining high energy antiprotons, though it is not a harmonic trap in this configuration.

This long electrode configuration consisting of several segments may be useful as a storage trap. Another possible use could be in a 'nested trap' mode [38] where opposite charge species can be simultaneously confined. This scheme can be used to study charge exchange and recombination mechanisms, and may be a possible environment for the formation of antihydrogen by merging antiprotons with confined positrons [38,40,41].

3.1.3 Calculated Magnetic Bottle

Magnetic gradients can result from a distortion of the field by the magnetic susceptibility of the nearby material forming the trap electrodes and insulating spacers. The leading order effect of field distortions arising from the trap (which is symmetric about the plane z=0) is typically of the form of a magnetic bottle field. Intentional magnetic bottles in Penning traps have played a key role in measurements of electrons and positrons [86] since cyclotron and spin frequencies are only observable by coupling into the axial motion. For precision mass spectroscopy it is important to quantify and, in most cases, minimize the bottle field.

To keep such distortions small, our trap is constructed of OFHC copper which is only slightly diamagnetic. The insulating spacers consist of MACOR rings, and 1 mm diameter sapphire (Al_2O_3) spheres. The magnetization dipole moment per unit volume of the trap in a 5.9 T field at 4 K for the relevant materials are (in cgs units)

M(Cu)	= -0.05	ref. [64]
M(MACOR)	= +0.78	ref. [93]
M(MACOR)	= +0.52	ref. [58]
M(Al_2O_3)	= -0.085	ref. [64]

The magnetization of sapphire and copper are small and they are diamagnetic. The MACOR is the dominant contribution.

We calculate the field distortion following Brown and Gabrielse [13]. The magnetic field perturbation near the trap center resulting from a ring of material, with cross section $d\rho' dz'$, and located at the cylindrical coordinates ρ',z' (or r',θ' in spherical coordinates) is given by

$$\Delta \mathbf{B}(\mathbf{r}) = \sum_{l=0}^{\infty} \beta_l r^l [P_l(\cos\theta)\hat{\mathbf{z}} - (l+1)^{-1} \sin\theta \frac{dP_l(\cos\theta)}{d\cos\theta}\hat{\rho}] \qquad (3.13)$$

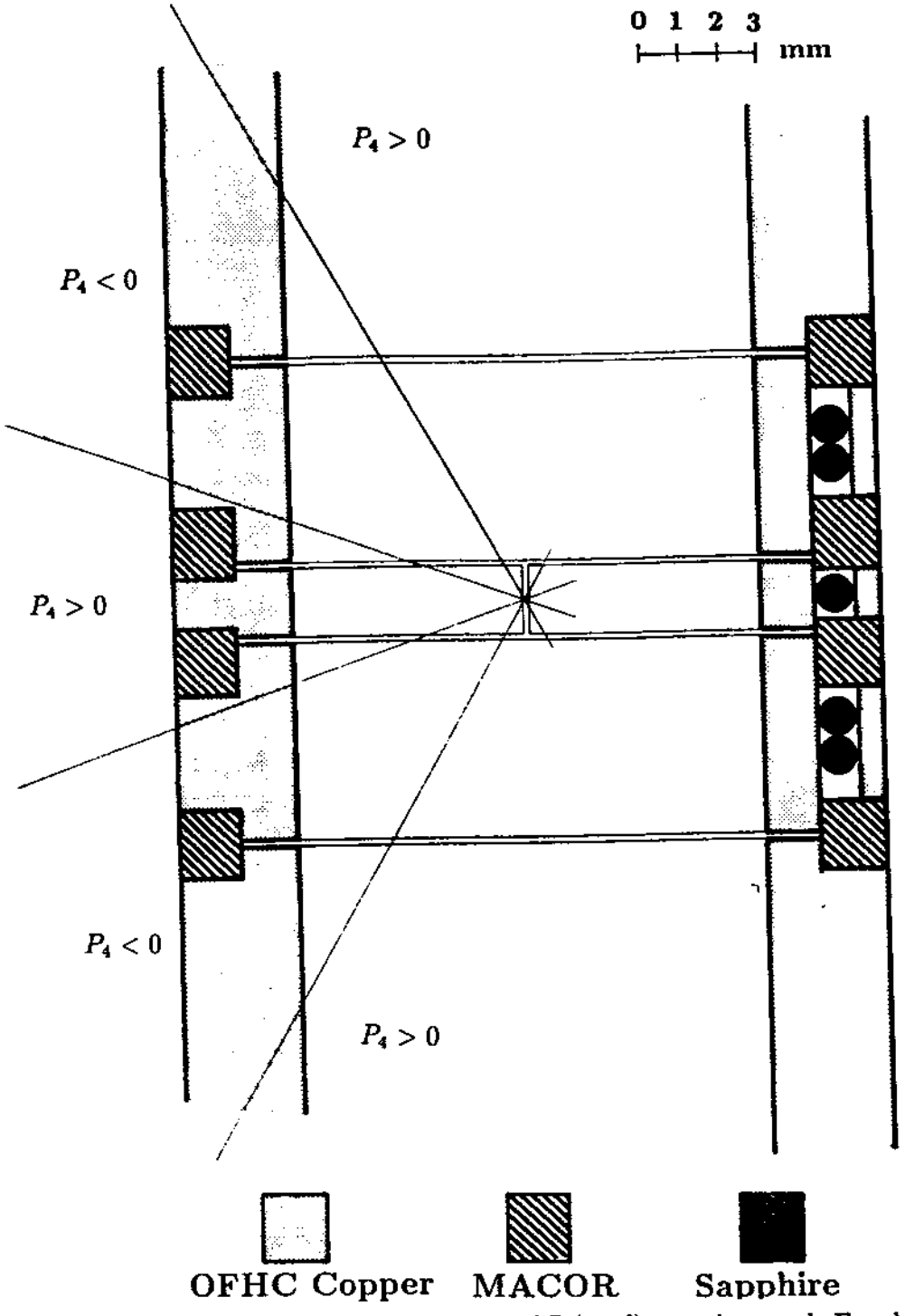

Figure 3.5: Open-endcap trap with the zeros of $P_4(cos\theta)$ superimposed. For clarity, the compensation electrodes are rotated azimuthally 45° and the endcap electrodes are truncated.

where

$$\beta_l = (l+1)(l+2)2\pi \int \rho' d\rho' dz' M(\rho', z')(r')^{-l-3} P_{l+2}(\cos\theta') \qquad (3.14)$$

The leading term $\Delta \mathbf{B_0} = \beta_0 \hat{\mathbf{z}}$ adds to the homogenous magnetic field. When the trap is symmetric under reflection z → -z, the integral in Eq. 3.13 vanishes for odd l so that $\beta_1 = 0$. The $l = 2$ term (often called a magnetic bottle), is

$$\Delta \mathbf{B_2}(\mathbf{r}) = \beta_2 r^2 [\frac{1}{2}(3\cos^2\theta - 1)\hat{\mathbf{z}} - \sin\theta\cos\theta\hat{\rho}]. \qquad (3.15)$$

From 3.14, it is evident that material placed at the zeros of $P_4(\cos\theta')$ will produce no magnetic bottle (i.e. at $\theta' \approx 30°$ and $\theta' \approx 71°$). Since the sign of $P_4(cos\theta')$ changes at the zeros, the effect of material in one region in producing β_2 can be cancelled by an appropriate amount of material in a region where $P_4(\cos\theta')$ is of opposite sign. Figure 3.5 shows the open endcap trap with the zeros of $P_4(cos\theta')$ superimposed on it. It is evident from the figure that the bottle resulting from the two inner macor rings is partially compensated by the outer two rings. For our existing trap construction, the coeficients resulting from the four innermost MACOR rings (assuming M=+0.78) calculated using 3.14 are

$$\beta_0 = -0.53\ Gauss, \qquad (3.16)$$

and

$$\beta_2 \leq +0.84\ \frac{Gauss}{cm^2}. \qquad (3.17)$$

Referring again to Fig. 3.5 it is evident that the trap could be improved and β_2 could be made to vanish by adding the appropriate amount of MACOR to the two outer rings.

The change in the axial component resulting from the presence of the trap in the strong 5.9 T homogenous magnetic field causes a proportional shift in the particle cyclotron frequency. The effect of the bottle on the cyclotron frequency resulting from $\beta_2 = +0.84$ G/cm^2 is

$$\frac{\Delta B_z}{B} \leq 1.4 \times 10^{-5}(z^2 - \frac{\rho^2}{2}). \qquad (3.18)$$

where z and ρ are measured in centimeters.

3.2 Trap Support and Cryogenic System

In many previous experiments where Penning traps have been used for high precision studies, the trap enclosure has been cryopumped and the detection electronics cooled to 4.2 K by immersing the apparatus in a bath of liquid helium. The need to interface the trap to an accelerator facility, led us to construct a cryogenic system where the the trap enclosure and the cooled pre-amplifiers reside in a vacuum and are heat sunk to a helium Dewar. This scheme has the major advantage that antiproton access into the magnet bore and to the trap is not impeded by liquid helium and the relatively thick wall enclosure necessary to make a liquid helium container.

The basic design consideration is to provide a liquid helium cooled support (or cold finger) to an enclosure containing the trap described in Section 3.1. This system must fit into a 100 mm diameter magnet bore (Section 3.3) and be able to hold the trap near 4.2 Kelvin in order to achieve the ultra-high vacuum necessary for sufficient antiproton containment times. It is also essential that the preamplifiers used for detecting the confined particle motions are as cold as possible in order to maximize signal to noise. Because of the frequency regime in which we operate (1-100 Mhz), it is necessary that this region be as close to the trap as possible to avoid capacitive coupling of the weak signals to ground before being detected. Other design constraints include the desire for long helium hold time, and the need to be able to remove, work on, and cycle the apparatus quickly.

3.2.1 Description

The developed trap support and cryogenic system consists of six modular components shown in Fig. 3.6. The whole system is assembled, wired, tested, and then lowered into the 100 mm diameter bore of a superconducting magnet. The following briefly describes each section of the apparatus required to hold and cool the open endcap cylindrical trap.

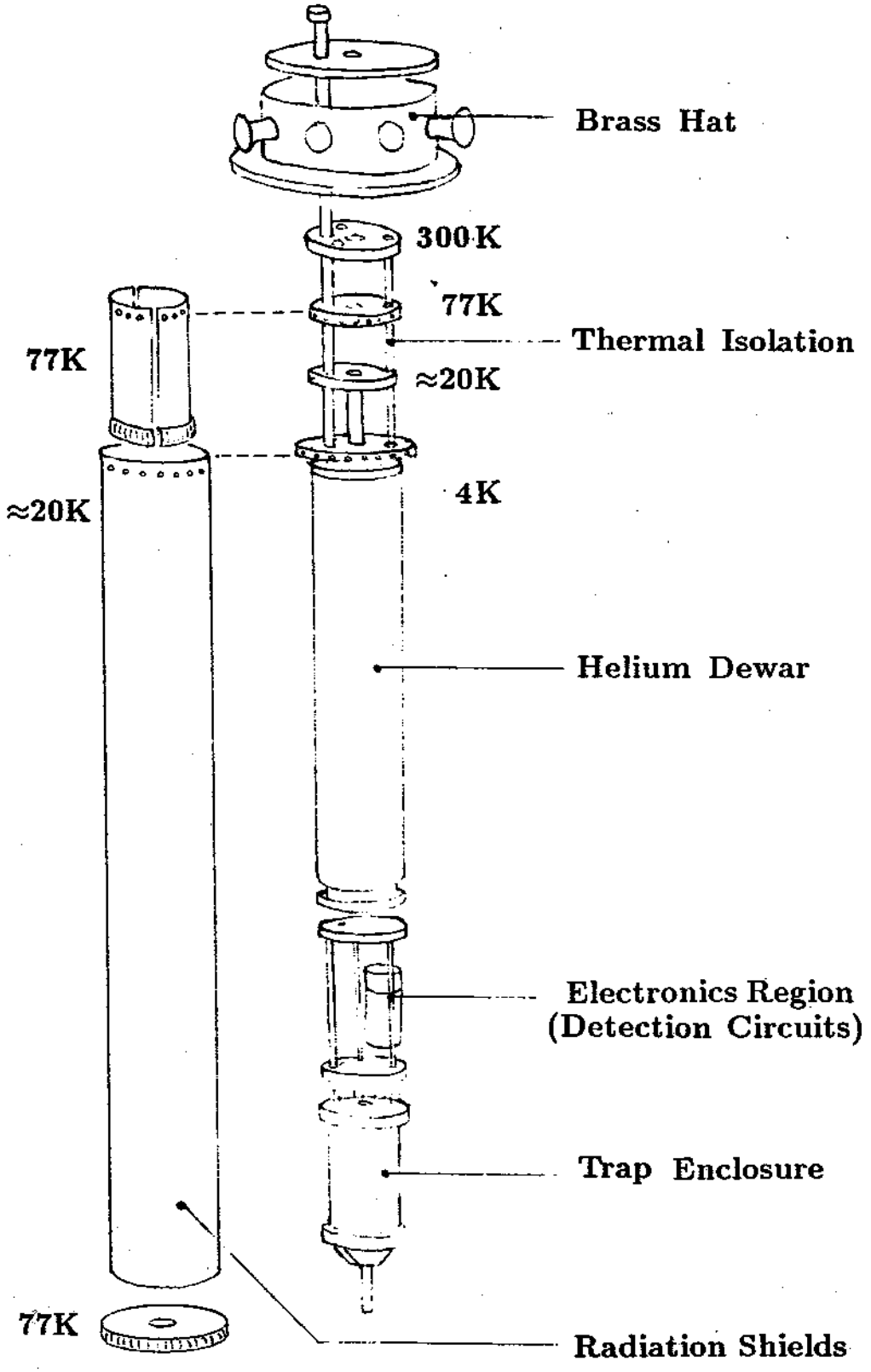

Figure 3.6: The cryogenic system shown assembled from its modular components.

The Brass Hat

The trap apparatus is suspended from a brass structure (often referred to as the 'hat') which forms the upper vacuum enclosure of the vertical magnet bore. This hat contains all electrical, vacuum, and cryogenic access to the helium Dewar and the trap itself. All dc lines are passed through commercial 8-pin constantan vacuum feedthroughs [17] which are welded or hard soldered into standard quick flange blankoffs (Tube OD=1.5"). Over each multipin connector an aluminum box is mounted containing connections to standard 50 Ω bulkhead BNC connectors. RC or LC filters with various time constants prevent unwanted RF leakage onto the dc lines. There is also a liquid helium level sensor and a temperature sensor both of which have a calibrated resistance measured using a standard 4-wire technique. Six RF drive lines and three RF detection lines pass through 50 Ω SMA feedthroughs. Two standard SHV feedthroughs are used to apply high voltages.

Thermal Isolation

A thermal isolation structure is constructed out of 0.375" ID G-10 tubing and 0.25" thick G-10 sheets[78]. G-10 is a strong, epoxied fiber-glass material with very low thermal conductivity. This structure contains a 0.005" thick, 0.5" OD stainless steel tube and bellows system that serve as the liquid helium fill and recovery access to the helium de mounted below. The fill tube is connected to the hat segment above and the helium Dewar below by stainless steel mini-conflat flanges. In addition this region has two OFHC copper plates which are heat sunk to the helium fill and recovery line. A shield constructed from a copper tube is bolted to the upper heat sinking plate and touches the bore of the magnet with silver plated copper beryllium 'fingers' [107] (the magnet bore can be independently kept at 77K). The lower heat sinking plate provides a mounting platform from which a floating thermal radiation shield is mounted. This shield fits over the entire apparatus and reduces the radiation load from the magnet bore to the trap enclosure at 4 K by shunting a portion of the radiative heat load to the helium gas in the recovery line. Finally the G-10 thermal isolation structure serves as a

guide for over 40 wires going to the trap.

The G-10 structure is assembled using small aluminum pins and epoxied together using Ren-Weld epoxy. Accurate assembly of this structure is critical to insure proper alignment and maximum performance of the cryogenic system. To keep tolerances tight, we epoxied this structure while it was jigged in a lathe.

The Helium Dewar

The helium de itself is constructed of OFHC copper to prevent thermal gradients along its length as the helium level changes. We wish to avoid such gradients because they might result in very small helium level dependent shifts of the trap center with respect to the magnetic field. The Dewar also has two 0.25" ID tubes through it which serve as access for the dc and RF lines which go to the trap. In addition, a 0.5" ID copper tube passes through the center of the Dewar for possible future access to the center of the trap. The 0.5" access has been preserved in the hat, the thermal isolation stage and the electronics region. Two access ports into the top of the dewar are sealed using S.S. mini-conflat flanges. One port is connected to the helium fill and recovery tube, and the other with a four pin cryogenic feedthrough [17]. This feedthrough is attached to a 20" liquid helium level sensor consisting of a superconducting wire [1]. The wire resistance, monitored using a standard 4 wire technique, is proportional to the liquid helium level. The entire Dewar system was assembled using Cu-Ag eutectic solder in a controlled hydrogen atmosphere at 805°C . The top and bottom endplates were then faced off to ensure they were parallel. The bottom plate was subsequently gold plated for better heat sinking of the trap apparatus below.

The Cold Electronics Region

This region consists of three OFHC 0.375" per side square copper rods connecting two OFHC copper plates which provide a support and heat sinking point for the tuned resonant circuits and FET amplifiers used for particle eigenfrequency detection (described in Chapter 5). These rods also serve as the 'cold finger' between the liquid helium Dewar above and the trap enclosure below. They are also

silver soldered but with lower temperature silver solder. This entire system is gold plated and is bolted to the Dewar above and the trap enclosure below with 48 M-4 brass screws to provide, by compression, good thermal conductivity across the joints [52]. Temperatures during cooldown are monitored with a calibrated carbon glass resistor[63] attached to this region.

The Trap Enclosure

In order to obtain the ultra-high vacuum necessary for long containment times, the trap is mounted in its own vacuum enclosure and cryopumped to 4.2 K. The trap enclosure is constructed of OFHC copper, and indium is used to make the vacuum seal. This system is typically evacuated to around 5 x 10^{-7} torr with a turbo-molecular and/or ion pump and lightly baked to 130°C to remove moisture and other adsorbed gases from the electrode and degrader surfaces. The active pump is removed by pinching off an annealed 0.375" OD copper tube [91].

Electrical leads are passed into the trap enclosure, using 24 single conductor feedthroughs [57]. The non-magnetic feedthroughs consist of a 70% Cu-30% Ni base and cap, and have a copper center wire. We soldered these in the copper pinbase at 805°C using Cu-Ag eutectic solder in a hydrogen atmosphere. (The center wire to pinbase capacitance is $\approx$ 8 pF.) There are also six smaller access ports into the enclosure, one on the top center, and 5 on the bottom flange. Two ports are used for additional electric feedthrough access, one for pumpout access, and one has a glass to metal seal to allow 164 GHz microwaves into the vacuum enclosure. The center port on the bottom is connected to a copper flange and tube. The tube is covered with a 10 μm thick titanium window sandwiched between two titanium rings and electron beam welded together. This thin window is the entrance for the antiproton beam received from LEAR at CERN.

The harmonic trap and the extension electrodes described earlier in this chapter are mounted from the top pinbase using three copper beryllium rods (Fig. 3.4). The trap is kept under slight compression using tungsten springs to accomodate the small length change that occurs when the system is cooled from 300 K to 4 K. The trap support mechanism is referenced to the inner vacuum enclosure walls to

insure vertical alignment.

The top pinbase is designed so that the vacuum enclosure can be removed leaving the entire trap and amplifiers in the electronics region in place or, if so desired, the trap enclosure can be unwired and the sealed vacuum enclosure removed from the rest of the dewar system.

Floating Thermal Radiation Shield

The entire dewar, electronics region, and trap enclosure are enclosed with an aluminum thermal radiation shield. This shield, which has only 1.5 mm clearance over the dewar system and 4.8 mm to the magnet bore is an essential component for minimizing the radiation heat load from the 77 K magnet bore. Currently the shield is prevented from shorting to the trap enclosure by using nylon screws as spacers. A longer pathlength support system should be introduced to reduce the conduction heat load through this path, although the existing thermal gradient is relatively small.

The tube is wrapped in 2 layers of aluminized mylar to reduce the surface emissivity and is heat sunk to the helium fill and recovery tube in the G-10 thermal isolation region to effectively shunt heat radiated from the 77 K bore into the colder helium gas leaving the center dewar, keeping this shield at temperatures well below 20 K. The shield also protects the delicate wiring when the experiment is inserted in the solenoid.

Wiring Harness

The apparatus requires about 32 dc leads, 7 RF Transmission lines, 2 high voltage lines, and a 10 GHz microwave pathway. The wiring must not be magnetic, must not conduct much heat to the helium Dewar, and must not take much space. The low voltage dc lines consist of 0.003" diameter constantan wire insulated with a thin coating of teflon [76]. Radiofrequency drives are applied via twisted pairs of these constantan wires. The 50 Ω detection lines are 0.06" OD coaxial cable with inner and outer conductors made of stainless steel [71]. The high voltage lines are also thin stainless steel coaxial cables interfaced to SHV connectors that have

been modified so that air can be pumped out of their interior regions. Microwaves at 164 GHz are necessary to carry out precision measurements with electrons. Because only small power levels are needed we transmit 10 GHz microwaves to the trap enclosure by using small copper coaxial cable in series with a short piece of stainless steel coaxial cable for thermal isolation, then multiply up to 164 GHz in a diode located near the trap.

Two complete cryogenic and trap systems were constructed to allow rapid replacement if a component failed while antiprotons were available. the possibility also existed to make radical changes or repairs on one system, while taking data with the other. Having two completely independent systems also provided a good opportunity for understanding the level of several important systematics, such as the effect of different trap alignment and imperfections, and the slightly different magnetic field within each system.

3.2.2 Performance

Three major heat transfer mechanisms contribute to the heat load on the 4 K liquid helium reservoir. Convection and conduction processes through gas are eliminated by evacuation of the magnet bore to a pressure better the 10^{-5} torr. Conduction through the thermal isolation region is minimized by material selection and by maximizing path lengths. A forced thermal shunt to the 77 K magnet bore also allows for a longer pathlength between 77 K and 4 K to the liquid helium Dewar. Absorbed radiation is reduced by low emissivity aluminized mylar surfaces and with the use of the floating radiation shield which takes advantage of the substantial heat capacity (i.e. cooling capacity) of helium gas between 4K and 300 K. The addition of this floating radiation shield properly anchored to the helium fill/recovery line more than tripled the Dewar hold time.

The assembled and tested system described in the previous section is lowered into the magnet bore slowly to allow eddy currents time to dissipate and prevent excessive stress on the magnet coils. The experiment can be installed into the magnet when the magnet bore is at 300 K or 77 K. To prevent moisture conden-

sation when the magnet bore is cold, we flow N_2 gas through it whenever it is open.

After the experiment is lowered into position, the magnet bore is pumped to better than 5×10^{-3} torr using a liquid nitrogen cooled sorption pump. This pump provides a smooth and gradual method of rough pumping against the delicate 10 μm thick titanium windows on the trap enclosure and on the incoming beamline system. The liquid helium Dewar system is precooled with liquid nitrogen, and the temperature of the trap enclosure monitored with a carbon glass resistor. The system reaches thermal equilibrium at 77 K after approximately 12 hours, limited predominantly due to the long time constant to remove the heat from the floating thermal radiation shield. This precool period has been forced to as short as 1.5 hours, but the helium boiloff is then extremely high for the first day requiring at least 2 more refills. After an optimum 12 hour wait or longer, we blow out the remaining liquid nitrogen and fill with liquid helium. The initial cooldown and fill of the 3.7 liter capacity takes approximately 9 liters (including transfer line cooldown losses), and subsequent fills take just under 5 liters. The trap enclosure is at 4.2 K by the time the helium has collected, demonstrating the effectiveness of our gold plated compression joints (no grease is used). Even though the vacuum is sufficient so that the trap can be immediately loaded, the tuned RF circuits have a cooling time constant of a couple hours as observed in the drift of their resonant frequency.

The hold time of the 3.7 liter Dewar in a completely wired state, but with the Field Effect Transistors (FET) off, is 6 days. This corresponds to a boiloff rate of less than 26 ml/hr or a total heat load to the liquid helium reservoir of 18 mW. With all three detection amplifier FET's on continuously, the heat load increases by 50% ($\approx$ 3 mW per amplifier) and the holdtime is reduced to about 4 days.

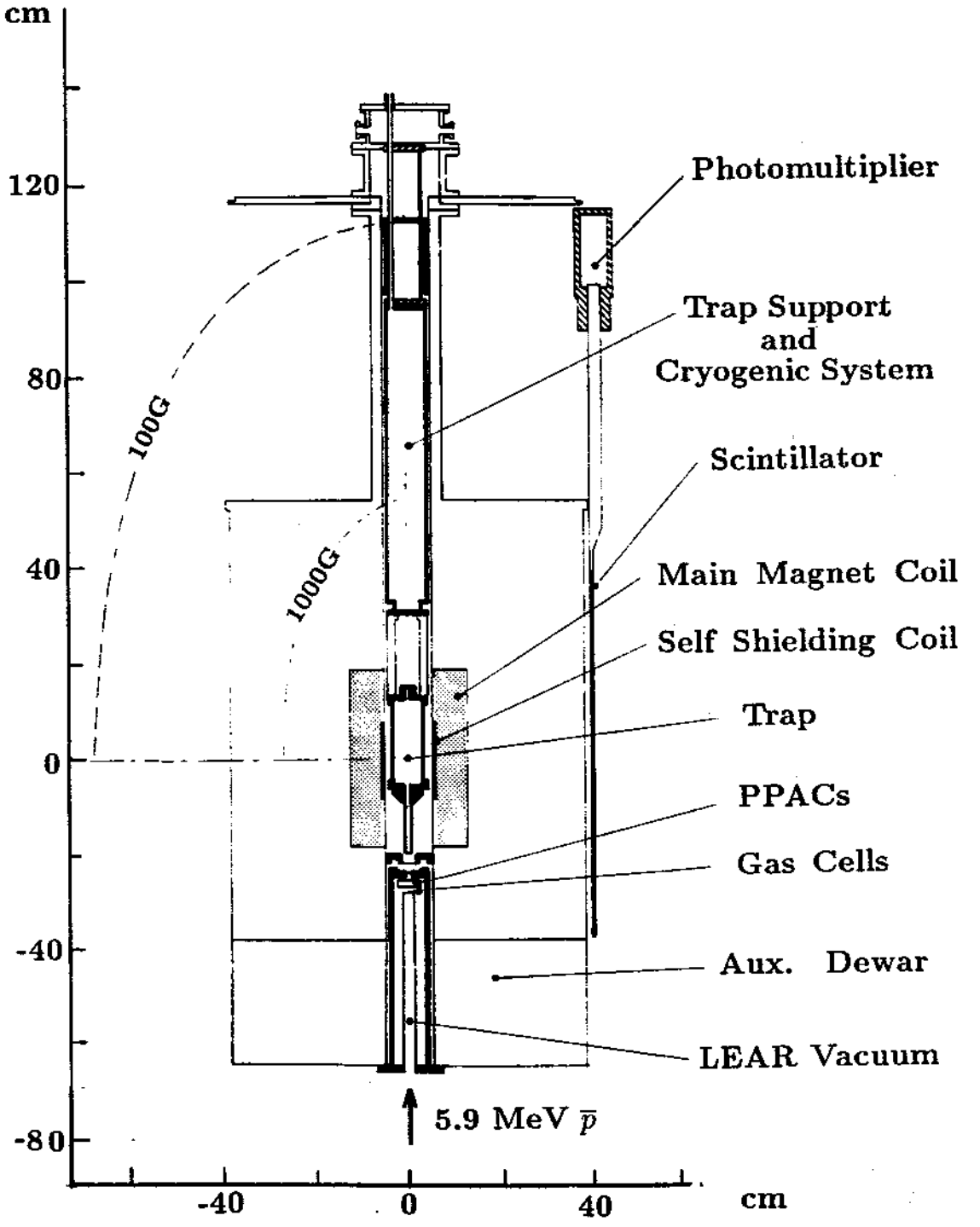

Figure 3.7: The Nalorac superconducting magnet with the antiproton trap and cryogenic system inserted into the bore and interfaced to the LEAR beamline.The magnet has a 100 mm diameter bore that can be cooled to 77 Kelvin.

3.3 Shielded Superconducting Magnet

3.3.1 Specifications and Field Shimming

The properties of the magnetic field in the trapping region are of crucial importance to the success of the mass comparison technique. Since we observe the modified cyclotron frequency of confined particles, the ultimate precision and accuracy of the measurement directly depends upon the magnetic field homogeneity and time stability over the trapping volume.

Because of the stringent field homogeneity and stability requirements for the highest precision mass comparisons, we acquired a state-of-the-art superconducting solenoid from the Nalorac Cryogenics Corporation [75]. The maximum field strength is 5.9 T and the bore diameter is 100 mm. With such a field strength the antiproton cyclotron frequency is in the FM radio band at about 89 Mhz, requiring a measurement of the cyclotron frequency to better than 0.1 Hz for 10^{-9} resolution.

For ease of access to the field center, the vertical magnet has a through bore so that the accelerator may be interfaced to the bottom, and the trapping apparatus inserted from the top (Figs. 3.6, 3.7, and 3.10). The bore of the solenoid is heat sunk to its own liquid nitrogen cryostat and can be operated at room temperature or cooled to 77 K to provide the necessary thermal isolation to maintain the particle trap at liquid helium temperatures. The bore is constructed of an OFHC copper tube to minimize thermal gradients along its length, and is thermally isolated from its external flanges by 15 cm long segments of 100 mm ID G-10 tube.

The main magnet solenoid resides in its own ultra low loss liquid helium cryostat (hold time $\geq$ 3 months), is constructed using single filament niobium titanium wire wound onto an aluminum spool. Differential currents in the main solenoid can be used to create parabolic field contours along the symmetry axis, but for the purpose of the mass comparison, we adjust coil currents to obtain maximum field uniformity along the z axis. Several additional superconducting shim coils allow for field compensation. Axial field correction is provided from zero through third order, and radial correction is provided from zero through second order.

There are also three shims which operate at room temperature allowing for small adjustments to be made at any time. They include shims for slightly changing the uniform field ΔB_0 and the first and second order axial gradients $\Delta B_1(z)$ and $\Delta B_2(z^2)$. The room temperature shim range is measured to be

Shim	Full Range	Fractional Shift
B_0	$\pm$ 1.3 G	$\pm$ 22 $\times$ 10^{-6}
B_1	$\pm$ 1.5 G/cm	$\pm$ 25 $\times$ 10^{-6}
B_2	$\pm$ 0.2 G/cm^2	$\pm$ 3 $\times$ 10^{-6}

These shims are very useful for cyclotron resonance identification, for tuning out the residual bottle field, and for performing systematic checks.

The decay of the persistent field is specified to be less than 1 part in 10^{-9} per hour.

Pulsed NMR Measurements

To check the magnet specifications and for initial shimming purposes we have constructed a simple pulsed Nuclear Magnetic Resonance (NMR) system. The advantage of such a system is that we are able to shim out field gradients over a much larger volume than is feasible using only confined particles in our Penning trap. The NMR sample is a 1 cm diameter sphere of high purity acetone and we measure the proton NMR precession frequency ($\approx$250 Mhz) at the field center where the Penning trap is to reside. For these measurements, the magnet bore is open to the atmosphere and at room temperature.

The protons in the NMR sample are driven near their natural precession frequency with a strong transverse magnetic field. After a strong drive pulse, the protons precess freely about the magnetic field axis, inducing a signal which is detected by the same coil used to drive them. The precession signal decays over time as the proton nuclear moments This Free Induction Decay(FID), is shown in Fig. 3.8 along with the Fourier transform. The linewidth of this transform is

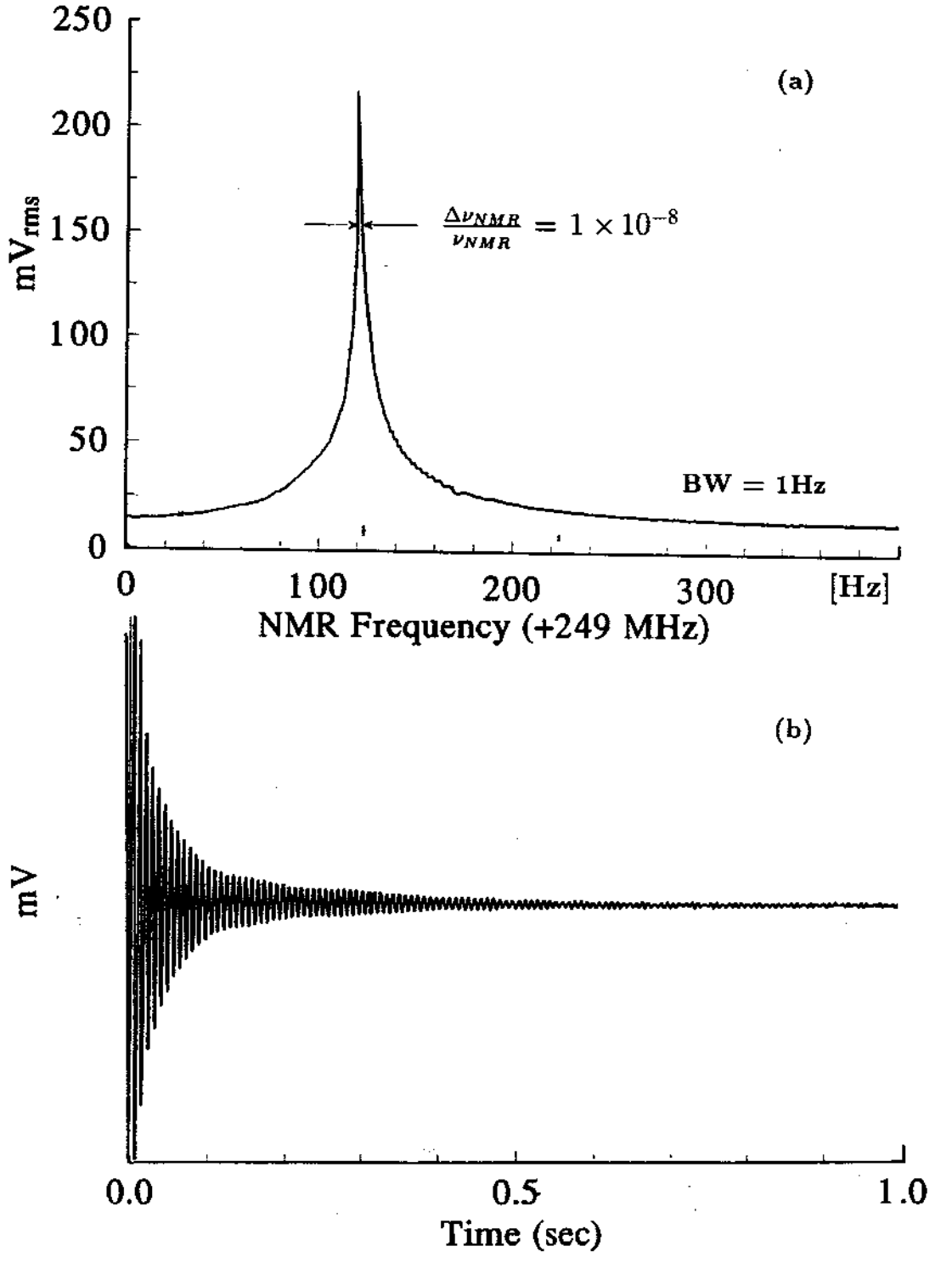

Figure 3.8: (a) Proton NMR signal mixed down from 249 MHz. (a) Fourier transform of the proton precession from a 1cm diameter spherical sample of acetone. The linewidth represents a field homogeneity of $\Delta B/B=10^{-8}$ over the sample volume. (b) Free Induction Decay of the precessing proton spins.

related to magnetic gradients present over the sample volume. By minimizing the Fourier transform linewidth and maximizing the amplitude while we adjust the superconducting shims, we tune out the large magnetic gradients maximizing the homogeneity over the 0.5 cm^3 acetone sample.

The gradient fields imposed on the magnet system are quite large in the experimental area, since the experiment is surrounded by very large concrete block walls required for radiation shielding from the nearby accelerator beamlines (see Fig. 3.10). Some of the large concrete blocks, with steel reinforcing inside, are as close as 1 meter from the magnet center. Directly below the superconducting solenoid are large bending magnets necessary to direct upwards the 5.9 MeV antiprotons from LEAR. Fortunately these strong magnetic sources are fixed in space so that most of the gradients imposed by their proximity can be permanently shimmed out of the trapping region by fine adjustment of the magnet currents.

The field can be shimmed using the superconducting shims to 1 part in 10^8 over the 1 cm diameter sample. The FID of the NMR sample is shown in Fig. 3.8. Unfortunately, by removing and reinserting the NMR probe into the magnet, the resonance can broaden up to 5 parts in 10^7. This suggests that the fine shimming is related to the NMR probe itself (constructed of aluminum, copper, G-10 and quartz) resulting from its own para- and diamagnetism. For effective shimming and homogeneity measurements at the most precise levels, and to take into account the residual bottle field from the trap electrodes themselves, higher precision measurements of the trapping field homogeneity must be made directly in the actual trap apparatus.

3.3.2 Self Shielding System

To compare the masses of the proton and antiproton to a precision of 10^{-9} in a 5.9 Tesla magnet requires that the time stability be better than 6 nT (60 μG) over one hour (a typical time necessary to prepare and compare the cyclotron frequencies of two species of ions). Fluctuations in the earth's magnetic field can vary more than ten times this amount. In many laboratories other sources of magnetic fluctuations, such as elevators and subway lines, have been a common

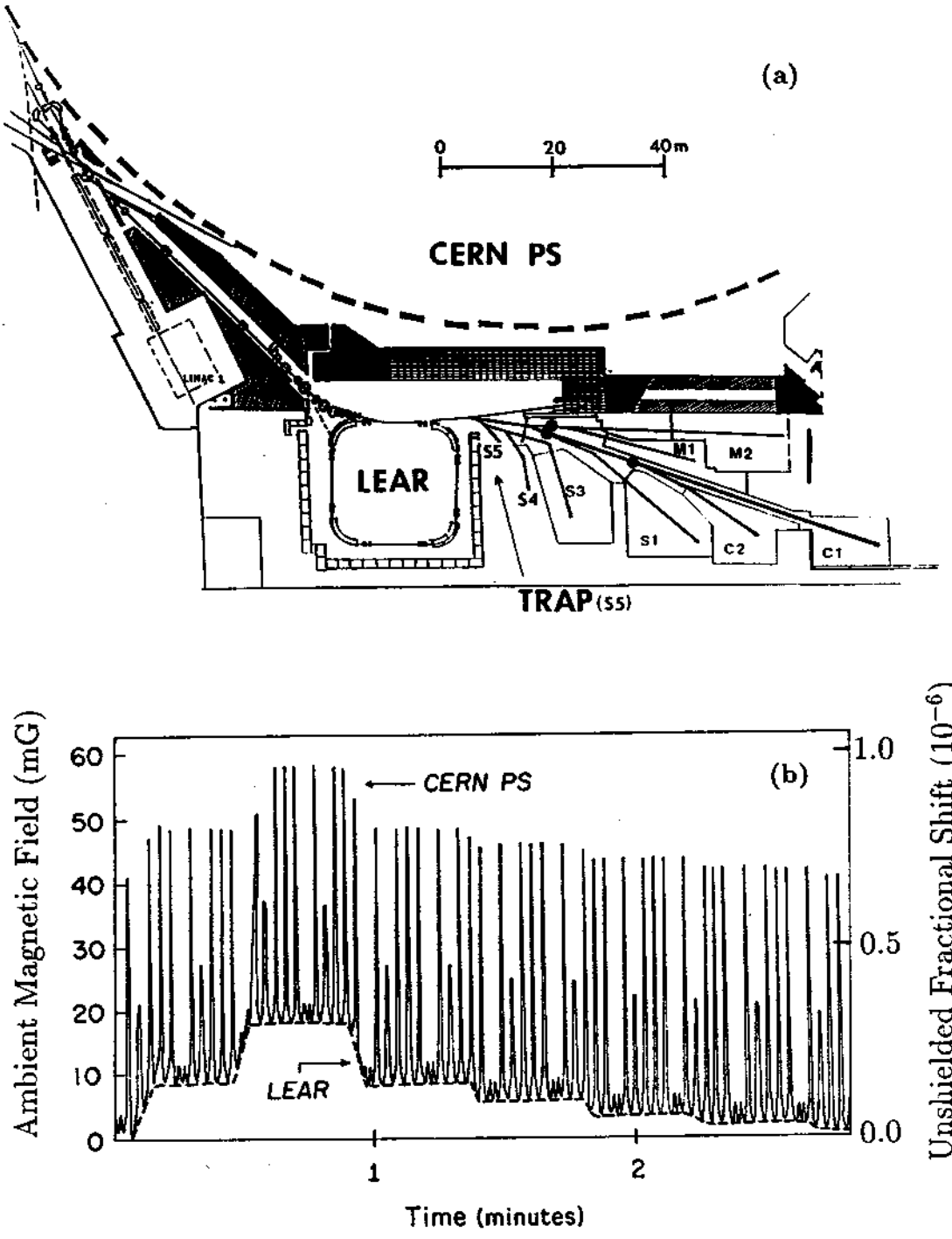

Figure 3.9: (a) LEAR and associated experimental areas with the CERN PS shown nearby. The trapping apparatus is located in zone S5. (b) Magnetic field fluctuations in zone S5 resulting from the PS and LEAR cycling their respective magnets. (The typical LEAR cycle takes about 15 minutes and is of opposite polarity shown here).

hindrance to the accuracy achievable in high precision measurements. Our need for antiprotons, which can only be obtained at high energy accelerator facilities, presents us with the difficult challenge of doing high precision mass spectroscopy in an environment where magnetic field perturbations can be much larger than normal.

Our experiment is located only 8 meters from the Low Energy Antiproton Ring, and approximately 19 meters from the Proton-Synchrotron of CERN (Fig. 3.9). In addition, two large 5.9 Mev bending magnets are 1 meter below our superconducting solenoid (Fig. 3.10), and two very large steel overhead cranes can move to within 2 meters of the magnet. A detailed quantification of the field in the experimental hall is given in Chapter 10, but it suffices here to note that the largest controllable fluctuations (e.g. from our bending magnet), are on the order of 20 μT (0.2 G) and the largest uncontrollable on the order of 4 μT (0.04 G). If there existed no field compensation at the center of the trap, the uncontrollable fluctuations would correspond to fractional changes in the trapping field of up to 7 parts in 10^7. While careful selection of measurement times avoids some of the largest perturbations, screening of the ambient field fluctuations is of prime importance towards success of the experiment. Passive shielding constructed of high permeability materials such as μ-metal is not feasible since they would saturate in the high field unless located farther from the superconducting solenoid than available space will allow. Type I superconductors such as lead or niobium cannot be used since the large magnetic field (several Tesla) is above their critical field. Active feedback to e.g. a Helmholtz coil could possibly be incorporated using a second sensor probe near the trap center at 4 K (e.g. a second particle trap or a ^{3}He NMR probe).

The solenoid provides partial self screening to external fluctuations, measured to be about a factor of -4.27(7) [46]. At best this reduces uncontrollable fluctuations to about 2×10^{-7}, still far from our ultimate goal of comparing the antiproton and proton masses beyond the 10^{-9} level. To obtain further screening, we had our Nalorac magnet fitted with an additional superconducting coil with dimensions based on a computation by Gabrielse and Tan [42]. The idea takes advantage

of the flux preserving properties of a superconducting coil. With the proper coil geometry, the induced current in the shielding coil resulting from a change in the ambient field generates a magnetic field at the coil center (the trap location) which is equal in magnitude but opposite in direction to the ambient fluctuation. Thus the effective magnetic field at the trap center where the trapped particles reside remains essentially constant.

In the relatively quiet laboratory at Harvard University, we measured the effectiveness of the additional shielding coil using pulsed NMR and by applying a nearly uniform magnetic field with two square coils 2.81 meters on a side and separated by 1.53 meters. The shielding was measured to be [46]

$$S = \frac{\Delta B_{outside}}{\Delta B_{inside}} = -156(6). \tag{3.19}$$

This is a significant improvement which greatly aids our ability to perform the antiproton mass comparison in the experimental hall at CERN. In addition to the shielding, the same NMR linewidth is observed with the shielding coil as without it, indicating that the spatial homogeneity is not compromised over the 1 cm diameter spherical volume of the NMR sample.

The shielding system is most effective for shielding spatially uniform fluctuations and linear gradients in the ambient field [42]. Since the experiment is located in an accelerator environment, the field fluctuations from nearby sources have a component which is not spatially uniform. Fluctuations are further distorted by the large amounts of ferromagnetic steel in the concrete shielding, resulting in a shielding factor which varies as a function of the source (see Chapter 10).

3.4 RF Shielding and Grounding

For mass spectroscopy with RF techniques, isolation from the ambient radio frequency environment is important. At CERN, the RF environment is especially troublesome because of the current switching and RF generation used for accelerating particles. The detected signals are small and, in addition, the cyclotron frequency of the antiproton is in the FM radio band and the antiproton axial fre-

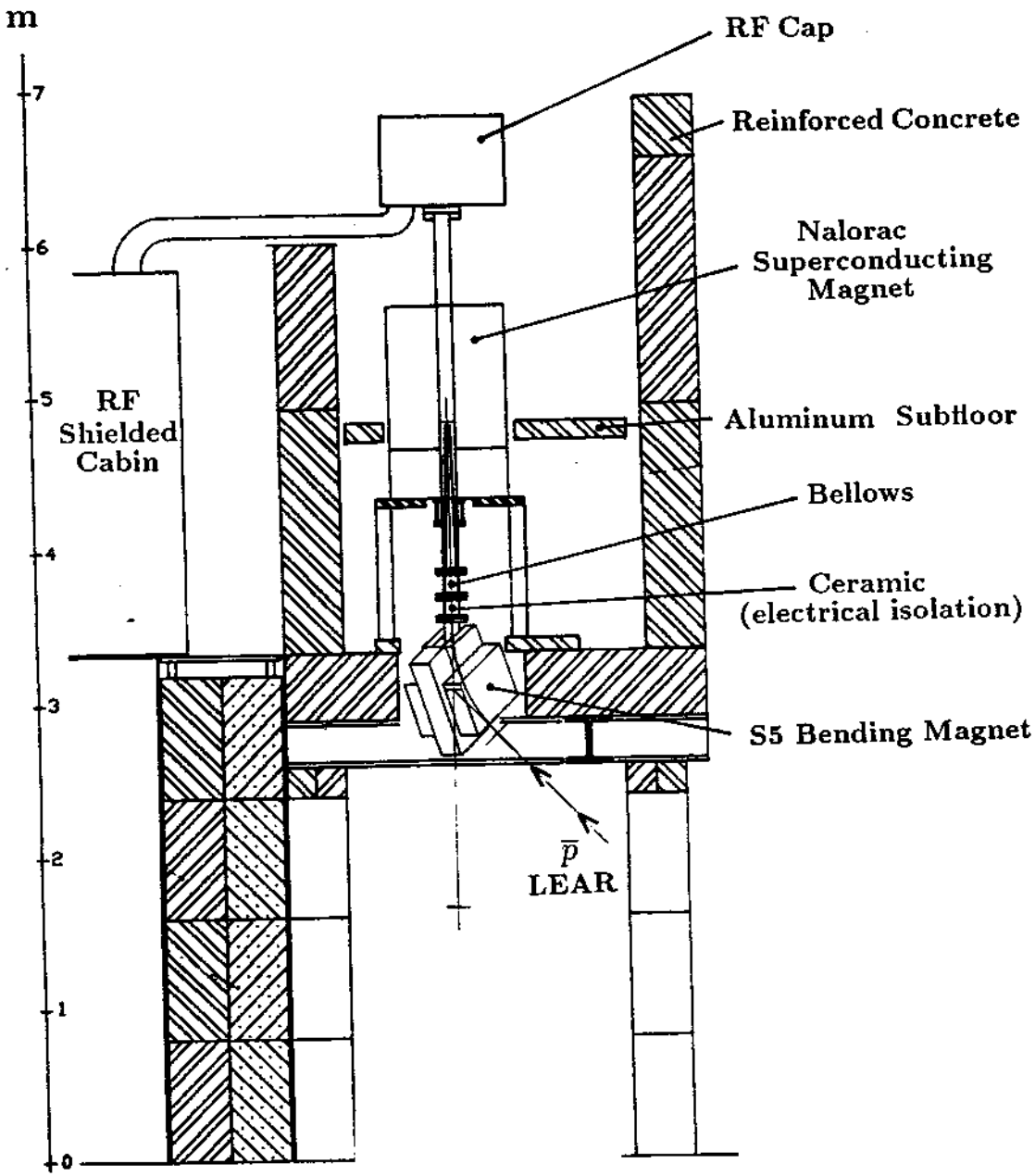

Figure 3.10: An overall view of the experimental zone showing the Nalorac magnet and the RF shielded region.

quency is near the AM radio band. If such signals leak into the trap, they may heat the particle motions.

There are many space constraints in the area of our experiment and placing the whole experiment in an RF enclosure was not possible. Instead, we have a smaller RF shielded cabin for the drive and detection electronics as shown in Fig. 3.10. The RF cabin is connected to the magnet vacuum enclosure using a large diameter corrugated aluminum tube containing all the electrical leads (mostly double shielded coaxial cables) between the electronic cabin and the trap apparatus located in the magnet bore. The cabin, tube, and magnet vacuum enclosure form a grounded RF shield. Part of the grounded 'shield' is a 30" diameter aluminum plate bolted on the top of the magnet. Amplifiers and other electronics which need to be physically close to the trap are bolted here. The region over the magnet is covered with an aluminum cap to complete the RF shield, and the magnet is electrically uncoupled from the LEAR complex by a ceramic connection to the beamline just below the superconducting solenoid.

Unfortunately, not all of the leads to the experiment access through the RF cap. Several leads are required for antiproton beam diagnostics at the bottom of the magnet. In addition, the cryogenic level sensor lines and the room temperature magnet shim leads enter the magnet from points outside of the RF cage formed by the cabin, tube, cap, and magnet bore. These external lines can be troublesome for allowing unwanted RF into the system either directly or perhaps by closing a ground loop. Generally, these are disconnected during the most sensitive measurements.

Chapter 4

Cryogenic Antiprotons

The antiproton is one of the few stable particles suited for long term storage and study in an ion trap. LEAR provides antiprotons which still have energies many orders of magnitude higher than the meV energies associated with confined electrons or protons in a trap cooled with liquid helium. To emphasize the new scale of our experiment, we recall that a supply of electrons and protons is obtainable using only a tiny field emission point (FEP) as an electron source. Our source for antiprotons, much of the CERN complex, covers more than $10^5\ m^2$. In this chapter, we describe our technique for trapping and cooling antiprotons for study at energies in thermal equilibrium at 4 K [37,44,45,28].

4.1 Antiprotons provided by CERN

Antiprotons are created at CERN near Geneva, Switzerland. Four to six bunches of protons accelerate to 26 GeV/c in the Proton-Synchrotron (PS) machine every 2.4 seconds and collide with a fixed Iridium target. Antiprotons are produced by pair creation and are collected into the Antiproton Accumulator Ring (AA) with a momenta of 3.5 Gev/c. The AA and the Antiproton Collector (ACOL) collect, cool and store antiprotons at high energy for various experiments. The largest consumer of antiprotons at CERN is the Super-Proton-Synchrotron(SPS), for collision experiments with protons at energies up to 310 Gev.

For lower energy experiments, antiprotons are sent to the PS, decelerated to around 600 MeV and transferred to LEAR. In LEAR their momenta can be fur-

ther increased (as high as 2 GeV/c) or decreased while keeping them cold using primarily stochastic cooling techniques. Presently, the lowest available momenta which LEAR generally provides is 105 MeV/c though recently 60 MeV/c antiprotons have been provided with substantially reduced beam quality. While these are low energies by CERN standards, it is still nearly 10 orders of magnitude higher than the cryogenic temperatures at which protons and electrons are studied in the trap (see Fig. 4.2).

LEAR typically slows about 10^9 antiprotons to 5.9 MeV per fill cycle. For most experiments, LEAR operates in a 'slow extraction' mode, delivering antiprotons slowly and continuously over 1-3 hours. To obtain much higher intensities for loading antiprotons in our trap, the LEAR staff developed a 'fast extraction' mode of operation where they bunch the beam in their machine and provide a 200 ns pulse containing up to 3×10^{-8} antiprotons. In 1986, after first demonstrating the external loading of 1 keV protons [38], we demonstrated the first loading of antiprotons into a Penning trap using 200 Mev/c antiprotons from LEAR [37]. At the present, we receive the pulse of antiprotons with a momentum of 105 MeV/c (kinetic energy 5.9 MeV).

4.2 Energy Reduction and Confinement in a Penning Trap

To load the trap, we first reduce the antiproton energy by passing the beam through the degrader with the thickness carefully chosen to range out the antiprotons. The straggling width of the antiprotons that survive is about 1 MeV. Of the antiprotons which emerge from the degrader, most of them still have kinetic energies much too high for confinement in a Penning trap. Since easily obtainable voltages across the small dimensions of our trap are no more than a few kiloVolts, only the lowest energy antiprotons can be captured. Many of the slow antiprotons emerge from the degrader at large angles from the direction of the incident beam due to multiple scattering. Because the degrader already resides in a highly uniform field, most of the the transverse energy goes into the cyclotron orbit about

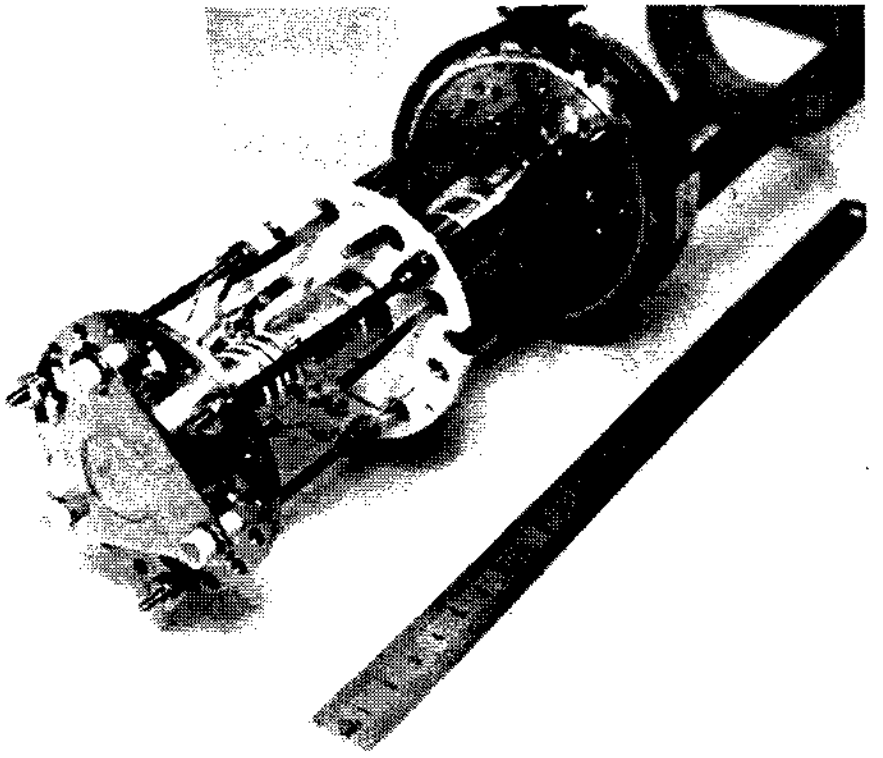

(a)

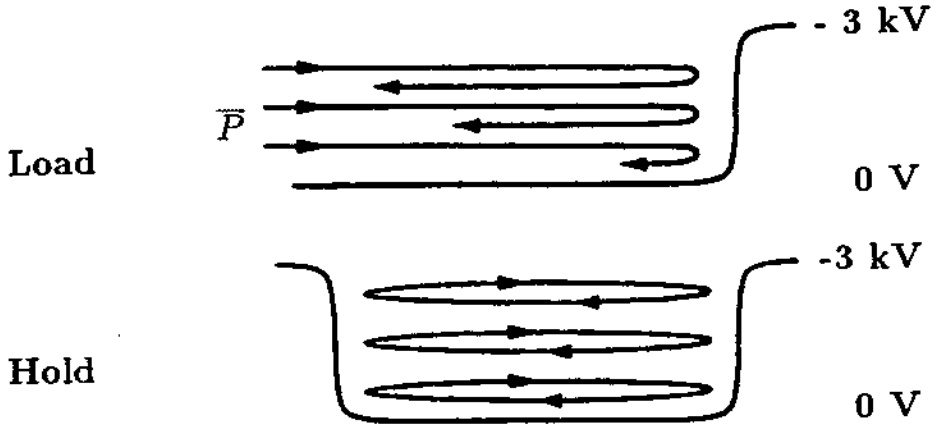

(b)

Figure 4.1: (a) The extended trap showing the gold plated aluminum degrader used to reduce the incoming antiproton energy to below 3 kV (scale in cm). (b) Schematic representation of the loading process and the potentials along the axis of the trap.

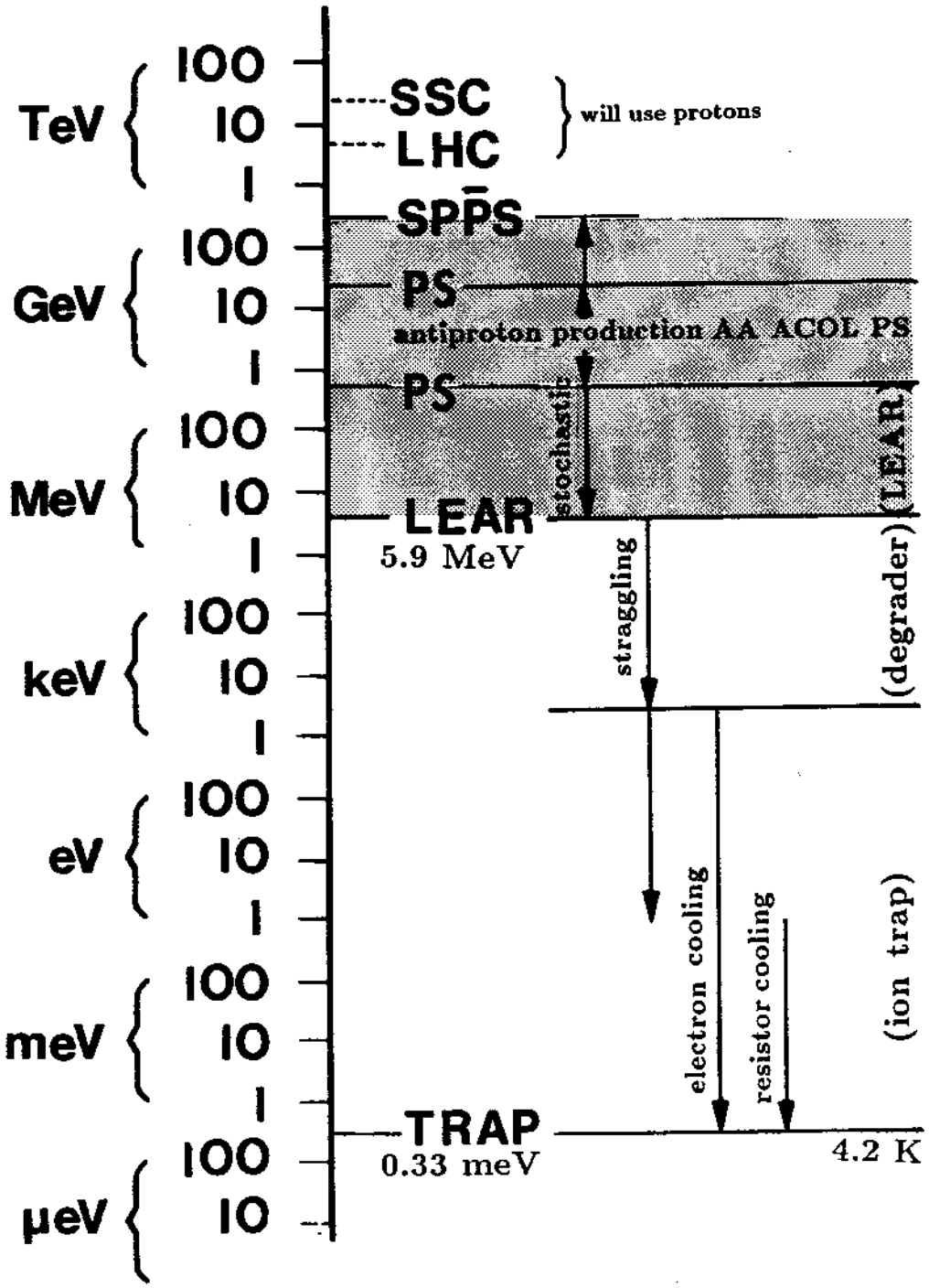

Figure 4.2: Antiproton energy scale summarizing our techniques to reduce the antiproton energy by more than 10 orders of magnitude.

a magnetic field line. Antiprotons with axial energies less than 3 keV travel slow enough to be captured in the trap shown in Figs. 3.4 and 4.1.

During the intense antiproton pulse, the degrader must be biased at more than +3 Volts to prevent low energy secondary electrons generated at the degrader from traveling into the trap (1.5 eV electrons travel with a similar velocity as 3 keV antiprotons). We typically bias the degrader with +100 V). The other trap electrodes are held at ground except the farthest electrode (the exit endcap) which is at -3 kV. With this arrangement, antiprotons emerging from the degrader with less than 3 keV of energy travel along the trap axis and turn around. Before the low energy antiprotons can escape through the entrance, the potential on the entrance endcap is suddenly lowered to -3 kV, confining the antiprotons along the trap axis completing the trap. The potential is switched in about 20 ns using a krytron switching circuit [27].

In the 1986 loading demonstration, the entrance electrode was a cylindrical ring around a beryllium degrader [37]. In the most recent version of the experiment, the degrader, seen in Fig. 4.1, is a 117 μm thick aluminum disk plated with a thin layer of gold (to prevent aluminum oxide buildup that might allow the degrader to charge in an uncontrolled fashion). The degrader, also used as the lower high voltage endcap, and upper high voltage endcaps are rigidly mounted on alumina insulators. The MACOR insulating spacers used in other regions of the trap were found to not be sufficient for holding potentials much above 1 kV.

In practice, the degrading matter consists of other materials such as titanium vacuum windows and aluminized mylar thermal shields. Fine tuning of the degrader thickness is accomplished using two gas degraders (Fig. 3.7). One degrader cell contains a mixture of helium and SF_6. The cell is kept at 1 atmosphere so that the pressure on the 10 μm thick titanium vacuum window is always kept constant. The relative ratio of the two gases allows a means of varying the effective density, and thus provide slight variations in the total degrader thickness. A second gas cell, also at one atmosphere, provides the possibility to make a larger discrete change by using either SF_6 or nitrogen gas. As an interesting sidenote, the total thickness of the degrading material to range out antiprotons and protons of equal

incident energy of 5.9 MeV was measured to be different by about 5%, due to the Barkas effect [44].

Finally, steering profile and intensity information about the incident antiproton pulse from LEAR is obtained by a parallel plate avalanche counter (PPAC) [66]. This device sits between the degrading gas cells, measuring the incoming antiproton beam profile with a resolution of 2mm. Two orthogonal detectors indicate the X and Y steering. The detector operates with 70 Torr of isobutane (C_4H_{10}) and is made of non-magnetic and low density materials. The detector anodes are made by etching aluminized mylar and the thin windows are supported on a 90% transmission molybdenum grid. The total energy loss from the 5.9 MeV incident beam due to the PPAC's is 220 keV. Even though the detector resides in a field of nearly 1 Tesla, its efficiency is still better than 50%.

Using the technique described in this section we have successfully loaded more than 130 000 antiprotons in the long cylindrical trap with energies ranging between 0 and 3 keV from a single pulse of antiprotons from LEAR. Using the number of antiprotons to leave LEAR, we capture with an efficiency of 4×10^4. The real efficiency is higher (since not all of the antiprotons leaving LEAR reach our experiment) and could be increased by applying a larger trapping potential to a longer trap.

4.2.1 Measuring the Antiproton Energy

We analyze the axial energy distribution of the confined antiprotons by linearly reducing the exit endcap from -3 keV through 0 volts. Those antiprotons with an axial energy exceeding the endcap potential leak out of the trap. They annihilate upon striking the vacuum enclosure above, producing on average 3 pions for each annihilation, which are detected in six plastic scintillators that surround approximately $0.5(4\pi)$ steradians of the trap in the superconducting magnet (pion coincidences in two or more scintillators occur for 36% of the detected annihilations). Annihilations are detected with an efficiency measured to be $46.4 \pm 2.4\%$. This provides an absolute determination of the number of confined antiprotons.

The voltage ramp is linear in time, so the annihilation spectrum recorded in a

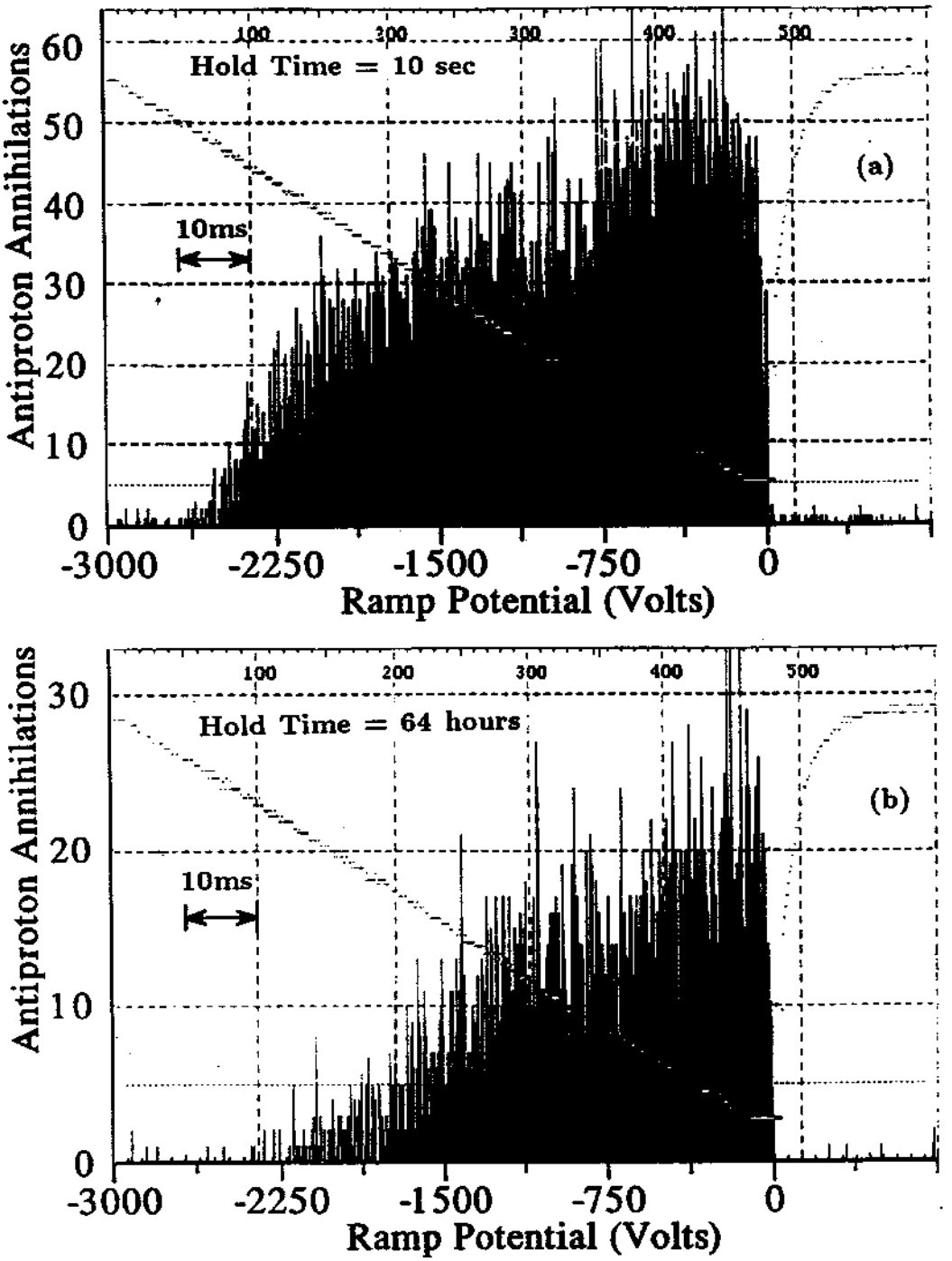

Figure 4.3: Energy spectrum for antiprotons after capture from LEAR into the long trap (a) after a 10 second holdtime and (b) after a 64 hour holdtime. The high voltage ramp as a function of time is superimposed for clarity.

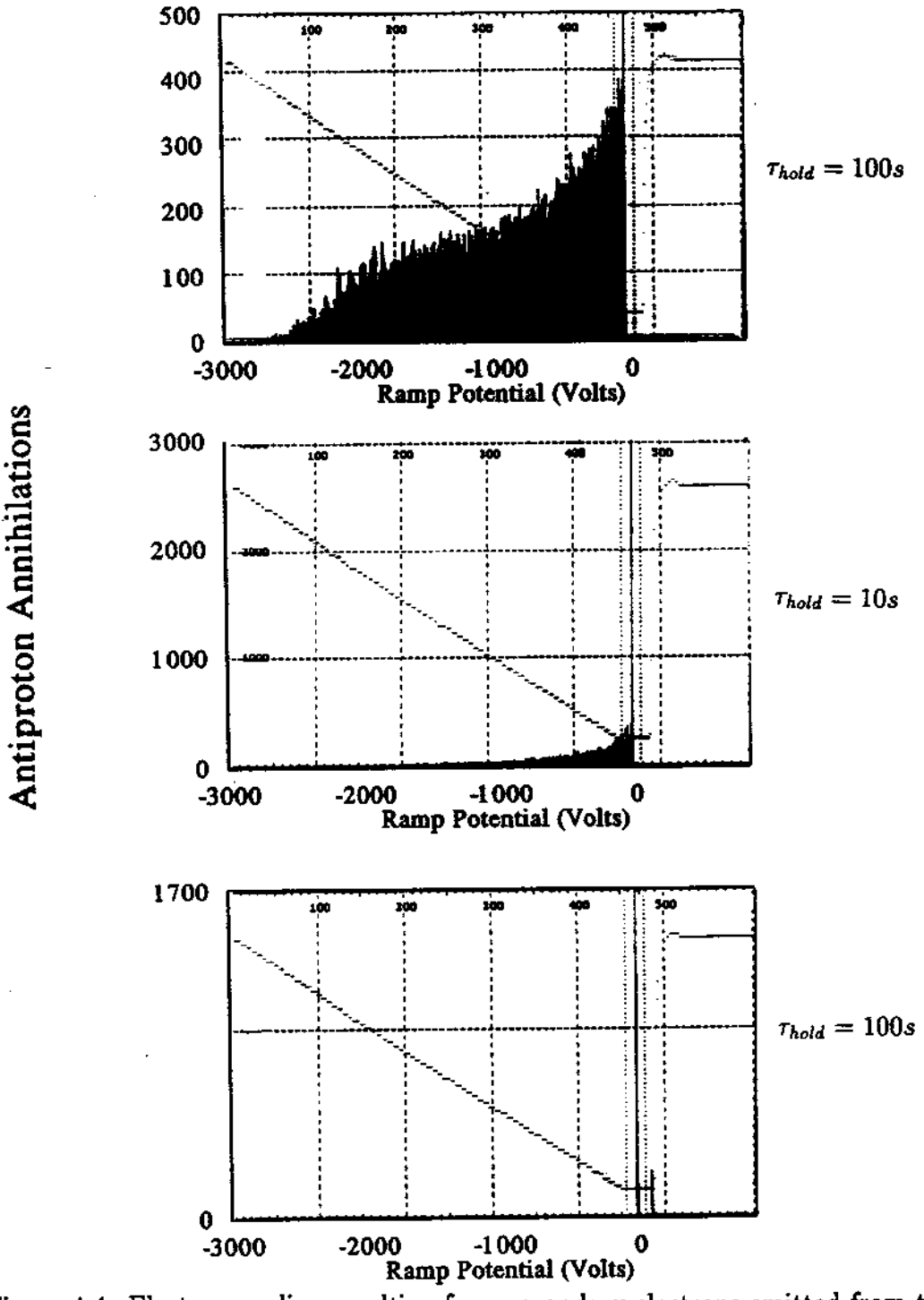

Figure 4.4: Electron cooling resulting from secondary electrons emitted from the degrader (a) in the long trap, and (b,c) in one-half of the long trap.

multiscaler during the ramp duration (typically 100 ms) is for our purposes here a direct measure of the antiproton axial energy spectrum. The energy distribution between 0 and 3 keV (Fig. 4.3) should be nearly uniform since it represents a narrow energy slice of the straggling spectrum emerging from the degrader (HWHM $\approx$ 100 keV). The lack of antiprotons above 2.5 keV results from the finite round trip length of the trap (ranging between 28 and 34 cm in different versions). The fall off of energies near the cutoff is a consequence of the incoming pulse having a duration near 200 nS.

In Fig. 4.3 we display energy spectra corresponding to two loads which originate from essentially identically steered shots and had nearly the same load intensity as seen in the PPAC detectors. The upper spectra is a very typical load of about 25000 antiprotons held in the long trap for 100 seconds. The lower spectra is a similar load, but confined in the trap for 64 hours. There appears to be some particle loss, which may be due to the stability of such a long trap for low energy particles [26]. The lack of damping in the energy spectra demonstrates the need for an efficient cooling mechanism to reduce the antiproton kinetic energy [61,84].

For sufficiently large shot intensities from LEAR, if the degrader is not biased with a positive potential, secondary electrons are emitted from the degrader. Electrons with an axial energy less than approximately 1.5 eV are also confined and will quickly synchrotron radiate to the 4 K trap environment and can cool the antiprotons. Figure 4.4 shows partial cooling of the antiproton spectrum. Since cold particles are not stable in the long trap and the densities are low, cooling is observed for only the most intense shots received from LEAR. When the trap length is shortened by a factor of 2 (Figs. 4.4(b) and (c)) the trap is more stable and the cooling is much more effective.

4.2.2 Electron Cooling into the Harmonic Well

Unlike the more massive antiprotons, electrons synchrotron radiate into thermal equilibrium with the environment with time constants on the order of 0.1 seconds. We control the cooling process by loading electrons into the harmonic well and then capture antiprotons in the long trap. The antiprotons oscillate the

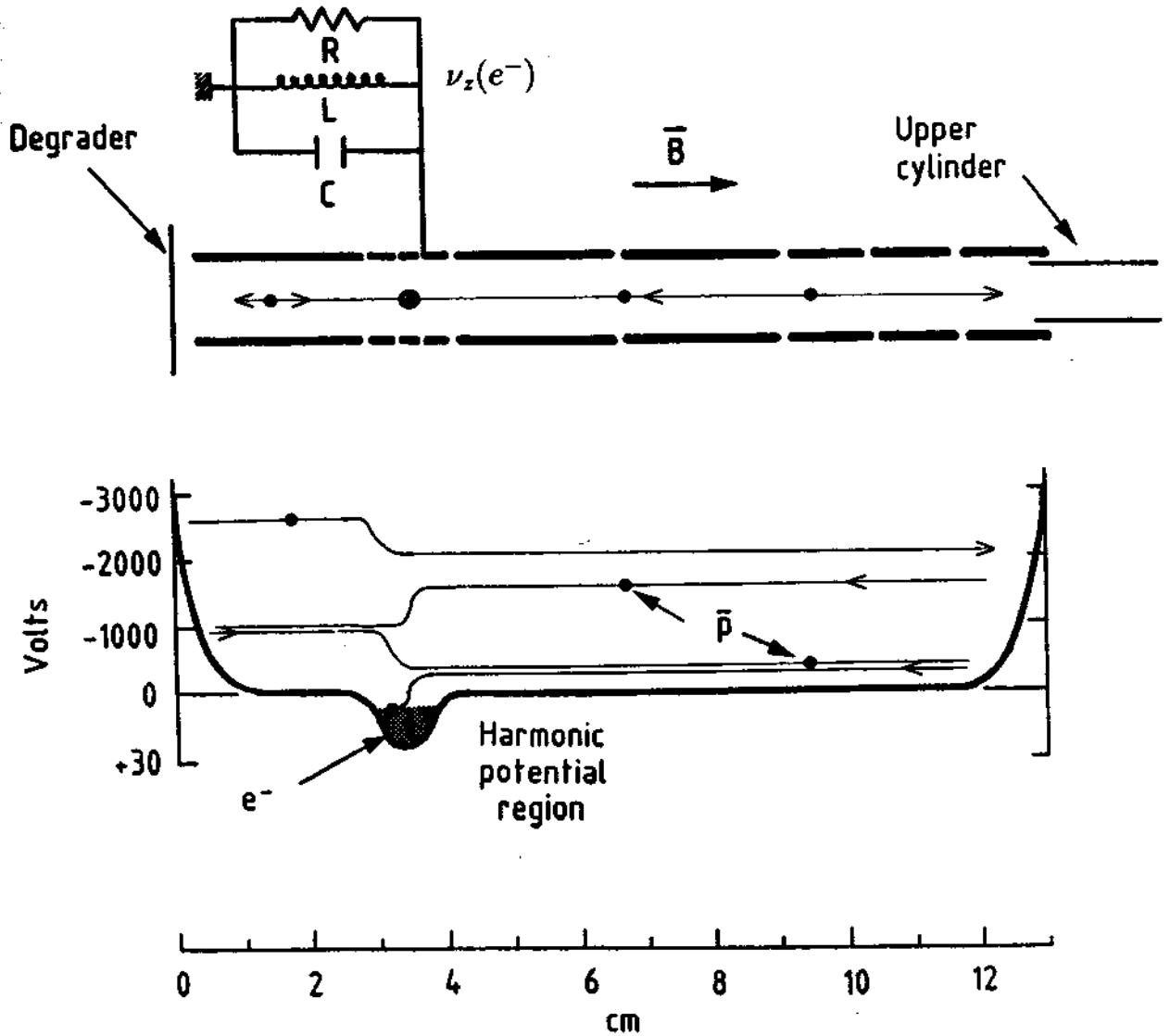

Figure 4.5: Schematic representation of the electron cooling process. The total cooling process occurs in less than 10 seconds.

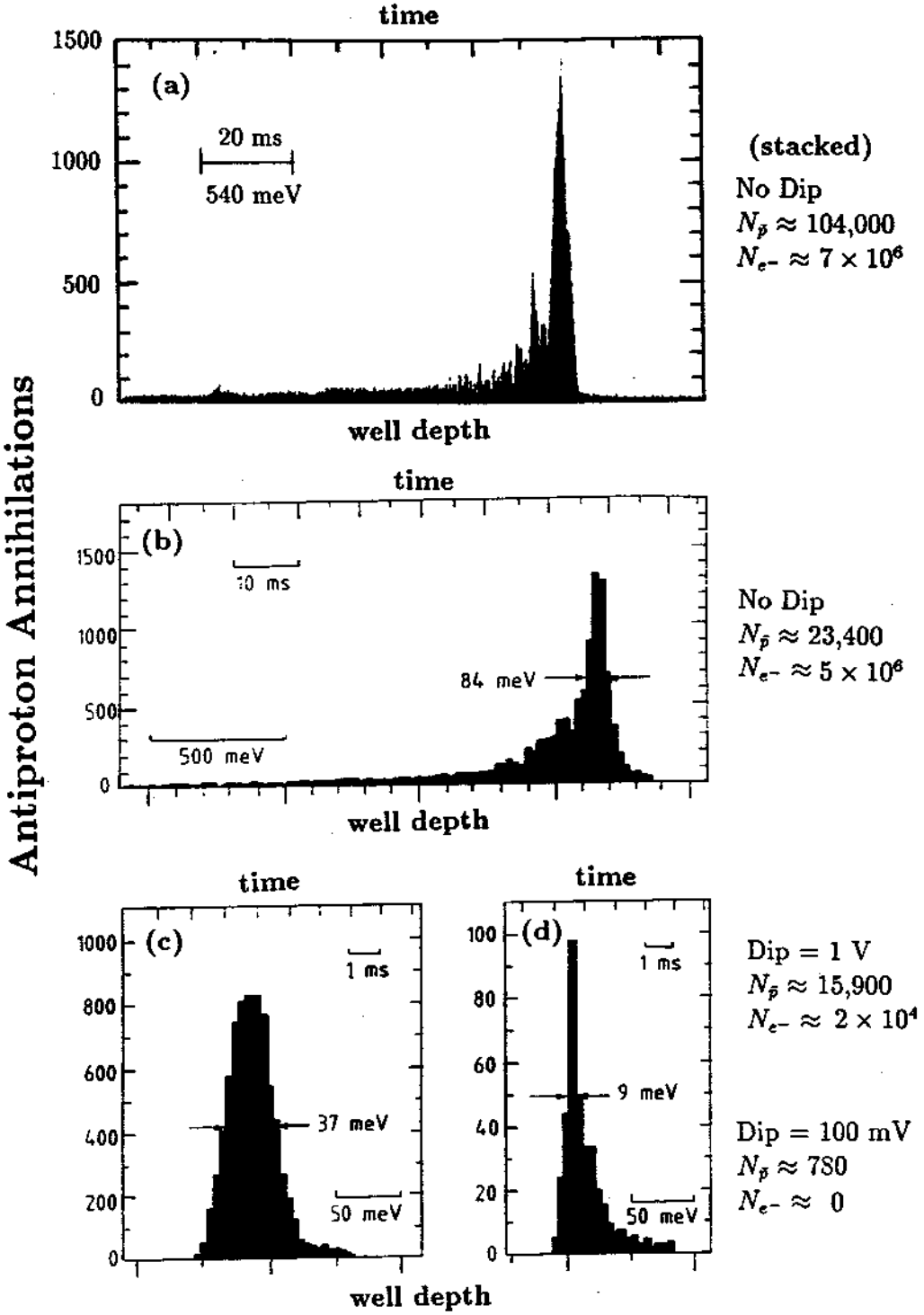

Figure 4.6: Antiprotons leaving the harmonic well as a function of well depth and particle number. (a) Annihilations from antiprotons stacked into the harmonic well. (b), (c), and (d) are obtained using only a single shot from LEAR.

length of the long well, losing energy via collisions with the cold electrons during each pass. The cold antiprotons eventually fall into the harmonic well with the cooling electrons at a rate depending upon the number(density) of antiprotons and electrons and the spatial overlap of the two particle species. The process is schematically shown in Fig. 4.5, and we typically use about 5×10^6 electrons to cool 2×10^4 antiprotons. With such ratios it typically takes less than 10 seconds to cool the 0-3 keV antiprotons to thermal equilibrium at 4 K, in good agreement with earlier cooling estimates [84].

After typically 100 seconds we lower the high voltage endcap and observe the remaining high energy spectrum. Usually a few remain, but the spectrum is shifted towards lower energies. Given enough time, if there exists sufficient spatial overlap between the antiprotons and the electrons, essentially all the antiprotons are cooled into the harmonic well. The size of the electron cloud is limited by space charge, and the location of the antiprotons depends upon how well the incoming antiproton beam is focussed and steered.

By linearly ramping the potential of the harmonic well and detecting annihilations in an analogous fashion to the previous section, we obtain energy spectra as seen in Fig. 4.6. The actual energy spectra observed are influenced by the ramping technique and the amount of charge in the trap. For larger numbers of cooling electrons and/or large numbers of antiprotons the spectra show the large axial heating of the antiprotons that results from the coulomb repulsion during the process of emptying the well (Figs. 4.6 (a) and (b)).

With electron cooling, the antiprotons residing in the harmonic well presumably are in thermal equilibrium at 4 K. Their energies are easily within a range where resistive cooling techniques are feasible.

Stacking

After an initial load and cool cycle, additional antiprotons can be loaded in the long trap between 0-3 keV and electron cooled into the harmonic well containing the cooling electron cloud and the cold antiprotons from the previous load. Within limitations, this process can be close to 100% efficient apparently until either the

electron or antiproton cloud fills the well to its space charge limit. From time to time, especially with larger electron clouds, sudden loss of the electron and antiproton cloud is observed evidently resulting from instability mechanisms which at this time are not well characterized.

To be assured that the harmonic well is not filled to its space charge limit, we deepen the well depth by 5 V increments each time a new shot is stacked. Figure 4.6(a) shows the dump spectra from the harmonic well after about 10 shots from LEAR were sequentially loaded and stacked. The spectra, having some structure not entirely understood, shows the coulomb repulsion (heating) resulting from 104,000 antiprotons and nearly 10^7 electrons in the harmonic well.

4.2.3 Reducing the Number of Cooling Electrons

After the antiprotons are cold and localized in the harmonic well we turn our attention towards observing the antiproton particles by non-destructive means using the RF resistive detection techniques (Chapters 5, 6, and 7). At this point, after a single shot from LEAR, 25000 antiprotons typically reside in the well along with approximately 10^7 electrons. The large number of electrons perturb the oscillation frequencies of the antiprotons, making it essential to reduce the number of electrons for measurements of high accuracy.

The DC potential applied to the trap containing the mixed electron and antiproton cloud is typically around +32 Volts (to observe $\nu_z(e^-)$). We selectively reduce the number of electrons by exciting the electron axial frequency $\nu_z(e^-)$ with a drive strength of 180 mV_{rms} and simultaneously sideband cool the electrons with a drive near $\nu_z + \nu_m$ also at 180 mV_{rms}. After the drives have been on for about 15 seconds we suddenly reduce the well depth in 2.4 ms. (By observing scintillator counts during such a procedure we can monitor the loss of any antiprotons). The well is held at the low potential (typically +4 Volts, +1 Volts, +0.5 Volts etc.) for 600 ms and then restored to the original potential ($\approx$ 32 Volts). We then apply strong electron axial sideband cooling and observe the remaining number of electrons as described in Chapter 6.

This procedure ('drive and dip'), is very effective in preferentially reducing the

electron number. We typically do not see annihilation pions during the first dip to +4 volts but do see a significant reduction in the number of cooling electrons (from $10^7 \rightarrow 10^5$, a 99% reduction). After the first dip we can easily detect the antiprotons by non-destructive means. In Chapter 8, we describe antiproton cyclotron measurements made with residual electrons remaining. In Chapter 9, we describe measurements made with essentially all the electrons removed by repeated application of the 'drive and dip' procedure.

4.3 Confinement Lifetime of 4.2 K Antiprotons

Antiproton collision and annihilation cross sections rapidly increase at lower energies placing stringent vacuum requirements in the trapping region. We obtain a low pressure by cooling the trap and its vacuum enclosure to 4 K. Shortly after we first successfully cooled antiprotons to 4 K we observed that the containment lifetime was much greater than 1 hour which is critical for performing mass comparisons at the highest precisions.

Recently, we had an opportunity to put a lower limit on our confinement lifetime. During January and February the CERN accelerators are shut down for maintenance and upgrading. On December 20 we loaded the trap, cooled the antiprotons to 4 K, and ejected most of the electrons using the drive and dip procedure. We then observed the antiproton cyclotron motion daily for nearly 2 months using non-destructive RF detection techniques (Fig. 4.7), and could observe no antiproton losses within the resolution of our system. After 58.7 days, on February 17 we opened the well and counted the annihilation pions. We measured $N_{\bar{p}} = 1850 \pm 40$ antiprotons.

To obtain a lifetime limit, we infer the original number of antiprotons loaded by comparing the integrated PPAC signal to the signal of the most efficient load we had. We then subtracted out the number of antiprotons lost during the drive and dip procedure. Imprecision in our knowledge of the number of antiprotons initially loaded limits the lifetime we can set to

$$\tau_{\bar{p}} > 8.9 \times 10^6 s \tag{4.1}$$

or a lower limit of 103. The 58.7 day hold time corresponds to the longest antiproton containment time at any energy. The Antiproton Accumulator (AA) has held a single load of antiprotons at 3.5 GeV/c for 11 days (only losing them due to a power failure) and were able to achieve a containment lifetime of 154 days or 1.3 $\times 10^7$ seconds, though because of the high energy, a rest frame lifetime can be set of $\tau_{\bar{p}} > 3.4 \times 10^6$ s [2].

The similar containment lifetimes, despite our much lower energy (13 orders of magnitude), is a reflection of the ultra high vacuum in our cryopumped vacuum

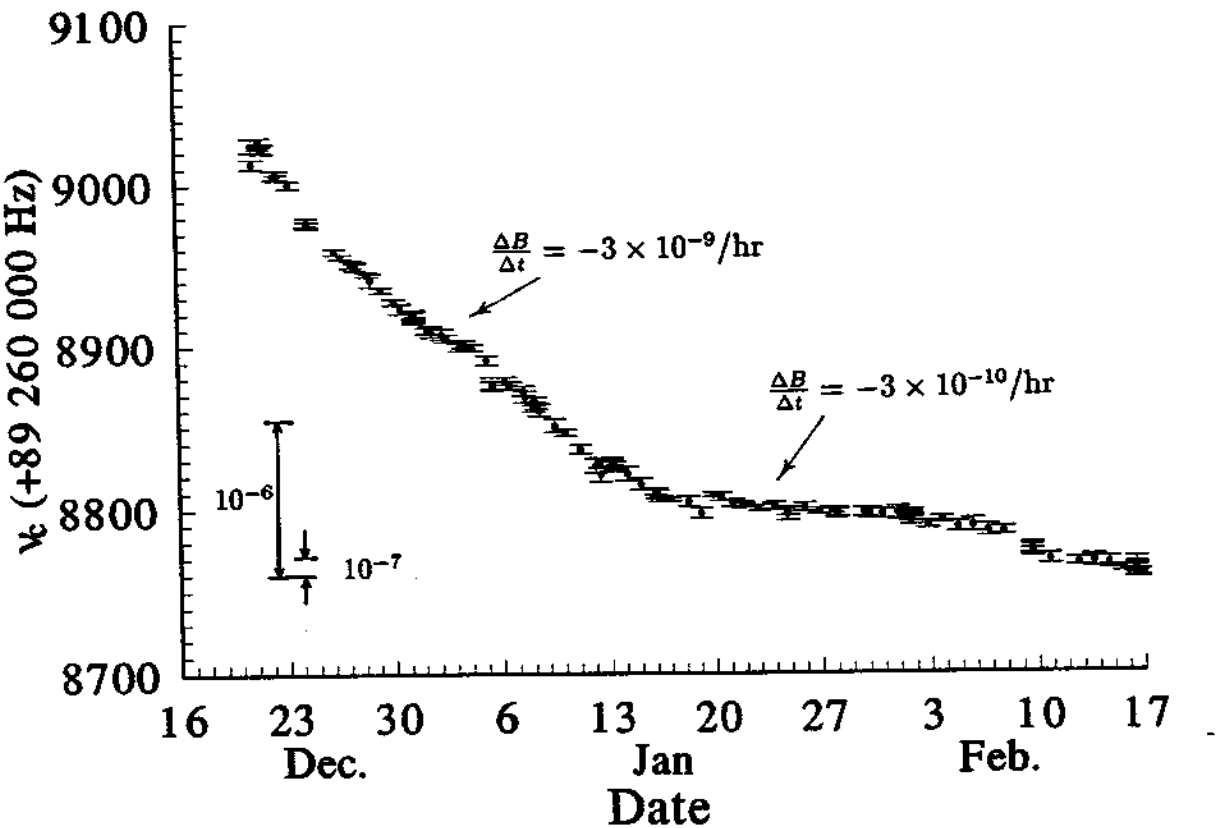

Figure 4.7: Antiproton cyclotron frequency measured on a cloud of 1850 antiprotons over a two month period using techniques described in Chapters 5 and 9.

enclosure. Based upon calculated annihilation cross sections [73,7], the containment time we observe requires a background density of less than 100 atoms/cm^3 [28]. For an ideal gas at 4.2 K this would correspond to a background gas pressure of

$$P < 5 \times 10^{-17}\ Torr. \tag{4.2}$$

The antiproton containment lifetime is normally very long in our Penning trap, though on one occasion the trap was contaminated with helium so that when attempting to load positive ions, only He^+ and He^{++} could be identified. Presumably some weakly cryoadsorbed helium was also present on the degrader. Nevertheless, antiprotons could be loaded and electron cooled into the harmonic well. Non-destructive cyclotron measurements (Chapter 8 and 9) could also be performed on the confined antiprotons even though the helium contamination was present. After about 2 hours antiprotons could no longer be detected either non-destructively, or when dumping the trap. The containment time, as expected, was compromised by the helium.

Chapter 5

Resistive Detection and Damping

The oscillation frequencies of charged particles confined in the harmonic well can be non-destructively interrogated and measured. Particle motions produce alternating currents in the conducting trap electrodes. These are monitored by sending them through a large effective resistor and observing the resulting alternating voltage drop at the frequency of the particle oscillation. A schematic version of this detection is shown in Fig. 5.1. The electron axial motion, and the antiproton's axial and cyclotron motion are detected similarly, at easily accessible radiofrequencies.

This scheme is also effective in damping the particles motion. Power dissipated in the resistor is lost from the particle motion, cooling this motion into thermal equilibrium with the resistor. The effective resistor is kept near 4.2 K to minimize noise and particle amplitudes.

The resistive damping rate and resulting detection linewidth of a single particle of mass m and charge q can be estimated by a simple model. The induced current I dropped across a resistor R produces a potential drop, which in turn produces an electric field at the center of the trap, resulting in an axial force on the particle of

$$\mathbf{f} = q\mathbf{E} = -q\kappa\left(\frac{IR}{2z_0}\right)\hat{\mathbf{z}}, \tag{5.1}$$

where κ is a geometrical coefficient, and $2z_0$ the axial dimension of the trap shown in Fig. 3.1. (If the detection electrodes were infinite plates of separation $2z_0$, κ would equal unity.) For the axial detection shown in Fig. 5.1, κ is equivalent

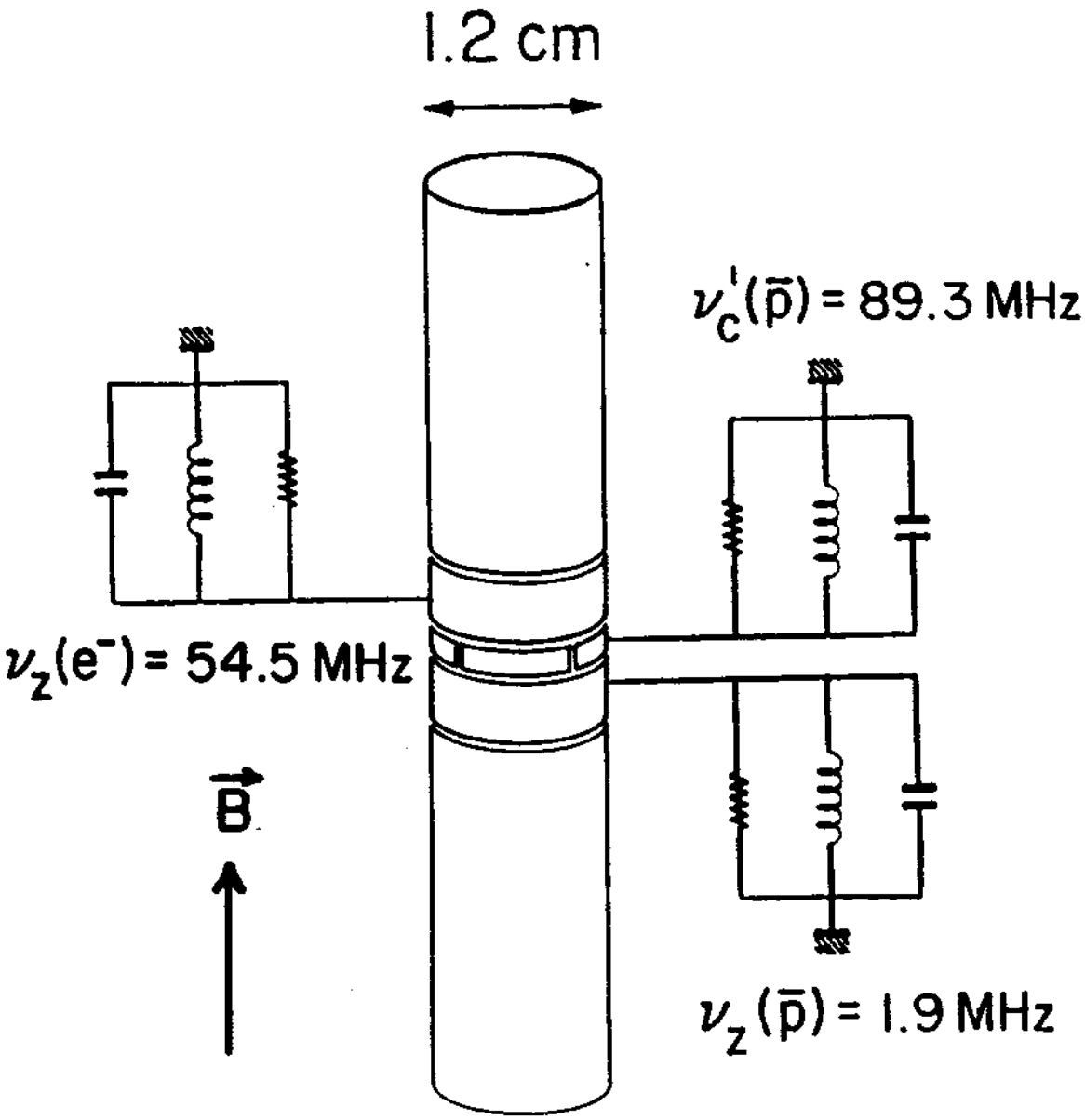

Figure 5.1: Schematic circuit for resistive detection and damping of the axial and cyclotron motions of antiprotons (protons) and electrons.

to the coefficient d_1 for the asymmetric voltage boundary condition applied to the compensation electrodes. (An analogous situation exists for detection and damping of the cyclotron motion with a resistor across two opposing quadrants of the segmented ring, except that z_0 is replaced with ρ_0 and κ is denoted κ' reflecting a different geometry).

The size of the damping force (f $\rightarrow$ 0 as $v \rightarrow 0$) is proportional to the size of the induced current, which depends upon the particle velocity (i.e. the square root of the axial energy). The particle axial energy E_z is dissipated in the resistor at a rate

$$\frac{dE_z}{dt} = -\dot{z}f = I^2 R_z. \tag{5.2}$$

The induced current is then

$$I = d_1 \left(\frac{q}{2z_0}\right) \dot{z}. \tag{5.3}$$

Noting that the damping force can be written as $-m\gamma_z \dot{z}$, the axial damping coefficient γ (or linewidth $= \gamma/2\pi$) for a single particle, using (5.1) and (5.2), is

$$(\gamma_z)_1 = \left(\frac{qd_1}{2z_0}\right)^2 \frac{R_z}{m}, \tag{5.4}$$

and analogously the single particle cyclotron damping coefficient is

$$(\gamma_c)_1 = \left(\frac{q\kappa'}{2\rho_0}\right)^2 \frac{R_c}{m}. \tag{5.5}$$

The damping time constant $\tau = 2\pi/\gamma$ (or linewidth $= 1/\tau$) depends upon the charge state and mass as q^2/m. Thus a proton (or antiproton) takes 1836 times longer to damp than an electron in the same trap for the same R and the linewidth will be 1836 times narrower.

The damping also depends on the size of the trap (z_0 or ρ_0), and on the geometry and location of the chosen detection electrode (d_1 or κ'). A small trap maximizes the damping and produces the largest detection signals. Since the compensation electrodes are large and closer to the trap center than are the endcaps, by detecting on them we improve our detection sensitivity by a factor of $d_1^2/c_1^2 = 7.2$.

To first order, the center of mass motion of a cloud of N particles oscillate at the same frequency as a single particle [115]. The generalized version for the total induced current is

$$I = d_1 \left(\frac{Nq}{2z_0}\right) \dot{Z}, \tag{5.6}$$

where $Z \equiv \sum_k^N z_k/N$ is the center of mass coordinate for the N particles.

For pure center of mass motion (uncoupled from other motions), the damping coefficient for N particles is increased to

$$\gamma_N = N\gamma_1. \tag{5.7}$$

Thus, the center of mass motion of N particles damps with a time constant proportional to 1/N of the single particle damping time. Energy present in the internal degrees of freedom is not as easily removed since it must first couple to the center of mass motion before it can damp.

5.1 Detection Amplifier

Resonant Circuits

In addition to the trap size, detection geometry, and particle number, the damping coefficient is linearly dependent on the size of the resistor R_z or R_c. In practice, this resistance is realized by placing an inductor L in parallel with the trap electrode and feedthrough capacitance (Fig. 5.1). On resonance, L cancels C so that the impedance of the circuit is purely resistive. The small induced current is observed as an rms voltage V_s across the resonant circuit. We select L such that each tuned circuit resonates at the appropriate resonant frequency of the motion to be detected.

The physical LC circuit has finite resistive losses and an observable resonant bandwidth. The resonant circuit quality factor $Q=\nu/\Delta\nu$, is a measure of the effective parallel resonance resistance R. The width $\Delta\nu$ partially results from loss of RF energy in the resonator coil and walls of the cavity due to the skin effect. Skin depths in copper at 300 K for RF frequencies in the 1→ 100 MHz range are about $\delta = 0.07 \rightarrow 0.007$ mm respectively, scaling with the conductivity for lower

temperatures. Circuit Q's also depend on several aspects of construction such as coil wire spacing, dimensions and joint quality [79,110]. In addition, the detection trap electrode is capacitively coupled to adjacent electrodes ($C \approx 1-3pF$), so that lossy couplings to adjacent electrodes must be avoided. For a resonant parallel LCR circuit, $R = Q\omega L = 1/\Delta\omega C$. To maximize the effective parallel resonance resistance, we desire Q and L as high as possible and C as small as possible.

The typical inductance required for each detection circuit is shown in Table 5.1. Each inductor is mounted in a 5 cm long, 3.5 cm ID cylindrical copper cavity. The cavity is bolted firmly for good grounding and heat sinking to the gold plated electronics region just below the liquid helium dewar and above the trap vacuum enclosure (Chapter 3). The three cavities are made large to maximize the volume (proportional to the energy stored) to the surface area (proportional to the cavity surface losses). Larger cavities were not possible because space near the vacuum enclosure is limited and the region below the trap enclosure is not available because of the need to interface to the antiproton beamline at LEAR.

The inductor for the 1.9 MHz axial antiproton circuit is made of 0.1 mm diameter enameled copper wire and is a 4.5 cm long, single layer coil ($\approx$ 200 turns) with a diameter of 2.4 cm. The antiproton cyclotron and electron axial resonant circuits have inductors wound from 2 mm diameter silver plated OFHC copper wire ($\approx$ 3-5 turns). In all cases, the lower end is attached to a trap feedthrough and the appropriate trap electrode through a hole in the cavity bottom, and the upper end is RF grounded to the cavity wall using low loss capacitors. The rms voltage is picked off the coil with a tap typically located between 1/3 and 2/3 up from the RF ground. The tap is capacitively coupled to the gate input of a GaAs field effect transistor (FET).

GaAs FET Pre-Amplifier

Pre-amplifiers, shown schematically in Fig. 5.2, are mounted close to the trap and cooled to 4 K. A GaAs FET and an impedance matching π network are used to match the small signal V_s to a 50 Ω transmission line and drive it. The transistor is a Mitsubishi GaAs FET MGF1100 (dual-gate N-channel Schottky barrier gate

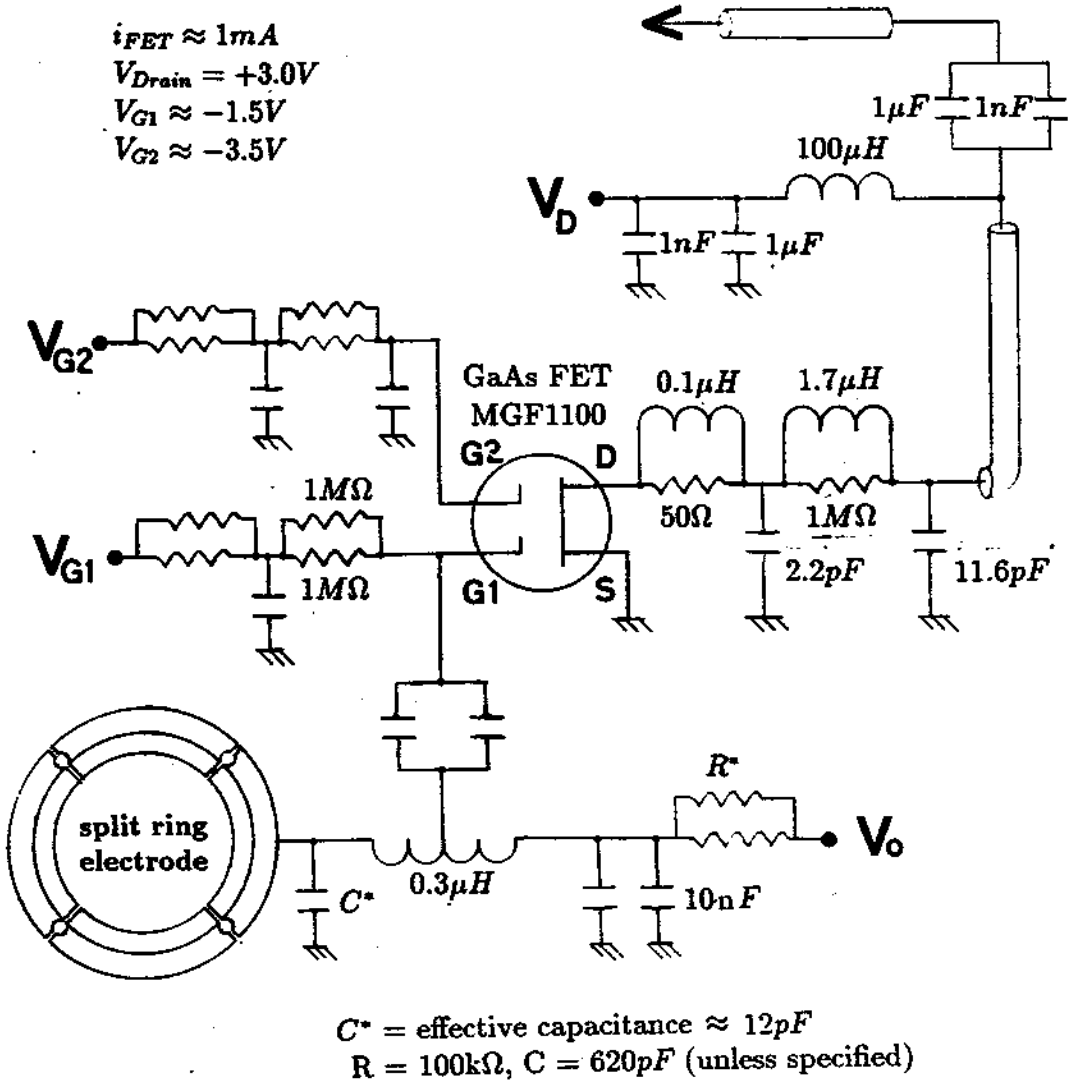

Figure 5.2: Detection resonant circuit, Field Effect Transistor circuit, and π network used for the 89 MHz cryogenic amplifier.

type). It is specified for operation in the 500 MHz to 4 GHz region and has a noise figure of 2.5 dB at 4 GHz. GaAs transistors perform well at 4 K, though the currently used FET is in a region far below their normal specifications. An FET is appropriate for for this application in that high input impedances are possible, though heat dissipated in the FET increases the helium boiloff and keeps the channel temperature above 4 K.

In Fig. 5.2 circuit values shown for direct detection of the antiproton cyclotron oscillation near 89 MHz. The rms voltage signal V_s is capacitively coupled to gate 1 (G1). Gate 2 (G2) provides capacitive isolation between the drain (output) and G1 (input). The Source (S) is held at ground and the signal output on the Drain (D) goes to a π network to impedance match the FET output to a 50 Ω transmission line. The values here match an output impedance of about 20 kΩ at 89 MHz to 50 Ω. (The axial amplifiers are similar except for modifications of the capacitor and inductor values to accomodate different frequencies.)

The amplifier has near unity voltage gain, but a power gain of 400 capable of driving 50 Ω. The drain is biased at +3 Volts with respect to the grounded source. Gates 1 and 2 both have dc biases supplied through RF filters. The bias ranges between $\pm$ 5 Volts, where -5 Volts stops the current flow between the source and the drain. The dc bias on the gates are adjusted (typically Gate 2 is almost completely open and Gate 1 is almost closed) so that the drain-source current is $\approx$ 1 mA. At such operating conditions the power dissipated into the cryogenic system is about 3 mW per amplifier, a significant but manageable heat load if all three are operated continuously since typical power dissipation in the cryogenic system is still only 27 mW.

The FET and π network circuit are contained in an RF enclosed region on the top of the copper cavities used to house the inductors. The resonant circuit region and the amplifier region are separated by a grounded copper partition that has a small hole for the tap lead to be connected to gate 1. In the amplifier region, the four leads from the FET straddle two sides of a piece of grounded double-sided copper clad G-10 circuit board. The gate dc leads, filters, and RF input are on one side, and the source, drain, and π network are on the other to minimize

possibilities of feedback.

Metal film resistors are used throughout because of their good stability over wide temperature ranges. Since the failure rate can be as high a 5%, we often place two in parallel as shown in Fig. 5.2 to insure that if one fails we can continue operating.

Measured Q's

The output signal of the cold FET-π network system is transmitted up and out of the magnet bore on a 1 meter long S.S. coaxial cable, ac coupled from the drain (which has a dc bias on it) and is further amplified. In Fig. 5.3 we show the noise spectra for each of the three amplifiers, when they near 4 K and are connected to the appropriate trap electrodes (the trap contains no particles). The three spectra shown are each observed with a 1 kHz bandwidth using a HP 8562A spectrum analyzer. The same broadband amplification was used for each trace ($\approx$+60 dB using six Anzac AM-107 in series). The noise resonance [108] is predominantly the thermal Johnson noise of the 4 K resonant circuit (the resistor) given by

$$v_R(rms) = \sqrt{4k_B RTB} \tag{5.8}$$

where B is the detection bandwidth in Hz, k_B is the Boltzman constant, and R the effective resistance at temperature T.

The Q of each resonant circuit is determined from the width of the noise resonance. The $Q=\nu/\Delta\nu$ with the resonance width $\Delta\nu$ defined as -3 dB down from the maximum power. In terms of these rms spectra, $\Delta\nu$ is measured at 0.707 V_{peak}.

In Table 5.2, the measured Q's and effective resistances for each circuit are shown, along with the inferred linewidths and damping time constants using Eqs. 5.4, 5.5, and 5.7. We note that the Q of the cyclotron amplifier is lower than the electron axial amplifier, which is at a lower frequency. This is likely due to RF grounding problems associated with the ring and the compromises made to accomodate all the detection and drive constraints on the neighboring electrodes.

Table 5.1: Actual tuned circuit parameters for the three resonant circuits tuned to ν_z (antiproton), ν_z (electron), and ν_c' (antiproton).

Circuit	ω	C	L	Q(300K)	Q(4K)	$\Delta\nu(300K \rightarrow 4K)$
$\nu_z(\overline{p})$	2π(1.91 MHz)	≈18pF	390μH	55	150	+55kHz (2.9%)
$\nu_z(e^-)$	2π(54.5 MHz)	≈18pF	0.5μH	180	1020	+1.23 MHz (2.3%)
$\nu_c'(\overline{p})$	2π(89.3 MHz)	≈12pF	0.3μH	210	520	+1.86 MHz (2.0%)

Circuit	R=QωL	$\gamma_N/2\pi$	$\tau_N = \tau_1/N$ †
$\nu_z(\overline{p})$	$7.0 \times 10^5\Omega$	N(8.4 mHz)	18/N sec
$\nu_z(e^-)$	$1.7 \times 10^5\Omega$	N(3.7 Hz)	0.3/N sec
$\nu_c'(\overline{p})$	$7.8 \times 10^4\Omega$	N(0.8 mHz)	190/N sec

† Estimated damping time of center of mass motion

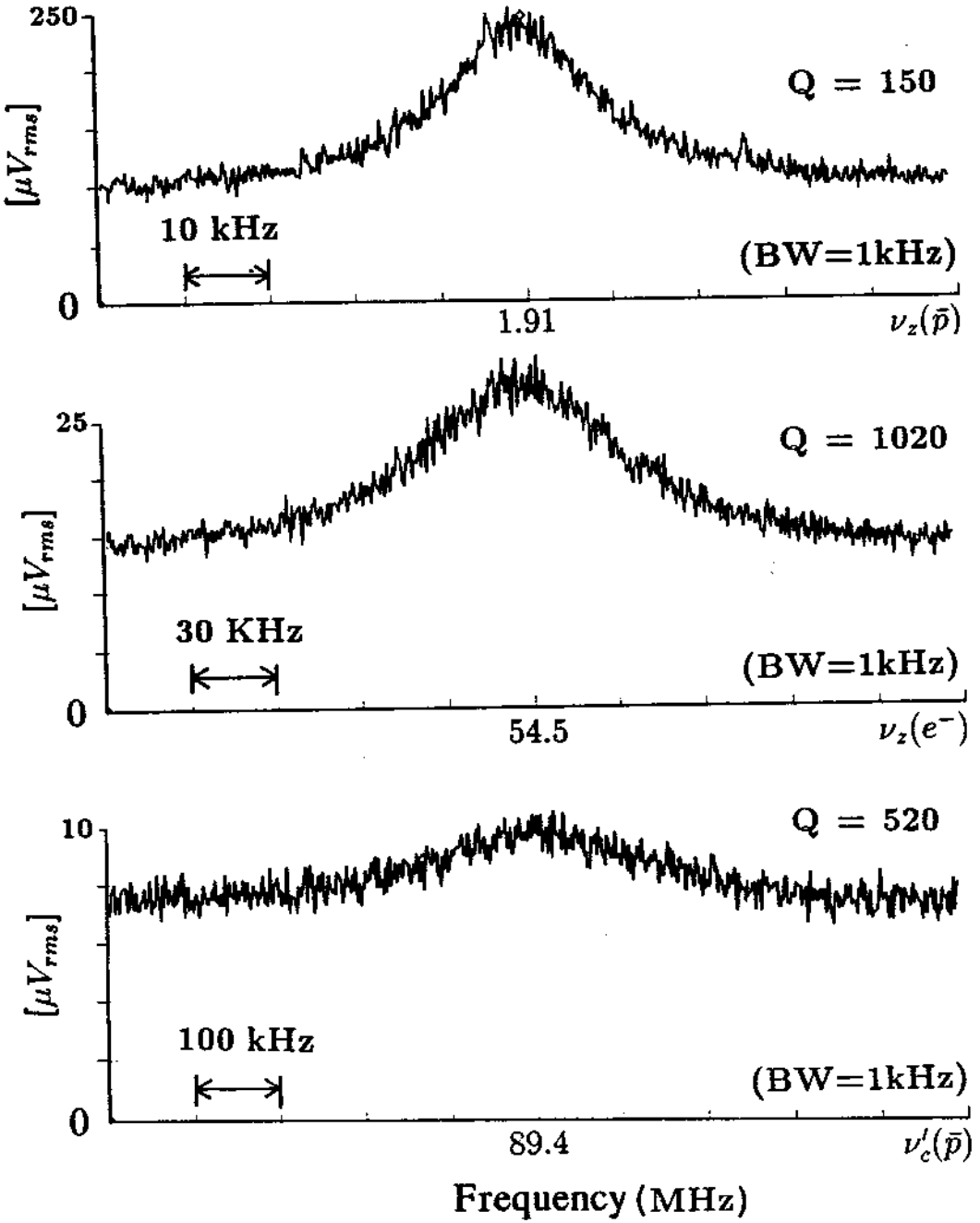

Figure 5.3: Voltage induced across the LCR resonant circuit at 4 K for the three amplifiers using the same broadband amplification for (a) the detection of $\nu_z(\bar{p})$, (b) the detection of $\nu_z(e^-)$, and (c) the detection of $\nu_c'(\bar{p})$.

5.2 Drive and Detection Scheme and Wiring

Gain and Detection

The two general detection techniques shown schematically in Fig. 5.4 are; (1) the direct observation of the induced voltage amplitude V_s as a function of frequency by Fourier transformation or by observing the rectified power in a given bandwidth (denoted 'square law detection' since $V_{out} \propto V_{in}^2$) and (2) the observation of the particle oscillation or center of mass motion of many particles using phase sensitive detection techniques. For both schemes, it is often desirable to apply external RF drives to the particles. Using drives one can resonantly increase the particle amplitude resulting in increased signal to noise, and/or drive the particles at a known phase.

Direct amplitude signals are observed either on a spectrum analyzer, or by square law detection as a function of frequency. The general scheme for amplitude and/or phase sensitive detection is shown in Fig. 5.4. The largest problems to overcome with phase sensitive detection are those related to insufficient damping, particle impurities (by causing dephasing by collisions), and direct feedthrough of the phase defining excitation drive. Elimination of direct feedthrough for coherent axial detection is accomplished by modulating the ring potential which generates FM sidebands on the particle axial motion. By driving on the sidebands, the drive is isolated from the preamplifier which is tuned to the fundamental axial motion [13]. With a coherent signal, the axial particle motion can be held fixed with a phase sensitive frequency lock using feedback voltage to the endcaps (or to the ring).

Phase sensitive detection techniques can be performed with the direct antiproton cyclotron signal as well but the direct feedthrough is more difficult to eliminate since, in practice, it is more difficult to modulate the magnetic field in an analogous way to the voltage modulation. A properly balanced drive helps in reducing the direct feedthrough. Another scheme is to alternate drive and detection cycles as is done in the pulsed NMR measurements.

Radio frequency drives applied at an appropriate frequency and symmetry

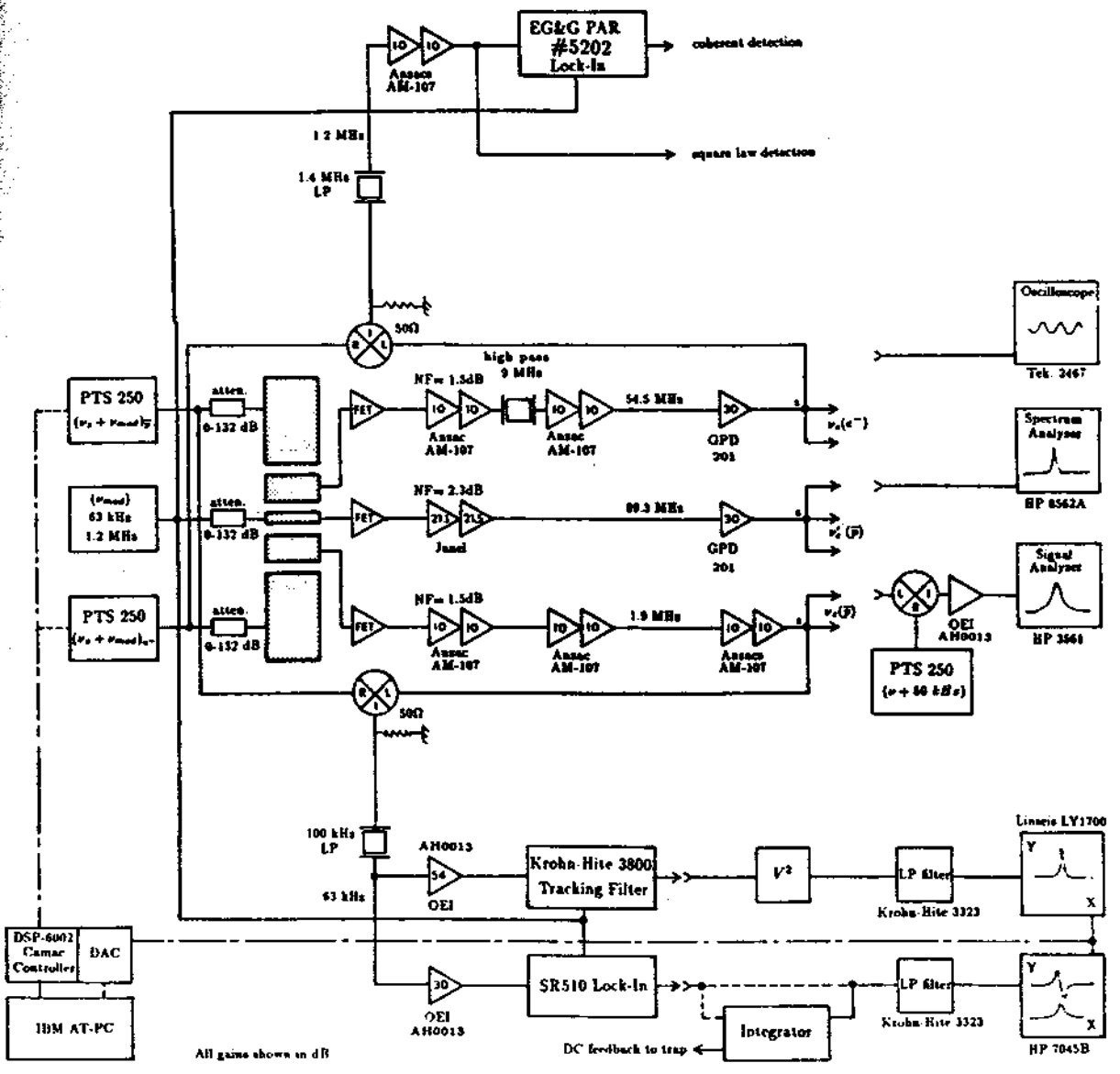

Figure 5.4: Gain and general detection scheme used for square law and phase sensitive detection of the antiproton axial and cyclotron motions ($\nu_z(\overline{p})$ and $\nu_c'(\overline{p})$) and the electron axial motion ($\nu_z(e^-)$).

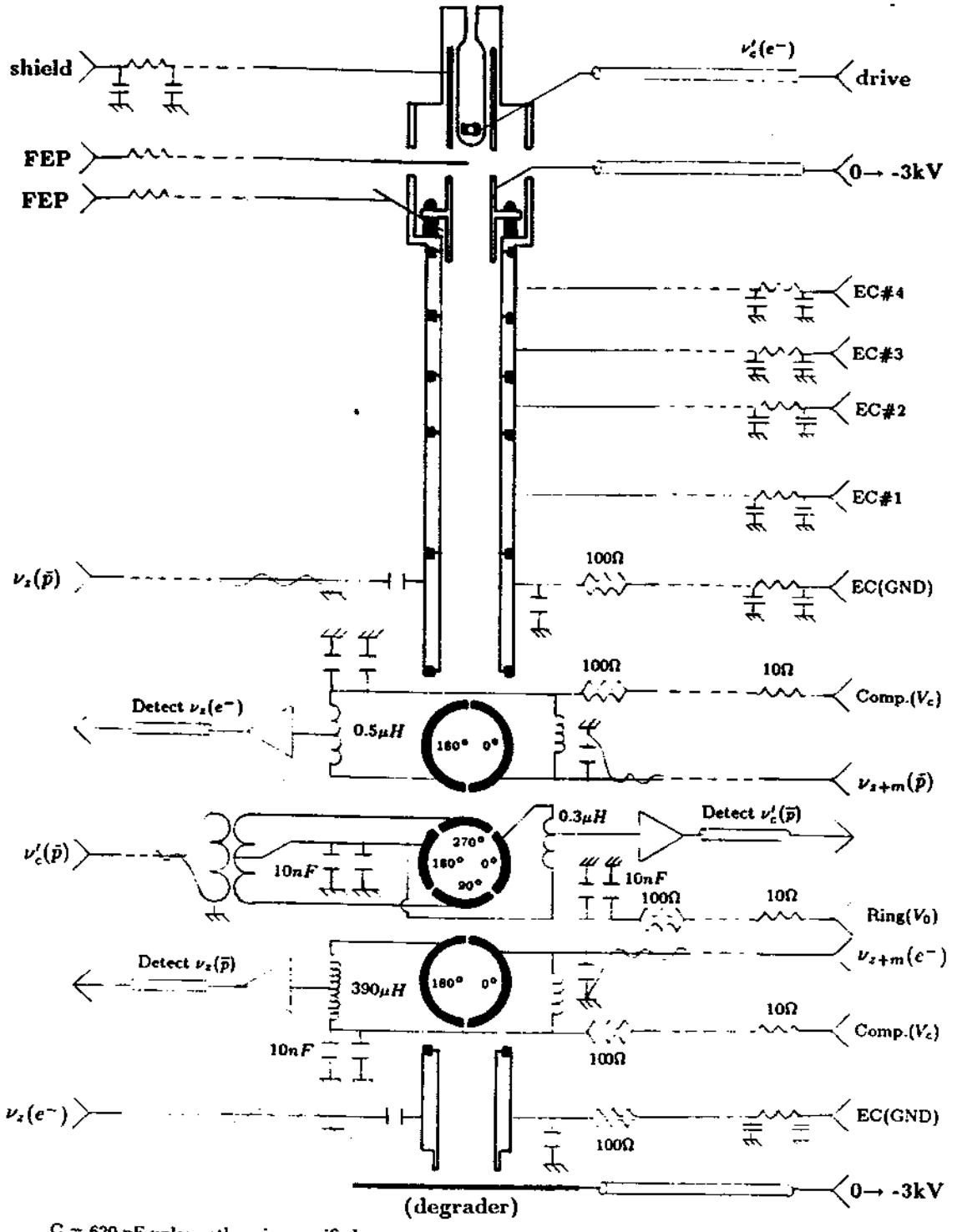

Figure 5.5: The trap wired showing all drives, dc lines, and RF filters. The filter values are compromised so that fast ramping of trap potentials can be done in addition to the resonant measurments.

on the trap are used to couple orthogonal particle motions. An example is the technique of motional sideband cooling to reduce the magnetron orbit radius by coupling to the axial motion (which is resistively damped). This form of sideband cooling requires application of a drive at $\nu_z + \nu_m$, with a symmetry that gives x and z gradients to the applied electric field [114,96]. Analogous applications are used to couple other orthogonal motions such as ν_c' with ν_z [22] and ν_c' with ν_m [85].

Trap Wiring and Filtering

In Fig. 5.5, we show the complete RF and dc wiring of the trap. We note that the filters on the dc leads have a rather small RC time constant. For high precison mass spectroscopy, it would be desirable to have these lines much more tightly filtered, but for these initial studies we also needed to retain the ability to quickly ramp the potential on the harmonic well for destructive energy measurements [45].

To simultaneously detect and damp the three motions $\nu_z(e^-)$, $\nu_z(\overline{p})$, and $\nu_c'(\overline{p})$ we connect the three amplifiers to electrodes making up the harmonic well as shown in Fig. 5.5. The direct cyclotron detection is on one quadrant of the ring, and the two axial amplifiers are on half segments of the split compensation electrodes. The opposing segments are left to accomodate magnetron sideband drives for both the electron and antiprotons, which both need the symmetry mentioned earlier.

The problem of capacitive coupling between the detection systems on the ring and compensation electrodes is solved with the detection side alternated on opposite sides as shown in Fig. 5.5. A clear image of the azimuthal orientation of the electrodes is visible in Fig. 3.3. To minimize direct axial drive feedthrough, the magnetron sideband (on the compensation electrodes) and axial drives (on the endcaps) corresponding to a detection scheme, are located on the opposite side of the plane z=0. Direct feedthrough of the direct cyclotron drive is minimized by use of a balanced drive, where the drive ν_c' is applied across two opposing quadrants of the ring and the detection is across the other quadrant [97].

Also shown in Fig. 5.5 are the high voltage electrodes capable of holding -3 kV for the confinement of high energy antiprotons (top HV endcap and degrader). Additional cylindrical electrodes, labeled Top HV #1 through #4, are used to

increase the antiproton capture efficiency by extending the trap length. A field emitting point (FEP) is included which serves as an electron source, and an HP 5082-2750 diode is directed into the trap for excitation of the electron cyclotron motion at 164 GHz.

5.3 Detection Sensitivity

The voltage signal V_F after the cryogenic pre-amplifier is

$$V_F^2 = (G_F IR)^2 + v_{noise}^2, \tag{5.9}$$

where IR is the signal from the center of mass oscillation and v_{noise} is the noise contributed from the resonant circuit and FET amplifier. The noise can be expressed as

$$v_{noise}^2 \approx (G_F v_R)^2 + v_{FET}^2. \tag{5.10}$$

The thermal Johnson noise v_R depends on the temperature of the effective resistor, and v_{FET} depends upon the FET temperature, tap ratio, 1/f noise that is frequency dependent. The 1/f noise can be large for the axial antiproton amplifier at 1.9 MHz and we have observed that it varies from one batch of FET's to another.

The cryogenic FET pre-amplifier increases the power to drive a 50 Ω transmission line. The voltage gain G_F is of the order one. The voltage output V_1 from the first external amplifier is then

$$V_1^2 = (G_1 V_F)^2 + (v_{NF})_1^2, \tag{5.11}$$

where G_1 is the voltage gain of the amplifier and v_{NF} is the amplifier noise. The relative noise contributions from the rest of the external amplifiers are less by a factor of G. The observed voltage after further amplification G is approximately

$$V_{rms} \approx GV_1 = GG_1\sqrt{(IR)^2 + (v_{noise})^2 + (\frac{v_{NF}}{G_1})^2}. \tag{5.12}$$

For optimum signal to noise we need to maximize the ratio,

$$\frac{V_{Signal}}{V_{Noise}} = \frac{IR}{\sqrt{(v_{noise})^2 + (v_{NF}/G_1)^2}}. \tag{5.13}$$

Table 5.2: Detection sensitivity

Calibration of v_{noise} for each Tuned Amplifier

Amplifier	V_{rms} $(G_1G = 10^3)$ $(G_1 = 3.2, (v_{NF})_1 = 0.4nV/\sqrt{Hz})$	$V_{rms}/\sqrt{Hz}$	v_{noise}(IR=0) $(V_{rms}/GG_1 - v_{NF}/G_1)$
$\nu_z(\overline{p})$	230μV (BW=1kHz)	$7.3\mu V/\sqrt{Hz}$	3.1 $nV/\sqrt{Hz}$
$\nu_z(e^-)$	30μV (BW=1kHz)	$0.95\mu V/\sqrt{Hz}$	0.8 $nV/\sqrt{Hz}$
$\nu_c'(\overline{p})$	10μV (BW=1kHz)	$0.32\mu V/\sqrt{Hz}$	0.2 $nV/\sqrt{Hz}$

Actual Amplification Used for Measurements

Amplifier	type	v_{NF}	G_1	G	V_{rms}(typical)	$V_{rms}/\sqrt{Hz}$
$\nu_z(\overline{p})$	Anzac	0.4 $nV/\sqrt{Hz}$	3.2	316	73μV (BW=100 Hz)	7.3 $\mu V/\sqrt{Hz}$
$\nu_z(e^-)$	Anzac	0.4 $nV/\sqrt{Hz}$	3.2	316	80μV (BW=100 Hz)	9.0 $\mu V/\sqrt{Hz}$
$\nu_c'(\overline{p})$	Janel	1.5 $nV/\sqrt{Hz}$	11.4	375	14μV (BW=100 Hz)	1.4 $\mu V/\sqrt{Hz}$

Required Image Current to Yield Unity Signal to Noise

Amplifier	v_{noise}	v_{NF}/G_1	$\sqrt{(v_{noise})^2 + (v_{NF}/G_1)^2}$	I/$\sqrt{Hz}$)
$\nu_z(\overline{p})$	3.1 $nV/\sqrt{Hz}$	0.13 $nV/\sqrt{Hz}$	3.1 $nV/\sqrt{Hz}$	4.4×10^{-15}
$\nu_z(e^-)$	0.3 $nV/\sqrt{Hz}$	0.13 $nV/\sqrt{Hz}$	0.3 $nV/\sqrt{Hz}$	1.8×10^{-15}
$\nu_c'(\overline{p})$	0.1 $nV/\sqrt{Hz}$	0.5 $nV/\sqrt{Hz}$	0.5 $nV/\sqrt{Hz}$	6.4×10^{-15}

For a fixed detection scheme (fixed R, tap ratio, trap size, noise sources) the only way to improve the signal to noise is to increase I. Thus we either increase the particle number (though this may require a broader bandwidth) or the particle amplitude (by driving harder) to increase the signal to noise. Unfortunately, larger amplitudes may result in the particle sampling imperfections in the trapping fields. For sufficiently high energies the measured frequencies may include relativistic shifts.

In Table 5.2 the sensitivity of each amplification chain is tabulated along with the necessary particle oscillation so that the induced signal is large enough to be observed above the noise. Coherent phase sensitive detection is a way to reduce the signal to noise requirements (and thus to reduce the required particle amplitudes and/or number). Since many of the measurements reported here are done by simply heating the motions, the parameters in Table 5.2 are useful for understanding the limitations of the technique.

5.4 Trap Voltage

The quality and stability of the dc voltage applied to the trap is important especially with regard to the stability of the axial frequency. Standard cells are often used to bias traps for high precision measurements because, when thermally regulated, they offer a potential source with very little noise.

For the measurements reported in this thesis, we have used a commercially available Fluke 5440 Voltage Calibrator. It is IEEE compatible allowing us to externally control the voltage, and has a two polarity range from -1100 V to +1100 V dc. The device is intended for use as a calibrator accurate to $\pm 4 \times 10^{-6}$ when calibrated against national standards and remains within specifications in a temperature range of $\pm 5°C$. The Fluke is useful since we want to compare opposite polarity particles. The output of opposite polarities has been measured at $\pm$ 71.6 Volts to be in agreement to better than 0.0005 Volts using a Fluke 8840A multimeter.

The noise specifications in our typical operating range of $\pm$ 22-275 Volts is 35

μV (BW 0.1 Hz to 10 Hz), and 150 μV (BW 10 Hz to 10 kHz). Voltage fluctuations of 150μV may shift (or broaden) the axial frequency by 10^{-6} corresponding to an uncertainty of 2×10^{-8} in the cyclotron frequency of a trapped antiproton. The source is improved by filtering and these specifications are not limiting for most of the observations reported.

The output of the Fluke V_0 is applied directly to the ring electrode of the trap and the endcaps are grounded. This is the superposition of $-V_0/2$ with the boundary conditions defined in Fig. 3.1 . With V_0 applied to the ring and the endcaps grounded, the compensation potential V_{comp} to applied is

$$V_{comp} \equiv V_c + \frac{V_0}{2} \tag{5.14}$$

The optimum tuning potentials are calculated to be $V_c = 0.381V_0$ or $V_{comp} = 0.881V_0$.

The compensation potential is obtained from the same supply using a voltage divider. From Eq. 3.6, less stability is required in V_c than in V_0 by a factor of $D_2/C_2 \approx 8 \times 10^{-3}$. The divider is adjustable with a 10 turn trimpot over a range $V_{comp} = 0.856V_0$ to $V_{comp} = 0.943V_0$.

Chapter 6

Electrons in the Cylindrical Trap

The non-destructive detection techniques outlined in Chapter 5 are used to observe electrons in the new open endcap Penning trap. Electrons are generated by the field emitting point, and guided to the degrader (see Fig. 5.5) at the far end of the trap by the 5.9 T magnetic field. Low energy secondary electrons from the degrader surface travel back through the harmonic potential region. A small reduction of energy (via collisions or coupling to the cyclotron motion which rapidly cools by synchrotron radiation) is sufficient for the electrons to become bound in the harmonic well.

6.1 Observing the Axial Motion

6.1.1 Damping Rates and Electron Number

Electrons loaded in the harmonic well can be observed using the signal from the detection circuit tuned on resonance with the electron axial frequency $\nu_z(e^-)$. The axial motion is coupled to a resistor, damping this motion with a time constant of $\tau_z \approx 0.3$ seconds for a single electron.

The electron cyclotron motion ($\nu_c' \approx 164$ GHz at 5.9 T) damps by synchrotron radiation to the 4K environment. The radiation damping rate is

$$\frac{dE}{dt} = -\gamma_c E, \tag{6.1}$$

where

$$\gamma_c = \frac{4}{3c}\left(\frac{e^2}{mc^2}\right)\omega_c^2. \tag{6.2}$$

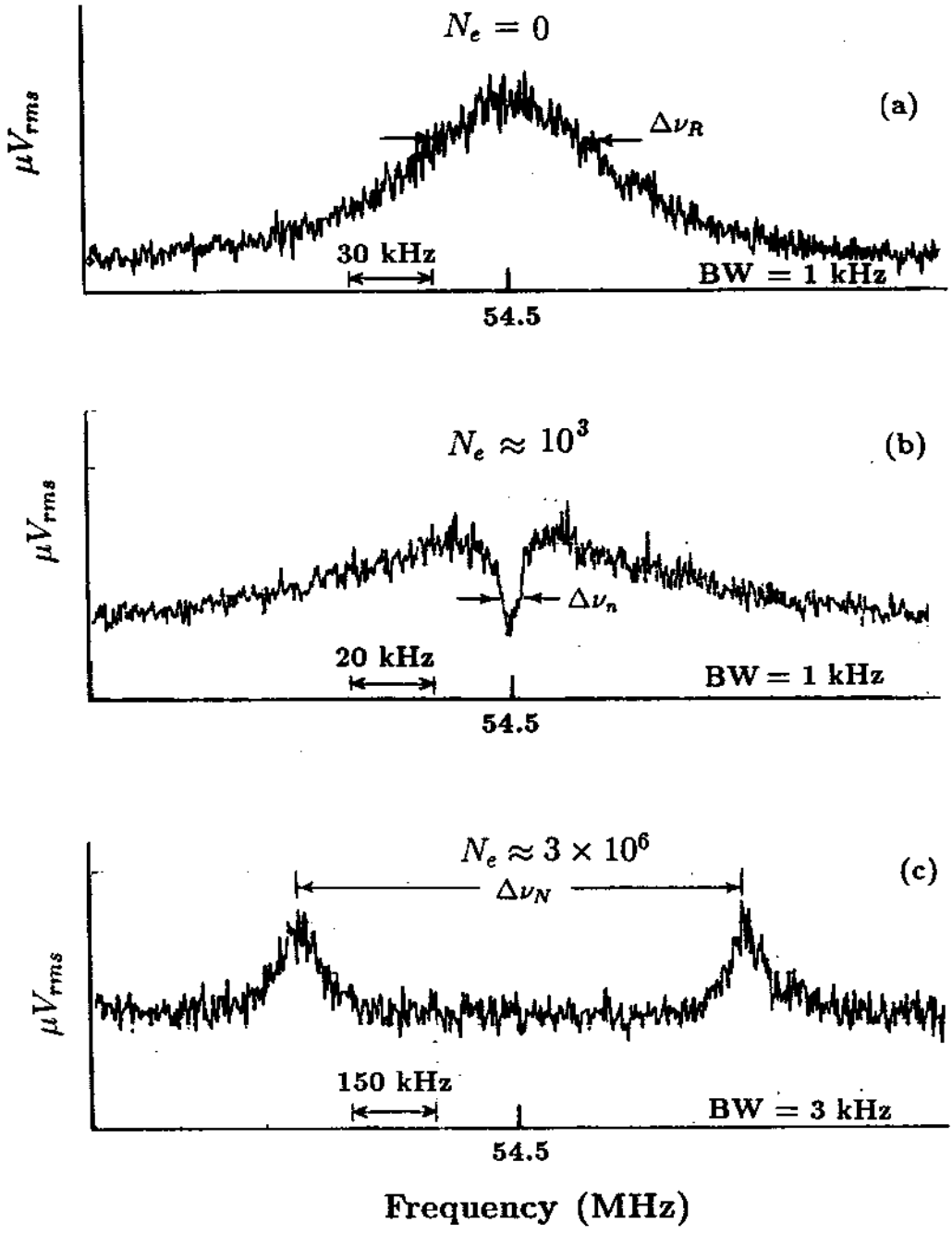

Figure 6.1: Voltage induced across the axial detection circuit with (a) no electrons loaded, (b) a small number of confined electrons, and (c) a large number of confined electrons.

For an electron with $\nu_c' \approx 164$ GHz, $\gamma_c^{-1} \approx 0.08$ seconds the rate is proportional to $1/m^3$ so that the energy loss by this mechanism for a particle as massive as the proton would be insignificant at the existing trapping fields.

The effect of electrons on the noise spectra of the axial detection circuit is shown in Fig. 6.1. Figure 6.1(a) shows a noise spectra with no electrons in the trap. In Fig. 6.1(b) and (c), electrons are tuned to the same frequency as the noise spectra in Fig. 6.1(a). An interpretation of such signals has been given by Wineland and Dehmelt [115]. The axial motion of a confined electron can be modeled as a series resonant lc circuit (with $l = md^2/e^2$ and $c = [(2\pi\nu_z)^2 l)]^{-1}$ in parallel with the detection LCR circuit. For sufficiently small numbers of electrons (when $(\omega l_1/n)/R \gg R\omega C$) the model can be generalized to n electrons by scaling $l \rightarrow l_1/n$ and $c \rightarrow nc_1$. An observable dip results from the series lc circuit shorting the LCR circuit on resonance at $2\pi\nu_z = 1/\sqrt{lc}$. The measured dip width $\Delta\nu_n$ gives the particle number by

$$n = 2\pi l_1 \frac{\Delta\nu_n}{R} = \frac{\Delta\nu_n}{\Delta\nu_1}. \tag{6.3}$$

The parallel resistance R of the LCR circuit is determined from the width of the measured noise spectra ν_{NR}. Using Eq. 6.3 and the single linewidth $\Delta\nu_1$ from Table 5.1, the number of electrons in Fig. 6.1(b) is about 1000.

For much larger numbers (when $(\omega l_1/N)/R \ll R\omega C$), the spectra shown in Fig. 6.1(c) is observed. The coupling between the lc and LC circuits is dependent on particle number. For sufficiently large numbers, the response frequencies split. The splitting $\Delta\nu_N$ is related to the confined number by

$$N = (2\pi\Delta\nu_N)^2 l_1 C = \frac{(\Delta\nu_N)^2}{\Delta\nu_1 \Delta\nu_{NR}} \tag{6.4}$$

where $\Delta\nu_N$ is measured from peak to peak, and C is given in Table 5.1. For the case shown in Fig. 6.1(c), approximately 3×10^6 electrons are stored in the trap with a density of order $10^7/cm^3$. The signal in Fig. 6.1(c) provides a measure of the number of electrons in the large clouds used for electron cooling antiprotons.

As a check, to determine electron number we have quickly removed the trapping potential on the harmonic well and directly collected and integrated the electrons

as they struck the degrader. Doing this we find agreement with the non-destructive linewidth determinations to better than a factor of 2.

6.1.2 Phase Sensitive Detection and Locking the Axial Motion

Using a small number of electrons such as shown in Fig. 6.1(b), we can obtain phase information of the oscillating center of mass axial motion. The electrons are driven with an external frequency source applied to the lower endcap as shown in Fig. 5.5. In practice, since the direct feedthrough of such a drive would saturate the sensitive detection preamplifier, the trap voltage is modulated at ν_{mod} producing FM sidebands on the particle resonant frequency of $\nu_z \pm \nu_{mod}$. We typically modulate the ring potential for electrons at $\nu_{mod}/\nu_z \approx 0.02$. The axial motion is driven on $\nu_z \pm \nu_{mod}$ leaving the detection region at ν_z far from the direct feedthrough.

The detected axial signal at $\nu_z \approx 54.5$MHz is mixed down with the axial drive at $\nu_z + \nu_{mod} \approx 55.7$ MHz using a double balanced mixer. The mixed signal near 1.2 MHz, goes to the input of a EG&G PAR model #5202 Lock-in amplifier with the reference being the modulating drive at ν_{mod}. The resulting Lorentzian lineshapes are well understood [13].

The shape of these coherent responses depends on the degree to which the trap is harmonic. For a trap with anharmonic components added (for example by adjusting the compensation ratio V_c/V_0), the response becomes that of an anharmonic oscillator. By observing the absorption lineshape as a function of changing the ratio V_c/V_0, the trap harmonicity can be optimized.

With the dispersion curve, the zero crossing serves as a sensitive error signal to lock the axial frequency to the external oscillator used to drive the axial motion. The frequency is held at the zero crossing by feeding back a voltage to the trap endcaps. By monitoring the feedback voltage, we observe changes or perturbations that would cause a shift $\Delta\nu_z$, but are compensated by the feedback circuit. Such shifts are easily calibrated by introducing a known change in the drive frequency and measuring the correction signal.

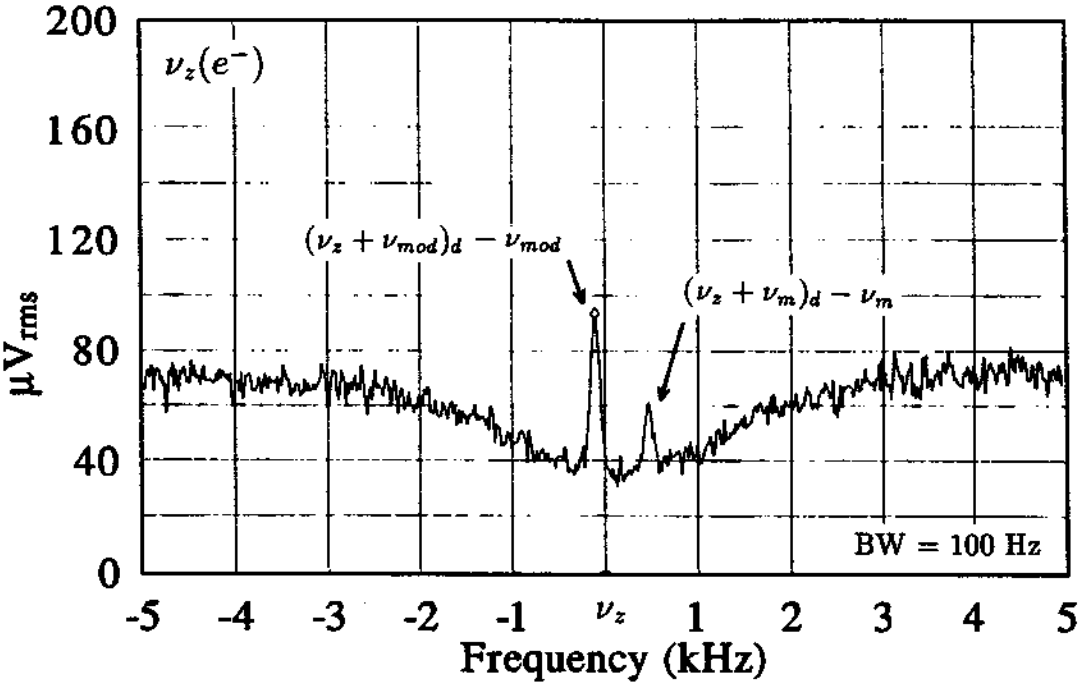

Figure 6.2: Locked axial electron responses to the axial and off resonant axial magnetron sideband drive.

The signal to noise obtainable using the lock correction signal depends on the circuit time constants and also on the application of magnetron sideband cooling. Sideband cooling insures that the electrons remain radially centered and oscillate in the optimally tuned region of the trap.

An artifact of the axial frequency being locked is that it can be simultaneously observed in the 'dip' in the noise spectra (Fig. 6.2). The response at ν_z is the electron response to a drive source at $(\nu_z + \nu_{mod})_d$ while the ring is modulated at ν_{mod}. The width of the response signal is extremely narrow (the width of the drive synthesizer) and is bandwidth limited in this figure. The other response in the figure is due to a magnetron sideband drive near $(\nu_z + \nu_m)_d$. This response (at $[(\nu_z + \nu_m)_d - \nu_m]$) where $(\nu_z + \nu_m)_d$ is approximately $\nu_z + \nu_m$ is interesting in two respects. First, the response at ν_z has no width except that due to the resolution of the analyzer. When the sideband response has an observable width, it can be used for the purpose of tuning the trap and to yield information on effects that may cause variations in ν_m . Second, a measurement of this sideband when subtracted from the cooling drive frequency yields a measure of the magnetron frequency. If $(\nu_z + \nu_m)_d$ is sufficiently strong, many sidebands can be directly observed.

6.1.3 Measurement of the Trap Orthogonalization

The coefficient D_2 (Chapter 3), which in a perfectly orthogonalized trap equals zero, can be determined by measuring the change in the axial frequency as a function of the trapping potentials V_0 and V_c by

$$\frac{D_2}{C_2} \approx \frac{\partial \nu_z / \partial V_c}{\partial \nu_z / \partial V_0}. \tag{6.5}$$

This is done by observing the shift of a narrow dip as a function of changing the trap potential, or by measuring the calibrated correction of the lock circuit due to tuning changes.

Though the parameters of the trap have not yet been measured with a single electron, measurements based on approximately 300 electrons yield a limit of

$$\frac{D_2}{C_2}(300\ e^-) \leq 8 \times 10^{-3}. \tag{6.6}$$

The degree of orthogonalization is observed to improve with decreasing particle number.

6.2 Detecting the Cyclotron Motion

The cyclotron motion ν_c' of electrons in a 5.9 T field is in the millimeter microwave regime at about 164 GHz, and is not accessible by direct detection. This motion, is instead measured by observing the axial signal as a function of cyclotron drive frequency. On resonance, energy is absorbed by the cyclotron motion, which can then couple to and be observed as small changes in the axial motion. The coupling mechanism can be by collisions, anharmonicity, magnetic gradients [101], or even special relativity [33].

6.2.1 Microwave Source

To excite the cyclotron motion of electrons requires a microwave source that can be swept over small regions near 164 GHz. To produce 164 GHz microwaves in the open endcap trap we have assembled a system schematically shown in Fig. 6.3. The fundamental frequency of 640 MHz is obtained from the fixed output of an HP 8662A frequency synthesizer and filtered with a copper cavity filter. The 640 MHz signal is amplified by +21.4 dB and put into an HP 33004A-H26 step recovery diode. The output goes through a filter at 10.240 GHz (bandpass = 0.275 GHz) which only passes the 16^{th} harmonic from the step recovery diode. The output is then amplified by 17 dB and sent through a WMI 8838 circulator to avoid reflections from the following mixer. The 10.24 GHz signal is then mixed with the variable output of the HP 8662A synthesizer. The mix frequency is about 700 MHz (amplitude $\approx$ -19 dBm). The mixed output is passed through a 10.94 GHz filter (bandpass 0.250 GHz) to select the high component. The 10.94 GHz output signal is amplified another 19 dB and then sent out of the RF cabin to the trap through an 8 meter long microwave transmission cable. The cable is measured to attenuate the 10.94 GHz signal by 13.2 dB. The signal is then amplified (to a maximum of +20 dBm) with an HP 8349B broadband amplifier. Before entering

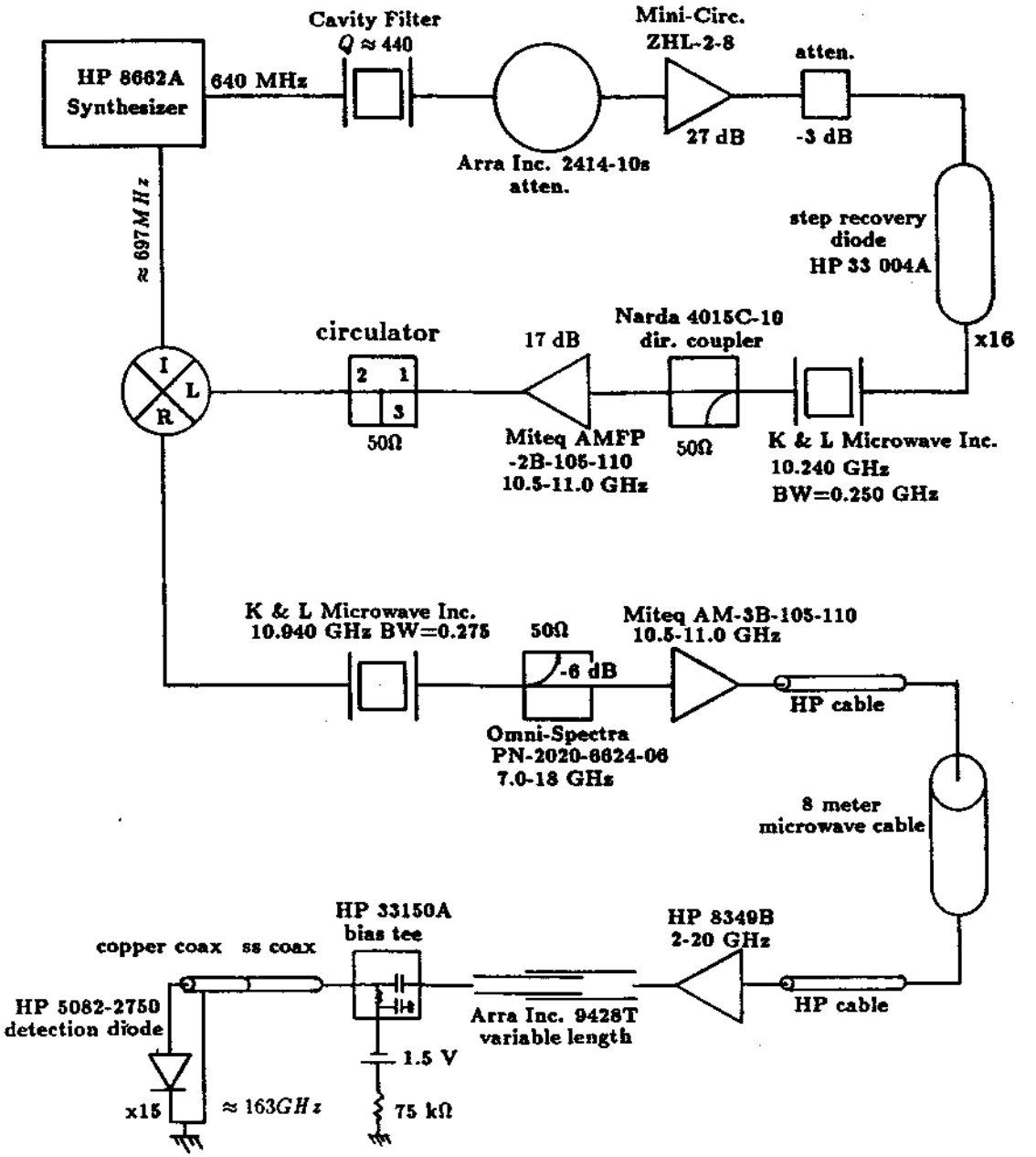

Figure 6.3: The microwave system used to excite the electron cyclotron motion at about 163 GHz.

the brass hat a variable length is included and the 10.94 GHz signal is coupled onto a dc bias line.

The signal enters the bore vacuum through a 50 Ω SMA feedthrough and travels down a 0.3 meter long, .050" diameter SS coaxial cable, then through a 0.7 meter long, .050" diameter copper coaxial cable. The coaxial cable is terminated with an HP 5082-2750 series detection diode which has a line of sight path to the trap center through a glass to metal seal in the trap vacuum enclosure (see Fig. 5.5).

The 10.94 GHz signal, which can be swept as wide as 0.25 GHz, drives the terminating detection diode. The cyclotron drive signal is the 15th harmonic given by

$$\nu_c'(e^-) = ((640 \times 16) + \nu_d) \times 15\ MHz \tag{6.7}$$

For a frequency input of $\nu_d = 700$ MHz, the diode produces a useful signal at 164.1 GHz with a possible range of 3.75 GHz or $\Delta\nu_c/\nu_c \approx 2\%$.

The diode is kept dc biased with a constant current of $I_{bias} = 20\mu$A. The minimum power on the diode necessary to excite the electron cyclotron frequency is about -3 dBm at 10.94 GHz.

6.2.2 Anharmonicity Coupling of ν_c' and ν_z

Techniques for detecting the cyclotron (or spin state) of an electron via small shifts in the locked axial frequency have been highly refined, particularly for measurements of the anomalous magnetic moment (or g-2) of the electron [101,13]. The coupling of the cyclotron or spin into the axial frequency has normally been accomplished with the inclusion of a magnetic gradient (an intentional magnetic bottle field) [25]. Such magnetic bottles lead to broad resonance lines and amplitude (power) dependent shifts that theoretical interpretation [9]. For mass spectroscopy at the level we report here, magnetic bottles are not necessary or desirable for detecting the electron cyclotron motion.

Without a magnetic bottle, the cyclotron resonance of a single electron can be detected using relativistic coupling [33]. However, at the precision reported here, there is no need to deal with only a single electron in the trap. Instead, we use small clouds consisting of $\approx 500 \rightarrow 2000$ electrons, and detect the excitation of

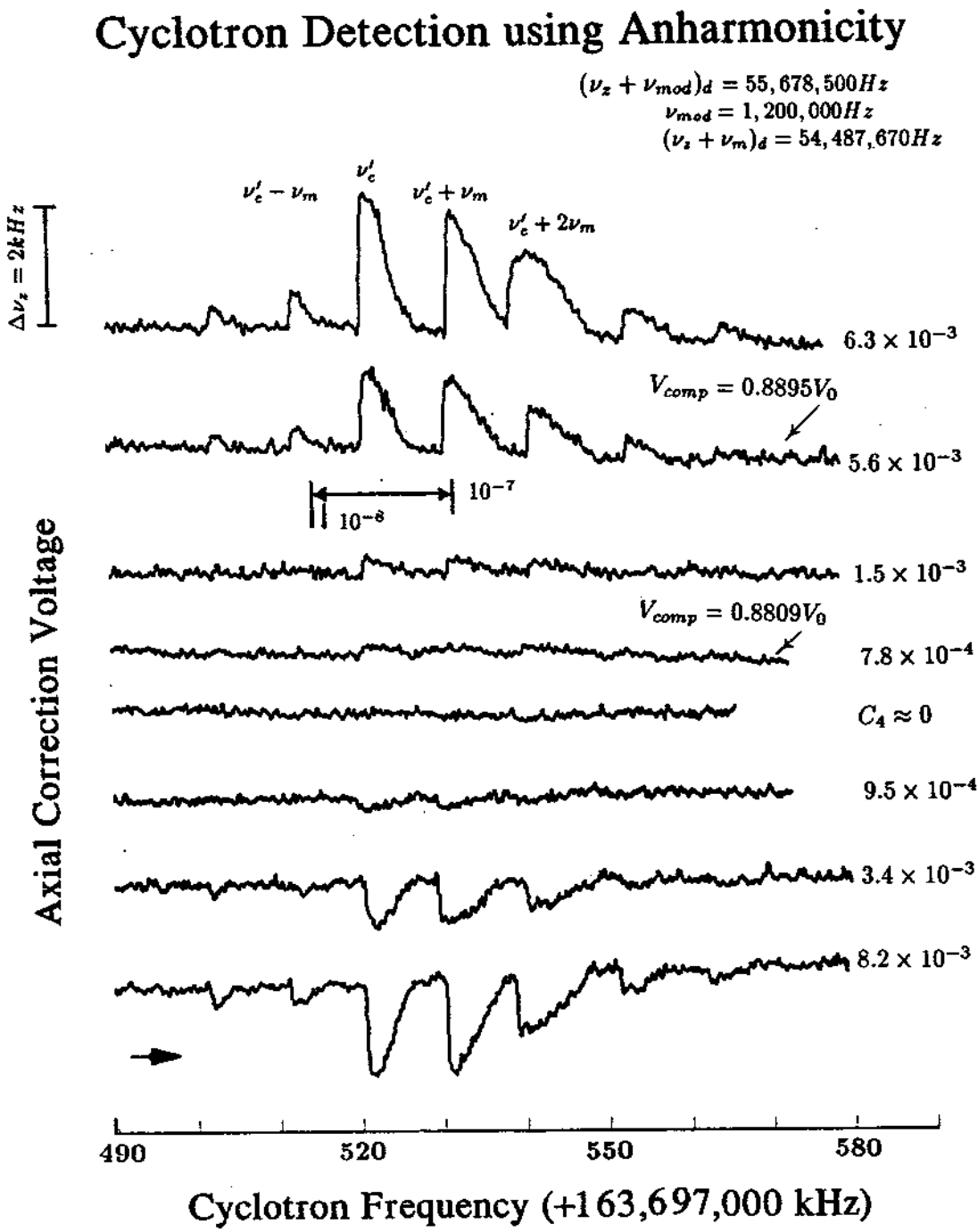

Figure 6.4: Locked axial feedback signal as a function of cyclotron drive frequency. Each trace corresponds to a different compensation setting V_{comp}/V_0. The applied microwave drive strength and sweep rate is constant for all traces.

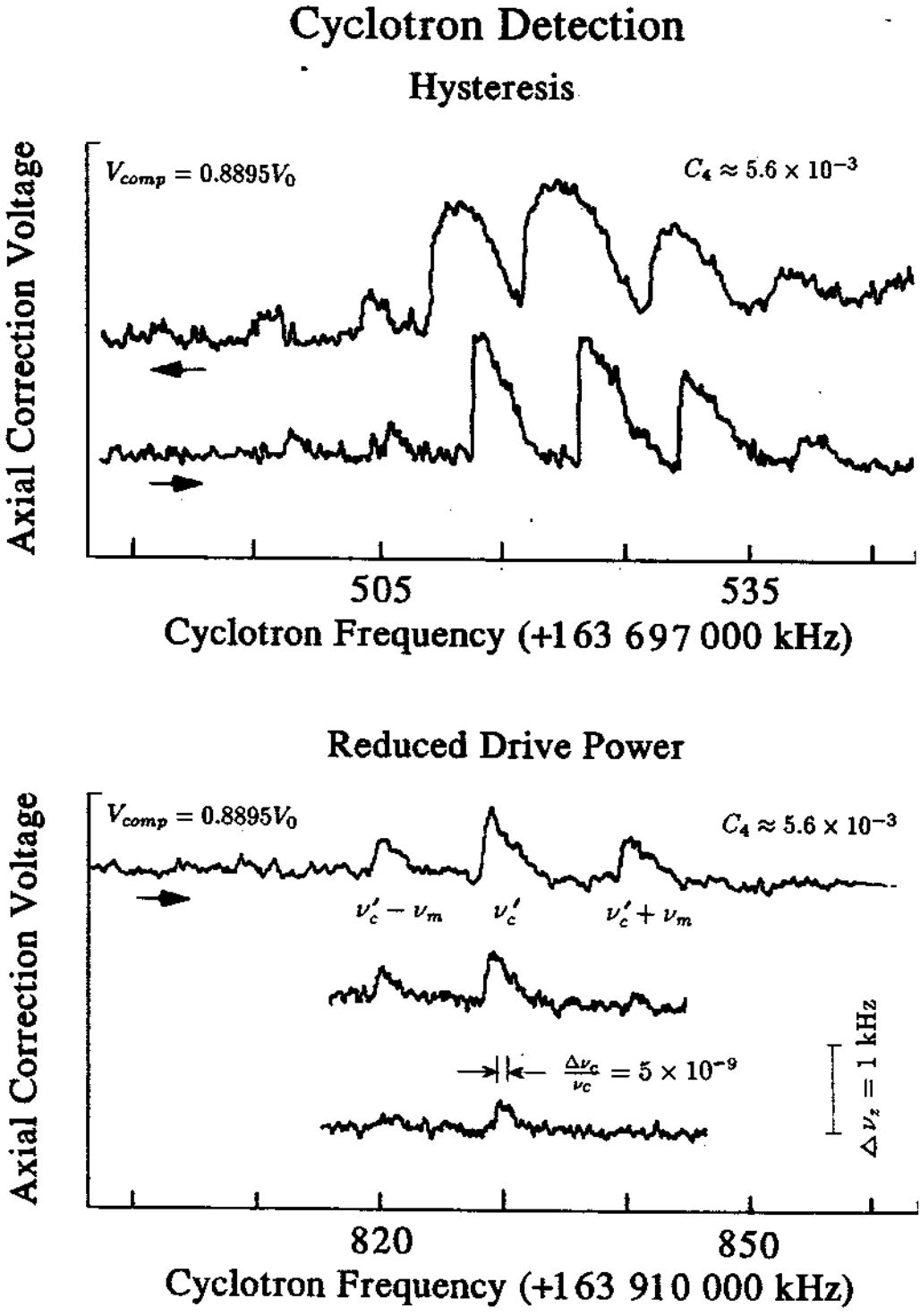

Figure 6.5: Cyclotron resonances as observed by monitoring the locked axial feedback signal as a function of cyclotron drive frequency. (a) Hysteresis depending upon sweep direction, and (b) effect of reducing microwave power to resolve on ν_c'.

ν_c' via the locked axial signal by intentionally introducing trap anharmonicity. The ability to do this is greatly enhanced by the orthogonalization of the trap.

The axial feedback signal as a function of microwave cyclotron excitation frequency is shown in Fig. 6.4. The correction signal (corresponding to $\Delta\nu_z$) depends on the degree of mistuning V_c/V_0 (i.e. an increase in the potential term proportional to C_4). The microwave drive amplitude, sweep rate, and direction are the same for all the traces shown. Several magnetron sidebands at $\nu_c' \pm k\nu_m$ (k=1,2,3...) are resolved as well as ν_c' .

For the trap tuned such that $C_4 \approx 0$ we observe little coupling of the cyclotron heating to the axial motion within the sensitivity of the detection. To see any perturbation on the locked axial signal for a tuned trap requires increasing the drive strength by more than 12 dB at 10.94 GHz. For the electron cyclotron measurements used in the mass comparison, we typically operate the trap with the compensation electrodes mistuned ($V_{comp} = 0.8895V_0, C_4 \approx 5.6 \times 10^{-3}$) so that less cyclotron heating is necessary to observe the coupling into the axial motion. In Fig. 6.4, we observe that changes in C_4 evidently does not shift the cyclotron frequency within the $5\times\ 10^{-9}$ resolution observable along the signal edge. The cyclotron motion is not very sensitive to the electostatic conditions of the trap, even though the axial frequency is very sensitive to changes in C_4.

In Fig. 6.5(a) we show frequency sweeps obtained using the same drive strengths and sweep rates in both directions. The signal shows a hysteretic behavior and resembles in many ways the anharmonic lineshapes commonly observed in axial lineshapes for a mistuned trap. While the shift in the axial frequency $\Delta\nu_z$ is clearly due to the inclusion of C_4, we do not see a change in the linewidth (i.e. $\Delta\nu_c'$) as a function of C_4 over the ranges of C_4 shown in Fig. 6.4.

In Fig. 6.5(b), we identify the modified cyclotron frequency ν_c' by reducing the microwave drive strength until it is the only one resolved. The total linewidth narrows as we reduce the drive strength and a resolution of better than 1 part in 10^8 is shown. It suffices to obtain the free space cyclotron from $\nu_c = \nu_c' + (\nu_z^2/2\nu_c')$ [8]. Because the measurements are done with the axial frequency locked, the correction term $\nu_z^2/2\nu_c'$ is determined to high accuracy and the measurement

is limited by our understanding of the cyclotron linewidth $\Delta\nu_c'$.

Cyclotron measurements of a few or more electrons need not be done using the locked phase sensitive detected signal. We can also observe such signals using a 'bolometric' observation technique [108] when phase information of the particle motion is difficult to attain. By observing the square law output over a region spanning the 'dip' shown for example in Fig. 6.1(b), cyclotron resonances can be observed using increased microwave drive strengths of about +10 dB at 10.94 GHz. (Related techniques will be extremely useful in the work with ions and antiprotons). The drawback is that more heat increases the possibility of undesirable systematic shifts.

6.3 Other Applications with Electrons

The experimental determination of the electron magnetic moment [101] is one of the most direct and precise tests to date of quantum electrodynamics. Such measurements are typically performed with a single electron residing in a hyperbolic trap. The observation of the inhibition of the radiative decay of the electron in the radiation field in the cavity formed by the trap electrodes has raised the possibility that there may exist shifts in the measured electron cyclotron and spin frequencies [34] . Since the existence of cavity modes may have important consequences for the high precision g-2 measurements, much effort has gone into understanding and quantifying the modes of several trap geometries.

Some indications of modes in one hyperbolic trap have been observed [103] though there appears to be no correlation with calculated modes in such a trap [12]. Because of the difficulties in calculating the modes of a hyperbolic cavity, much effort has gone into quantifying the cyclotron motion of the electron in microwave cavities with simpler cylindrical [11] and spherical [14] geometries. Recently, a single electron has been observed in a cylindrical trap with flat endcaps [88] and modes with excellent signal to noise have been observed with a new technique [89].

The two approaches to removing the potential cavity perturbation from influencing high precision electron measurements are to either do the measurement

in a trap where the modes are known and quantified, or to build a trap which does not easily support modes. The open endcap cylindrical trap may provide an environment free of cavity modes. Because the endcaps are open cylinders, any standing wave mode that exists in the trapping region should be very weak. The open endcap Penning trap developed here for use with high energy antiprotons may have advantageous applications in the g-2 measurement of the electron.

Chapter 7

Protons

Trapping protons (and other positive ions) in a Penning trap differs from trapping electrons in several ways. First, the polarity of the dc trapping potential must be reversed from that used for electrons. Second, many positive ions can be trapped with the protons, while pure electron clouds are almost unavoidable since negative ions are difficult to form. Third, damping is less effective for the heavier protons since resistive damping scales as $1/m$ and synchrotron damping of the cyclotron motion goes as $1/m^3$.

7.1 Loading Protons and Other Positive Ions

Several methods have been used to load protons and other ions into a Penning trap. The simplest method is to use electron bombardment to ionize background neutral gas which is present or injected into the trapping region. In our case, the electron source is a field emission point produced by etching a 0.5 mm diameter tungsten rod in a sodium hydroxide solution. Typical bias voltages between the point and grounded electrodes approximately 0.5 cm away range from -150 to -2500 Volts depending upon the sharpness of the point. Emission currents can be controlled between 0.01 nA and 1 μA.

For experiments at room temperature, the pressure is sufficiently high that protons or other ions can be loaded directly from the background gas. For this cryogenically cooled experiment, the pressure is very low (less than 10^{-16} Torr) so that this is not possible. Since the number of particles needed is small, it is

sufficient to generate common ions by first dislodging adsorbed neutral gas from a trap electrode surface using electron bombardment and then ionizing it within the trap. The small inner trap lacks a surface perpendicular to the 5.9 T magnetic field (Fig. 3.1), making loading protons and other ions difficult. In an earlier trap configuration, electrons struck a hydrated titanium disk at the end of the lower endcap. In the present trap, configured to load antiprotons and interfaced to LEAR, electrons instead strike the gold-plated aluminum degrader located about 4 *cm* from the center of the harmonic well (Fig. 3.4). Both surfaces are a sufficient source of neutral hydrogen, most likely originating from organic compounds.

There are two main problems with obtaining ions from the residual neutral gas content on the degrader surface. First, many other ion species are generated other than H^+, predominantly carbon, oxygen, and nitrogen. Second, the electron beam only strikes a very small region. Since the degrader surface is at 4 K there is likely little surface migration of adsorbed gases and the source becomes less effective with time. As the source depletes, additional gas can be generated with a higher field emission current which increases exponentially with applied bias voltage.

7.2 Axial Signals

In principle, the axial detection of protons is the same as for electrons discussed in Chapter 6. Because of the larger mass, the resistive damping time (proportional to q^2/m) of the proton is slower than the electron by a factor of m_e/m_p.

Figure 7.1(b) shows a proton signal superimposed on the noise resonance, quite analogous to Fig. 6.1(b) showing the electron dip. The striking difference is that instead of observing a dip, we observe a peak even when the motions are not driven. Given enough time, this peak will damp down so that it is not visible with respect to the noise resonance, though we do not see the proton signal as a dip. Modeling the protons as a series *lc* circuit [115], the proton reactive impedance as a function of frequency is approximately $[i2\pi(\nu - \nu_z)md^2/ne^2]$, where $i = \sqrt{1}$ and n is the proton number. On resonance, the protons are an effective shunt, but the linewidth will be more narrow and difficult to resolve than for electrons.

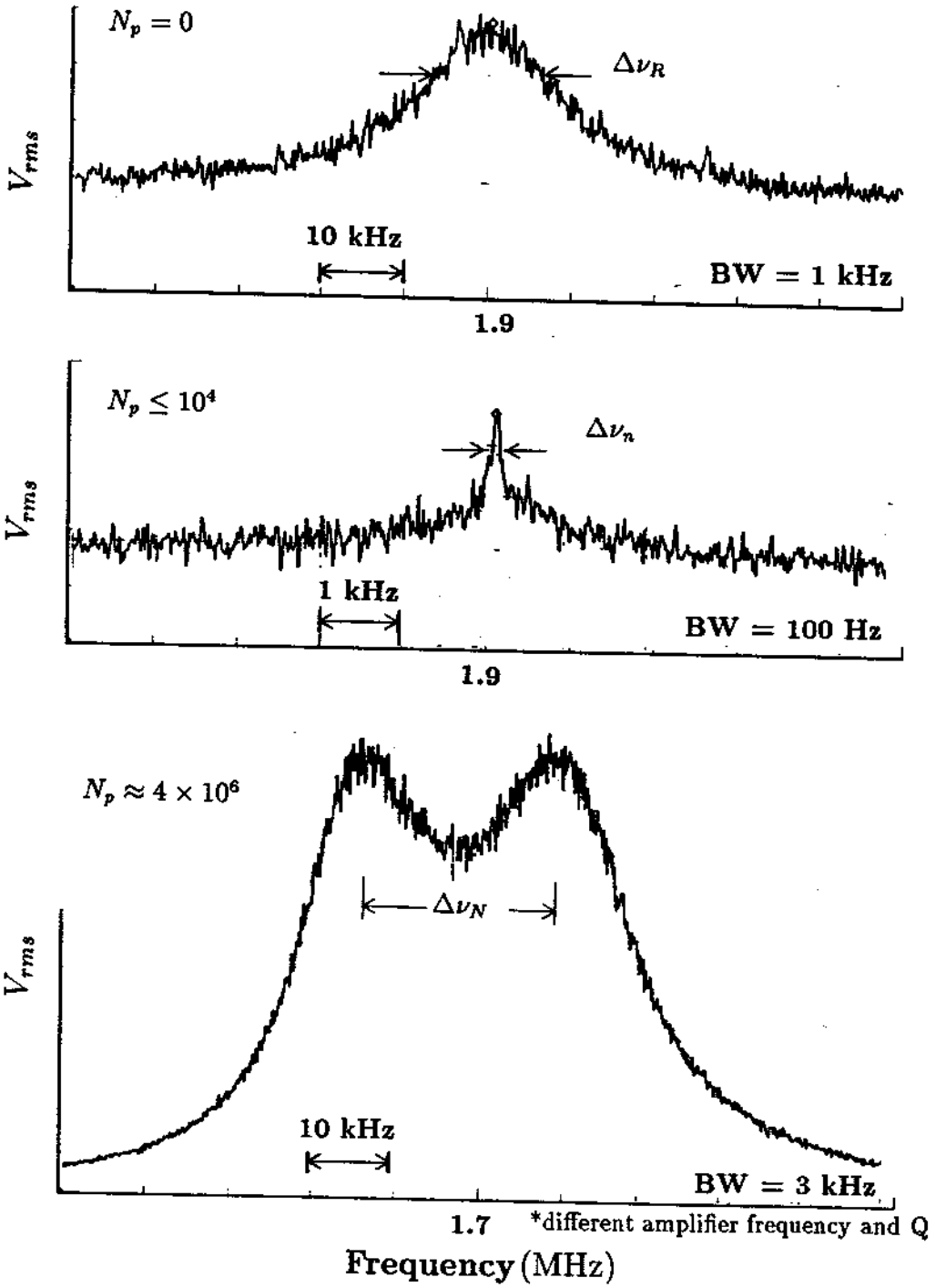

Figure 7.1: The voltage induced across the resonant tuned circuit at the proton axial frequency with (a) no protons loaded, (b) a small number of protons in the trap, and (c) the response resulting from an extremely large proton cloud. Note the difference with Fig. 6.1 for electrons.

Protons and other ions appear as a peak because they are much hotter than the tuned circuit, unlike electrons which damp much faster by synchrotron radiating to the 4 K environment. The peaks are reflective of the higher energies the protons are and how much more difficult it is to remove energy from them. At normal trapping frequencies, protons are only resistively damped. In addition, other ions may be in the trap and not on resonance with a detection amplifier. For such ions, not even resistive damping exists and the only way to damp their motion is by collisional coupling to the resistively cooled protons. These collision coupling times are typically quite long.

Electrons can also be seen as a peak if a sufficient heating source is provided to overcome the much faster synchrotron and resistive damping. (For example, Fig. 8.1 shows axial electron peaks in a mixed electron-antiproton cloud, where the electron axial motion is continuously heated by strong antiproton cyclotron excitation.)

In the case of very large proton numbers we observe the signal shown in Fig. 7.1(c). The two peaks correspond to the parallel resonances formed when the reactance impedance of the proton cloud is nearly equal and opposite to the impedance of the detection LC circuit. (Compare with Fig. 6.1(c) for electrons).

7.2.1 Identifying Ions

In Fig. 7.2(a) we identify a series of ions by detecting their axial motion after loading the trap using a typical field emission current (20-200 nA for protons as compared with 1 nA for electrons). For this particular field emitting point we applied a potential of -1.8 kV. The vertical axis in Fig. 7.2 is the square law output in a detection bandwidth of 1 kHz at $\nu_z \approx 1.9$ MHz. As the trapping potential is swept from -50 to -250 Volts, ions with different charge to mass ratios are brought into resonance with the tuned circuit and are observed in the detection window. Many single charged heavy ions are not visible on this scan. For our trap it would require a potential > 300V (the maximum we were able to put on the filter capacitors) to make their axial frequency resonant with the 1.9 MHz detection circuit. The observed signal is dependent upon particle number, particle

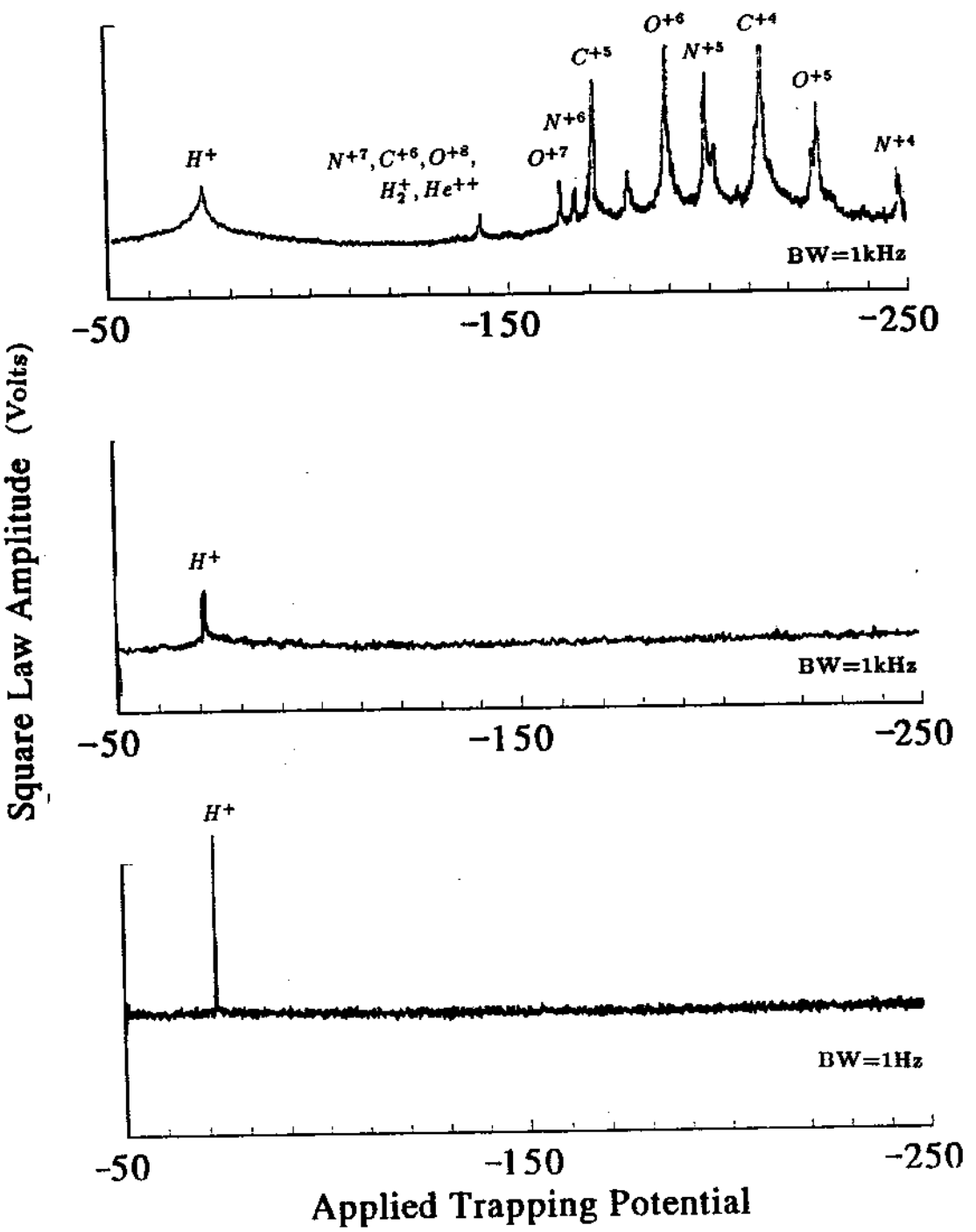

Figure 7.2: Axial signals of identified positive ions (a) loaded with high energy nested electrons, (b) loaded with lower energy nested electrons, and (c) after applying a noise broadened axial drive sequence to the unwanted ions during loading.

axial temperature, observation bandwidth, and sweep rate. Highly stripped ions are energetically possible because 2 keV ionizing electrons are obtainable from this particular FEP.

Assuming the particle species are highly coupled and in thermal equilibrium as we expect for this large cloud of ions, the amplitude of each ion type is a measure of the relative composition of the confined cloud if the detection sensitivity for each type is taken into account. The spectra displayed in Fig. 7.2 were generated from electron bombardment of the gold plated aluminum degrader. Other targets generate different compositions. For example, a hydrated titanium foil produced higher proportions of protons to other ions, but other ions were still present.

The axial signals can easily show very small amounts of helium and therefore can be used for sensitive detection of leaks. In most cases with the present detection sensitivity, He^{++} and He+ axial signals are not observed even though a 5×10^{-9} Torr partial pressure has been identifiable with an Ametek quadrupole gas analyzer during pumpout of the vacuum enclosure with a turbomolecular pump. (An ion pump was also active in the system and the trap enclosure was at 120°C at the time of the measurement.)

7.2.2 Coupled Cyclotron Observations

The multiple ion system provides an opportunity to measure the cyclotron frequency of several ions by a bolometric (or heating) technique. Axial heating can be observed as a function of the cyclotron excitation frequency. The technique is analogous to the more sensitive technique of observing the electron cyclotron frequency but relies on collisional coupling to transfer energy of the exited cyclotron motion into its axial motion (or into the axial motion of another species).

A valuable application is for indirect cyclotron measurements of ions not accessible in the range of existing detection amplifiers. A major limitation with this technique is that the only damping available for such ions is by the same indirect coupling mechanisms so that damping can be very slow. In Fig. 7.3 we show typical bolometric axial observations as a function of cyclotron heating of H^+, O^+4, and several carbon ionization states. The mass ratios determined from the data

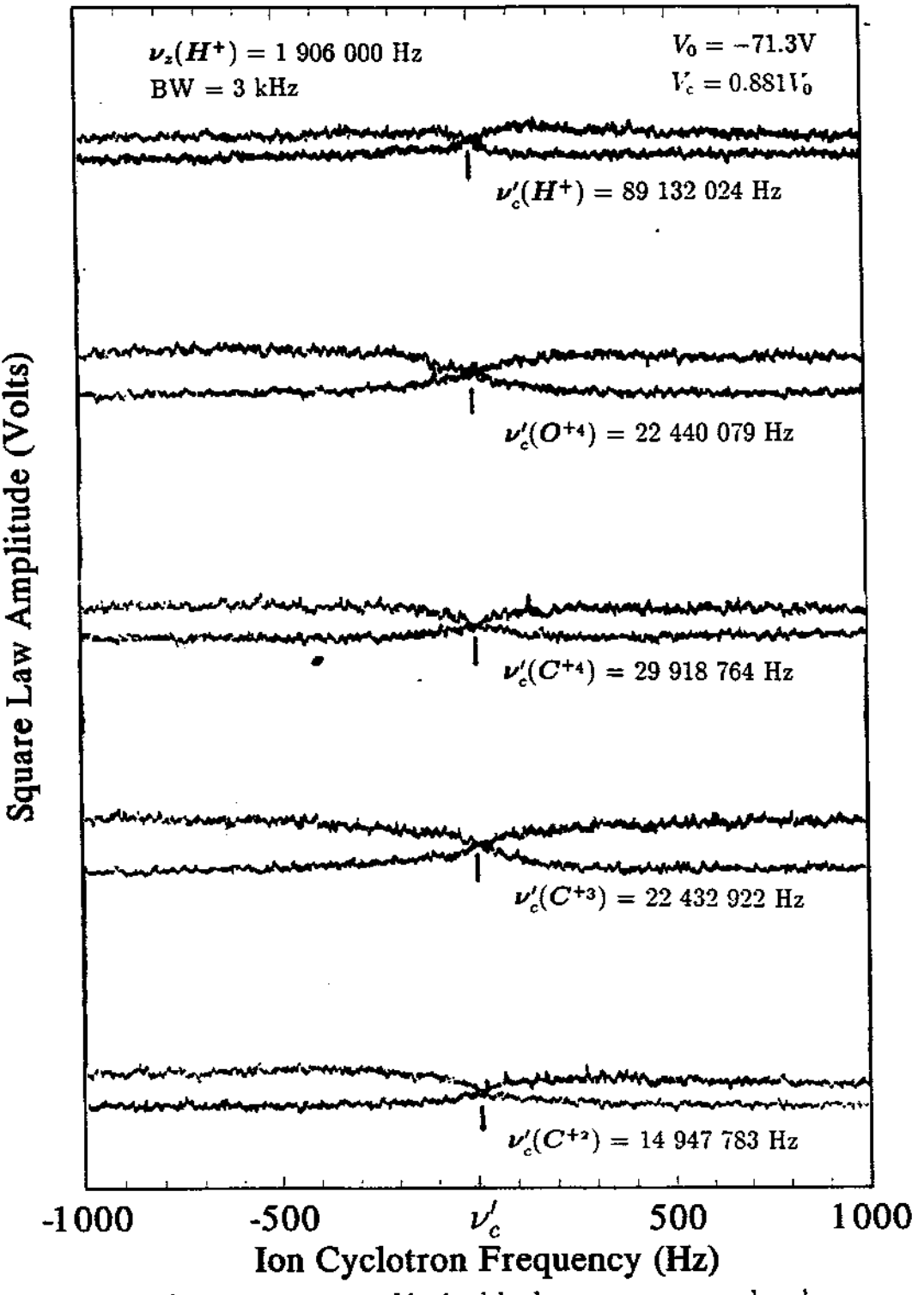

Figure 7.3: Ion cyclotron resonances of ionized hydrogen, oxygen, and carbon as observed through the axial heating of the proton axial motion. All traces are from the same confined cloud.

in the figure are

$$m(O^{+4})/m(p) = 15.877\,208(36)$$
$$m(C^{+4})/m(p) = 11.911\,148(20)$$
$$m(C^{+3})/m(p) = 11.911\,704(36)$$
$$m(C^{+2})/m(p) = 11.912\,252(40),$$

where the uncertainty given reflects only the observed resolution of approximately ± 50 Hz. Our measured value of $m(C^{+4})/m(p)$ is 1.1×10^{-6} higher than the more accurate measurement reported by Moore et. al. [72]. The frequency measurements require strong resonant drives at ν_c' and a shift to lower frequencies is in general observed for increased heating. The 'crossing' signature in Fig. 7.3 reflects the long damping time of the ions and results in a lineshape that is difficult to interpret to high precision. (The effect of heat on the cyclotron lineshape and the heat dependent shift become more apparent using direct detection techniques as shown in Fig. 10.13). Even though resolutions approach 10^{-7} with this technique, energy dependent systematic shifts limit achievable accuracies to about 10^{-6}. An important use of this coupling scheme will be discussed in Chapter 8 using the unique two component system of antiprotons and electrons. Unlike the positive ion system mentioned here, we will then be aided by the ability of the electrons to synchrotron radiate much of the energy and keep the antiproton energies low, yet allow for collisional coupling to be effective.

7.3 Eliminating Contaminant Ions

For the highest precision measurements on protons, it is necessary to eliminate all other ions from the trapping region. In this section we summarize a few of the avenues that we have explored.

Single Ion Source

One possible way to obtain a single species cloud is to load from a specific gas let into the trapping region. Because of the initial uncertainty on the achievable antiproton lifetime, we did not want to risk compromising the vacuum in our

trap vacuum enclosure by adding H_2 neutral gas. Such gas would be only weakly cryopumped, and we had the concern of pressure surges during antiproton loading that might result in high annihilation rates for low energy antiprotons.

Instability of Very Small Traps

A Penning trap can be made unstable if the radial component of the electric field is large enough to overcome the radial binding due to the magnetic field. The potential needed to exceed the stability condition $\nu_z < \nu_c/\sqrt{2}$ depends on the size of the trap. Our open endcap trap could be made stable for only protons, but unstable for all heavier ions if we applied 18 keV. This potential is not possible to achieve on our trap because of small tolerances and the presence of sensitive detection electronics. However, for much smaller geometries, potentials required for instability are more accessible. We have constructed a trap with an effective trap dimension of d = 0.12 cm. In principle, only protons will be stable with an applied potential of 1100 Volts in the 5.9 T field. In order to make room for the long trap for loading antiprotons this trap is presently incorporated into the trapping scheme described in Chapter 3, and its usefulness for ion work still remains to be demonstrated.

Ionizing Electron Energy and Nested Traps

The number of multiply stripped ions can be reduced by keeping the electron beam energy lower than most ionization thresholds. The field emission point most frequently used emits about 1 nA at -1600 Volts. To increase the loading efficiency, yet reduce the number of multiply stripped ions, we load the trap in a low energy nested well configuration as shown in Fig. 7.4.

Figure 7.2(a) and (b) shows ions trapped when the outer trap has a depth of -1600 Volts (Fig. 7.4(c)) and -100 Volts (Fig. 7.4(d)). In both cases the incident electrons have a kinetic energy of 1800 eV. Without the nest each emitted electron only passes through the trap once. With the nest, primary and secondary electrons are confined increasing the probability of ionizing neutrals. High energy electrons generate neutrals from the degrader surface (most likely by local heating), yet the

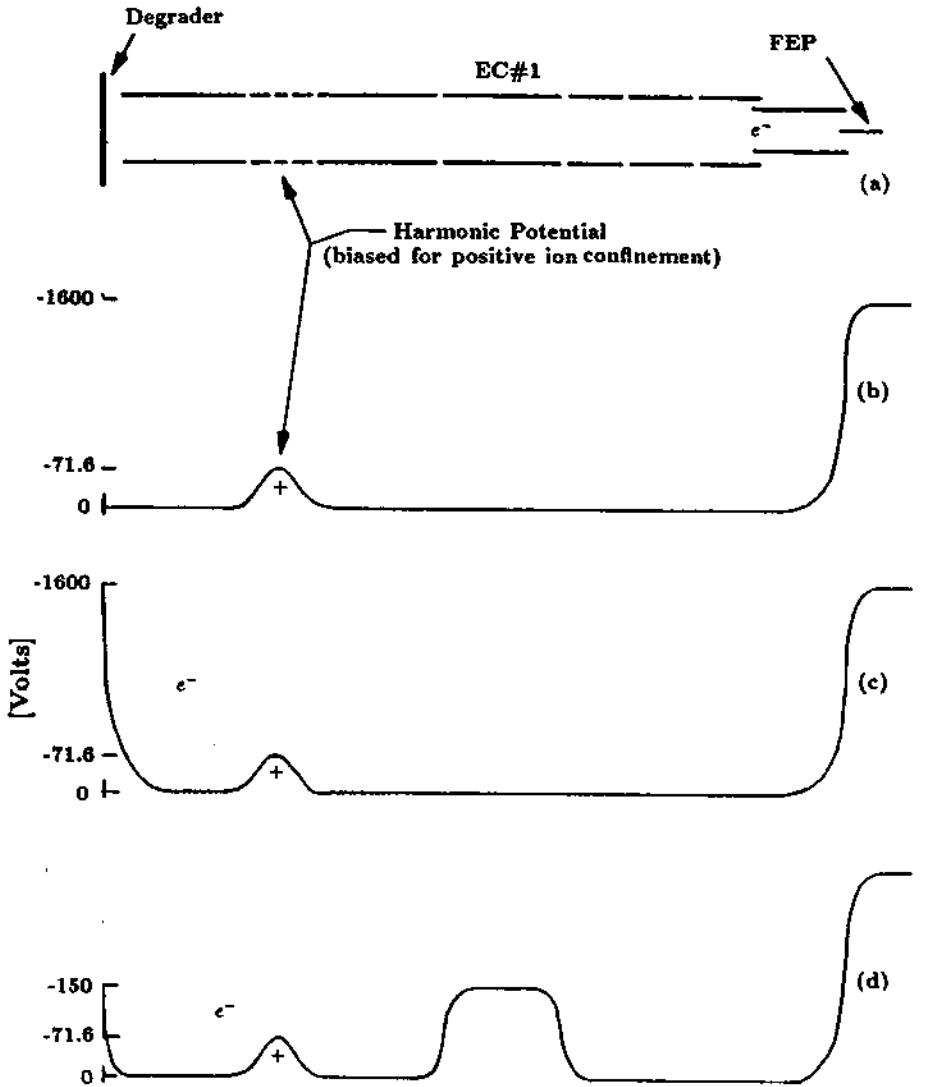

Figure 7.4: Nested trap configurations for energy selection of loaded ions.

ionizing seems dominated by the low energy nested electrons (which have higher cross sections and multiple passes). Ideally the ionizing electron beam could be reduced to near 13.6 eV, the binding energy of hydrogen. Most other ions would not be formed since only a few have ionization potentials smaller than this energy. At the present, effective loading requires a minimum of 70 Volts between the applied outer trap potential and the harmonic well bias (7.4(d)).

Resonance Ejection: Noise Broadened Excitation Drives

Several trapping groups have found that driving on the resonant frequency of the ion can be an effective way in reducing unwanted ions from being confined in the trap . Two techniques have shown promise. Church and coworkers have applied ν_c' and ν_m excitation during the loading process to only allow specific charge to mass ratios to fall into the trap [55,20]. Other groups [72,21] have had success with cleaning techniques applied after the trap is loaded by applying strong noise broadened axial excitations to drive the axial amplitude into the endcap of a traditional hyperbolic trap. The noise broadening is needed to take account of possible amplitude dependent changes in ν_z due to trap anharmonicity. Since our trap endcaps have no surface perpendicular to the trap axis we have found it difficult to resonantly drive ions out once they have been loaded.

In our trap, the use of very strong noise broadened axial excitation drives to the unwanted ions *during* the loading process has proven to be effective. We use a white noise source from a HP 3561A signal analyzer to FM modulate the selected axial drive frequency generated by an HP 8662A frequency synthesizer. A 30 kHz modulation and an axial drive amplitude of -10 dBm is applied to a trap endcap.[1] The effectiveness of the technique seems dependent on the proper amplitude (too strong keeps the protons from loading, too weak allows other ions to load). During the loading process, we repeatedly step through the various axial frequencies of possible contaminant ions, each for a duration of 1 second. For loading protons, we pass the drive through a 1.2 MHz low pass filter to avoid harmonics of the strong

[1]Helpful suggestions for effective noise broadening and drive amplitudes were provided by W. Jhe and D. Phillips.

drive form overlaping with the protons. When ions are first formed in the trap, they are only weakly bound and the strong noise broadened drive is sufficient to prevent the ion from damping and staying bound. By concentrating on the parent ions of more highly stripped ions (O^+, N^+, C^+), we prevent most contaminants from loading.

The results of applying this technique are shown in the potential scan shown in Fig. 7.2(c) using the configuration in 7.4(d) with the noise broadened drive added. The cleanliness of the proton cloud is verified in two ways. First, the contaminant level is low enough that we not able to observe heating of the proton axial and/or cyclotron motions by driving hard on the cyclotron frequency of the undesired ions. Second, we can obtain coherent axial resonance signals which appear to only be possible in a single species cloud.

Chapter 8

Indirect Antiproton Observations: Electron Damping

For the first time, the unique two component cloud consisting of antiprotons and electrons can be non-destructively studied in a Penning trap. Unlike the case with another ion species mixed with protons (Chapter 7), the companion electrons are much less massive and synchrotron radiation removes cyclotron energy with a time constant of approximately 0.1 seconds. During the initial loading and cooling studies only the axial preamplifiers (for $\nu_z(e^-)$ and $\nu_z(\overline{p})$) were connected to the trap. The electrons aid in the cooling of the antiprotons during resonance measurements. Using electron damping, we have performed a preliminary mass comparison of $m_{\overline{p}}/m_e$.

8.1 Observations via Axial Heating of Electrons and Antiprotons

Non-destructive observations of the antiproton cyclotron frequency are obtained using indirect collisional coupling to the axial motion of either the electrons or the antiprotons. We monitor the square law voltage developed across the axial resonant circuits at $\nu_z(e^-)$ and $\nu_z(\overline{p})$ in a finite bandwidth (typically 1 to 3 kHz) as a function of antiproton cyclotron heating. Heated antiproton axial signals are not easily observable immediately after loading and cooling when the trapped electron number still significantly outnumbers the antiprotons. When the electron number

is sufficiently reduced by the drive and dip methods described in Section 4.3, the electrons are often no longer resolved as a dip in the noise spectra. However, if either the antiprotons or electrons are heated, the heated motion can be detected using the tuned circuits in a fashion analogous to the proton bolometric technique.

When the antiprotons are driven resonantly at their cyclotron frequency, we observe axial heating of both electrons and antiprotons as shown in Fig. 8.1(a) and (b). When the resonant heating drive is turned off, both of the heated signals decay with the same time constant, presumably the time required to transfer energy from the antiprotons to the electrons which then cool much more rapidly. The antiproton damping time constant (for a fixed drive strength), typically ranges between 1 and 1000 seconds depending upon particle numbers and spatial overlap. Figure 8.1(a) and (b) shows the best resolution that we achieved by the careful control of the heat input, and by sweeping very slowly. Electrons are still present as observed by the heating of the electron axial signal. Figure 8.1(c) shows the resulting square law output as a function of cyclotron heating when too much heat or too few electrons are in the trap. If insufficient electrons remain in the trap, we observe no heated electron signal at $\nu_z(e^-)$ and the antiprotons can remain heated for many hours. With such little damping it is difficult to make a return sweep that can give the 'crossing' signature of the cyclotron resonant frequency.

8.2 Preliminary Mass Comparison

By performing a series of indirect cyclotron measurements on this mixed system we have made preliminary mass comparison. To measure the antiproton cyclotron frequency, the trapping potential is adjusted to $V_1 \approx 71$ Volts for which the maximum axial antiproton signal resulting from the heated cyclotron motion is observed at the frequency $\nu_z(1)$. The square law signal is then monitored as the antiproton cyclotron drive is swept slowly upward and downward through resonance. The free space antiproton cyclotron frequency (2.12) is

$$\nu_c(1) = \nu_c'(1) + \frac{(\nu_z(1))^2}{2\nu_c'(1)}. \tag{8.1}$$

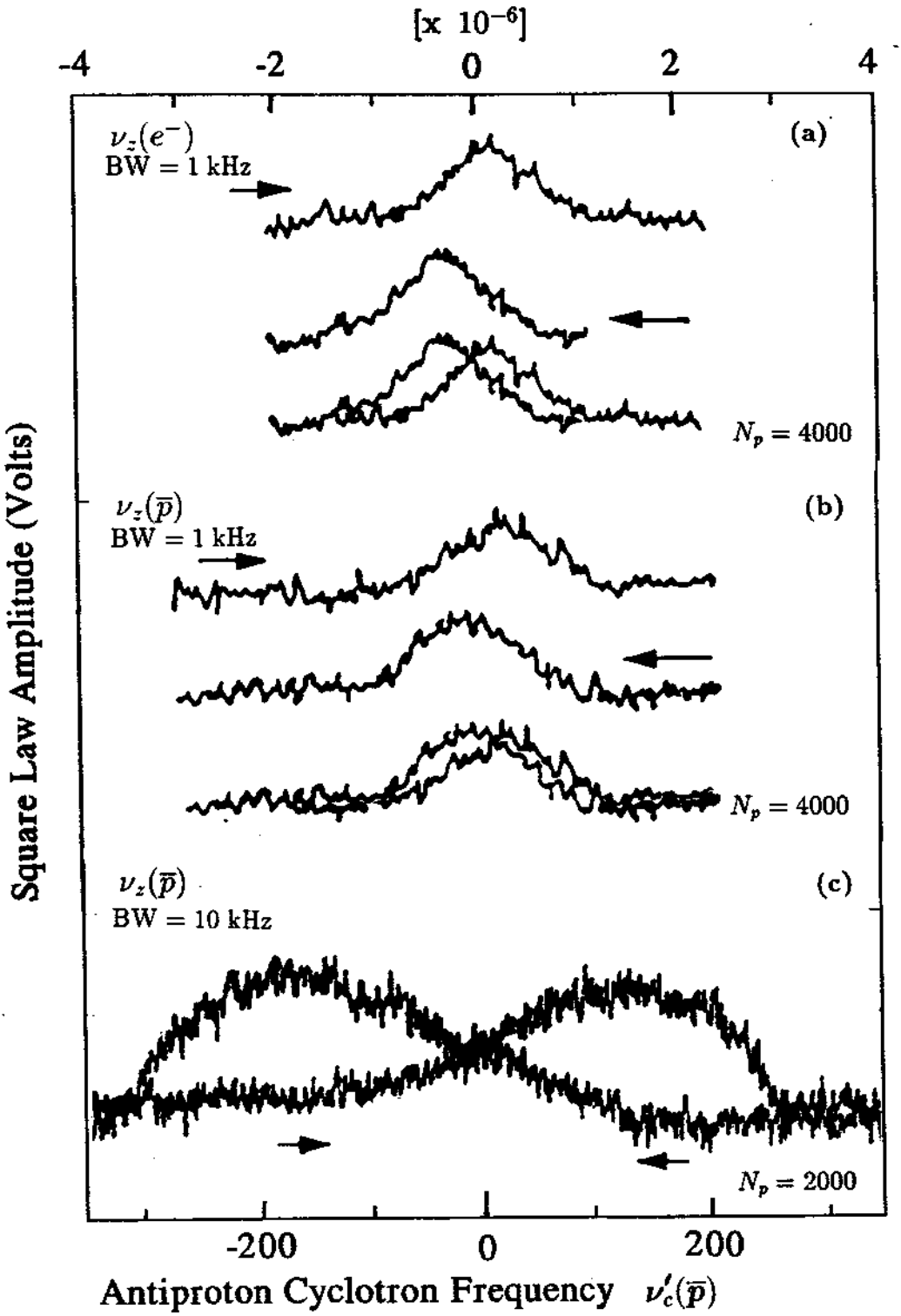

Figure 8.1: Detected axial heating of the electrons (a) and antiprotons (b) as a function of driving on the antiproton cyclotron frequency $\nu_c'(\overline{p})$. (c) The resulting axial antiproton signal resulting from either increased cyclotron drive power or reduced number of electrons.

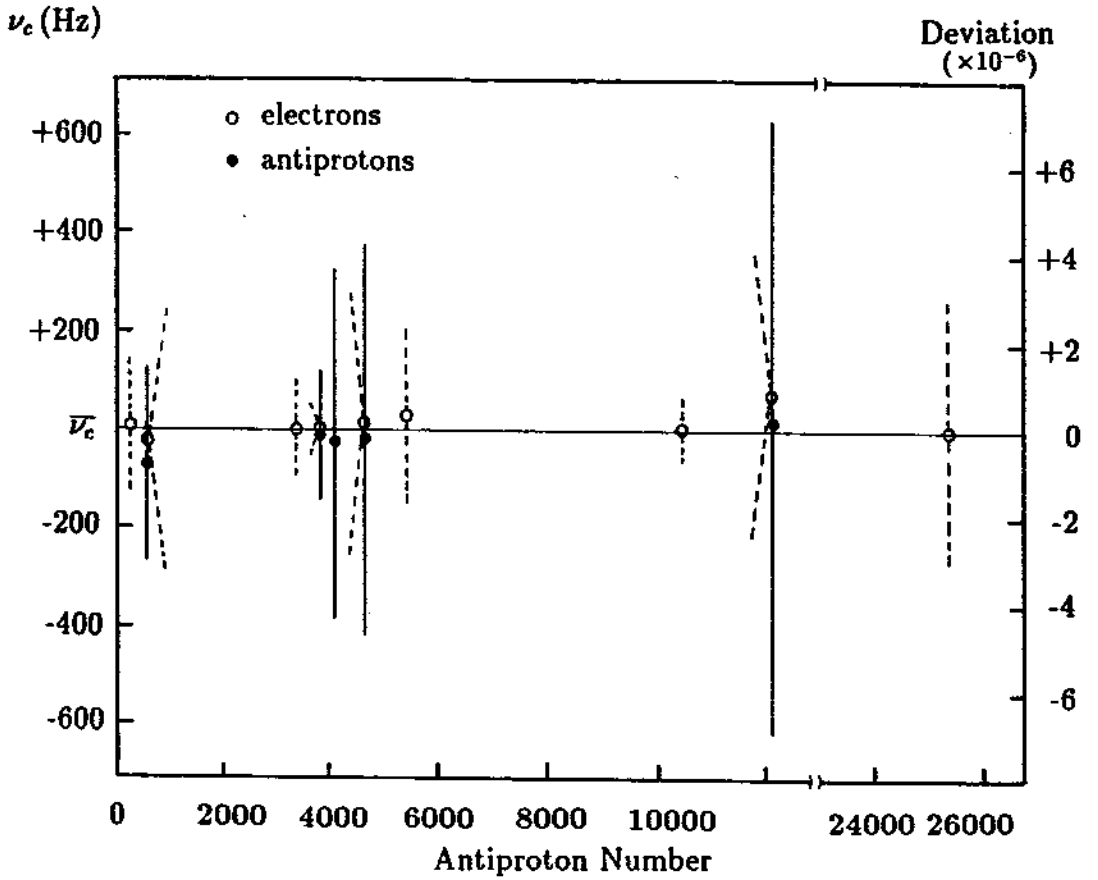

Figure 8.2: Antiproton cyclotron frequency as a function of antiproton number as measured through the axial heating of both antiprotons and electrons by collisional coupling.

Similarly, the trapping potential is adjusted to a new value $V_2 \approx 32$ Volts so that the electrons are resonant with their tuned circuit. The heated electron signal is monitored as the antiproton heating drive is again swept upward and downward through resonance at the cyclotron frequency $\nu_c'(2)$ which is different from $\nu_c'(1)$ because of the different trapping potential. This gives a second free space cyclotron frequency *for* the antiproton but measured ***using*** the electron expressed as

$$\nu_c(2) = \nu_c'(2) + \frac{\nu_z^2(1)}{2\nu_c'(2)}\frac{V_1}{V_2}. \tag{8.2}$$

In Fig. 8.2 we show that the measured cyclotron frequency does not shift when the antiproton number is varied by 2 orders of magnitude. In all cases, the measured cyclotron frequencies as observed through the antiproton heating or the electron heating agree. We use the total heated linewidth as the uncertainty since the lineshape is not well understood though much of the hysteresis results from the damping time of the antiprotons.

By performing cyclotron measurements on small clouds of electrons as described in Chapter 6, a mass comparison of antiprotons to electrons is made. A comparison of cyclotron frequencies gives

$$\frac{\nu_c(e^-))}{(\nu_c(\overline{p}))_w} = 1836.1534(16), \tag{8.3}$$

where we have taken the weighted average of the antiproton data shown in Fig. 8.2. Using the best value for the proton-electron mass ratio by VanDyck et.al.[100,72]

$$\frac{m_p}{m_e} = 1836.152\ 701(37) \tag{8.4}$$

we infer the antiproton to proton mass ratio to be:

$$\frac{\nu_c(e^-)}{\nu_c(\overline{p})}\left(\frac{m_{e^-}}{m_p}\right) \Rightarrow \frac{m_{\overline{p}}}{m_p} = 1.000\ 000\ 35(87). \tag{8.5}$$

Even with the indirect technique of detecting the antiproton cyclotron frequency, this fractional uncertainty of 8.7×10^{-7} is nearly 60 times more accurate than inferred from exotic atom methods.

The precision and accuracy of this technique are limited in two ways. First, since we observe axial heating in a relatively large bandwidth, the precision of the

correction $\nu_z^2/2\nu_c'$ is limited by our inability to identify a precise axial frequency. Second, shifts in the axial and cyclotron frequency are observed when too much heat is put in the system. Such shifts, which can be many parts in 10^6, most likely result from the large spatial extent of the cloud and the sampling of field imperfections. Substantial particle heating results from the strong cyclotron drives used to transfer energy to the axial motion by predominantly collisional mechanisms. For more precise and accurate measurements the perturbations resulting from such large amounts of resonant heating will be prohibitive.

Chapter 9

Direct Antiproton Observations: Electronic Damping

Direct observations of the cyclotron motion of the antiprotons are made by using a resonant preamplifier at $\nu_c'(\overline{p})$ connected across two of the segments of the quad ring [97]. This scheme, also provides direct resistive cooling of the antiproton cyclotron motion, and alleviates the need to rely on the electrons for damping.

In this chapter we present the use of direct cyclotron detection, the obtainable resolution, and describe use of this technique in performing systematic studies regarding trap polarity in order to compare protons and antiprotons. We also discuss more refined measurements of the axial frequency of antiprotons including coherent detection and the locking of the axial frequency to an external oscillator analogous to the electron system (Chapter 6). The techniques described in this chapter apply equally well to the detection and measurement of protons.

9.1 Direct Cyclotron Detection

Direct detection of the cyclotron oscillation is analogous to the axial detection except, unlike the axial motion which depends only on the electrostatic quadrupole field, the cyclotron motion also depends on the state of the magnetic field. A resonant circuit tuned to about 89 MHz is connected to the ring electrode as shown in Fig. 5.5. At 5.9 T, the modified cyclotron frequency is nearly centered in the detector resonant bandwidth. At 4 K, a signal at $\nu_c'(\overline{p})$ is not observable,

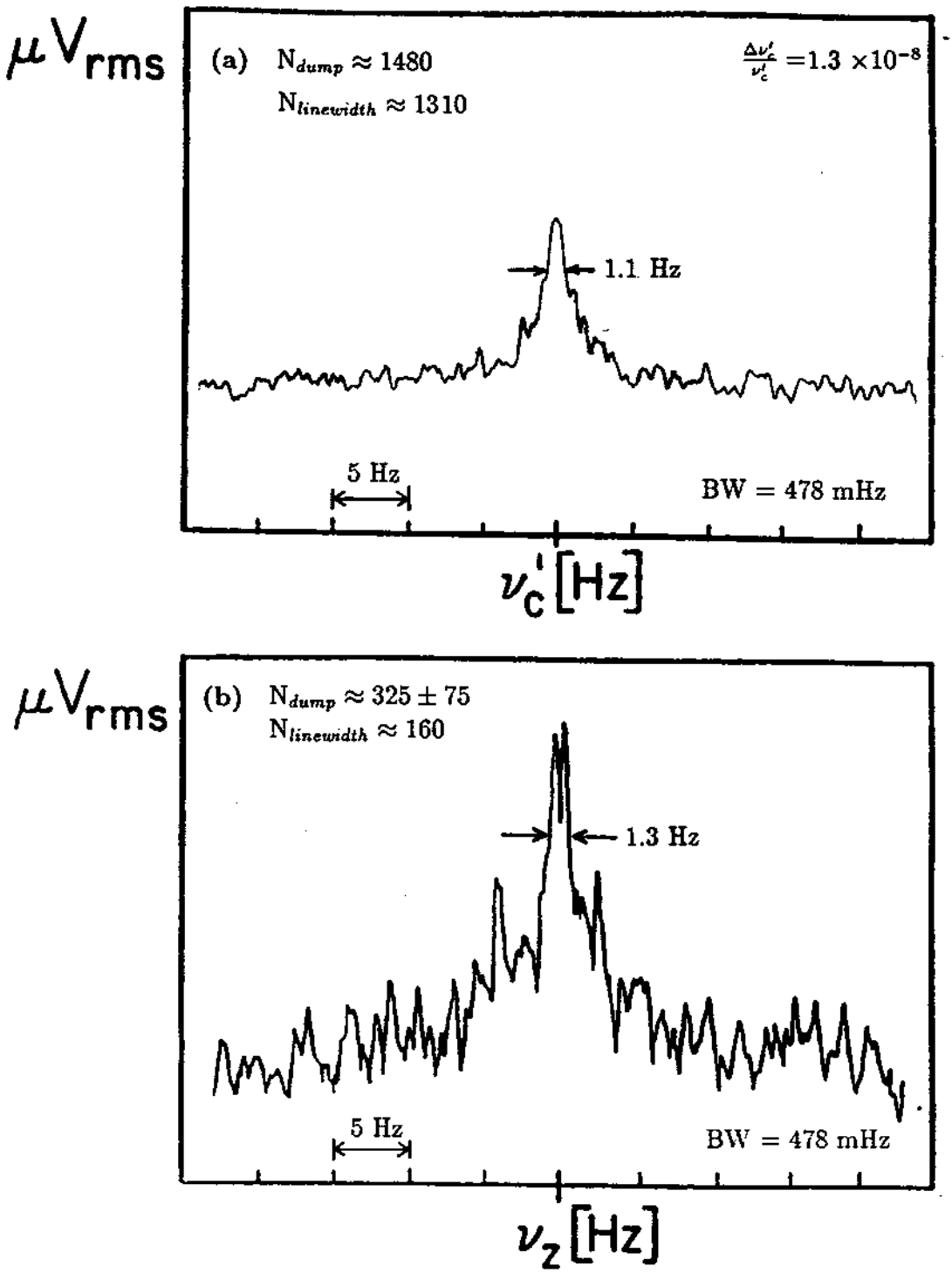

Figure 9.1: Direct observations of the antiproton oscillation frequencies on an HP 3561A signal analyzer after being mixed down to approximately 50 kHz. (a) The antiproton modified cyclotron frequency. (b) The antiproton axial frequency.

but for sufficient heat ν_c' ($\overline{p}$) can be directly observed as shown in Fig. 9.1(a). Without electrons in the trap, the antiproton damping time τ is on the order of hundreds of seconds, thus for sufficiently high temperatures, one can directly observe the residual heat of the particles by observing the frequency spectrum at 89 MHz. Unlike the bolometric technique described in Chapter 8 no external resonant drives are applied to the system during aquisition of the signal. With this technique we are sensitive to as few as 40 antiprotons (or protons) though systematic shifts are observed for the levels of resonant ν_c' heating required to observe so few with our present detection sensitivity (Chapter 5).

A system of more than 200 antiprotons is easily observed with only slight heating applied by driving on the magnetron sideband frequency $\nu_c' + \nu_m$. This frequency, applied either to the balanced drive on the ring or on both endcaps, serves to cool (i.e. reduce) the magnetron orbit, centering the antiprotons in the trap with a lower cooling limit than is possible with the drive at $\nu_z + \nu_m$ [13].

For large amounts of heating, the lineshape grows asymmetrically to lower frequencies (Chapter 10, Fig. 10.13). In general, a corresponding broadening as a function of cyclotron heating is not observed in the axial signal.

9.1.1 Simultaneous Measurements of ν_c' and ν_z

Along with the ability to directly detect cyclotron signals with reduced amounts of heat, small and narrow axial signals can be observed as shown in Fig. 9.1. For purposes of the mass comparison, the cyclotron ν_c' and axial ν_z signal can now be simultaneously but *independently* measured. Both measurements are then used to compute the correction frequency $\nu_z^2/2\nu_c'$ to obtain the free space cyclotron frequency by the now familiar relationship

$$\nu_c = \nu_c' + \frac{\nu_z^2}{2\nu_c'}. \tag{9.1}$$

The simultaneous observation of ν_c' and ν_z at a fixed voltage is the method we have used most extensively for determinations of the antiproton (and proton) free space cyclotron frequencies reported in this thesis. Unlike the ν_c' versus voltage method, this method is independent of absolute trap voltage, since the sum of

ν_c' and $\nu_z^2/2\nu_c'$ is independent of voltage. Figure 9.1 shows the high resolution that can be obtained by direct observation of ν_c' and ν_z. Both detected spectra shown were observed using an HP3561A Signal Analyzer after the signals were mixed down to about 50 kHz (see Fig. 5.4). No external drives are applied during the detection of these signals. The signals are just observations of the residual heat in the respective orthogonal oscillations of the confined antiprotons.

If allowed to resistively damp to 4 K, the signals disappear into the noise floor but a dip, as in the case of electrons, is not observed. To get sufficient signal to noise we must add small quantities of heat. To give a perspective of the much smaller amounts of heat we apply, we can usually heat the motion enough to observe the cyclotron frequency for many minutes with a -35 dBm drive applied on the sideband $\nu_c' + \nu_m$ for 5 seconds. With the bolometric technique described in chapter 8, we continuously apply about -20 dBm on ν_c' .

For small clouds (< 2000) and with only little heating, the axial and cyclotron motions seem completely uncoupled if the trap compensation is adjusted properly. Heat can be applied to either degree of freedom by direct drives or using the appropriate magnetron sideband drives.

The ability to easily study the heat exchange between the two modes is very useful. For small clouds, we can turn on the coupling by mistuning the trap anharmonicity (analogous to the electron case in Chapter 6) or by driving the particles to extremely large amplitudes. If sufficient cooling electrons remain in the trap, the coupling seems aided by collision mechanisms. For large clouds, collisional mechanisms appear to keep the normal modes nearly in thermal equilibrium with each other.

With present sensitivities, the best resolution obtained with this method of observing residual heat in the normal modes is $\Delta\nu_c' \approx 1$ Hz (10^{-8}), and $\Delta\nu_z \approx$ 400 mHz (2×10^{-7}). The limiting cyclotron linewidth appears to be an indication of the trapped number, although field stability, or broadening by the sampling of field gradients or trap anharmonicity may result from the slight heating of the antiprotons.

9.1.2 Cyclotron Measurements vs. Voltage

Directly observing cyclotron frequencies by the method outlined in the previous section has some very important advantages. With just this one amplifier it is possible to determine the free space cyclotron frequency by measuring ν_c' as a function of trapping voltage. The extrapolation to zero trap voltage (where V=0 is when $\nu_z = 0$) gives a measurement of the free space cyclotron frequency, since the perturbation of the quadrupole potential no longer exists. In Fig. 9.2(a), measurements of ν_c' are plotted as a function of voltage. In Fig. 9.2(b), the residuals of the measured points from the least squares fit are shown which in this case are distributed in a near random fashion.

The analysis of these measurements is an extremely valuable check on electrostatic systematics. The functional form of $\nu_c'(V_0)$ for a perfect trap deviates slightly from a line at high trapping potentials. From (2.12) the cyclotron frequency ν_c' is

$$\nu_c' = \nu_c - \frac{\nu_z^2}{2\nu_c'} + F(\epsilon, \theta). \tag{9.2}$$

The term $F(\epsilon,\theta)/\nu_c'$ is 3.6×10^{-11} with our present operating parameters. Neglecting this term, we can expand in terms of the small parameter (ν_z/ν_c') giving

$$\nu_c' = \nu_c - \frac{\alpha V_0}{2\nu_c} - \frac{\alpha^2 V_0^2}{4\nu_c^2 \nu_c'} - ..... \tag{9.3}$$

where $\alpha \equiv (C_2 e/md^2)$. For low voltages (where most perturbations have the largest influence), the second order term is small and the linear form is sufficient.

Because antiprotons and protons are essentially identical, but of opposite charge, this technique can be used to perform and understand systematic studies with regard to electrostatic perturbations and trapping polarity. The importance of understanding systematics related with comparing particles of opposite polarity in Penning traps is well known [97] but has proven troublesome as evident in early attempts to compare the mass of the proton and the electron [99,100]. These earlier measurements were limited in the uncertainty of the relative positions of opposite polarity particles in the trap.

For the antiproton-proton mass comparison, we have performed several determinations of $\nu_c'(\overline{p})$ as a function of voltage and studied the slope, intercept, and

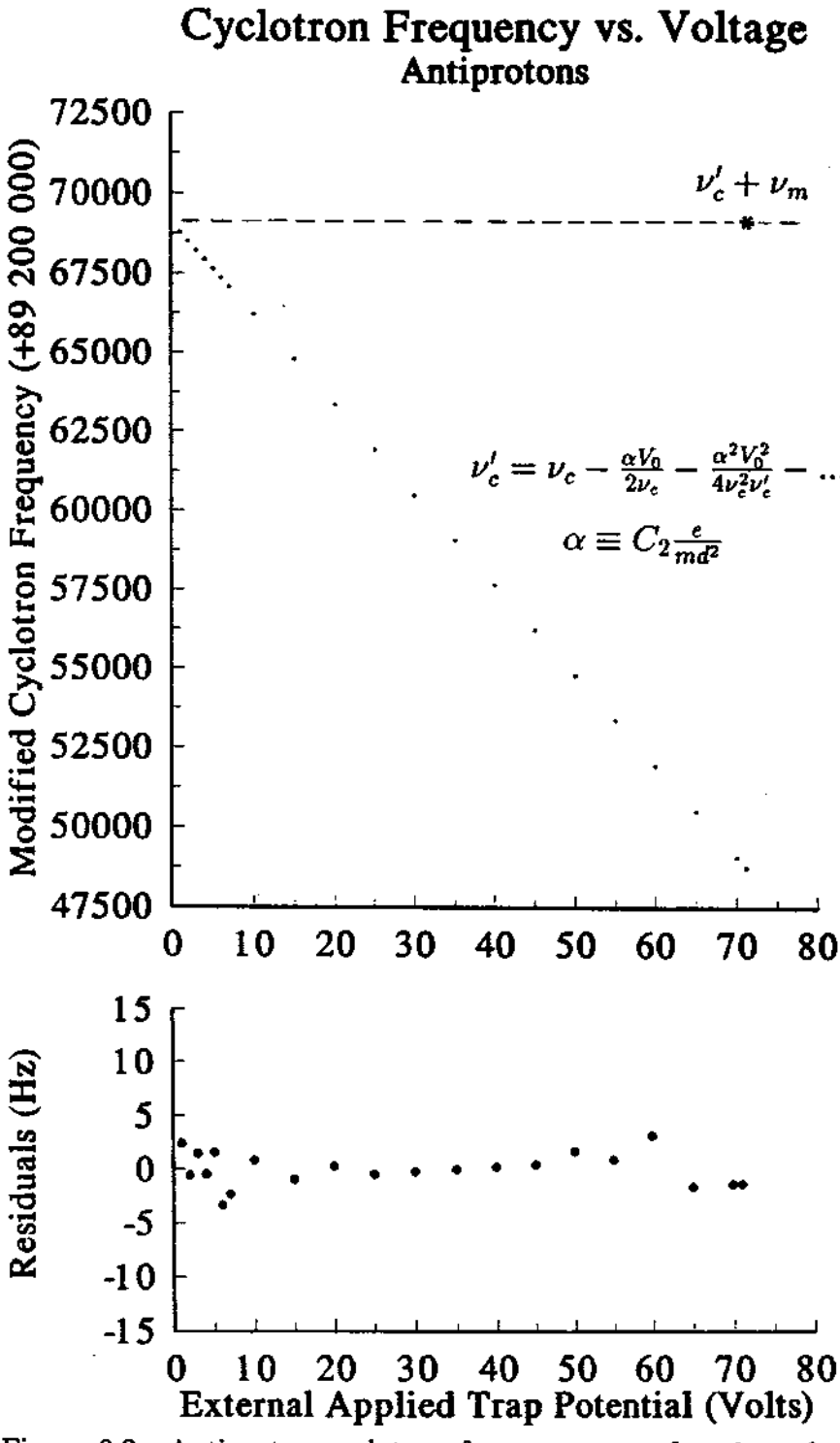

Figure 9.2: Antiproton cyclotron frequency as a function of trap voltage and the residuals of the linear fit. Analogous measurements, but with opposite trap polarity, are performed using protons.

scatter of such measurements. The extrapolated intercepts are direct measurements of the free space cyclotron frequency which can be compared to measurements made at a fixed voltage. For the extrapolation to be accurate, the absolute zero voltage point on the trap must be known. In fact, offsets in the trap voltage (evidently from contact potentials) are clearly observed with this technique when we reverse the trap polarity. In Chapter 10, we present comparison data using protons and antiprotons. We also compare these observations with observations of the axial frequency taken at a fixed trapping potential, but with opposite polarity.

9.2 Phase Sensitive Detection

9.2.1 Axial Motion

Cleaning Residual Electrons

The direct and simultaneously detected 'heat' signals are easily observable even though there may remain small numbers of electrons from the initial reduction procedure outlined in Chapter 4. For high precision measurements it becomes necessary to eliminate the possible perturbations arising from impurity ions. We have been able to obtain antiprotons clouds of up to 2000 antiprotons which have several signs of being free of electrons. The clean clouds are obtained with repeated applications of the drive and dip procedure to yet lower voltages, typically 300 mV and then 100 mV. Often in these last two steps, we observe antiprotons leaking from the trap. The effectiveness on expelling the last few electrons seems correlated with the use of the axial magnetron sideband drive to keep the electrons centered and on resonance during the drive and dip procedure.

We observe the effectiveness of our technique in three different ways. First, we look for axial heating of the few remaining electrons by severe cyclotron heating of the antiprotons as described in chapter 8. Second, we can measure the damping constants of the axial and cyclotron motions of the antiprotons and observe that they increase as a function of dipping and converge to the expected resistive damping rates which are much slower than when electrons are present. A third indicator is when we can obtain coherent axial antiproton responses to an external

drive analogous to the observations with electrons in Chapter 6. We also cannot obtain coherent axial resonances of electrons when antiprotons are simultaneously present in the trap. Similarly, coherent proton resonances can only be achieved when few ($N_{ions} << N_{protons}$) or no other positive ions are identified to be present in the trap. The proton observations are consistent with the experience of others [106].

Coherent Axial Response

The success of preferentially removing electrons from the trap has allowed us to use phase sensitive detection on the axial motion of the antiprotons. The scheme is entirely analogous to the case for electrons except that the signal is much weaker for the more massive, slow moving antiprotons (since the resistive damping of the axial motion is proportional to 1/m). The typical trap voltage is +71.6 Volts producing an antiproton axial frequency of about 1.91 MHz. The ring is modulated at $\nu_{mod} = 63.07$ kHz, or ν_{mod}/ν_z=0.032 (for electrons ν_{mod}/ν_z=0.022 was used).

An example of a coherent axial response of antiprotons is shown in Fig. 9.3. The response signal is obtained from a Stanford Research Systems SR510 Lock-in Amplifier when the axial and ring modulation drive strengths are finely adjusted. As with the electrons, the ability to achieve good signal to noise is dependent upon simultaneous application of axial magnetron sideband cooling near $\nu_z + \nu_m$, but not directly on it. When drive strengths and trap harmonicity are optimally tuned, coherent signals can be detected even as the directly observed 'heat' signals of $\nu_z(\overline{p})$ and $\nu_c'(\overline{p})$ damp away. The ability to observe the antiprotons with much less heat should result in less perturbed measurements on smaller numbers.

Locked Axial Frequency

Once we obtain the dispersion curve as shown in Fig. 9.3, we can lock the axial frequency to an external oscillator analogous to the technique for electrons. Figure 9.4(a) shows the locked axial response of antiprotons at $\nu_z(\overline{p})$ analogous to the locked electron response shown in Fig. 6.2. This observed trace is highly

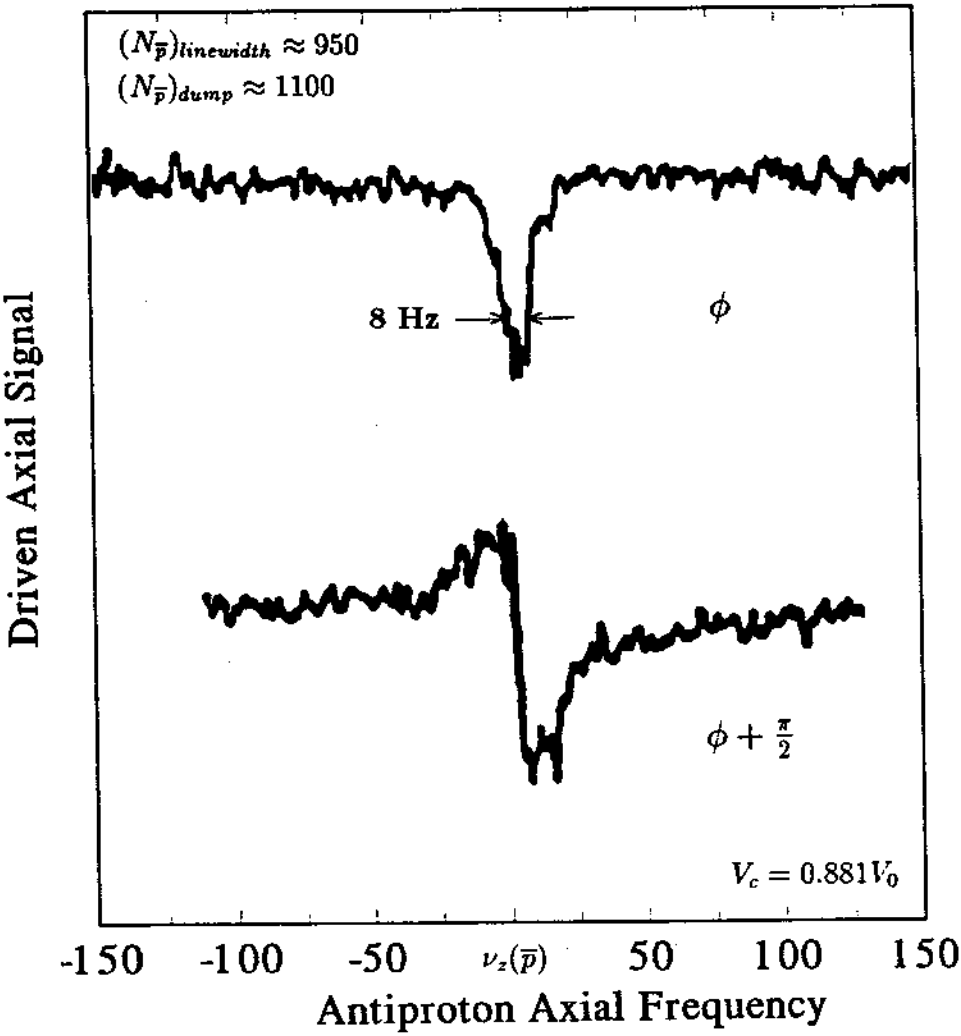

Figure 9.3: Phase sensitive detected axial signal of weakly driven antiprotons.

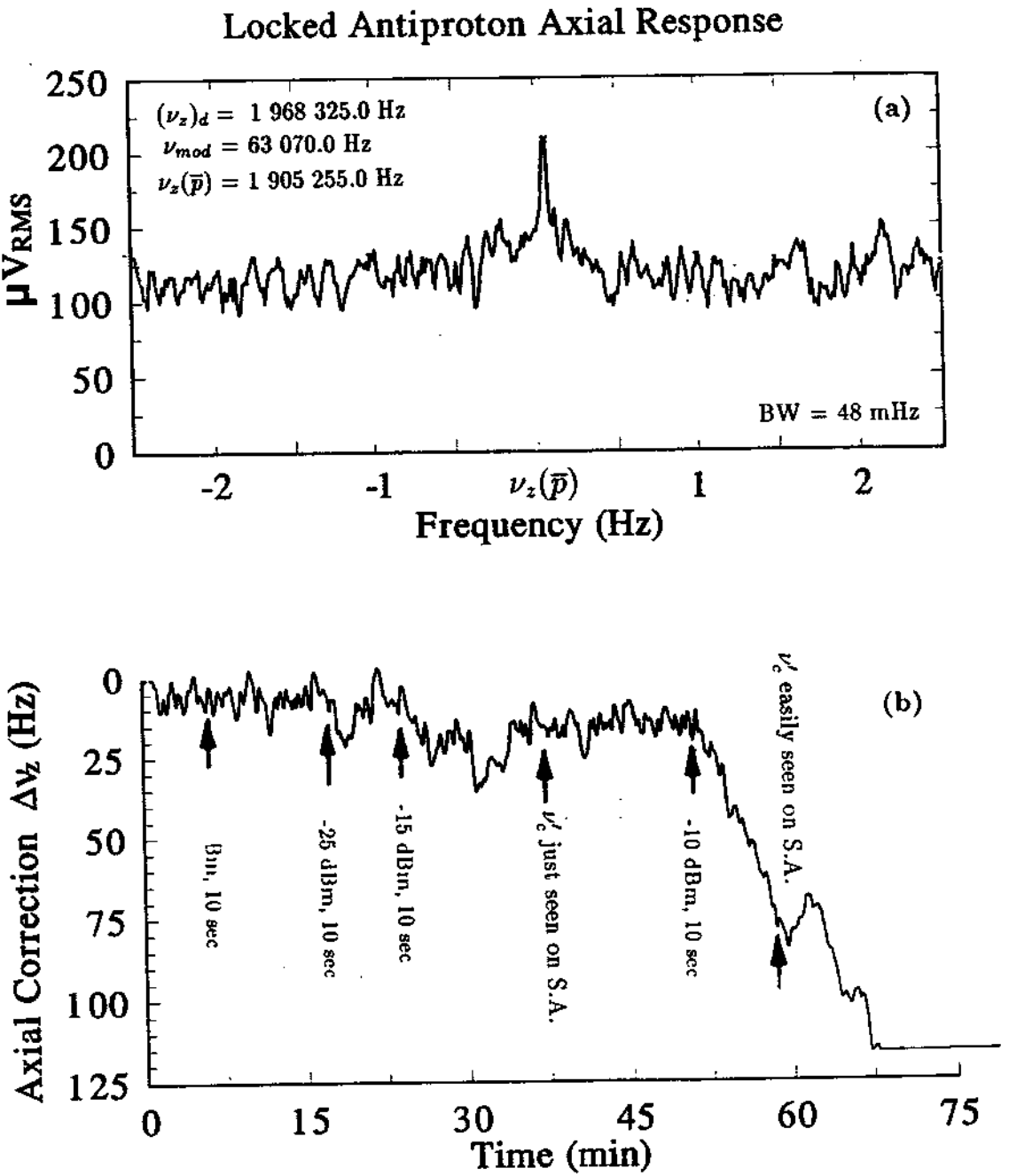

Figure 9.4: (a) Highly averaged locked antiproton axial response to drives at $(\nu_z + \nu_{mod})_d$ with the ring potential modulated at ν_{mod}. (b) Trap voltage feedback signal correcting for heating introduced with a weak cyclotron sideband drive at $\nu_c' + \nu_m$.

averaged using an HP3561A Signal Analyzer with a bandwidth of 48 mHz which limits the observed linewidth.

Figure 9.4(b) shows the voltage feedback signal to keep the axial motion of about 380 antiprotons locked. The lock, which is accomplished with a feedback integration time of about 20 seconds, can be held for hours. In Fig. 9.4(b) the lock is severly perturbed by applying successively stronger excitation drive signals at $\nu_c' + \nu_m$ while attempting to simultaneously observe direct cyclotron heating as described in Section 9.1. Eventually, the signal is kicked out of lock, though a direct cyclotron signal with a linewidth of less than 1 Hz was observed this way, thus being our first *direct* cyclotron measurement of antiprotons with a linewidth resolution of less than 10^{-8}. We can also observe locked axial signals as a function of a weak cyclotron drive as a means of indirectly measuring the cyclotron resonance. This method may prove to be more sensitive than the direct cyclotron observations and has already been used by others to study a single proton in a much smaller trap [72].

As seen in Fig. 9.4(b) the sensitivity of the locked axial motion to cyclotron excitation is not yet significantly better than the direct cyclotron observations. As we saw in Chapter 6 with electrons, the sensitivity of the locked axial signal to the cyclotron excitation depends upon the achievable signal to noise to detect changes in the axial frequency $\Delta\nu_z$ and on the mechanism to couple energy in the cyclotron motion to the axial motion. Magnetic bottles and/or anharmonicity are effective in coupling the motions at some level, but both mechanisms introduce perturbations and possible systematic shifts on the measured eigenfrequencies. One way to avoid the need for such coupling mechanisms is to use phase sensitive detection techniques directly on the cyclotron motion though experimentally this is more difficult to implement than axial detection. Another technique is to apply rf voltages on the sideband drives at the sum or difference frequencies of the modes to be coupled. A short pulse can be used and if the duration and amplitude are correctly adjusted, such a pulse can exchange the motion between the two modes. An application of the technique at the magnetron sideband $\nu_c' + \nu_m$ has recently been applied to cool the magnetron motion of heavy ions [85]. Another recent

application using the axial sideband ν_c' - ν_z has been used to couple the cyclotron and axial motions for damping and detection of the cyclotron motion of single ions [21,22].

9.2.2 Cyclotron Motion

The direct detection method described detects the residual heat in the confined antiprotons. The method relies on the amplitude of the induced signal which depends on trap size, particle number and particle temperature. Ultimately there exist limitations to such a scheme, because large particle amplitudes and numbers can contribute to undesirable systematic effects. Therefore we continue to develop other more sensitive methods of direct particle detection to improve signal to noise, thus requiring fewer particles and smaller amplitudes.

One way to increase signal to noise is to observe the phase of the motion analogous to the schemes outlined with axial detection techniques. Eliminating direct feedthrough of the phase defining drives is more difficult since it can involve modulating the magnetic field. We have examined three different schemes to minimize feedthrough. At times, we have added a fraction of the drive signal to the detection line and adjusted the phase and amplitude to cancel the direct feedthrough. A factor of 50 in rms voltage reduction of the direct feedthrough signal is easily obtainable. Another way to realize such cancelation is to drive on opposite segments of the quad ring electrode in a balanced drive configuration [97]. By properly adjusting the phase of the signals to the two opposite segments, the direct feedthrough signal observed across the remaining segments is minimized.

For active drive techniques we can also minimize direct feedthrough by alternating the drive and detect cycles. To demonstrate this, we have adapted electronics developed for our pulsed NMR system to apply a strong drive pulse, and alternate it with the detection cycle. We show in Fig. 9.5 the detected cyclotron response signal mixed down to about 1 kHz. Different applied trapping voltages indicate that the visible ringing is from the trapped antiprotons.

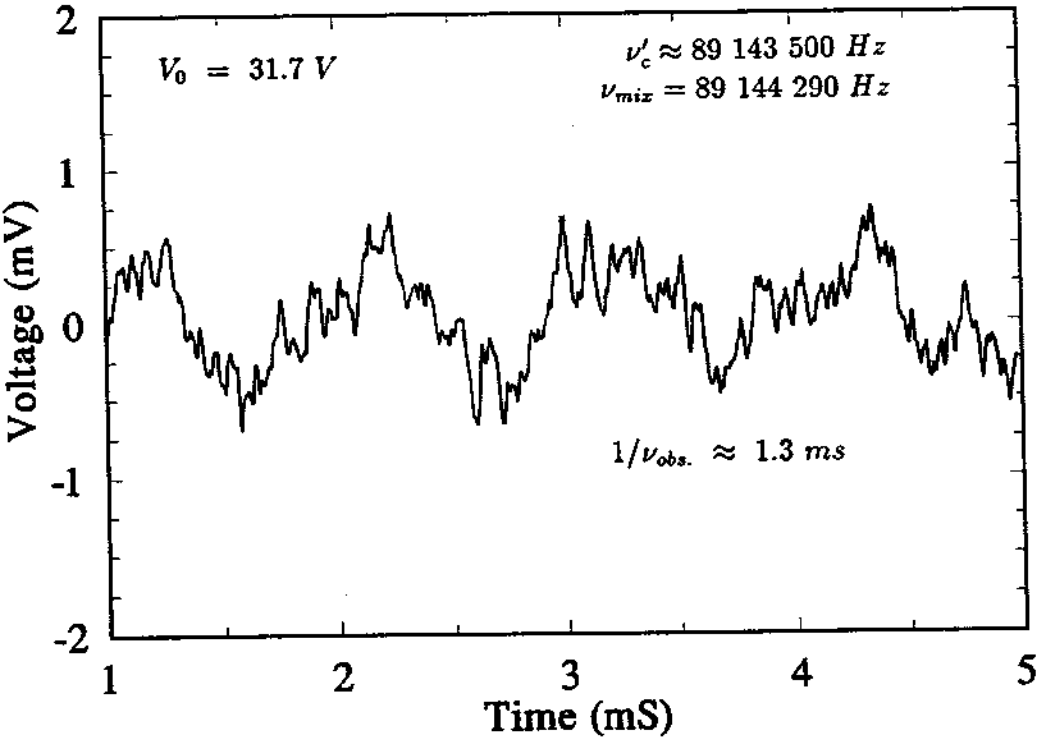

Figure 9.5: Oscillations in the directly detected ν_c' signal after strong pulsing.

Chapter 10

Systematic Effects

In this chapter, we study and quantify the various mechanisms that can contribute to systematic effects and shifts in our measurements. We classify the possible influences in accurate frequency measurements into three categories. The first category concerns imperfections in the magnetic and electric field. A second derives from imprecision in our knowledge of where the confined particles reside. A third is the degree our detection affects the unperturbed oscillations.

10.1 Deviations From a Stable, Uniform Magnetic Field

10.1.1 Homogeneity

NMR without Trap Apparatus

A pulsed NMR system is used to shim the superconducting solenoid so that a NMR linewidth is 1×10^{-8} over a 1 cm diameter spherical volume of acetone. The field is perturbed by the trap apparatus, and in particular by the trap electrodes.

With the trap in place, the proton cyclotron frequency is measured and can be compared to the proton NMR measurement if it is made in the same magnetic field by

$$\frac{\nu_c}{\nu_{NMR}} \approx \frac{1}{\gamma_p'}\left(\frac{e}{m_p c}\right) = 0.3583112 \tag{10.1}$$

where γ_p' is the gyromagnetic ratio for protons in water. The proton cyclotron measurements usually agree with the NMR measurements to within 1 part in 10^5,

depending on the actual trap apparatus and the time between the measurements. In addition to possible chemical and temperature dependent shifts in the NMR measurement, shifts at the 10^{-5} level also result from paramagnetism of the nearby trap components. (For example, using the calculated coeficient $\beta_0 \approx$-0.5 G from the MACOR spacers in the trap, paramagnetism is responsible for a shift of $\approx$ -8×10^{-6}).

Axial Displacement of the Confined Particles

The trap apparatus resides in vacuum and is cooled to 4.2 K. The volume of the confined particles is so small that to measure the field homogeneity we displace the particles up and down along the z axis and measure their cyclotron resonance to obtain information about possible magnetic field gradients.

The center of the axial oscillation is shifted by application of a small anti-symmetric dc potential $\pm V_A$ to the trap endcaps [31]. The resulting equilibrium position of the confined particle(s) is shifted from z=0 to the new position [43]

$$z_{equil.} = -\frac{d^2}{2z_0}\frac{c_1}{C_2}\frac{V_A}{V_0} = -0.2742\,\frac{V_A}{2V_0}\;cm. \tag{10.2}$$

The resonant axial frequency will also shift an amount proportional to the product c_1c_3 (where c_1 and c_3 are defined in chapter 3) given by

$$\frac{\Delta\omega_z}{\omega_z} = -\frac{3}{4}\left(\frac{d}{z_0}\right)^4\frac{c_1c_3}{C_2C_2}\left(\frac{V_A}{V_0}\right)^2 = -0.1081\left(\frac{V_A}{V_0}\right)^2. \tag{10.3}$$

Figure 10.1 shows the measured free space cyclotron frequency when antiprotons are displaced up and down by 0.5 mm in the trap. The measurement is taken by simultaneously measuring the modified cyclotron and axial frequency to determine $\nu_c(z,\rho)$ as described in Chapter 9. For comparison, we superimpose in Fig. 10.1 a linear gradient of 16 mG/cm (2.7×10^{-8}/mm) and the maximum magnetic bottle gradient based on the calculation in Chapter 3 of 1 G/cm^2 (1.7×10^{-7}/mm). The measured points demonstrate that even if the diameter of the cloud were as large as 1 mm, the gradients are not a limitation on the experiment at the level reported here. Gradient studies can also be performed by applying linear

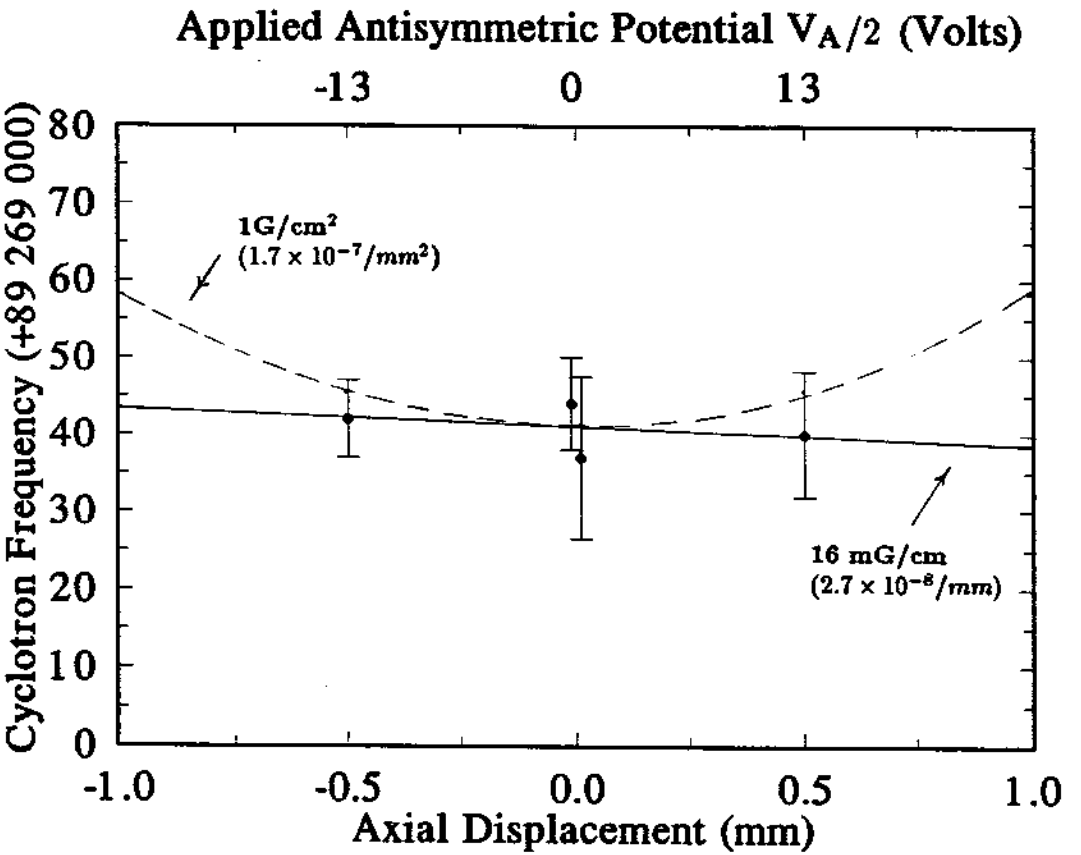

Figure 10.1: Antiproton cyclotron frequency as a function of axial location in the trap.

and quadratic gradients with the room temperature shims of the Nalorac magnet, though the maximum applied gradients of ± 1.5 G/cm and ± 0.2 G/cm^2 are too small to significantly affect our typical signals.

10.1.2 Field Drift Over Time

Average Long Term Decay

The magnetic field resulting from the persistent superconducting solenoid decreases over time. After initial energization, the solenoid is under severe stress so that over time the wires physically move small amounts until a mechanical equilibrium is reached. We attempt to reduce this time by operating the solenoid for a few minutes at a higher field than desired during energization. This has the effect of temporarily putting additional stress into the coil to speed its movement to a mechanical equilibrium. We then lower the field to the final value.

For our magnet (NCC 6.0/100/123), the decay rate $(\Delta B/\Delta t)/B$ converges to between 3 and 8 $\times 10^{-10}$ per hour after about 1 month. The field drift is shown in Fig. 10.2 using antiproton, proton, and electron cyclotron measurements over a period of three months starting with magnet energization and shimming. If mass comparisons are done over a time interval longer than the time drift of comparable precision, the drift of the magnet must be taken into account.

Internal Short Term Variations

Small variations in the drift rate occur between 3 and 8 $\times$ 10^{-10} /hour which are not directly explained by changes in the ambient field. Even though the cyclotron measurements are taken with nearly identical ambient field conditions, the measurements often reveal a short term oscillation on a time scale of 24 to 48 hours. Such fluctuations may be due to variations of the magnetic field produced by the solenoid.

Part of an explanation to the 'internal' magnetic variations may be related to an apparent correlation of the drift rate to a change of the mechanical stress on the magnet. For example, changing the on/off state of the large nearby bending

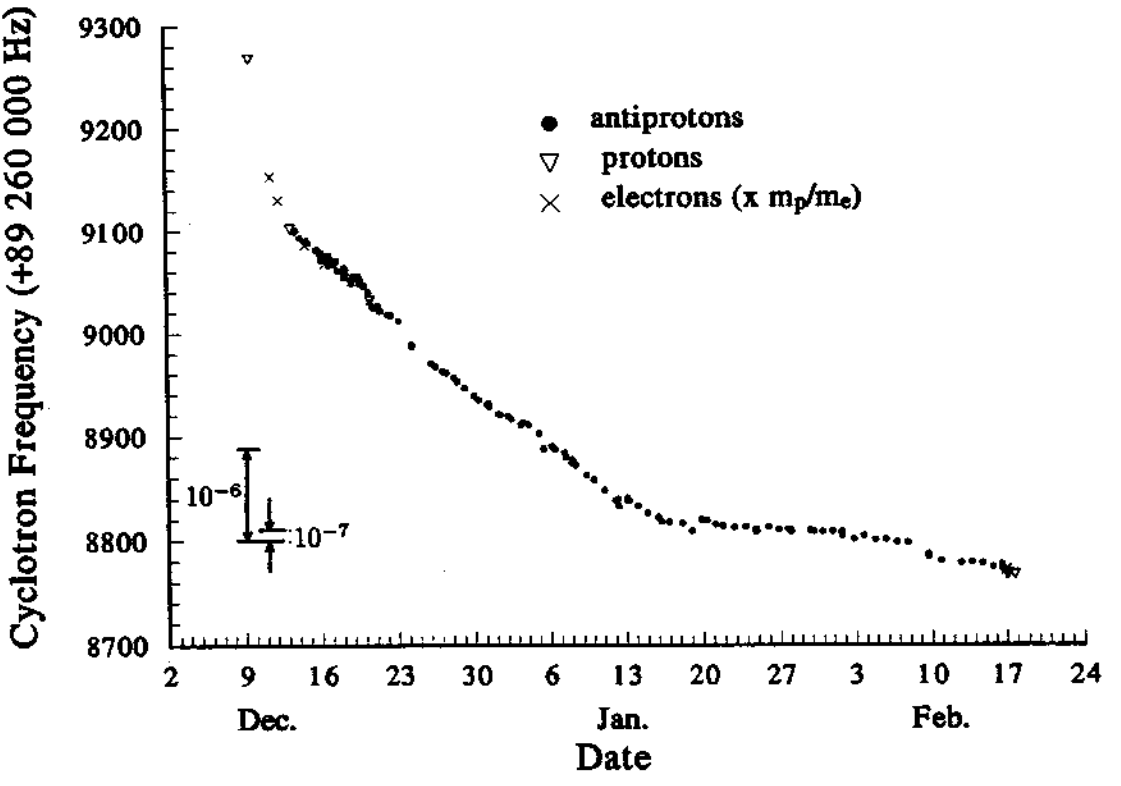

Figure 10.2: Decay of the magnetic field over several months since magnet energization on December 8^{th}.

magnet changes the stress on the solenoid so that it apparently creeps to a new mechanical equilibrium. Such a rate change can be seen in Figs. 11.1(a) and 11.2(a) which was correlated with our systematic studies of the S5 bending magnet on December 20.

We can subtract the long term drift from the measured values, but this is not totally satisfactory for short term variations. The error due to the residual local drift can be included in the uncertainty associated with the scatter of the points (chapter 11). For the highest precision measurements, the local drift must be mapped thoroughly and the time interval between comparisons should be kept to a minimum.

10.1.3 Fluctuations in the Ambient Field

Since a mass comparison between two species can take more than an hour, it is important to control short term field fluctuations that result from changes in the ambient field. In Chapter 3, we discussed the addition of a single superconducting self-shielding coil to our magnet [42] . With the scheme incorporated in our magnet, the most effective shielding is for a fluctuation in the ambient field that is uniform in the $\hat{z}$ direction. For a uniform perturbation the shielding factor increased from S=–4.27(7) (the magnet solenoid alone) to S=–156(6) with the persistent self shielding coil [46]. The shielding is less effective for magnetic gradients, and as a result, each magnetic source in the experimental hall is shielded differently.

In Table 10.1, we summarize the maximum field fluctuations observed outside and inside the shielded magnet system located in an experimental hall at CERN. The outside field fluctuations are measured using a Schonstedt DM2220 Magnetometer rigidly mounted approximately 1.5 meters from the high field solenoid. In Fig. 10.3 the major field fluctuations are shown as a function of time and several sources are identified.

The fluctuations at the trap location in the magnet bore ΔB_{int} are measured at room temperature with a magnetometer (Fig. 10.4), or in most cases with cyclotron resonance measurements of electrons and antiprotons (Fig. 10.5). We

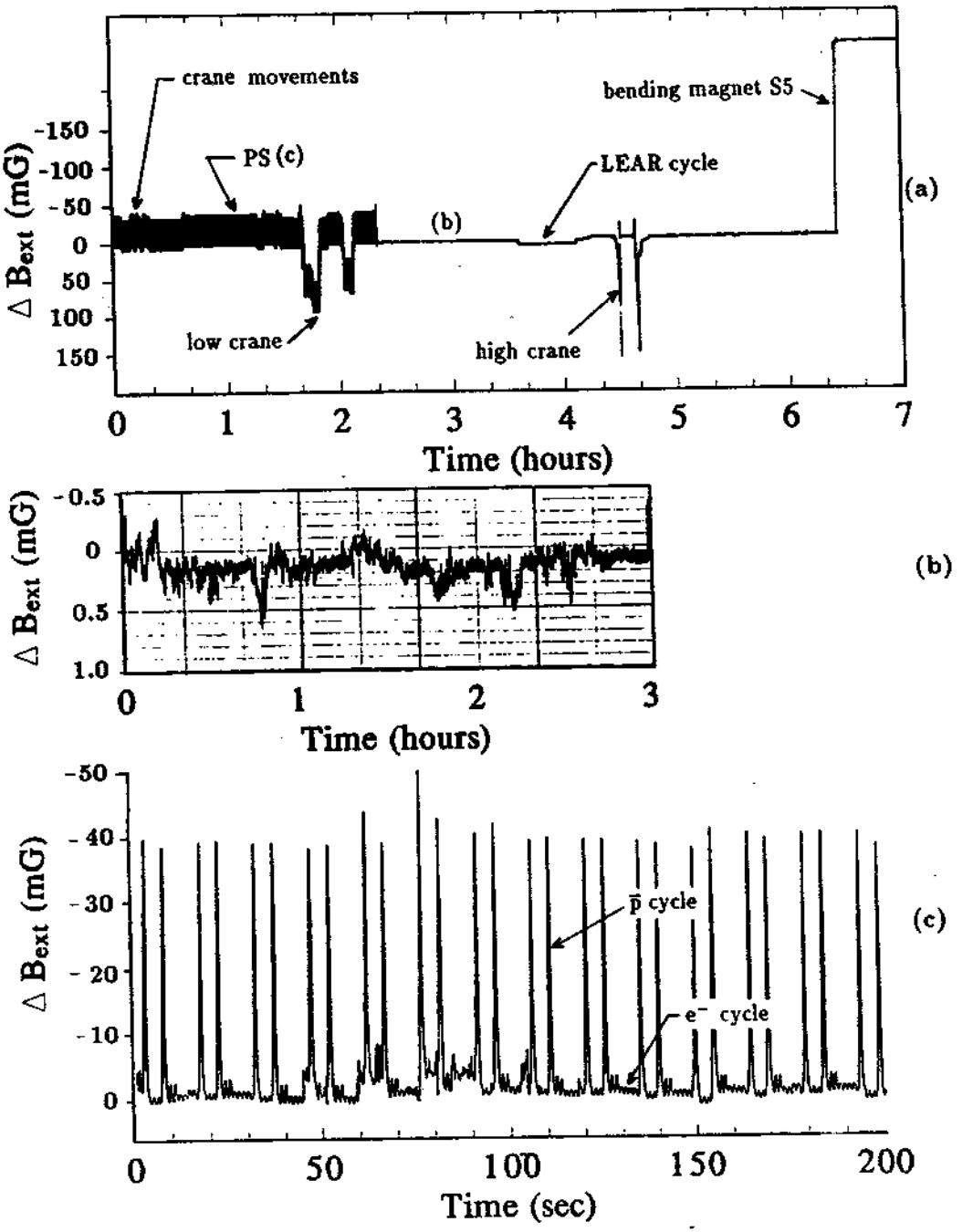

Figure 10.3: (a) Several of the major field fluctuations identified in the experimental hall 1.5 m from the trap. (b)Amplified measurment of fluctuations during a quiet period with the accelerator magnets off. (c) Expanded view of the PS cycle.

Table 10.1: Summary of the external magnetic perturbations. All values are with respect to magnet 'off' values. The magnet 'on' state refers to a polarity for antiprotons.

Source	ΔB_{ext} [mG]	ΔB_{int} [mG]	$S = \frac{B_{ext}}{B_{int}}$	$\frac{\Delta M}{M}$
S5 Mag.(on)	+230	8.3	≥ 27	1.4×10^{-7}
S4 Mag.(on)	+173	2.8	≥ 60	4.8×10^{-8}
High Crane(above)	+146	≤ 3	≥ 50	5×10^{-8}
Low Crane(beside)	+88	≤ 1.2	≥ 75	2×10^{-8}
PS (P cycle)	-37	0.33*	110	6×10^{-9}
PS (e^- cycle)	-3	–	110	5×10^{-9}
LEAR (cooling)	+19	0.4*	50	7×10^{-9}
ΔB_{earth}(max.)	≤ 5	–	≈ 156	5×10^{-10}

* Measured with magnetometer with magnetic field off but solenoid and shield superconducting.

also quantify the approximate shielding effectiveness for each source and tabulate the fractional systematic shift that each source contributes to a cyclotron (mass) measurement. When the internal field is measured with a magnetometer, the finite size of the probe may limit the observed shielding factor. Also for the cases of bending magnets S4 and S5, the solenoid is closer to the source than the magnetometer to measure the external field. Therefore the shielding we report is the minimum factor observed and it may actually be larger in some cases.

A few comments about the largest field shifts follow.

- S-5 Bending Magnets for 5.9 MeV Antiprotons

  Two 45 degree bending magnets, with a quadrupole between, are a part of our beam line. The upper segment ends less than 1 meter from the center of our high precision trapping field. Even though the magnet being on or off is the largest magnetic perturbation in the hall, the shielding limits this shift to only $\Delta\nu_c'/\nu_c' = 1.4 \times 10^{-7}$ at the magnet center. The on/off state of these magnets is under our direct control since it is only in our beamline. Therefore we can make sure that the field remains constant during the measurement.

- S-4 Bending Magnets

$$S_{PS} = \frac{\Delta B_{ext}}{\Delta B_{int}} \approx -110 \qquad S_{LEAR} = \frac{\Delta B_{ext}}{\Delta B_{int}} \approx -50$$

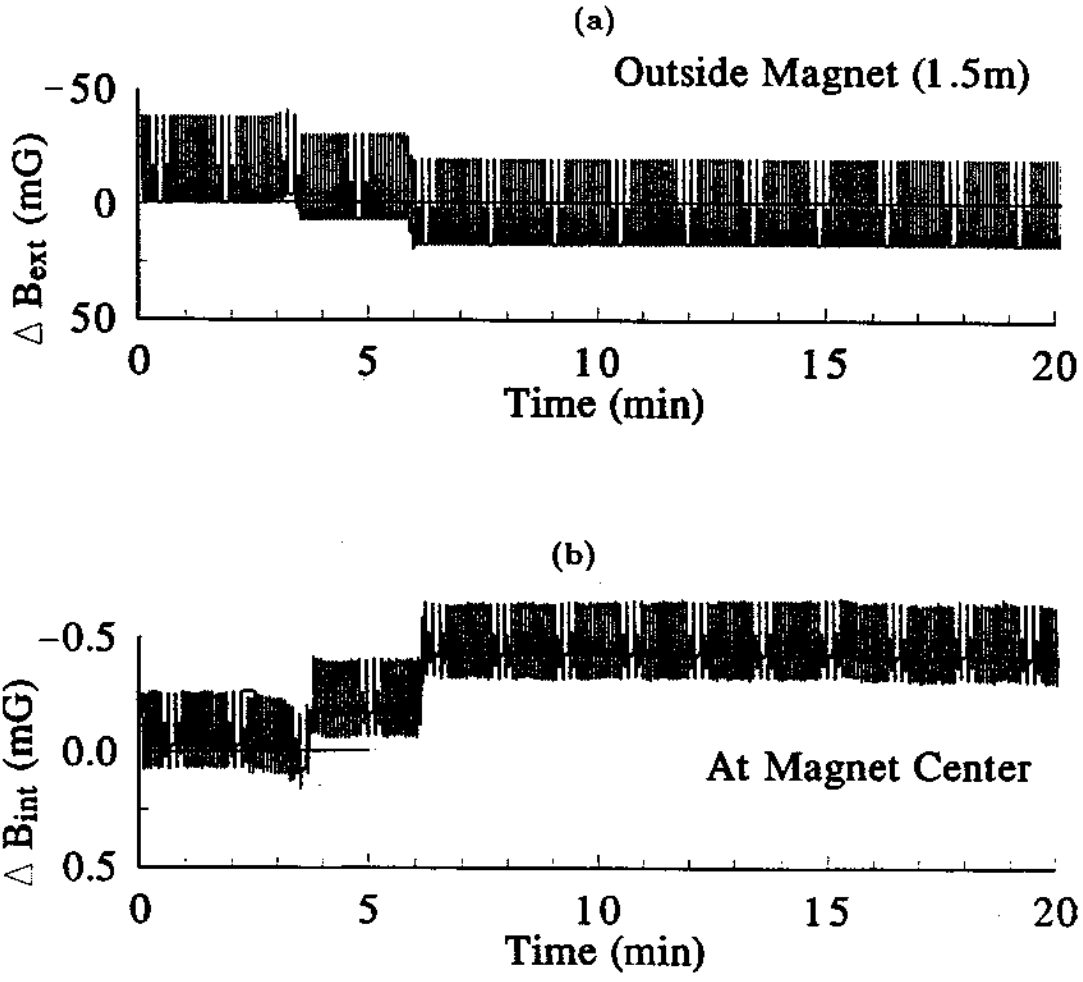

Figure 10.4: Magnetic Fluctuations from the CERN Proton Synchrotron superimposed on a LEAR deceleration cycle. (a) Measured with a magnetometer outside of the magnet and (b) measured with an identical magnetometer inside the self shielding solenoid.

$$S_{S4} = \frac{\Delta B_{ext}}{\Delta B_{int}} \geq -60$$

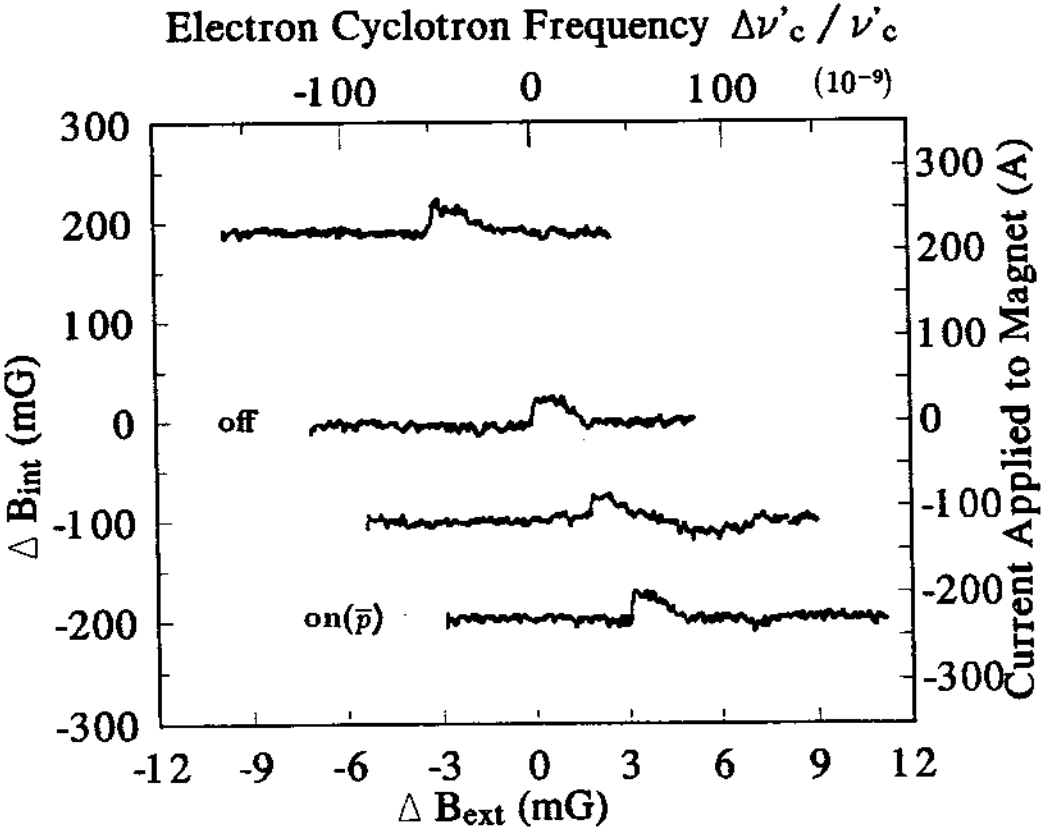

Figure 10.5: The magnetic field shift due to bending magnet S4-BHN01 at the trap center as measured by a shift in the electron cyclotron resonance.

A beamline adjacent to our experiment has an identical 45° bending magnet as in our beamline except that it is horizontal and is slightly further away. This beamline was installed after the data presented in chapter 10 was taken. The absolute shift from the off/on state of this magnet is $\Delta\nu_c/\nu_c = +4.8\times10^{-8}$ (Fig. 10.5). The rest of the beamlines in the experimental hall consist of much smaller bending magnets and quadrupoles and are not visible at the 10^{-9} level.

- Steel Overhead Cranes

  Two very large steel cranes can move as close as 1.5 meters from the magnet. Both cranes are normally stored far away from the experiment. A high crane can move over the top of the experimental region (see Fig. 3.10) and a lower crane can move up beside it. The largest systematic shift due to the cranes are $\Delta\nu_c'/\nu_c' \leq 3x10^{-8}$ in the shielded solenoid.

  Mass comparisons are not done when the cranes are moving, or near the experiment. Typically the cranes only operate extensively during accelerator shutdowns when no antiprotons are available. When antiprotons are available, the cranes are seldomly used, and if so are usually limited to Weekdays, 8:00 am to 5:00 pm.

- CERN Proton Synchrotron (PS)

  The magnets of this accelerator-decelerator ring are typically ramped every 2.4 seconds (see Figs. 10.4 and 10.3) when high energy protons are accelerated for the the Antiproton Accumulator (AA), the East Hall, or the Super Proton Synchrotron (SPS). The fluctuation is fast and is partially screened by eddy currents in the solenoid spool [42]. In a worse case scenario, if the fluctuation were a dc field shift, $\Delta\nu_c'/\nu_c'$ would be a shift less than $5x10^{-9}$ or about 0.5 Hz. We note that the magnitude of the frequency shift is about the same as the modulation frequency of 2.4 seconds. Since the modulation index is high, it may be possible that the observed cyclotron resonance line is broadened by the existence of FM sidebands.

  The PS cycle to fill the Large Electron Positron collider (LEP) uses much

smaller magnetic fields as seen in Fig. 10.3(c). For measurements at the 10^{-9} level, possible perturbations from the PS can be avoided by field monitoring and measurement timing.

- CERN Low Energy Antiproton Ring (LEAR)
  The LEAR decelerator ring is about 10 meters from our magnet and is observable during the antiproton load and deceleration cycle in LEAR (see Figs. 10.4 and 10.3(a)). This cycle occurs for about 15 minutes once every 3 hours. Since the maximum field perturbation in the shielded magnet is about $\Delta\nu_c' / \nu_c' = 6\text{x}10^{-9}$, this cycle will have to be avoided during measurements at the highest precisions.

By monitoring the magnet time drift and the major external perturbations (mainly the on/off state of the antiproton beamline bending magnets) the magnetic field systematics are not relevant for comparisons at the 4×10^{-8} level. The gradients are sufficiently small that the accuracy of our measurements are not compromised, even if the cloud has the very large spatial extent of 1 mm^3. For a spherical shaped cloud the effect of the calculated bottle would be at most 2×10^{-8}. The cloud dimensions for reasonable energies are typically much smaller. A broadening due to possible linear gradients is less than 10^{-8}/mm. Small magnetic gradients result from our use of a large trap and also because the magnet bore can be operated at room temperature making it possible to shim away external gradients to high precision over a large volume (0.5 cm^3) using an NMR probe. This later feature is especially meaningful in our application since very large magnetic perturbations close to our solenoid must be compensated (for example, reinforced concrete shielding and bending magnets).

By avoiding the major external field fluctuations, summarized in Table 10.1 , they are not relevant at our present level of accuracy. As the mass comparison progresses to higher precision, the external fluctuations become more critical, but should be manageable with proper measurement timing or active external correction. The short term time variation of the field is best monitored with cyclotron measurements made as close together in time as possible. For the purpose of our

comparisons, these variations are small and are incorporated into the analysis in Chapter 11 as an uncertainty associated with scatter.

10.2 Deviations From the Pure Quadrupole Electric Field

Magnetic perturbations described in the previous section affect ν_c' to first order but have little effect on ν_z . Electric field perturbations affect all three eigenfrequencies. In an ideal trap, a change in any of the eigenfrequencies will be accompanied by corresponding changes in the other two so that ν_c is invariant to such changes. In this section, we put limits on perturbations from the ideal quadrupole potential that can have an effect on the accuracy of our measurements of the free space cyclotron frequency.

10.2.1 Trap Geometry and Alignment

Orthogonalized Cylindrical Traps

The open endcap trap, described in chapter 3, was designed and constructed so as to produce a sufficiently high quality quadrupole potential at the trap center. High precision measurements are possible only because particles in thermal equilibrium with 4 K typically have small orbits. Away from the center of the trap, the approximation that the cylindrical trap forms a pure quadrupole potential begins to break down. As a result, particle energies should be as low as possible during resonance detection.

Trap Distortions and Misalignments

The invariance theorem given by (2.19) serves as a prescription to determine the free space cyclotron frequency in terms of the real measured eigenfrequencies $\overline{\nu}_c'$, $\overline{\nu}_z$, $\overline{\nu}_m$ of a single particle in a non-perfect trap.

This expression can be expanded in terms of a distortion parameter ϵ and

misalignment angle θ [13], giving

$$\frac{\omega_c}{\overline{\omega}'_c} = 1 + \frac{1}{2}\left(\frac{\overline{\omega}_z}{\overline{\omega}'_c}\right)^2 + \frac{9}{16}\left(\frac{\overline{\omega}_z}{\overline{\omega}'_c}\right)^4 (\theta^2 - \frac{2}{9}\epsilon^2) + ... \qquad (10.4)$$

which we identify as $\nu_c = \overline{\nu}'_c + \overline{\nu}_z{}^2/2\overline{\nu}'_c$ with an additional term as a function of ϵ and θ.

For our rather large 1.2 cm diameter trap $(\overline{\omega}_z/\overline{\omega}'_c)^4 = 2\times10^{-7}$. The trap was machined with tolerances of 5 μm (0.0002"). The maximum angle that the trap could be tilted with respect to the magnetic field is 0.3°. (assuming the apparatus is shorted to the wall of the magnet bore). Since the magnet bore is not directly connected to the solenoid it is possible that the solenoid is not perfectly aligned with the bore. If we assume the conservative values of ϵ=1% or $\theta = 1°$, the last term in Eq. 10.4 is still only $\Delta\nu_c = 3.6\times10^{-11}$. Therefore, the imperfections of the trap electrodes and internal and external misalignments do not contribute a significant systematic and a measurement of ν'_c and ν_z is totally sufficient to infer the free space cyclotron frequency well beyond the 10^{-9} level.

The invariance theorem was derived for the case of a single particle in a Penning trap with imperfections to the trapping potentials resulting from the actual electrodes and their alignment. For more particles, deviations from ideal quadrupole field resulting from the presence of other charges in the trap must be examined.

10.2.2 Field Effects From Electrode Potentials

For a distortion free, perfectly aligned trap containing no particles, the resulting electric field depends upon characteristics of the potential applied to the trap electrodes. This includes the quality of the voltage source, the electrode surface quality, and the absolute potentials applied to the various trap electrodes.

Stability and Accuracy of the DC Potential

Assuming the absolute worse fluctuations in the unfiltered voltage source of $\Delta V_0 = 150\mu$V then $\Delta\nu_z/\nu_z = 10^{-6}$ and $\Delta\nu_c/\nu_c = -\Delta\nu_m/\nu_c = -(\nu_z/\nu_c\nu'_c)\Delta\nu_z \approx 2\times10^{-8}$.

Symmetric Perturbations: Anharmonicity

The shape of the axial potential well is tunable using the set of compensation electrodes. For a trap that is symmetric axially and about the plane z=0, only even order terms are present in the multipole expansion in equation 3.1.

Using the notation from Chapter 3, anharmonicity in this context refers to the presence of higher even order terms in the trap potential with coeficients $C_4, C_6, C_8, ...$, where $C_k = C_k^{(0)} + (V_c/V_0)D_k$. By the nature of a trap formed with cylindrical electrodes, the trap cannot be made harmonic over all interior regions. Thus the effect of anharmonicity strongly depends on the spatial extent motion of the particles.

All mass comparison measurements were performed with the compensation potential set at 88.09% of the potential applied to the ring with the endcaps grounded. This is the theoretical setting which produces $C_4 = 0$ and $C_6 = 0$ at the trap center. Our measurements on electrons, protons, and antiprotons have indicated that $V_{comp} = 0.8809V_0$ is nearly the optimum tuning for well cooled and center particles (e.g. see the electron traces in Fig. 6.4).

We measure the effect of anharmonicity on our measurements of the antiproton cyclotron frequency by deliberately mistuning the trap. Figure 10.6 shows a series of measurements of ν_c as a function of changing the trap compensation potential ratio V_{comp}/V_0. Because the trap is not perfectly orthogonalized, mistunings of V_{comp}/V_0 result in small shifts of the axial frequency accompanied by a shift in the measured ν_c' . For a perfect trap, ν_c is invariant to these shifts since $\nu_c = \nu_c' + \nu_m$ where $\nu_m = {\nu_z}^2/2\nu_c'$. Any shift in ν_c is an indication that the anharmonicity is large enough so that these relationships are no longer valid. Even with the trap mistuned so that $C_4 = 3 \times 10^{-3}$ no correlation with a shift in ν_c is observed with the present resolution. Similarly, with the electron cyclotron measurements with a trap mistuning producing $C_4 = 5.6 \times 10^{-3}$, no correlated shift in ν_c is observed (see Fig. 6.4).

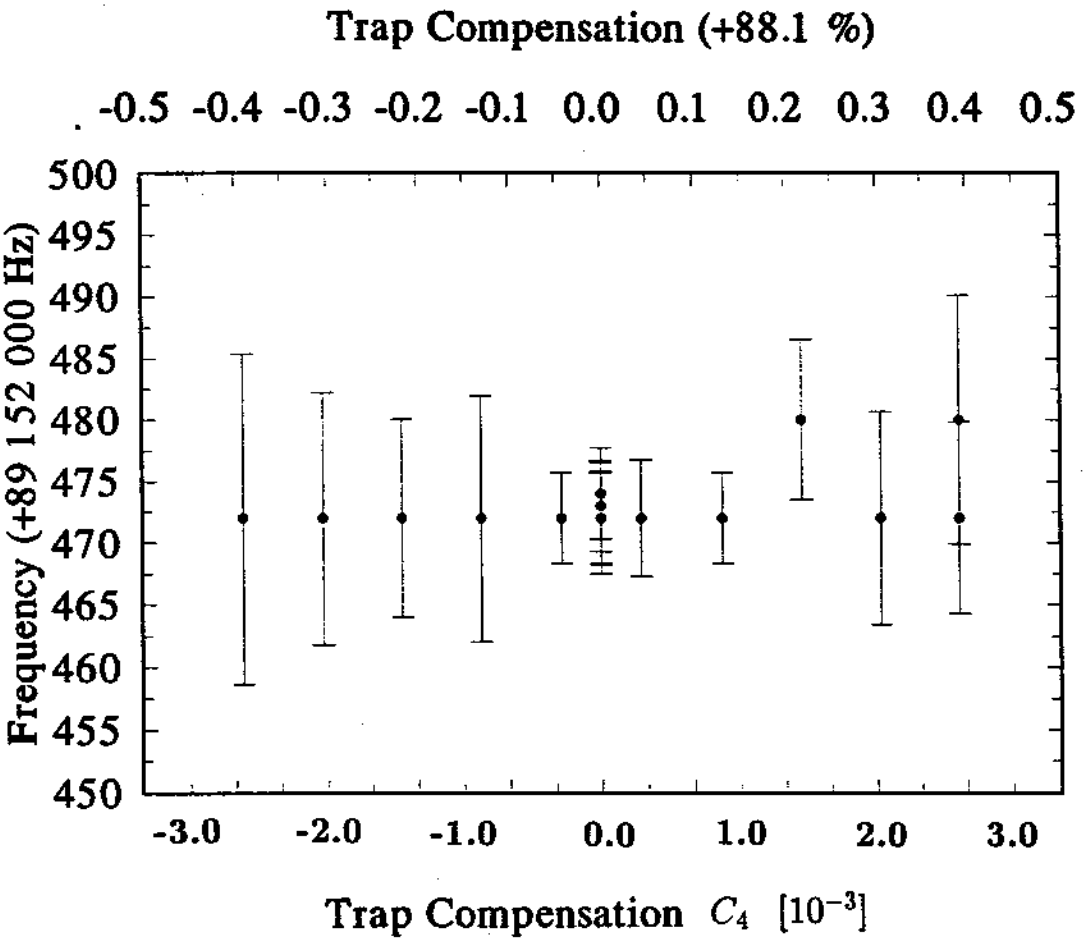

Figure 10.6: Antiproton cyclotron frequency as a function of trap compensation.

Asymmetric Perturbations: Contact Potentials and Patch Effects

Asymmetric potentials can be intentionally introduced as described in Section 11.1.2 to displace the average position of the particles in the trap. Unfortunately, small unintentional shifts can result from asymmetric potentials applied to the trap electrodes by mechanisms such as contact potentials, patch effects, or stray charges that may be present on the surface of the electrodes.

If particles are electrostatically shifted, then opposite polarity particles are displaced in the opposite direction. Such shifts could have major consequences if the electric or magnetic field significantly differs in the two regions since our comparison technique relies on the particles experiencing the same field.

In Fig. 10.7 we show evidence that the actual potential on the trap is not the same as the applied potential from the Fluke 5442A supply. We show measurements of ν_z for both antiprotons and protons with the same applied trapping potential (except opposite in sign) and the identical compensation tuning. The spectrum analyzer scales are identical in both traces. The antiproton axial frequency for the antiproton is higher than for the proton. In Fig. 10.7 we also compare measurements of ν_c' . Here we observe that the antiproton ν_c' is lower than the protons (The measurements were taken over a time where the magnetic field drift is negligible). The free space cyclotron frequency $\nu_c = \nu_c' + \nu_m$ is invariant to the voltage offset suggesting that shifts in ν_z and ν_c' result from different trapping potentials.

We determine the size of this offset potential from

$$\omega_z^2 = C_2 \frac{eV_0}{md^2} \equiv \alpha V_0, \tag{10.5}$$

so that a shift in the axial frequency as a function of only voltage is

$$\frac{\Delta\omega_z}{\omega_z} = \frac{1}{2}\frac{\Delta V_0}{V_0}. \tag{10.6}$$

Let V_{cp} denote the offset potential, then (10.5) becomes for the antiproton and proton respectively

$$(\omega_z^2)_{\bar{p}} = \alpha(|V_0 + V_{cp}|) \tag{10.7}$$

Antiprotons

14:00

$V_0 = +71.6\ V$

$V_c = 0.881\ V_0$

Protons

17:00

$V_0 = -71.6\ V$

$V_c = 0.881\ V_0$

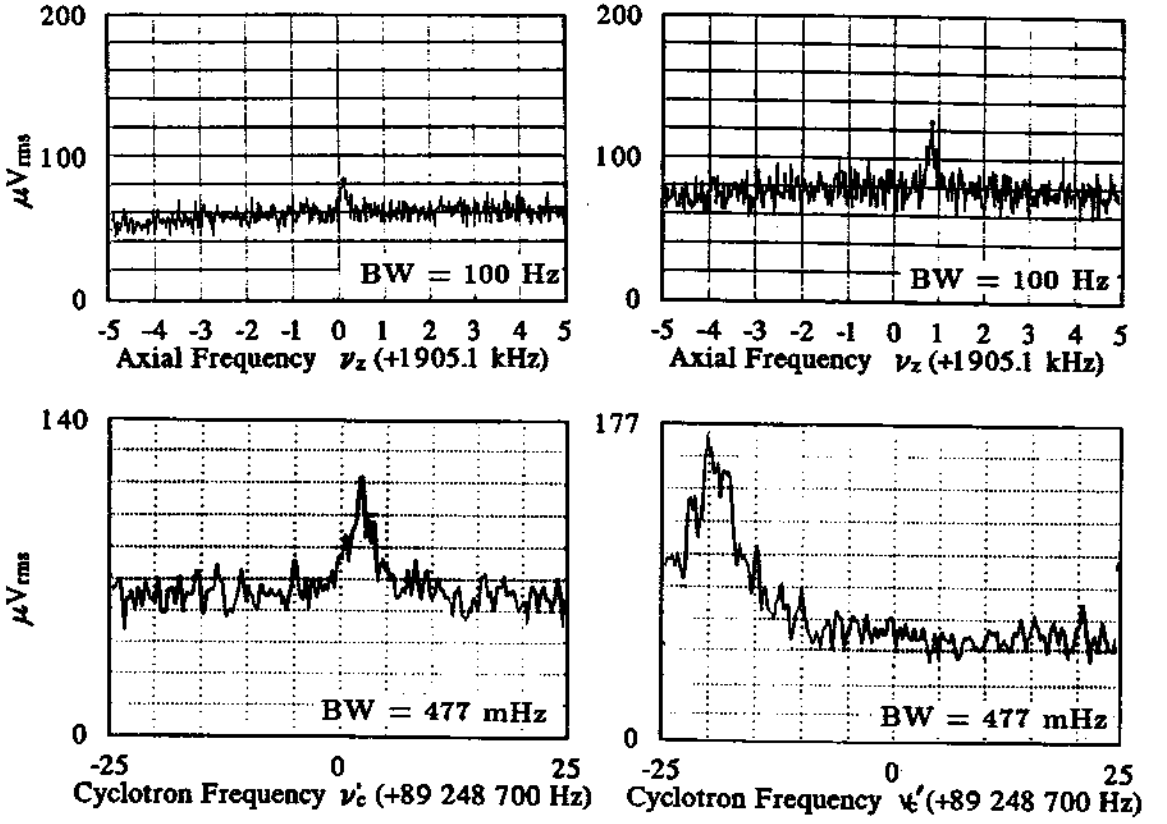

$$\Delta\nu_z = \frac{+}{2}\frac{730}{2}\ \text{Hz}$$

$$\Delta V_0 = 27 \pm 5\ \text{mV}$$

Figure 10.7: Antiproton and Proton axial and cyclotron resonances showing the effect of reversing the trapping potential.

and

$$(\omega_z^2)_p = \alpha(|V_0 - V_{cp}|). \tag{10.8}$$

Solving these two equations using the values observed in Fig. 10.7 for the axial frequencies gives an offset potential of

$$V_{cp} = 27 \pm 5mV. \tag{10.9}$$

This amount of offset could easily be a contact potential, since the dc lines from the Fluke voltage supply to the trap electrodes consist of constantan, copper, and tin-lead. There also exists a temperature gradient of approximately 300 K.

This offset, as observed through the axial frequency of the antiprotons and protons, is reproducible even if the trap apparatus has been warmed up and cooled down again. Therefore, it most likely is not due to stray surface charges which may not be so reproducible. The trap electrodes are plated with a thin layer of gold and a patch effect may be a possibility.

The axial frequency shift is most sensitive to the effect on the harmonic potential. Displacements (dependent upon c_1 or d_1) of the confined particles could result from asymmetric perturbations and the 27 mV offset gives an approximate scale of such possible perturbations. In a worst case scenario we assume that there exists a 100 mV offset between the compensation electrodes. Then using Eq. 10.2 (except now we use d_1 and d_3 since the potential is applied to the compensation electrodes) the maximum particle displacement along the z axis would be $\Delta z \approx 1.5\mu m$. Similar displacements in Δx or Δy could occur by potential offsets across segments of the split compensation or the quad ring electrodes. Our magnetic gradients are sufficiently small that displacements on this scale are insignificant.

Finally, correcting the applied voltage with this offset, we get a measure of the trap coeficient α relating ω_z^2 and V_0 as defined in Eq. 10.5 to be

$$\nu_z(p,\overline{p})_{meas.} = 0.22594\frac{MHz}{\sqrt{Volt}} \tag{10.10}$$

compared to the theoretical value for our trap dimensions [43] of $\nu_z(p,\overline{p})_{calc.} = 0.22477\frac{MHz}{\sqrt{Volt}}$. This is in agreement to 0.5% as would be expected based on the machining tolerances of the trap. This is the same level of agreement obtained

with the actual and calculated values for D_2. The calculation does not include the effect of the splits in the ring and compensation electrodes and also does not take into account the inner surfaces along the gaps between electrodes.

10.2.3 Field Effects from the Presence of Other Particles

For the highest precision mass spectroscopy even a single ion can lead to a perturbations in the measured eigenfrequencies [104]. The measurements reported in this thesis are done with more than one particle and sometimes the clouds contain other particle species. Antiprotons may be accompanied by residual electrons from the cooling process and protons accompanied with other positive ions (most often carbon, oxygen, and nitrogen). The electron measurements are most likely with single species clouds since negative ions are relatively hard to generate and are only weakly bound.

We distinguish between the perturbations caused by the number of a pure species and the perturbations due to the space charge of other ions sometimes present in the trap.

Number Dependence: Image Charge Field

The number dependence reported as a systematic in earlier measurements on the proton to electron mass ratio vary greatly in magnitude and direction [98,53]. At the time, the determined correlation to particle number may have been more related to the uncertainty in cloud volume which can also result from a number dependency. For example, a large number of particles could sample a larger trap volume and possibly sample field regions with different anharmonicity and/or magnetic bottle properties.

A model first proposed by Wineland and Dehmelt [115] is useful towards understanding the source of number dependence shifts. They model the trap electrodes as a parallel plate capacitor, with plate separation d, and interpret the number dependent perturbation as a result of the field produced at the trap center due to the image charge of the confined particles reflected about the conducting surfaces.

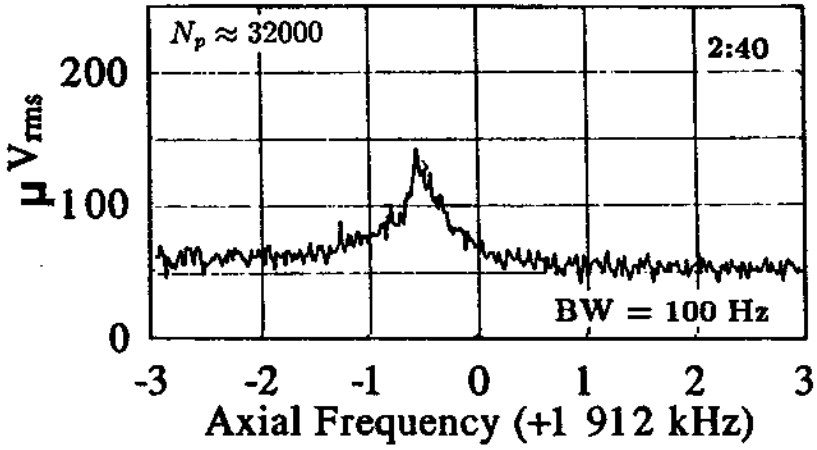

dip to -1.5 V on ring

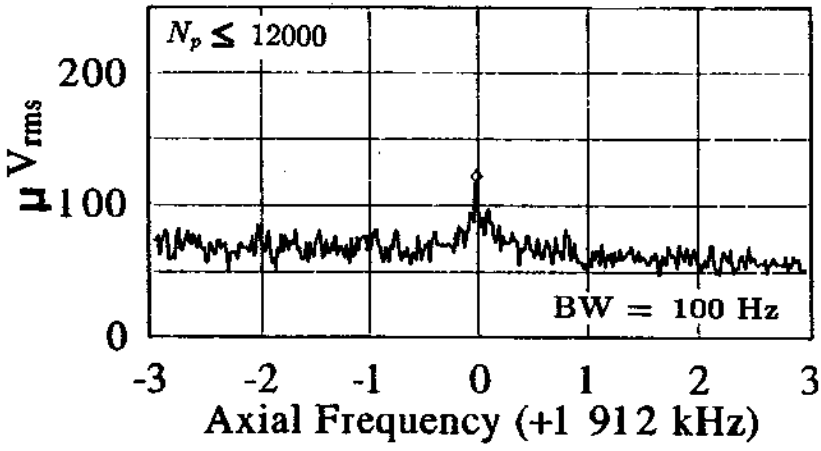

Figure 10.8: Axial shift for protons when reducing particle number in the trap. The axial signal (a) before and (b) after a drive a dip procedure to reduce proton number. The axial frequency increases for reduced particle number.

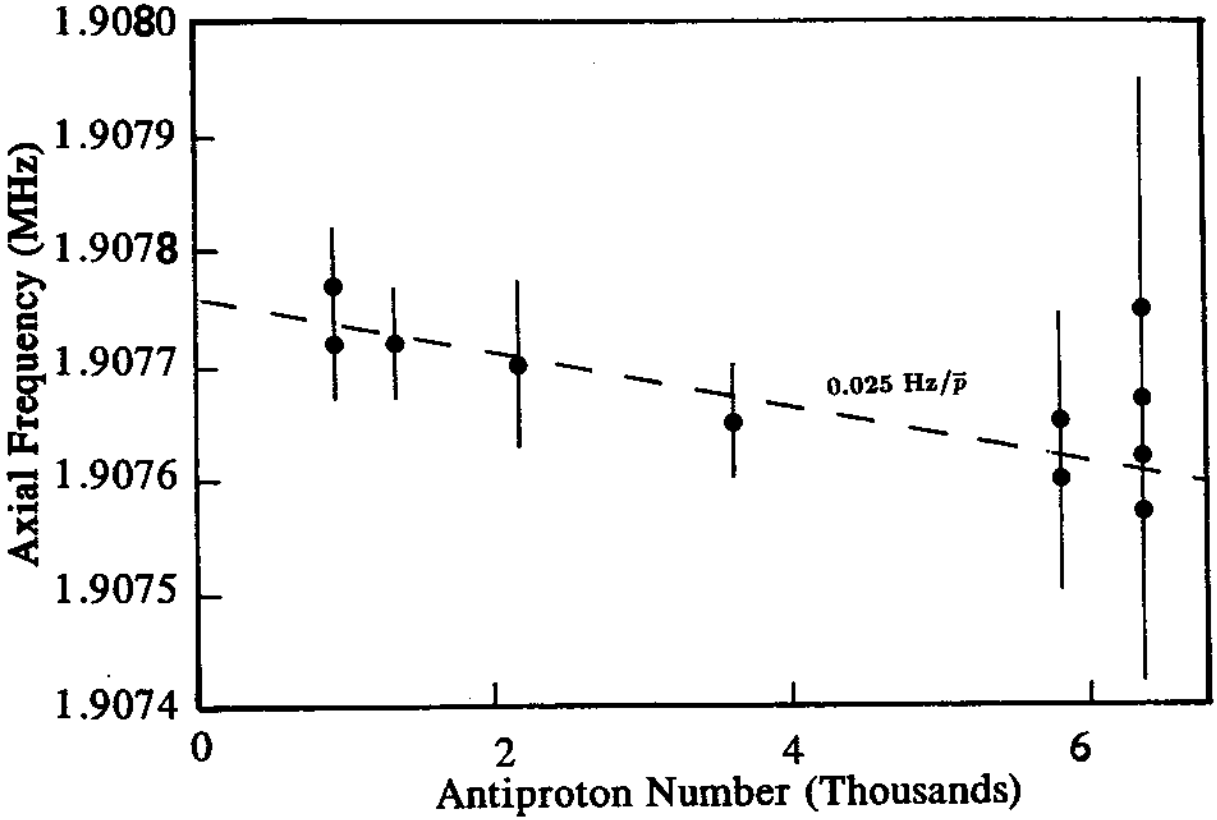

Figure 10.9: Axial shift for antiprotons as a function of the drive and dip procedure to reduce the antiproton number in the trap.

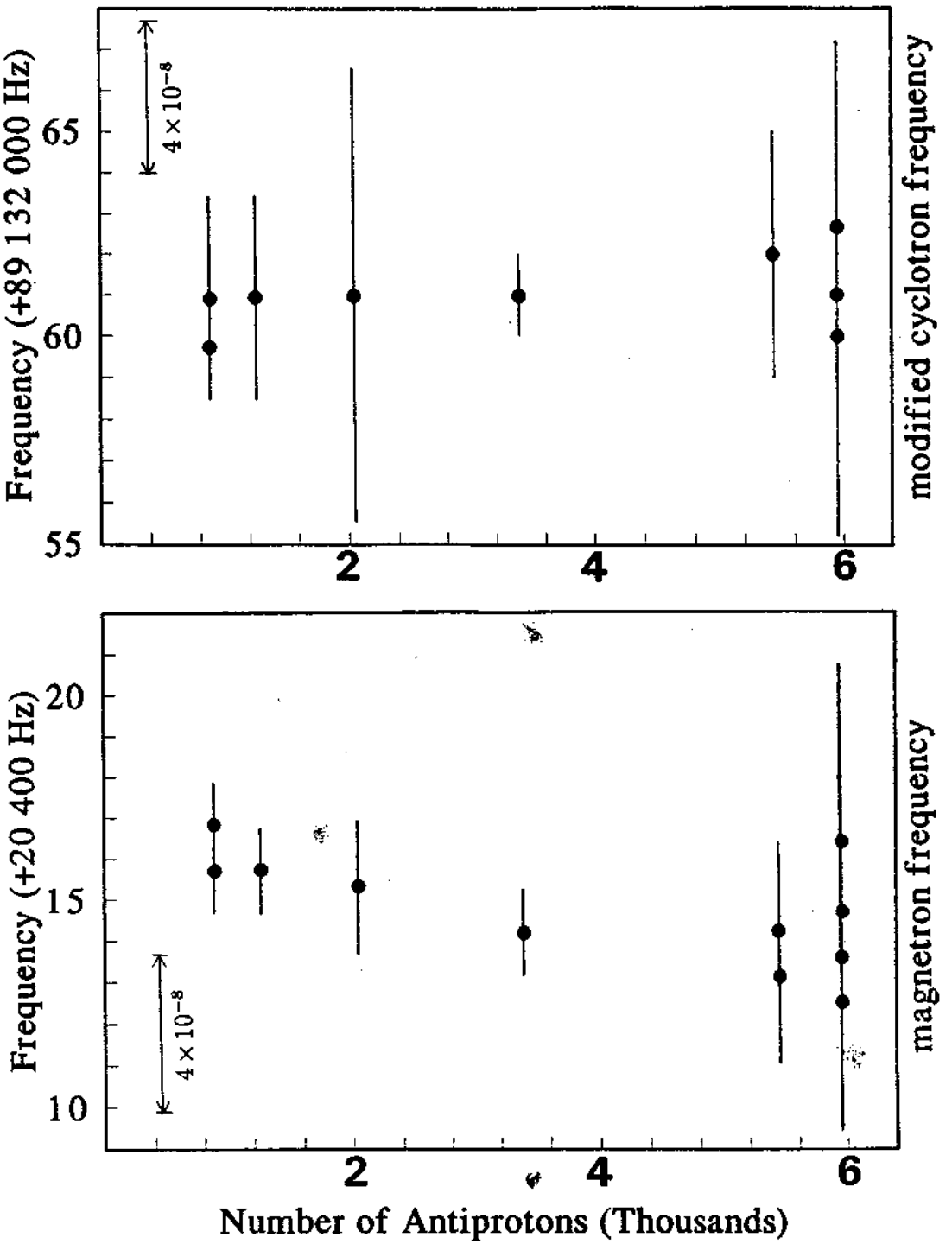

Figure 10.10: (a)The dependence of the magnetron frequency $\nu_z^2/2\nu_c'$ on particle number. (b) The dependence of the modified cyclotron frequency ν_c' on particle number.

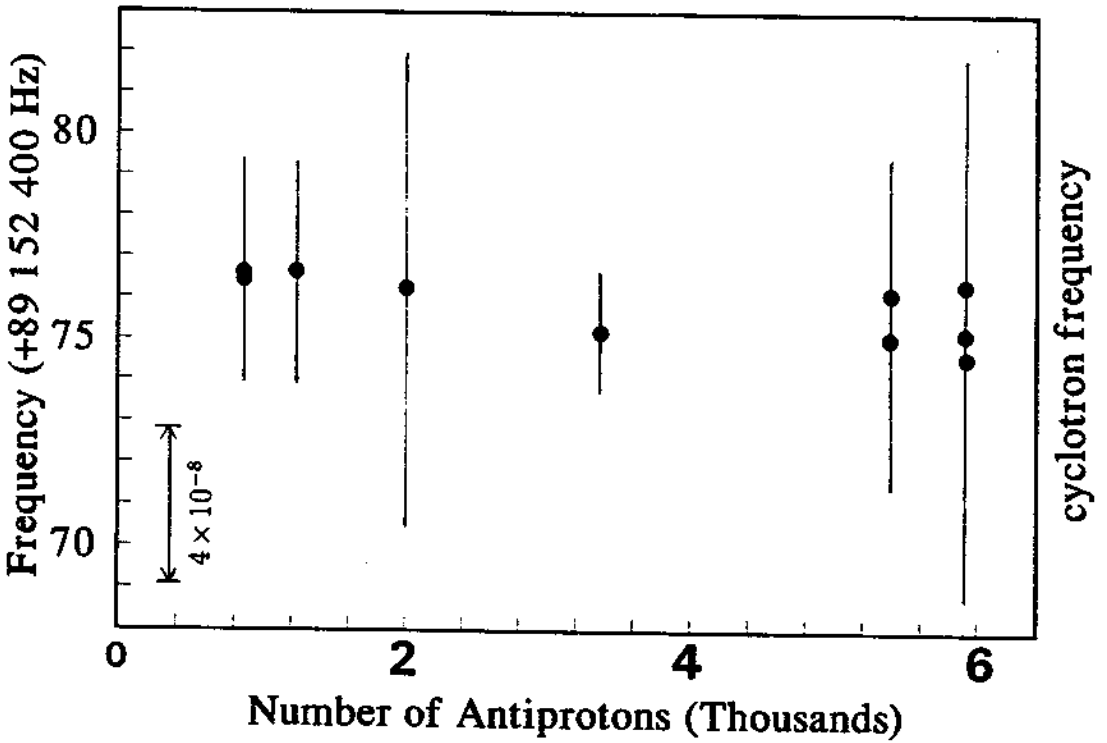

Figure 10.11: Measured antiproton cyclotron frequencies as a function of number of antiprotons in the trap.

With this model they determine the shift in the axial frequency to be

$$\frac{\Delta\omega_z}{\omega_z} = -4\frac{ne}{dV_0}, \tag{10.11}$$

where N is the number of charges e in the trap. This expression can simply be understood as the ratio of the potential produced by the image charge at the trap center ($\propto ne/d$) to the potential applied to the trap V_0.

Using Eq. 10.11 and the characteristic dimension of our trap as an approximate distance scaling, we estimate the axial frequency shift in our trap to be of order

$$\frac{\Delta\omega_z}{\omega_z} \approx -0.03Hz/\bar{p}. \tag{10.12}$$

This agrees favorably with the observed shift using antiprotons as shown in Fig. 10.9. In Figs. 10.8(a) and (b) we show the axial shift (and linewidth) change of protons as a function of number from about 3×10^4 to significantly fewer. The axial signal shifts down in frequency for increased particle number.

The image charge model has been experimentally studied by VanDyck et. al. [104]. The number dependent shifts on the magnetron and modified cyclotron frequencies within a spherical conducting cavity of radius a are quantified. Aside from a geometrical factor, the axial shifts are the same as Eq. 10.11.

The relative shift in the observed magnetron frequency scales as the total trapped mass nm_1, and is independent of charge as [104]

$$\frac{\Delta\nu_c'}{\omega_c'} = \left(\frac{3m_1c^2}{2a^3B_0^2}\right)n. \tag{10.13}$$

VanDyck et. al. measure a number dependence in the measured modified cyclotron frequency of 0.23×10^{-9}/proton. For our trap, which is effectively 3 times smaller, the relative magnetron shift should be reduced by a factor of a^3 to as

$$\frac{\Delta\omega_c'}{\omega_c'} \approx 6 \times 10^{-12}/proton. \tag{10.14}$$

Therefore, a 10^{-8} shift may result from about 1700 antiprotons (See Fig. 10.10). A nearly equal but opposite shift occurs in the modified cyclotron frequency as in the magnetron frequency, thus the free space cyclotron frequency is not particularly sensitive to number dependency. The measured free space cyclotron frequency shift

in the VanDyck trap is $\Delta\nu_c/\nu_c \approx 1.5 \times 10^{-11}$/proton. Scaling this as $1/a^3$, the equivalent shift in our trap is $\approx 4 \times 10^{-13}$/proton. Therefore to have a shift at the reported 4.2×10^{-8} level would require approximately 10^5 protons or antiprotons.

The particle numbers typically range between 200 and 2000 antiprotons for the mass comparison measurements. Because our trap is relatively large, number dependent systematics are not significant at the level reported in this thesis.

Space Charge

In an ideal trap consisting of a perfect quadrupole field and a uniform magnetic field, no space charge shifts are observed when detecting the center of mass motion of a single trapped species, provided the cyclotron motion is excited by a constant electric field [25]. In practice, impurity ions are sometime present and the excitation fields are not uniform so that internal degrees of freedom may be excited resulting in space charge shifts. Such shifts are larger on ions of larger mass [116] and can become important for our antiproton and proton work.

Even though we perform measurements on more than one antiproton (or proton) at a time, we can minimize the effect of contaminant ions in several ways. The size of the perturbation is dependent upon the proportion of contaminant ions to the measured species and to the density of the charge. We attempt to reduce or eliminate contaminant electrons (or ions) from the antiproton (proton) clouds using the techniques described in Chapters 7 and 9. Since we have yet to try to resolve a single ion in this trap and study the small perturbations of even a single perturbing ion, we can not be absolutely certain that all possible contaminant ions are removed for our measurements. We also perform measurements only on relatively small clouds, typically 200 to 2000.

Of the few possible remaining contaminant ions, one way to attempt to see any effect is to perform measurements while varying the density. The technique of directly observing ν_c' as a function of V_0 is such a measurement.(see Section 9.1.2). In Fig. 10.12(a) we show measurements of ν_c' versus applied trapping voltage for both antiprotons (positive applied voltage) and protons (negative applied voltage). The associated linewidths of the measured resonance at ν_c' are very small on this

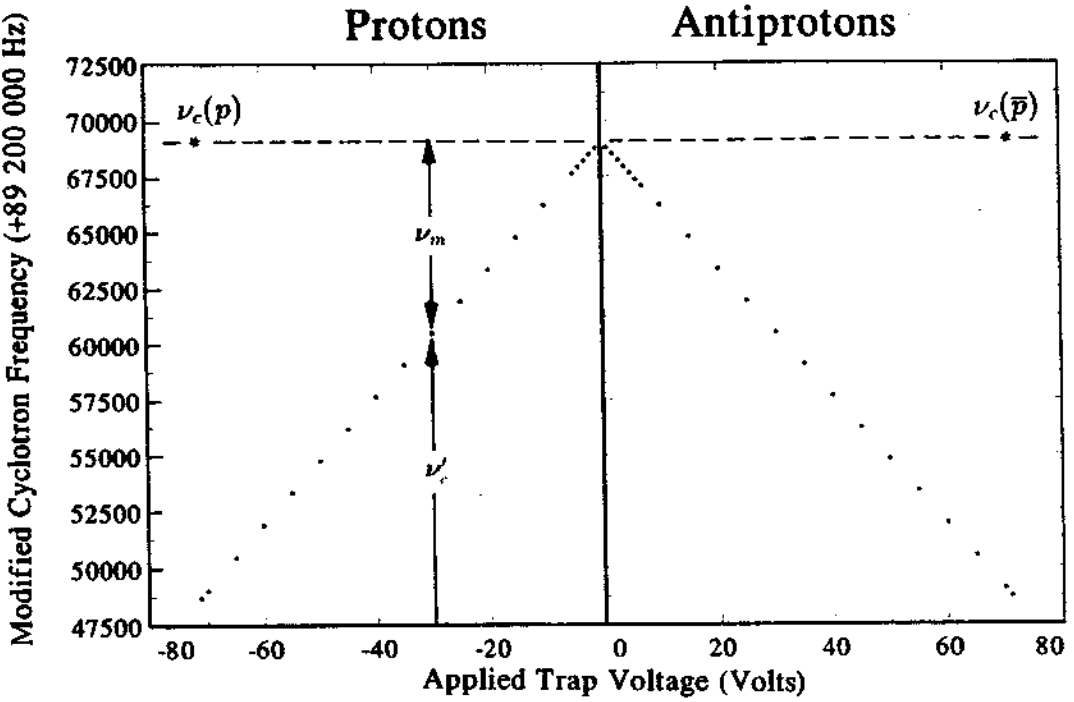

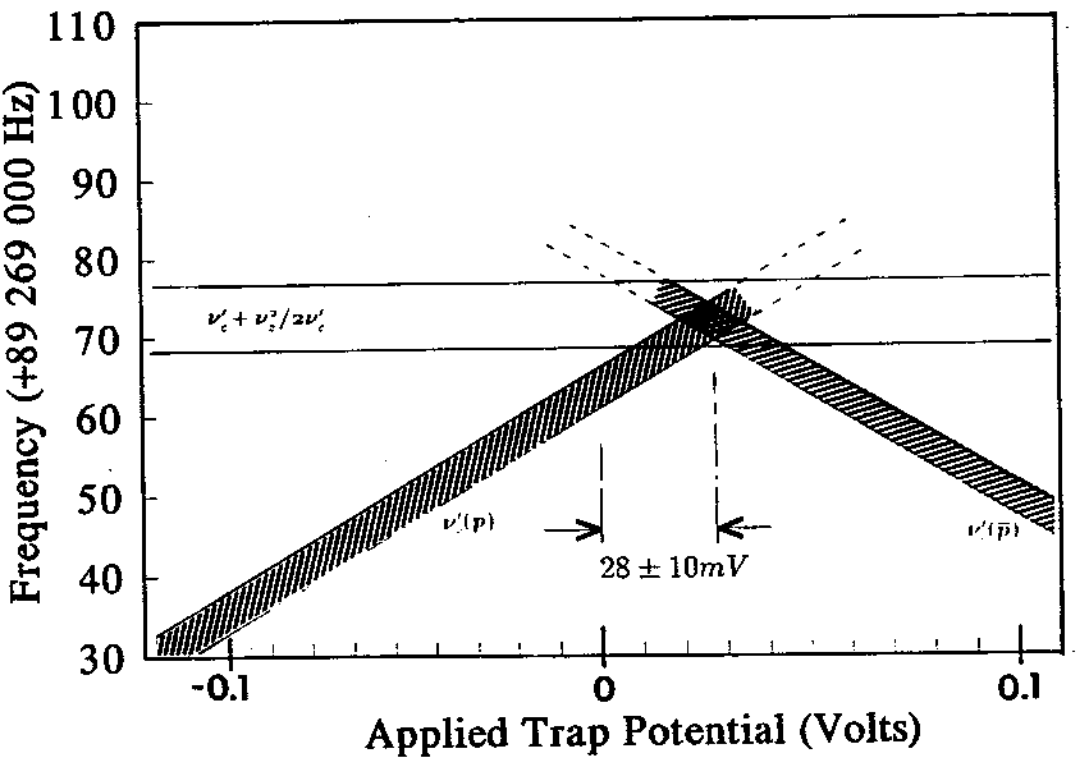

Figure 10.12: (a)Antiproton and proton cyclotron frequency ν_c' as a function of applied trapping voltage. (b) Blown up view of the extrapolated free space cyclotron frequency compared to measurments using the invariance theorem $\nu_c' + \nu_z^2/2\nu_c'$. A potential offset is evident.

scale. To first order, these points should fall on a straight line, and a linear fit gives an intercept at zero trapping potential that in principle is equal to the free space cyclotron frequency ν_c . Such an intercept can be compared with measurements of ν_c based upon making measurements of ν_c' and ν_z at a fixed voltage (about $\pm$ 71 Volts in our case) and using the invariance theorem.

Repeated measurements of ν_c' as a function of voltage and extrapolating to vanishing trapping potential showed that $\nu_c = \nu_c'$ (V_0=0) for the antiproton was slightly higher than a measurement performed at +71 Volts using $\nu_c = \nu_c' + \nu_m$. Similar measurements using protons gave a similar shift but now $\nu_c = \nu_c'$ ($V_0 = 0$) was slightly *lower* than a measurement done at -71 Volts and using $\nu_c = \nu_c' + \nu_m$. For similar space charge distributions, we would expect deviations of ν_c' to be in the *same* direction independent of the sign of the trap polarity.

Figure 10.12(b) shows the intercept region for proton and antiproton measurements taken close in time that the magnetic field has drifted only a negligible amount. The fitted lines do not intersect at the applied $V_0 = 0$ point, but rather at +28 mV. This is the same offset that was observed using the axial signals and shown in Fig. 10.7. We see that this intersection point also lies on the line $\nu_c' + \nu_m$ defined by independent measurements of the proton and antiproton at -71 Volts and +71 Volts respectively (measurements that are voltage independent).

This offset was reproducible over 3 months using 10 different clouds with different particle compositions. The experiment was warmed and recooled during this 3 months, and the magnet was de-energized and re-energized with completely new shim settings. The observed offset voltage pertains to a small change in the ideal quadrupole field. The reproducibility of the potential offset which is consistent with the offset observed axially also gives us confidence in understanding the voltage environment on the trap electrodes even with the polarity reversed.

While the intercepts of the antiproton and proton ν_c' vs. V_0 measurements provide valuable information about the true trapping potential, it is the slope which provides the most direct information on the effects of space charge (or number) dependence. This is because the space charge density can be included in expansion Eq. 9.3 with a term that goes as the trapping voltage [117]. By

examining the variation in the slopes of the proton and antiproton measurements for the ten measurements done, we put a limit on the possible effects of space charge and contaminant ions at 2×10^{-8}. These results are strong indications that possible space charge shifts are negligible in measurements with our typical cloud sizes and compositions.

While the ν_c' verse voltage technique has been presented elsewhere as an attempt to understand systematics [50], this is the first application of such a technique to the observation of a particle-antiparticle pair. It serves as a mass measurement technique, a probe for studying space charge, and a valuable tool in studying opposite polarity measurements which have been troublesome spots in high precision measurements.

Collective Modes

When ions of slightly different mass and the same charge are stored in an ion trap, a collective oscillation may be observed rather that the independent motions necessary to perform high precision mass spectroscopy. Observations have been made in a radio frequency electric quadrupole trap that suggest that precision measurements of the particle frequencies for species with nearly identical charge to mass ratios can be severly perturbed [60].

For the comparisons described in our Penning trap, only particles of similar charge can be simultaneously confined. For a positively biased trap (ring), only electrons and antiprotons are easily confined which have very different masses. For a negatively biased trap, other ions can be confined with the protons, but since only protons have a charge to mass ratio near 1 (mass in amu), collective oscillations are not a concern for small clouds of the particle species we have chosen to compare.

10.3 Particle Energy and Detection

10.3.1 Spatial Extent of Particle Motion

Due to limitations of our detection sensitivity and the fact that the detector is at a nonzero temperature, the particles have finite orbit sizes ρ_c, z, and ρ_m. The size of the excursion from the center of the trap determines the degree to which the particles sample magnetic field gradients and/or higher order non-quadrupole components in the electric field. The energy of the particles necessary to provide sufficient signal is a critical value and if too high, shifts due to special relativity may occur.

Each of the three major perturbations (electrostatic, magnetic bottle, and relativistic) produce shifts in the eigenfrequencies and each shift is linear to the classical excitation energies E_c, E_z, and E_m. The particle amplitudes are related to the particle energy in each eigenmode by

$$E_c = 1755\ \rho_c^2\ \frac{eV}{mm^2} \tag{10.15}$$

$$E_z = 0.84\ z^2\ \frac{eV}{mm^2} \tag{10.16}$$

$$E_m = -9 \times 10^{-5} \rho_m^2\ \frac{eV}{mm^2}. \tag{10.17}$$

In equilibrium, the cyclotron and axial motions are coupled to their respective resonant detection circuits which are kept near 4 K. The particle motions must be driven to higher energies during the measurements in order that these motions can be detected.

Changes in the particle energy produce corresponding shifts in the measurable eigenfrequencies $\omega \rightarrow \omega + \Delta\omega$. The leading shifts have been summarized for a single particle by Brown and Gabrielse [13]. We now consider shifts to the unperturbed eigenfrequencies which are most visible under extreme heating conditions. We emphasize that the drive levels used for the mass comparison are much less than those used to obtain the lineshapes we show here. These observations are instructive towards understanding and probing the environment in the trap.

In Fig. 10.13(a) we show three observations of the directly detected antiproton cyclotron motion after being severely heated with a strong excitation drive at ν_c'.

The line broadens as it is heated but is very asymmetric shifting towards lower frequencies (i.e $\Delta\nu_c'$ is negative for increased energy). For these cyclotron observations we infer that the heat dependent shift shown in figure 10.13 is primarily due to energy in the cyclotron motion E_c. This seems likely since the motion is excited with excitation drives at either ν_c' or $\nu_c' + \nu_m$. The cyclotron energy damps with time constant of 2.8×10^3 seconds as shown in Fig. 10.13(b). Resistive cooling by the cyclotron resonant circuit appears to be the predominant cooling mechanism. If the observed broadening is due to C_4 and B_2 as a result of a large magnetron radius we should not observe the linewidth narrow unless magnetron sideband drives are explicitly used. It is possible that the broadening results from an expansion of the cloud volume due to increased temperature, though even under heated circumstances we cannot observe any effect on the lineshape by changing B_2 with the magnet shim. Changing C_4 a large amount has some effect on the lineshape under certain conditions that seem correlated with large particle number and/or high axial energies. The general large asymmetric feature resulting from the heating normally seems unaffected by changes in C_4 within our tuning range. The assumption that the broadening (shifting) is due predominantly to energy in the cyclotron motion is also strengthened by the observation that under typical conditions (<2000 antiprotons and trap well tuned) no simultaneous heating of the axial motion is observed along with the excessive cyclotron heating (Sec. 12.3, Figs. 10.17 and 10.18).

Shifts or line broadening mechanisms are often difficult to deconvolve. To quantify the source of one perturbation requires that the others are made much less significant. Energy dependent frequency shifts of the center of mass cyclotron frequency based on single particle calculations are given by [13]

$$\left(\frac{\Delta\nu_c'}{\nu_c'}\right)_{anharm.} = \frac{6C_4}{eV_0}\left[\frac{1}{4}\left(\frac{\nu_z}{\nu_c'}\right)^4 E_c - \frac{1}{2}\left(\frac{\nu_z}{\nu_c'}\right)^2 E_z - \left(\frac{\nu_z}{\nu_c'}\right)^2 E_m\right] \quad (10.18)$$

$$\left(\frac{\Delta\nu_c'}{\nu_c'}\right)_{bottle} = \frac{1}{eV_0}\frac{B_2 d^2}{B}\left[-\left(\frac{\nu_z}{\nu_c'}\right)^2 E_c + E_z + 2E_m\right] \quad (10.19)$$

$$\left(\frac{\Delta\nu_c'}{\nu_c'}\right)_{rel.} = -\frac{1}{mc^2}\left[E_c + \frac{1}{2}E_z - \left(\frac{\nu_z}{\nu_c'}\right)^2 E_m\right] \quad (10.20)$$

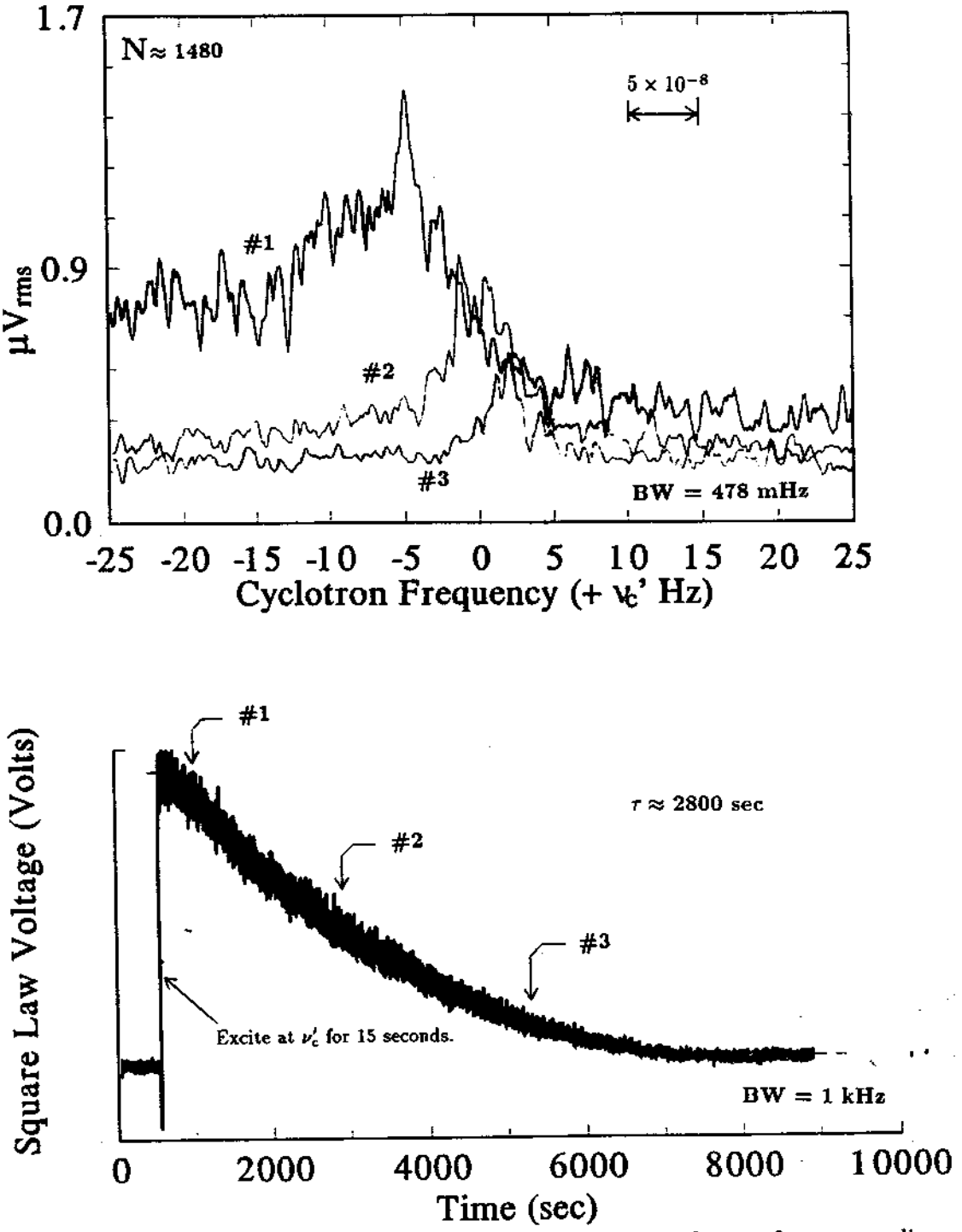

Figure 10.13: (a) Three measurements of the antiproton cyclotron frequency directly observed from a segment of the ring electrode. (b) Damping of the cyclotron center of mass motion as observed with a square law detector centered at $\nu_c(\overline{p})$.

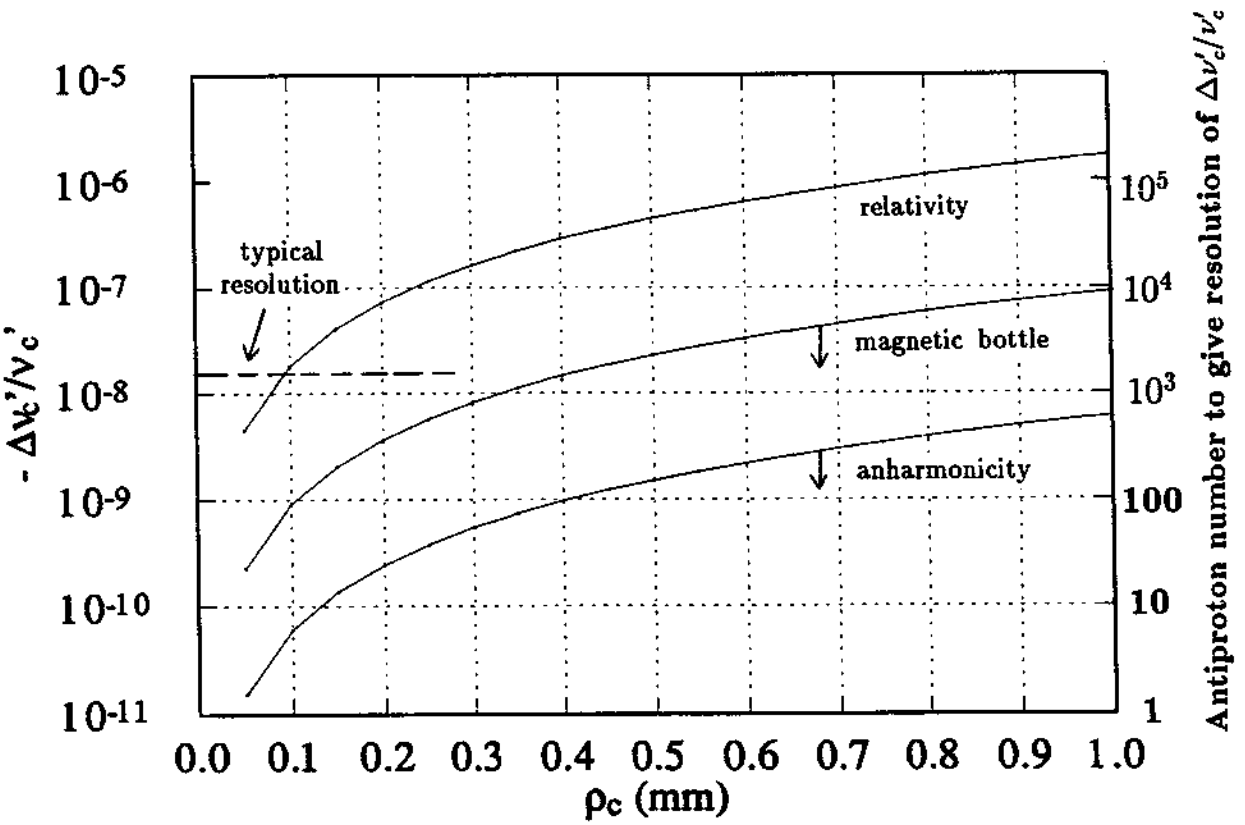

Figure 10.14: The cyclotron frequency shift $\Delta\nu_c'$ of a single antiproton as a function of the cyclotron radius due to special relativity, a magnetic bottle (+1 G/cm^2), or trap anharmonicity ($C_4 \leq -7.8 \times 10^{-4}$). The shift due to C_4 can be in either direction depending upon the compensation of the trapping potentials.

Based on the earlier arguments, let us assume that the shifts (broadening) in Fig. 10.13 are only due to energy in E_c. Then Eqs. 10.19, 10.20, and 10.20 become

$$\left(\frac{\Delta\nu_c'}{\nu_c'}\right)_{anharm.} \leq \pm 6\times 10^{-9}\rho_c^2 \ /mm^2 \tag{10.21}$$

$$\left(\frac{\Delta\nu_c'}{\nu_c'}\right)_{bottle} \leq -7.7\times 10^{-8}\rho_c^2 \ /mm^2 \tag{10.22}$$

$$\left(\frac{\Delta\nu_c'}{\nu_c'}\right)_{rel.} = -1.8\times 10^{-6}\rho_c^2 \ /mm^2, \tag{10.23}$$

$$\tag{10.24}$$

where we have used $C_4 \leq 7.8\times 10^{-4}$ and $B_2 \leq 0.84\ G/cm^2$ in the more general expressions.

In Fig. 10.14 we plot Eqs. 10.22, 10.23, and 10.24 as a function of the cyclotron radius. The most evident feature is that for our trap the bottle and anharmonic components are small enough such that the dominant shift in the cyclotron frequency resulting from energy in the cyclotron motion would be due to relativity. On the right scale of the figure we show the number of antiprotons that would contribute to a similar broadening of the linewidth. For most of our highest resolution measurements (See for example, Fig. 9.1)), the linewidth appears limited by the particle number in the trap.

To estimate the maximum possible energy in the cyclotron motion, let us assume that the observed linewidth corresponds to a relativistic shift of an ensemble of antiprotons. A resolution of 10^{-8} then corresponds to an energy of E_c on the order of 10 eV. If the observed asymmetric broadening of up to $\Delta\nu_c' \approx -400Hz$ is due to relativistic shifts, we would be dealing with a cyclotron motion center of mass energy greater than 1 keV. This seems extremely high, but may be possible since the antiprotons are only weakly damped, and under the right conditions the axial motion is essentially uncoupled from this motion. A counter arguement is that we do not observe loss of particles due to possible collisional transfer of energy into the axial motion which is bound in a well of only around 50 eV.

Heat dependent shifts are also observed in the axial motion as a function of particle temperature. In Fig. 10.15 we show an example of the axial frequency shift as a function of axial energy. The linewidth or shape does not noticeably

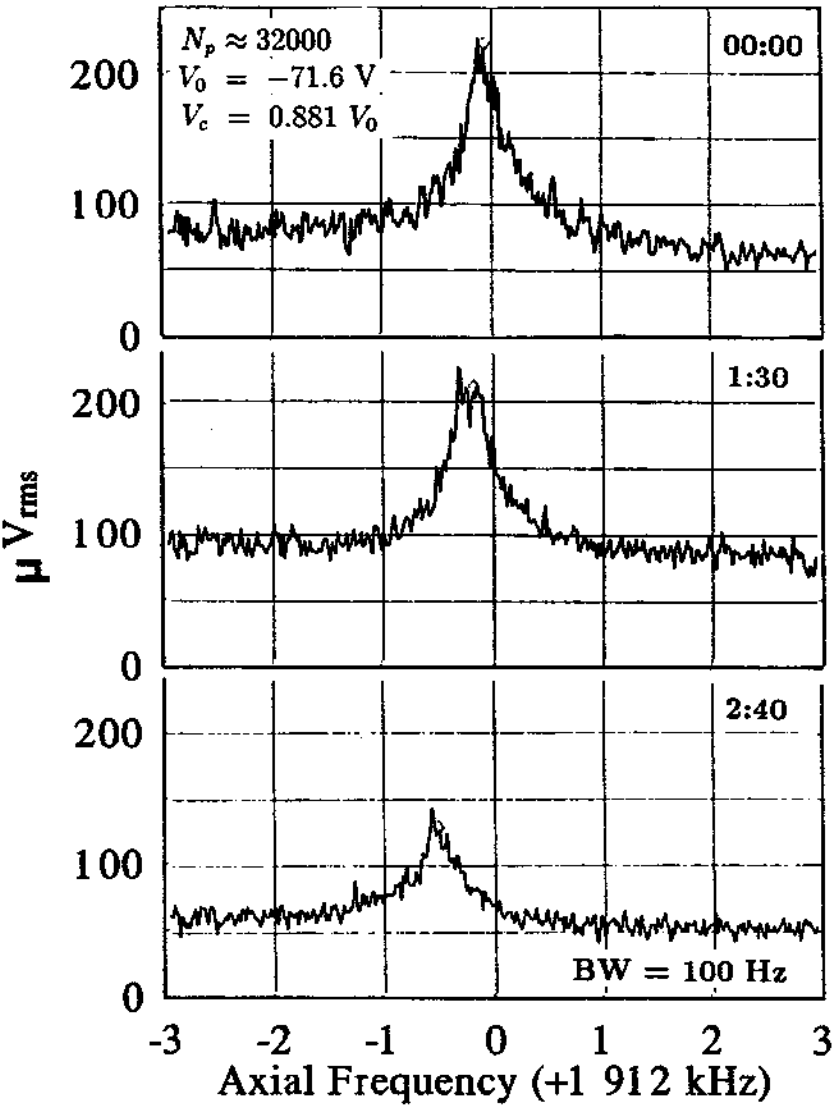

Figure 10.15: Axial shift for a fixed number of protons as a function of temperature in the axial motion

change as it damps indicating the linewidth is limited by particle number in this case. Shifts in the axial frequency for a single particle can also be expressed in terms of the center of mass energy in the three motions. Shifts due to the major perturbations are [13].

$$\left(\frac{\Delta\nu_z}{\nu_z}\right)_{Anharm.} = \frac{6C_4}{eV_0}\left[-\frac{1}{2}\left(\frac{\nu_z}{\nu_c'}\right)^2 E_c + \frac{1}{4}E_z + E_m\right] \tag{10.25}$$

$$\left(\frac{\Delta\nu_z}{\nu_z}\right)_{bottle} = \frac{1}{eV_0}\frac{B_2 d^2}{B}[E_c - E_m] \tag{10.26}$$

$$\left(\frac{\Delta\nu_z}{\nu_z}\right)_{rel.} = -\frac{1}{mc^2}\left[\frac{1}{2}E_c + \frac{3}{8}E_z - \frac{1}{4}\left(\frac{\nu_z}{\nu_c'}\right)^2 E_m\right]. \tag{10.27}$$

The shifts in Fig. 10.15 correspond to $\Delta\nu_z/\nu_z \approx 3\times10^{-4}$ which is much too large to be due to relativity. The shift is most likely due to anharmonicity. As seen in Eq. 10.25 the axial shift is more sensitive to the axial energy than the cyclotron energy by a factor of $2(\nu_z/\nu_c')^2 \approx 1/1250$. In general, the two largest observed shifts in the axial signal are due to this heat dependent shift (up for increased energy) or to a change in particle number (down for increased number).

In Chapter 6 (for example, see Fig. 6.4), the need to incorporate anharmonicity in order to increase detection sensitivity of the excited electron cyclotron motion was demonstrated. When the trap was tuned so that $C_4 \approx 0$, and the magnetic bottle was minimized, the observed shifts in $\Delta\nu_z$ for increased E_c were very small. By increasing the leading anharmonic component to $C_4 \approx 5.6\times10^{-3}$, cyclotron resonances could easily be observed as a shift in the axial frequency.

With the antiprotons and protons we can observe the cyclotron frequency directly. Figures 10.13 and 10.15 show how the signal amplitudes and linewidths vary as function of heat in the cyclotron and axial motions. In Fig. 10.16, 10.17, and 10.18 we show three separate situations where the cyclotron signal and axial signal are simultaneously recorded. In the first case, both degrees of freedom show some heating. After the signals damp, the number of antiprotons is then reduced and the cyclotron motion is reheated with an excitation drive near ν_c'. Fig. 10.17 shows that the cyclotron motion is severly heated, but that the axial signal is much less so. Figure 10.18 shows the same cloud about one-half hour

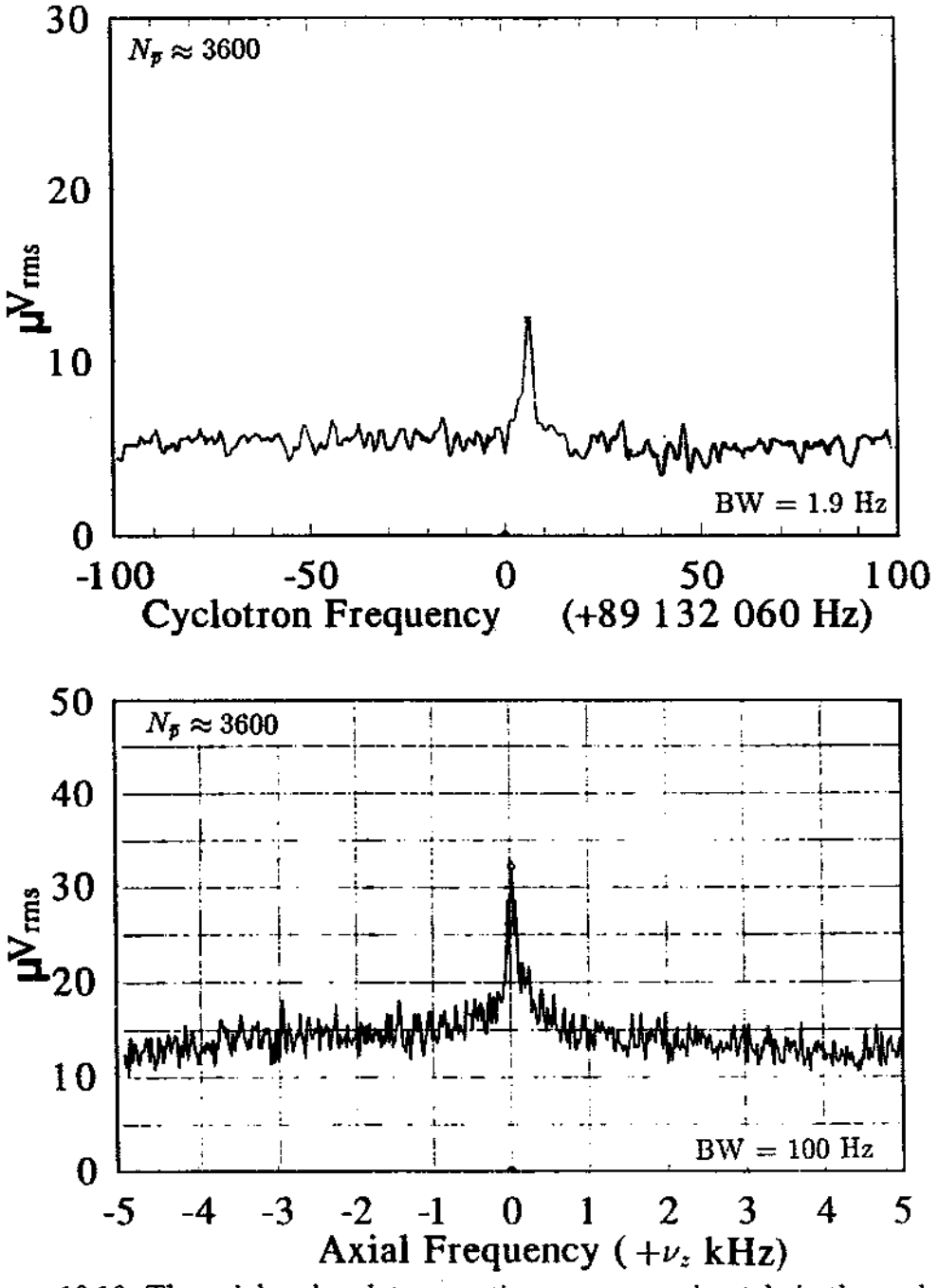

Figure 10.16: The axial and cyclotron motions are approximately in thermal equilibrium.

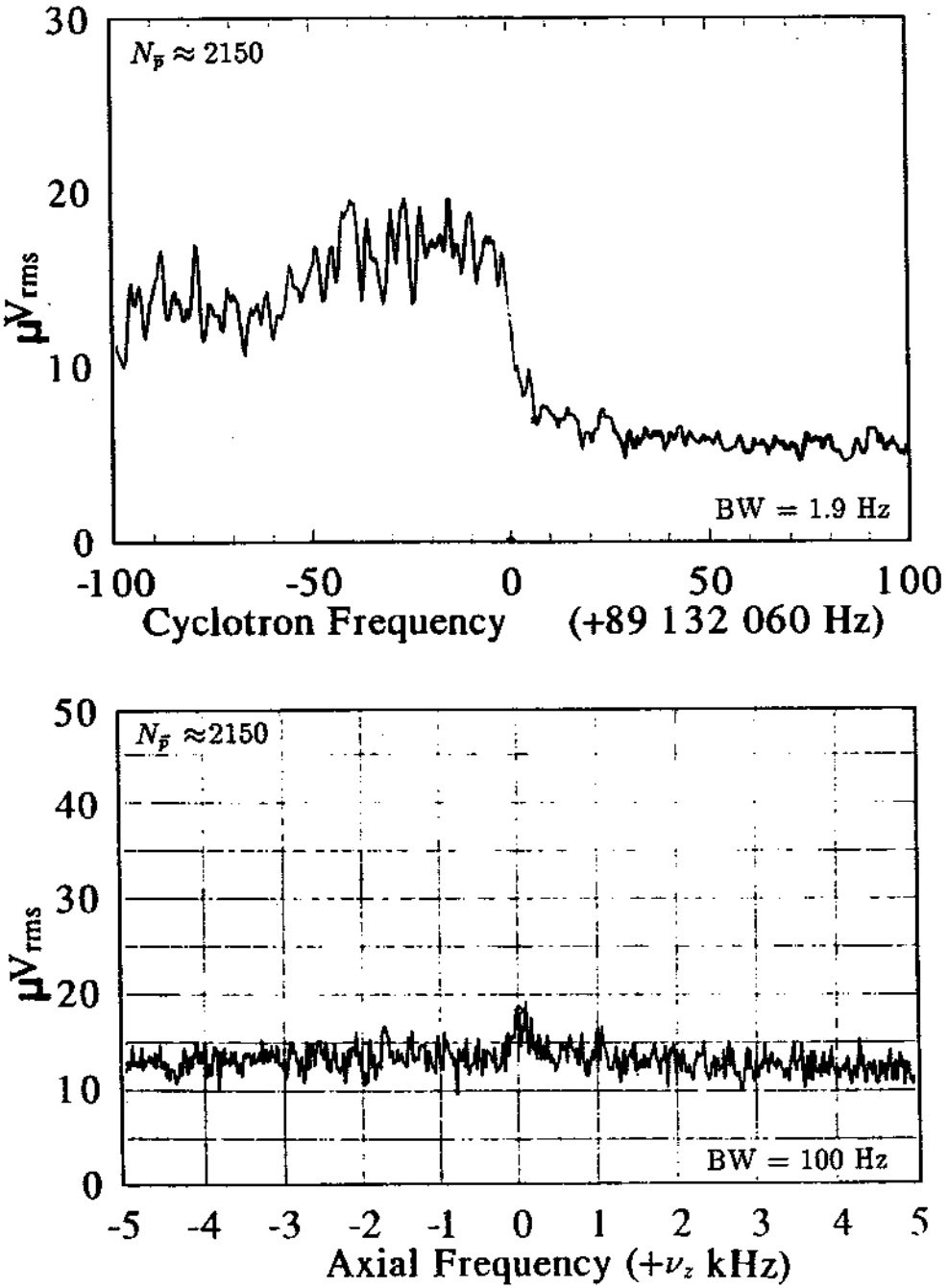

Figure 10.17: Large amount of heat in the cyclotron motion while the axial motion remains cool.

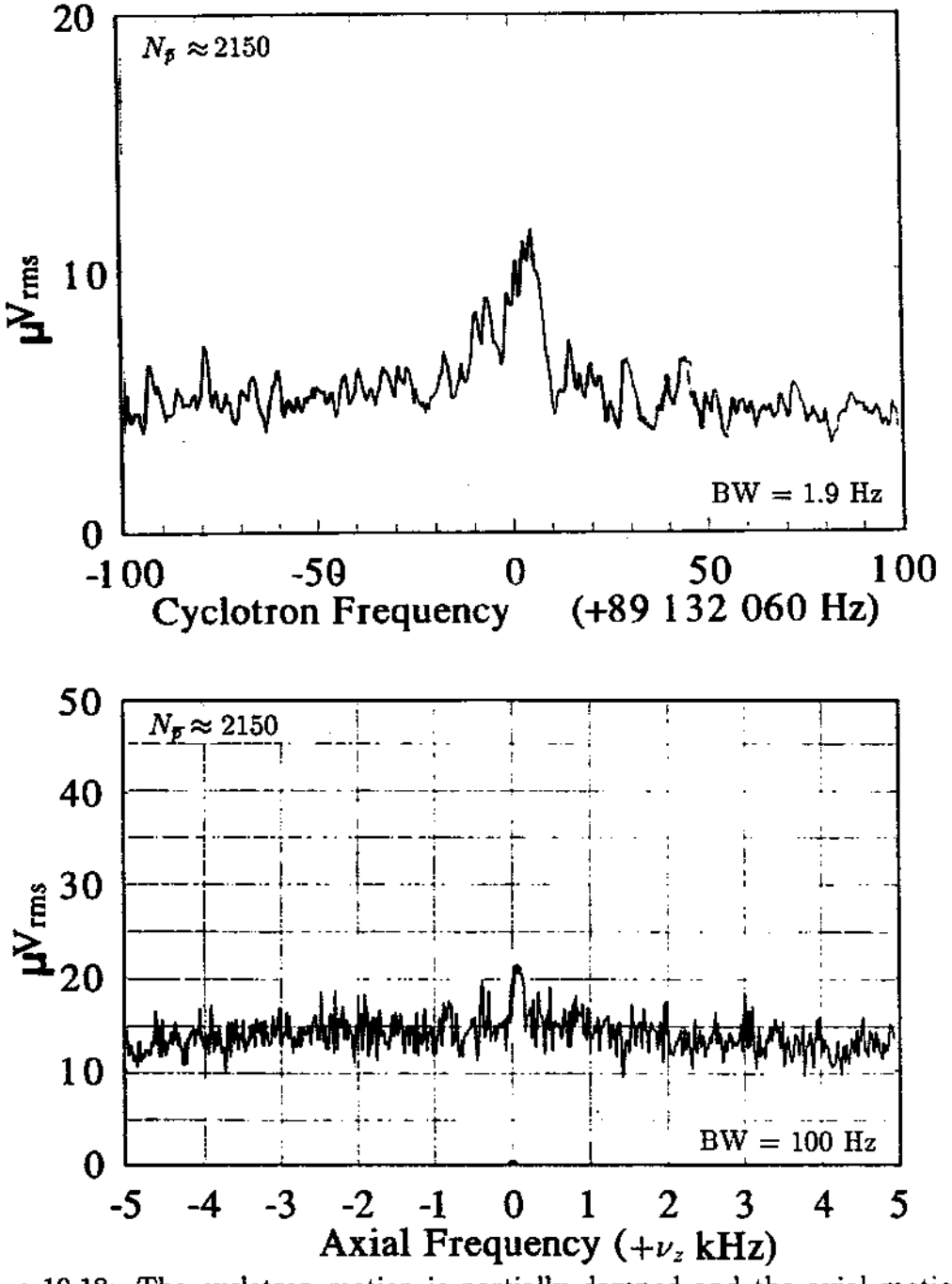

Figure 10.18: The cyclotron motion is partially damped and the axial motion remains cold.

later as the cyclotron motion has apparently resistively damped. The axial signal shows little change. The trap was optimally tuned for these three situations. By mistuning the trap, energy from the hot cyclotron motion can be coupled to the axial motion, though in general if the particle number is low and C_4 minimized, large heating of the cyclotron motion is observable without a corresponding rise in the axial energy as seen in Figs. 10.17 and 10.18. For higher numbers, the axial and cyclotron motions are much more coupled presumably via collisions.

10.3.2 Detection Effects

Shifts From Oscillator Coupling

Coupling between the particle oscillator and the detection resonant circuit can cause a shift in the particle eigenfrequency. The pulling of the particle frequency can be significant at high precisions. For direct detection of the cyclotron motion the pulling of the coupled circuits directly contributes to the uncertainty. For our detection parameters and detuning, the pulling on ν_c' for our typical number of antiprotons is estimated to be about 1 Hz. For similar mass particles, a comparison of the cyclotron frequencies will be relatively insensitive to such pulling since it nearly cancels when we take the ratio. For the proton to electron comparisons the pulling uncertainty can become significant depending on the mistuning. For the measurements reported in this thesis, ν_c' is substantially detuned from the center frequency of the detection resonant circuit and the pulling is $\leq 10^{-8}$.

Frequency Standard

All of the frequency synthesizers are frequency locked using the 10 MHz output of a Ball Efratom Modular Rubidium Frequency Standard (Model MRT-LN). Specifications at 5 MHz report a long term time drift of

$$\Delta\nu/\nu \leq 1 \times 10^{-11}/month, \tag{10.28}$$

The effects of frequency variation due to temperature and magnetic field fluctuations are $\leq 10^{-10}$ (from -10° C to +50° C) and $\leq 3 \times 10^{-11}$/G respectively.

10.4 Systematic Summary

In Table 10.2 we summarize and place limits on possible systematic effects described in this chapter. Because of the large trap, the small bottle, and the ability to tune away anharmonicity, most of the systematic limits summarized are insignificant at the 10^{-8} level. To account for the limits summarized here we add the fractional uncertainty

$$\sigma_{sys} = 2 \times 10^{-8} \tag{10.29}$$

to our results presented in Chapter 11.

The cyclotron and axial lineshapes for the antiproton(proton) and the cyclotron lineshape for the electron are not totally understood as demonstrated by the hight heat shifts. Since the resolution is so good for low heat situations, we choose not to split the measured resonance line for any of the observations used for the mass comparison. Thus we assign the fractional uncertainty of

$$\sigma_{width} = 2.8 \times 10^{-8}. \tag{10.30}$$

associated with the typical linewidth of 2.5 Hz during our frequency measurements.

Table 10.2: Summary of Systematic Errors ($\Delta\nu_c/\nu_c$)

MAGNETIC FIELD DEVIATIONS	
Homogeneity	
Linear Gradient ($< 1.6 \times 10^{-8}$/mm)	$\leq 3 \times 10^{-10}$ (E=0.3 meV)
Bottle ($< 1.7 \times 10^{-7}$/mm^2)	$\leq 5 \times 10^{-11}$ (E=0.3 meV)
Drift	
Long Term	$< 8 \times 10^{-10}/hr$
Field Fluctuations	
Bending Magnets	$< 1 \times 10^{-8}$
PS/LEAR	6×10^{-9}
QUADRUPOLE FIELD DEVIATIONS	
Trap Geometry	
Distortions, Misalignment ($\epsilon \leq 1\%, \theta \leq 1^\circ$)	$\leq 4 \times 10^{-11}$
Effects From Electrode Potentials	
Stability of Trap Potential ($\Delta V_0 << 150\mu$V)	$< 2 \times 10^{-8}$
Tuning and Harmonicity ($C_4 \leq 7.6 \times 10^{-4}$)	$< 9 \times 10^{-11}$ (E=0.3 meV)
Effects From the Presence of Other Particles	
Number Dependence ($\Delta\nu_c/\nu_c \approx 5 \times 10^{-13}/\bar{p}$)	$< 10^{-9}$ (for 3000 $\bar{p}$)
Space Charge (slope average of ν_c' *vs.* V_0)	$< 2.0 \times 10^{-8}$
DETECTION RELATED EFFECTS	
Amplifier Pulling	$< 10^{-8}$
Frequency Standard Stability	$< 10^{-11}$
Relativistic Shift	2×10^{-13} (E=0.3 meV)

Chapter 11

The Antiproton, Proton, and Electron Mass Comparison

The Penning trap is a flexible device capable of comparing very different masses and particles of opposite charge. Nevertheless, possible systematic errors are minimized in a Penning trap by comparing mass doublets of a single charge polarity. With nearly the same charge to mass ratio the orbit sizes, particle location, and trap potential and polarity are similar. Examples of measurements on mass doublets of similar charge are comparisons of CO^+ and $N_2{}^+$ [21] and $^3He^+$ and $^3H^+$ [105,68]. More difficult comparisons are those involving very different masses and/or different sign of charge. An example of the former is a comparison of p^+ and e^- [50,53,98,99,100], and of the later is a comparison of e^+ and e^- [86]. As stressed in the last chapter, the major difficulty centers on being absolutely certain that the particles to be compared oscillate in the same magnetic field.

In this chapter we present a series of comparisons where we load and measure the cyclotron frequency of antiprotons and protons using our most recent techniques discussed in Chapters 7 and 9. The measurements are performed on small clouds of antiprotons or protons (typically 200 - 2000). These clouds both have the possibility of being contaminated with impurity ions that are very different (in one case electrons, in the other positively charged ions). As a check in our measurements we also compare both the antiproton and proton to the electron mass. The electron is relatively easy to study at the level of precision of our existing work and since the electron mass is very different from the antiproton mass,

it also provides an additional check of possible systematic effects. Our approach is to perform a self-consistent three way mass comparison each with a different variation of mass or charge polarity.

In Fig 11.1 we show a series of measurements of the cyclotron frequencies of antiprotons, protons, and electrons. We specifically analyze five sets of measurements where antiproton, proton, and electron cyclotron frequencies have each been measured. For comparing protons to electrons we extend the data to seven sets. This data represents only the most recent of several hundred antiproton frequency measurements and is chosen because all three particles were measured relatively close in time. The measurements use our most developed techniques to interrogate the particle motion with as little as heat as possible. Each measurement set is taken over an average time span of about 20 hours. Although the time to prepare a new particle species for a measurement is about one hour, we begin each measurement set with several measurements on a small antiproton cloud, then after ejecting the antiprotons, we prepare and measure electrons and protons as described in Chapters 6, 7, and 9. We complete a comparison set by again loading antiprotons and measuring their resonant frequencies.

Cyclotron measurements taken over the comparison time are shown in Fig. 11.1 and each data set used in subsequent analysis is identified. All antiprotons and proton measurements are performed at about $\pm$ 71 Volts by simultaneously observing the frequencies ν_c' and ν_z as described in Chapter 9. The electron measurements are taken with the axial frequency locked as described in Chapter 6.

The free space cyclotron frequency is determined by

$$(\nu_c)_i = (\nu_c')_i^2 + \frac{(\nu_z)_i^2}{2(\nu_c')_i}. \tag{11.1}$$

The uncertainty assigned to each point is the quadrature sum of the cyclotron and magnetron linewidths defined by

$$\sigma_i^2 \equiv (\Delta\nu_c')_i^2 + \left(\frac{\nu_z}{\nu_c'}(\Delta\nu_z)_i\right)^2. \tag{11.2}$$

For the antiproton and proton measurements, $\Delta\nu_c'$ and $\Delta\nu_z$ are the HWHM linewidths of the Fourier transform power spectrum (measured as 0.707 V_{rms}) of each frequency.

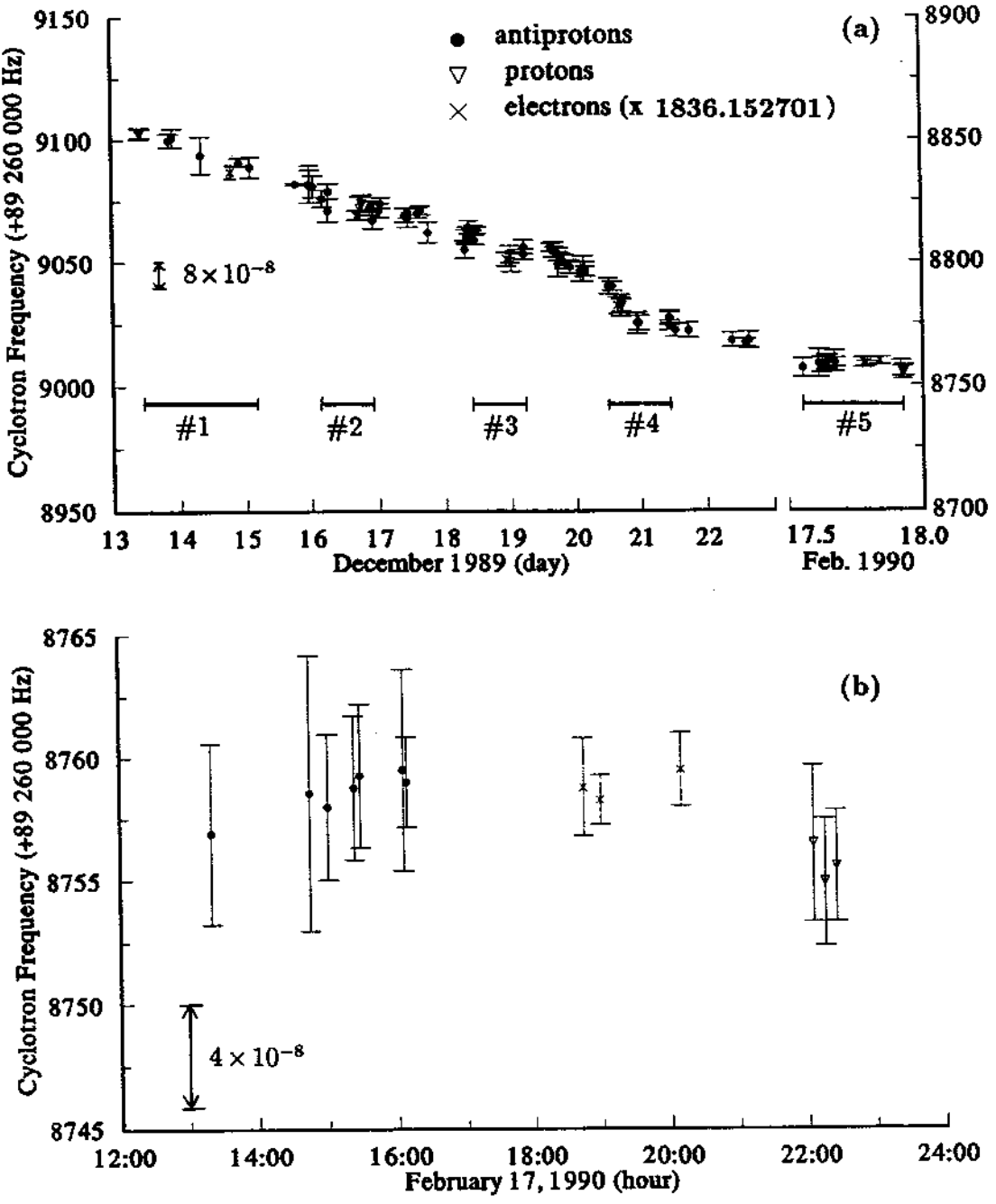

Figure 11.1: (a) Series of cyclotron measurements for antiprotons, protons and electrons over time. The 5 three way comparison sets are shown. (b) Expanded view of comparison set #5.

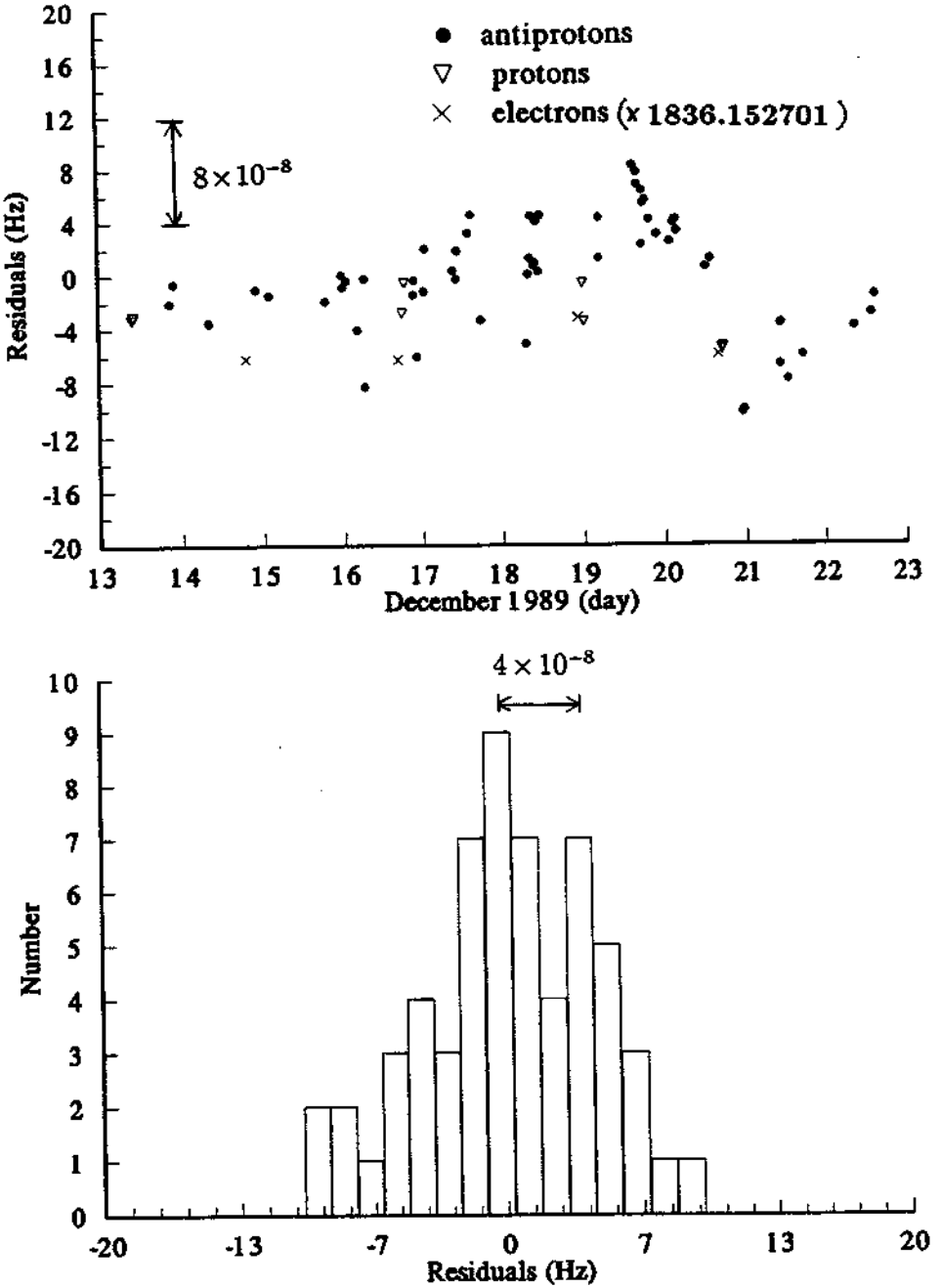

Figure 11.2: (a) The data in Fig. 10.1 with the magnetic field drift subtracted out. (b) The residuals about the least squares fit showing the scatter of the antiproton measurements taken over the 10 day period.

Table 11.1: Statistical Data of the 5 (and 7) Mass Comparison Sets.

Set		Time [hours]	Meas. # beg.	Meas. # end	$\overline{\nu_c}$ Mean	$\overline{\nu_c}$ Weighted	Standard Deviation [Hz] Scatter	Linewidth	Total
					89 269 000+				
	$\overline{p}$			3 2	218.81	219.25	1.75	1.19	2.11
1	e^-	40.6		1	(214.38)†			(2.80)	(3.30)
	p		2		217.36	217.37		1.43	2.26
	$\overline{p}$		3	3	217.33	219.52	3.22	1.39	3.50
2	e^-	17.7		1	(214.69)†			(1.63)	(3.61)
	p			2	218.61	218.94		2.77	4.25
	$\overline{p}$		3	2	224.23	224.31	2.71	0.81	2.82
3	e^-	18.8		1	(217.49)†			(2.72)	(3.84)
	p			3	221.61	222.11		2.15	3.45
	$\overline{p}$		2	4	215.74	216.90	3.65	1.01	3.78
4	e^-	22.4		1	(214.85)†			(3.27)	(4.90)
	p			4	217.26	217.32		1.49	3.94
					89 268 000+				
	$\overline{p}$		7		758.56	758.68	1.49	1.11	1.86
5	e^-	9.0		3	(758.84)†	(758.65)		(0.69)	(1.64)
	p			3	754.07	755.40		1.47	2.09
6	e^-	7.0		2	(638.45)†	(638.45)	1.16	(1.00)	(1.53)
	p		4		637.23	637.80	1.16	2.03	2.34
7	e^-	47	1		(633.4)†		0.90	(1.00)	(1.34)
	p			2	634.55	635.00		2.30	2.47

† To facilitate comparisons, $\nu_c[e^-]$ is tabulated as the nearly equivalent proton frequency $(m_e/m_p)\nu_c[e^-]$ using the ratio m_p/m_e=1836.152 701.

Table 11.2: Mass Ratio Weighted Averages and Uncertainties.

Antiproton / Proton

Set	$1-(m_{\bar{p}}/m_p)$	$\Delta(m_{\bar{p}}/m_p)$				
1	$+2.1\times10^{-8}$	3.5×10^{-8}	Average	=	1.3×10^{-8}	
2	$+0.65\times10^{-8}$	6.3×10^{-8}	Weighted average	=	2.3×10^{-8}	
3	$+2.5\times10^{-8}$	5.0×10^{-8}	σ_{scat}	=	1.6×10^{-8}	
4	-0.45×10^{-8}	6.1×10^{-8}	σ_{line}	=	1.9×10^{-8}	
5	$+3.7\times10^{-8}$	3.1×10^{-8}	σ_{sys}	=	2.0×10^{-8}	
			σ_{width}	=	2.8×10^{-8}	

Antiproton / Electron

Set	$m_{\bar{p}}/m_{e^-}$	$\Delta(m_{\bar{p}}/m_{e^-})$				
	1836.152...					
1	600	079	Average	=	1836.152 623	
2	601	101	Weighted Ave.	=	1836.152 648	
3	560	096	σ_{scat}	=	0.000 055	(3.0×10^{-8})
4	658	125	σ_{line}	=	0.000 035	(1.9×10^{-8})
5	700	050	σ_{sys}	=	0.000 037	(2.0×10^{-8})
			σ_{width}	=	0.000 050	(2.8×10^{-8})

Proton / Electron

Set	m_p/m_{e^-}	$\Delta(m_p/m_{e^-})$				
	1836.152...					
1	639	081				
2	613	113				
3	605	104	Average	=	1836.152 666	
4	658	127	Weighted Ave.	=	1836.152 693	
5	768	054	σ_{scat}	=	0.000 058	(3.2×10^{-8})
6	714	056	σ_{line}	=	0.000 027	(1.5×10^{-8})
7	668	057	σ_{sys}	=	0.000 037	(2.0×10^{-8})
			σ_{width}	=	0.000 050	(2.8×10^{-8})

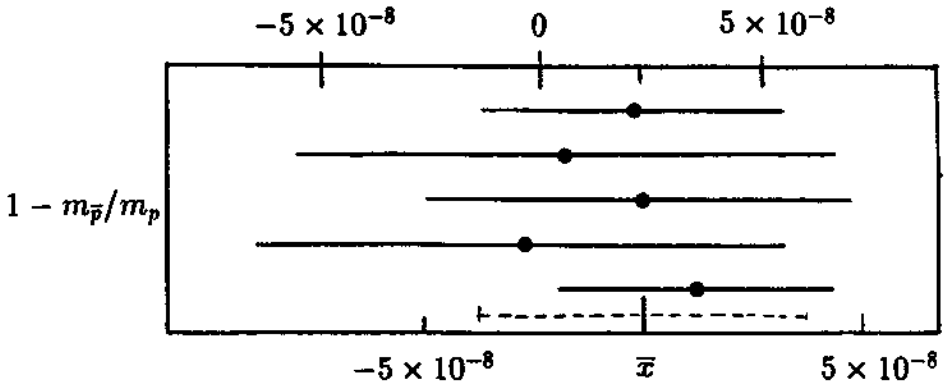

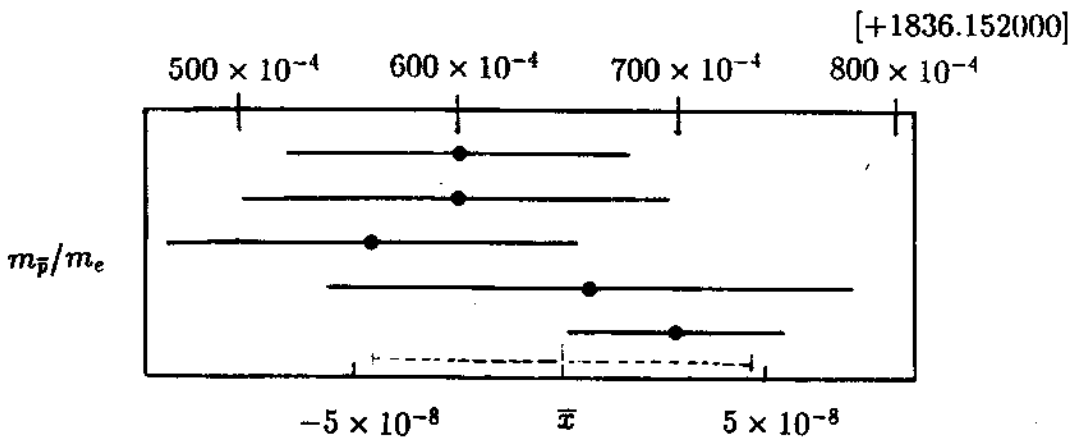

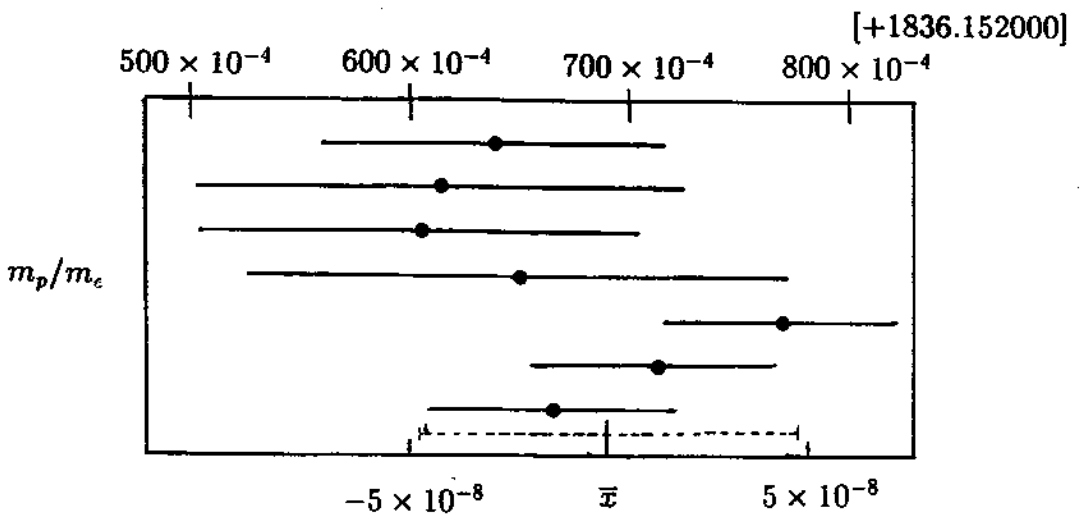

Figure 11.3: Mass comparisons $m_{\bar{p}}/m_p$, $m_{\bar{p}}/m_p$, and m_p/m_e-. The weighted average and assigned uncertainty is shown in dashed lines.

The points in Fig. 11.1 are plotted as a function of time. So that the measured electron cyclotron frequencies can be presented on the same scale, they are reduced by the high precision proton to electron mass ratio m_p/m_e=1836.152701 previously measured by R. VanDyck et al. [100,72]. This is for convenience only. All mass comparisons discussed and reported are completely independent of this earlier measurement.

For the first four data sets shown in Fig. 11.1 there exists a large drift in the magnetic field. This is a result of the magnet being energized and shimmed only a few days before this particular set of measurements were taken. In addition, a few of the points in the figure have been corrected for a field shift resulting from the S-5 bending magnet (see Fig. 3.10) being on or off. Of the five data sets, #3 and #5 were taken with the bending magnet off. This shift was carefully measured and was discussed in Chapter 10.

Since the magnet drift is so high for the first four data sets, it must be taken into account. To do this, we fit the antiproton points during the days of December 13-21 to a straight line. The assumption is made that the shifts due to small variations in cloud number and size are not significant on this scale and that the antiprotons can be used to map the magnetic field. In Fig. 11.2(a), we show the residuals of the points over the region that includes the first four data sets after subtracting the least squares fit. In Fig. 11.2(b) we show a histogram of all the antiproton data points in this region about the fit. The distribution of residuals represents the long term drift uncertainties and incorporates local fluctuations in the field that are in part responsible for the scatter of the points.

After correcting the data for the long term field drift each data set is then individually analyzed. Short term variations in the field drift are not subtracted out but are accounted for in the scatter of the points within a given data set calculated by

$$\sigma^2_{scat} \equiv \frac{\sum_{i=1}^{N}((\nu_c)_i - \overline{\nu_c})^2}{N-1}. \tag{11.3}$$

In Table 11.1 we show the summarized analysis of each data set (again for convenience, we tabulate the electron measurements by dividing $\nu_c(e^-)$ by 1836.152 701. For example, in data set #2, we have six antiproton measurements, three

at the beginning and three at the end of the set. One electron and two proton measurements were performed in between. The average and weighted average (where the associated weight of each measurement is the inverse of the variance $1/\sigma_i^2$) of the particle cyclotron frequencies are obtained respectively by

$$\overline{\nu}_c = \frac{1}{N}\sum_{i=1}^{N}(\nu_c)_i, \tag{11.4}$$

and

$$(\overline{\nu}_c)_w = \frac{\sum_{i=1}^{N}\frac{(\nu_c)_i}{\sigma_i^2}}{\sum_{i=1}^{N}\frac{1}{\sigma_i^2}}. \tag{11.5}$$

The values for $(\nu_c)_i$ and $(\sigma)_i$ are defined by Eq. 11.1 and Eq. 11.2. An assigned linewidth to each particle species in a given set is defined in terms of the individual linewidths by

$$\frac{1}{\sigma_{line}^2} \equiv \sum_{i=1}^{N}\frac{1}{\sigma_i^2}. \tag{11.6}$$

As suggested in contemporary literature on the subject of errors in precision measurements [74,90], each point is assigned with an associated uncertainty defined by

$$\sigma^2 \equiv \sigma_{scat}^2 + \sigma_{line}^2. \tag{11.7}$$

As seen in Table 11.1 much of the uncertainty is in the scatter over the relatively long comparison times within most data sets. Each data set is now represented by three measurements, one each for the antiproton, proton, and electron with weighted average $(\overline{\nu}_c)_w$ and associated uncertainty σ. In most cases the weighted average is similar to the average since measurement linewidths are nearly the same for most points.

We now take the mass ratios between each of the three points in a given measurement set and calculate an uncertainty from the two input uncertainties. The ratios 1-$(m_{\overline{p}}/m_p)$, $m_{\overline{p}}/m_{e^-}$, and m_p/m_{e^-} with the corresponding uncertainty are tabulated in Table 11.2 and plotted in Fig. 11.3. The average and weighted average are now taken over the five mass comparison sets (in the case of protons and electrons we use seven sets). The averages are calculated analogously to the earlier analysis and the weighted average over the data sets (Table 11.2) yield the

final mass ratio value. The uncertainty is determined by calculating the scatter of the 5 (or 7) points about the mean ratio value analogous to Eq. 11.3 except with the mean cyclotron frequency replaced by the mean of the ratio values. We also determine a 'linewidth' uncertainty σ_{line} using Eq 11.6 . The total uncertainty for each ratio measurement is defined by

$$\sigma^2 \equiv \sigma_{scat}^2 + \sigma_{line}^2 + \sigma_{sys}^2 + \sigma_{width}^2, \tag{11.8}$$

where σ_{sys} represents the 2×10^{-8} fractional systematic uncertainty and σ_{width} reflects our unwillingness to split the observed resonance lines as discussed in Chapter 10. The values for each of these error terms is tabulated in Table 11.2.

The weighted average of the ratio comparison gives the final measured result. The antiproton to proton mass ratio is measured to be

$$\left(\frac{m_{\overline{p}}}{m_p}\right)_w = 0.999\ 999\ 977(42). \tag{11.9}$$

Comparing the antiproton mass to the electron's yields the ratio

$$\left(\frac{m_{\overline{p}}}{m_{e^-}}\right)_w = 1836.152\ 648(89). \tag{11.10}$$

Comparing the proton mass to the electron's yields the ratio

$$\left(\frac{m_p}{m_{e^-}}\right)_w = 1836.152\ 693(88). \tag{11.11}$$

The weighted average and total uncertainty added in quadrature are included in Fig. 11.3 and denoted in dashed lines. These values differ a slight amount from our most recent published values [48] as a result of small differences in the analysis of the scatter. These insignificant differences are only about 5 parts in 10^9 or about 15% of the assigned uncertainty.

A few observations can be made from the data in Fig. 11.3. These data sets were taken over a relatively long time period. A correlation seems to exist in the scatter of the antiproton to electron and the proton to electron comparisons, but not in the antiproton to proton comparisons. This may suggest that the fluctuating variable observable in this scatter is in the electron measurements or in our interpretation of the observed electron cyclotron lineshape.

Chapter 12

Conclusions

The long term storage and non-destructive interrogation of cryogenic antiprotons have made it possible to measure the antiproton-proton mass ratio 1000 times more accurately than with any previous technique (Fig. 12.1). We have measured the antiproton to proton mass ratio to be

$$\frac{m_{\overline{p}}}{m_p} = 0.999\ 999\ 977(42). \tag{12.1}$$

This measurement has a fractional uncertainty of 4.2×10^{-8}, making it the most stringent test of CPT invariance using baryons.

In addition, as part of a thorough systematic study using the much lighter electron, we have independently compared the antiproton and proton to the electron inertial mass. We obtain

$$\frac{m_{\overline{p}}}{m_e} = 1836.152\ 648(89), \tag{12.2}$$

and the fundamental ratio

$$\frac{m_p}{m_e} = 1836.152\ 693(88). \tag{12.3}$$

The standard deviation of the later, representing a fractional uncertainty of 4.8×10^{-8}, is smaller than all previous proton-electron comparisons with the exception of the most recent measurement by VanDyck, et al. (Fig. 12.2) for which a standard deviation 2.4 times smaller is reported [100]. Our ratio agrees with their most recent measurement of 1836.152 701(37) and disagrees with their earlier measurement which had a systematic problem [100]. The technique used to measure the

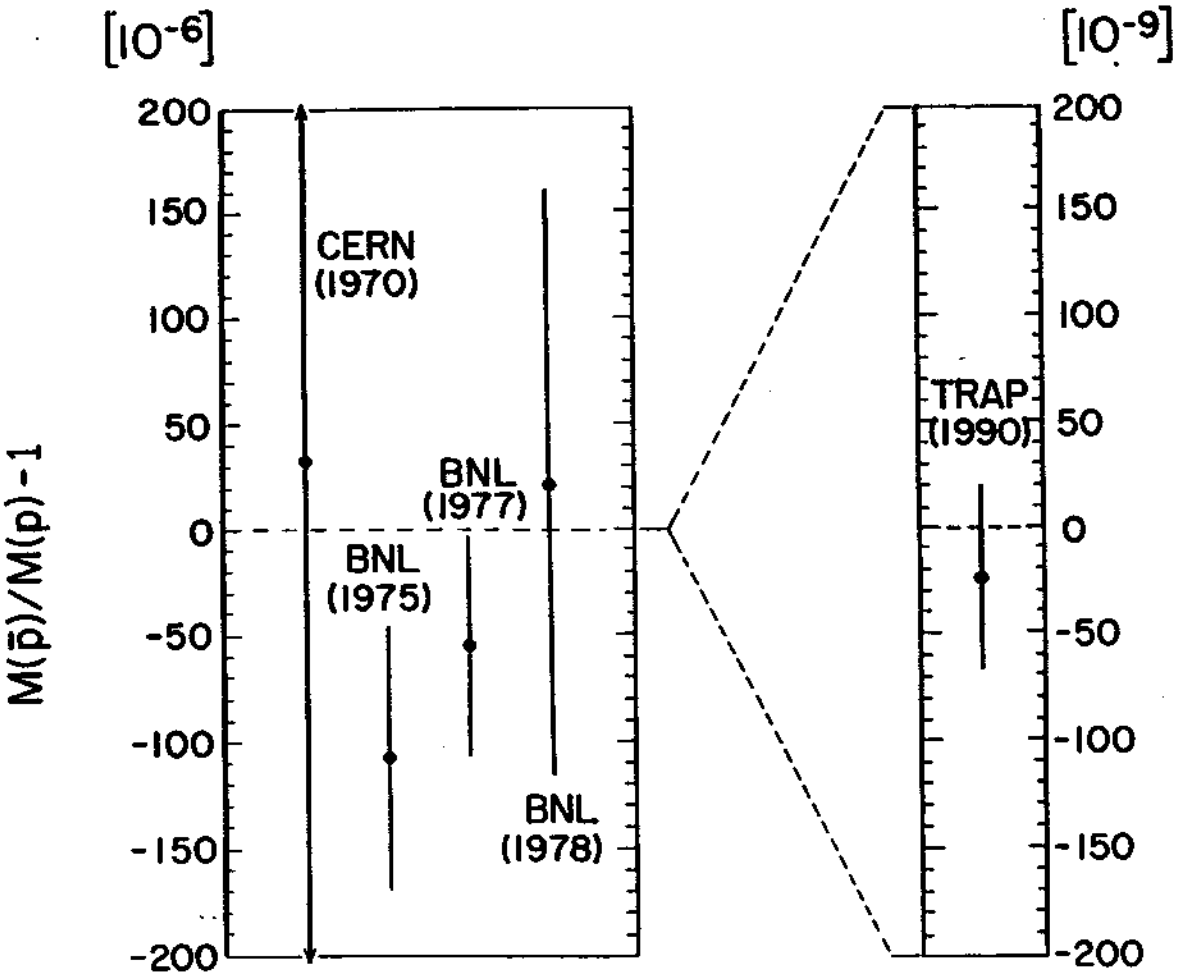

Figure 12.1: Measurements of the ratio of antiproton to proton inertial masses. Our new measurement shown on the right is an increase in accuracy of 1000.

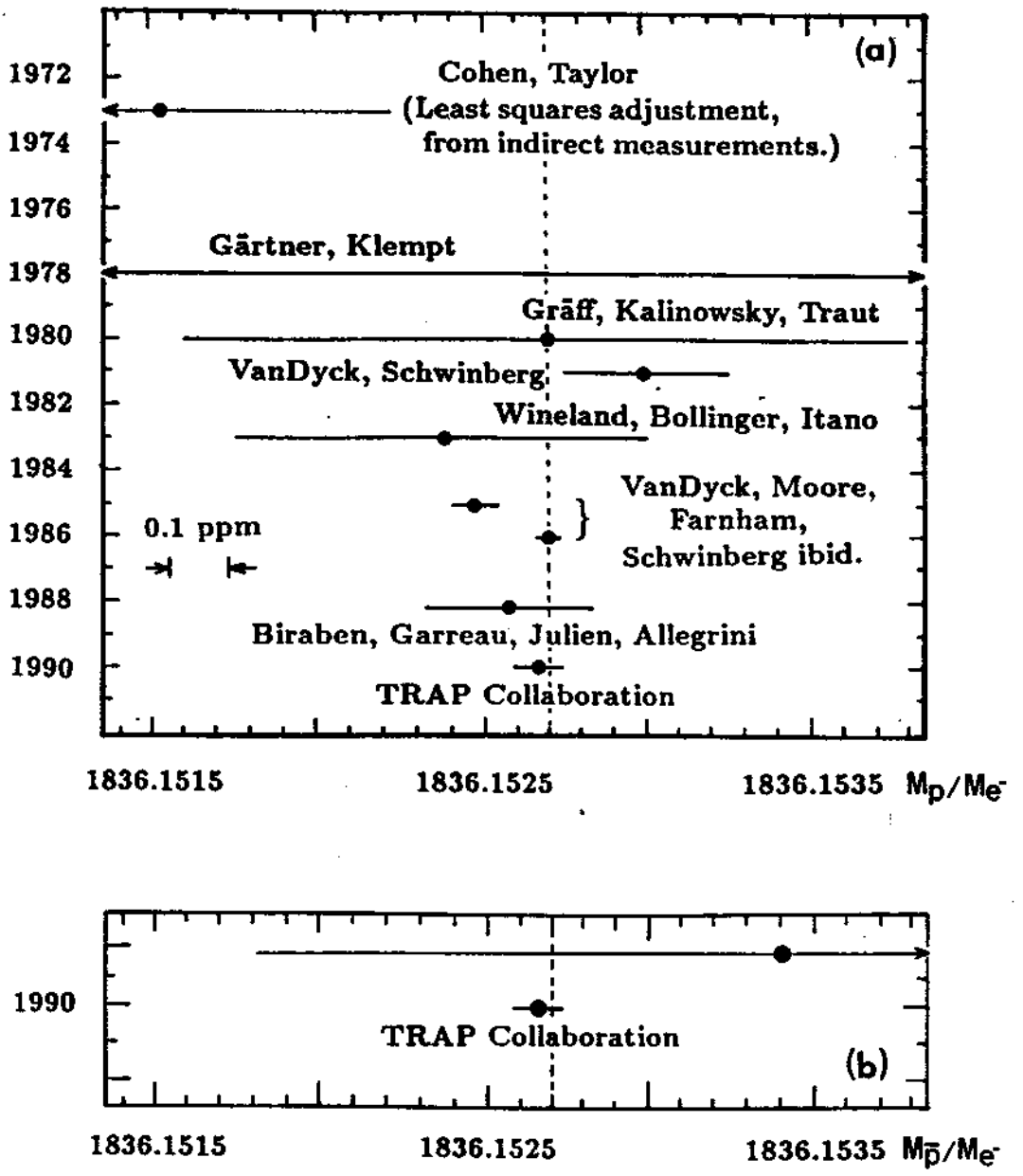

Figure 12.2: (a) Previous Measurements of the proton-electron mass ratio with our new measurement performed in the new open endcap trap. It is in agreement with the most recent, higher precision measurement by VanDyck et. al. . (b) Our new measurement of the antiproton-electron mass ratio.

mass ratio is similar except in our case no magnetic bottle is introduced, cylindrical electrodes are used rather the hyperbolic electrodes, and the effective size of our cylindrical trap is approximately six times larger than the hyperbolic electrodes used for the previous measurements.

Our large trap minimizes many potential systematic perturbations. Measurements are much less sensitive to misalignment of the quadrupole field with respect to the magnetic field and to distortions in the trap electrodes. Measurements are also much less sensitive to perturbations due to particle number or contaminant ions. Distortions to the magnetic field (the magnetic bottle) resulting from the residual paramagnetism and diamagnetism of the trap electrodes are also greatly reduced as is the effect of possible voltage offsets which could displace the physical center of the confined particle(s).

This work demonstrates that the cylindrical Penning trap can produce a sufficiently good quadrupole potential for high precision mass spectroscopy. The cylindrical trap is easier to construct than traditional hyperbolic traps. It is also orthogonalized, making possible deliberate mistuning which is useful for systematic studies or as a coupling mechanism between the various eigenmodes. With the use of compensation coupling in the electron measurements, cyclotron resonances are measured with a resolution of better than one part in 10^8. At the level of the comparisons made in this thesis, no line splitting is required in either the electron, proton, or antiproton measurements.

The use of direct detection of the cyclotron motion for antiprotons and protons, has been used for studying polarity dependence effects and as a means to probe the effect of space charge due to contaminant ions in the trap. This is the first use of such a detection scheme for opposite but similar mass particle-antiparticle pairs (the positron and electron have presently only been measured by indirect detection techniques) For ion measurements, direct detection allows the observation of the lineshape as a function of energy, particle number, and spatial extent. An understanding of the cyclotron lineshape is often difficult to obtain with indirect detection through the axial motion, which is commonly used in Penning mass spectroscopy experiments. The extrapolations of the cyclotron frequency as

a function of trap voltage for antiprotons and protons to directly determine the free space cyclotron frequency have also been used as an independent check of measurements determined using the invariance theorem.

Since the inertial mass measurement was performed at the CERN accelerator complex, much attention was paid to the fluctuating magnetic field environment. The self shielding magnet system developed and constructed especially for this project and was shown to be capable of shielding uniform fluctuations in the magnetic field by a factor of 156 [42,46]. This system should have applicability in future mass spectroscopy measurements and in NMR research. With the self shielding, uniform fluctuations in the magnetic field were measured to be reduced at the trap region by a factor of 156.

Even though for the inertial mass comparison we need only a small number of antiprotons our techniques to obtain and cool antiprotons have broader applicability. To date, we have loaded and electron cooled more than 100,000 antiprotons into the high precision region of the trap. Because of the extremely good vacuum with a pressure estimated to be less than 5×10^{-17} Torr (100 atoms/cm^3), we once held approximately 1850 antiprotons for 59 days. This provides a conservative containment lifetime (which subsequently is the longest measured antiproton lifetime limit) of

$$\tau_{\bar{p}} \geq 103 \ \ days. \tag{12.4}$$

The availability of a cold antiproton source with a long confinement time should lead to other intriguing experiments.

Bibliography

[1] American Magnetics Inc.; Oak Ridge, TN 37831.

[2] B. Autin, et al., in Proc. of Eur. Part. Accel. Conf. (1990); also S. Maury, private communication.

[3] A. Bamberger, U. Lynen, H. Piekarz, J. Piedarz, B. Povh, H.G. Ritter, G. Backenstoss, T. Bunaciu, J. Egger, W.D. Hamiltion, and H. Koch, Phys. Lett.**33B**, 233 (1970).

[4] E.C. Beaty, Phys. Rev. A **33**,3645(1986). E.C. Beaty, J. Apl. Phys.**61**, 2118 (1987).

[5] St. Becker, G. Bollen, F. Kern, H.-J. Kluge, R.B. Moore, G. Savard, L. Schweikhard, H. Stolzenberg, preprint CERN-EP/89-126 (1989).

[6] F. Biraben, J.C. Garreau, L. Julien, and M. Allegrini, Phys. Rev. Lett. **62**, 621 (1989).

[7] L. Bracci, G. Fiorentini, and O.P. Pitzorra, Phys. Lett. B **85**, 280 (1979).

[8] L.S. Brown and G. Gabrielse, Phys. Rev. A **25**, 2423 (1982).

[9] L.S. Brown, Phys. Rev. Lett. **52**, 2013 (1984)
L.S. Brown, Ann. Phys. **A 159**, 62 (1985).

[10] Lowell S. Brown, Gerald Gabrielse, Kristian Helmerson, and Joseph Tan, Phys. Rev. Lett. **55**, 44 (1985).

[11] L.S. Brown, G. Gabrielse, K. Helmerson, and J. Tan, Phys. Rev. **A 32**, 3204, (1985).

[12] L.S. Brown, G. Gabrielse, J. Tan, and K.C.D. Chan, Phys. Rev. **A 37**, 4163 (1988).

[13] L.S. Brown and G. Gabrielse, Rev. Mod. Phys. **58**, 233 (1986).

[14] L.S. Brown, K. Helmerson, and J. Tan, Phys. Rev. **A 34**, 2638 (1986).

[15] J. Byrne and P.S. Farago, Proc. Phys. Soc. Lond. **86**, 808 (1965).

[16] J. Byrne, P.G. Dawber, J.A. Spain, A.P. Williams, M.S. Dewey, D.M. Gilliam, G.L. Greene, G.P. Lamaze, R.D. Scott, J. Pauwels, R. Eykens, and A. Lamberty, Phys. Rev. Lett. **65**, 289 (1990).

[17] Ceramaseal, New Lebanon, NY 12125.

[18] Owen Chamberlain, Emilio Segre, Clyde Wiegand, and Thomas Ypsilantis; Phys. Rev. **100**, 947 (1955).

[19] J.H. Christenson, J.W. Cronin, J.C. Fitch, R. Turlay; Phys. Rev. Lett. **13**, 138 (1964).

[20] D.A. Church, in **Physics of Electronic and Atomic Collisions**, S. Datz ed., (North-Holland Pub. Co., 1982).

[21] E.A. Cornell, R.M. Weisskoff, K.R. Boyce, R.W. Flanagan, Jr., G. Lafyatis and D.E. Pritchard, Phys. Rev. Lett. **63**, 1674 (1989).

[22] E.A. Cornell, R.M. Weisskoff, K.R. Boyce, and D.E. Pritchard, Phys. Rev. A **41**, 312 (1990).

[23] E.A. Cornell, R.M. Weisskoff, K.R. Boyce, R.W. Flanagan, Jr., G. Lafyatis and D.E. Pritchard, Phys. Rev. Lett. **64**, 2099 (1990).

[24] H. Dehmelt, R. VanDyck, P. Schwinberg, G. Gabrielse, Bull. Am. Phys. Soc. **24**, 757 (1979).

[25] H. Dehmelt and P. Ekstrom, Bull. Am. Phys. Soc. **18**, 727 (1973);
H. Dehmelt, Proc. Natl. Acad. Sci. U.S.A. **83**, 2291 (1986).

[26] C.F. Driscoll, K.S. Fine, and J.H. Malmberg, Phys. Fluids **29**, 2015 (1986).

[27] X. Fei, R. Davisson and G. Gabrielse, Rev. Sci. Inst. **58**, 2197 (1987).

[28] X. Fei; Ph.D. Thesis, Harvard U., 1990.

[29] T.J. Francl, M.G. Sherman, R.L. Hunter, M.J. Locke, W.D. Bowers, and R.T. McIver, Jr. , Intl. J. of Mass Spec. and Ion Proc., **54**, 189-199 (1983).

[30] G. Gabrielse, Phys. Rev. A **27**, 2277 (1983).

[31] G. Gabrielse, Phys. Rev. A **29**, 462 (1984).

[32] G. Gabrielse and F.C. Mackintosh, Int. J. Mass Spec. Ion Proc. **57**, 1 (1984).

[33] G. Gabrielse, H. Dehmelt, and W. Kells, Phys. Rev. Lett. **54**, 537 (1985).

[34] G. Gabrielse and H. Dehmelt, Phys. Rev. Lett., **55**, 67 (1985).

[35] G. Gabrielse, H. Kalinowsky, W. Kells, and T. Trainor,
CERN Report No. CERN/PSCC/85-21PSCC/P83, 1985 (unpublished)

[36] G. Gabrielse, H. Kalinowsky, and W. Kells, in **Physics with Antiprotons at LEAR in the ACOL Era**, eds. U. Gastaldi, R. Klapisch, J.M. Richard, and J. Tran Thanh Van, (Editions Frontièrs, Gif-Sur-Yvett, 1985), p.665.

[37] G. Gabrielse, X. Fei, K. Helmerson, S.L. Rolston, R. Tjoelker, T.A. Trainor, H. Kalinowsky, J. Haas, and W. Kells, Phys. Rev. Lett. **57**, 2504 (1986).

[38] G.Gabrielse, K. Helmerson, R. Tjoelker, X. Fei, T.A. Trainor, W. Kells, and H. Kalinowsky,
in **Proceedings of the First Workshop on Antimatter Physics at Low Energy**,
edited by B.E. Bonner, L.S. Pinsky (Fermilab, Batavia, 1986), p.211.

[39] G. Gabrielse, in **Fundamental Symmetries**, pp. 59-75 (Plenum, New York, 1987).

[40] G. Gabrielse, X. Fei, L. Haarsma, S.L.Rolston, R.L. Tjoelker, T.A. Trainor, H. Kalinowsky, J. Hass, and W. Kells, Physica Scripta **T22**, 36 (1988).

[41] G. Gabrielse, S.L. Rolston, L. Haarsma and W. Kells, Phys. Lett. **A129**, 38 (1988).

[42] G. Gabrielse and J. Tan, J. Appl. Phys. **63**, 5143 (1988).

[43] G. Gabrielse, L. Haarsma and S.L. Rolston, Int. J. Mass Spec. Ion Proc. **88**, 319 (1989); ibid. **93**, 121 (1989).

[44] G. Gabrielse, X. Fei, L.A. Orozco, S.L. Rolston, R.L. Tjoelker, T.A. Trainor, J. Haas, H. Kalinowsky, and W. Kells, Phys. Rev. A **40**, 481 (1989).

[45] G. Gabrielse, X.Fei, L.A. Orozco, R.L. Tjoelker, J. Hass, H. Kalinowsky, T.A. Trainor, and W. Kells, Phys. Rev. Lett. **63**, 1360 (1989).

[46] G. Gabrielse, J. Tan, L.A. Orozco, S.L. Rolston, C.H. Tseng, R.L. Tjoelker, in press, J. of Mag. Resonance (1990).

[47] G. Gabrielse, Phys. Rev. Lett. **64**, 2098 (1990)

[48] G. Gabrielse, X.Fei, L.A. Orozco, R.L. Tjoelker, J. Hass, H. Kalinowsky, T.A. Trainor, and W. Kells, Phys. Rev. Lett. **65**, 1317 (1990).

[49] G. Gabrielse, J. Tan, and L.S. Brown, in **Quantum Electrodynamics**, ed. T. Kinoshita, (World Scientific, Singapore, 1990).

[50] G. Gärtner and E. Klempt, Z. Phys. **A 287**, 1-6 (1978).

[51] S.L. Gilbert, J.J. Bollinger, and D.J. Wineland, Phys. Rev. Lett., **60**, 2022 (1988).

[52] L.J. Salerno, P. Kittel, W.F. Brookes, A.L. Spivak, and W.G. Marks Jr., Cryogenics **26**, 217 (1986).

[53] G. Gräff, H. Kalinowsky, and J. Traut, Z. Phys. A **297**, 35-39 (1980).

[54] D.J. Heinzen, D.J. Wineland, Bull. Am. Phys. Soc., **35**, 1019 (1990).

[55] H.M. Holzscheiter and D.A. Church, J. Chem. Phys. **74**, 2313 (1981).

[56] E. Hu, Y. Asano, M.Y. Chen, S.C. Cheng, G. Dugan, L. Lidofsky, W. Patton, C.S. Wu, V. Hughes, and D. Lu, Nucl. Phys. **A 254**, 403 (1975).

[57] Insulator Seal, Hayward, CA 94545.

[58] R. Jakobi and J. Haas; Mainz U., private communication.

[59] J.B. Jeffries, S.E. Barlow, and F.H. Dunn, Int. J. Mass Spec. Ion Proc., **54**, 169-187 (1983).

[60] K. Jungmann, J. Hoffnagle, R.G. DeVoe, and R.G. Brewer, Phys. Rev. A **36**, 3451, (1987).

[61] W. Kells, G. Gabrielse, and K. Helmerson,
Fermilab Report Conf. No. 84/68 E (unpublished)

[62] J.G. King, Phys. Rev. Lett. **5**, 562 (1960); L.J. Fraser, E.R. Carlson, and V. Hughes, Bull. Am. Phys. Soc. **13**, 636 (1968).

[63] Lake Shore Cryotronics, Westerville, OH 43081

[64] Landolt-Börnstein, **Numerical Data and Functions Relationships in Science and Technology**, New Series II, (Springer-Verlag; NY) p.265.

[65] D.J. Larson, J.C. Berquist, J.J. Bollinger, W.M. Itano, and D.J. Wineland, Phys. Rev. Lett. **57**, 70 (1986)

[66] D.D. Leach, H. Simon, and T.A. Trainor; Annual Report, Nuclear Physics Laboratory, University of Washington, May 1988.

[67] T.D. Lee, and C.N. Yang; Phys. Rev. Lett., **104**, 254 (1956).

[68] E. Lippman, et. al., Phys. Rev. Lett. **54**, 285, (1985).

[69] G. Lüders, Ann. of Phys. **2**, 1-15 (1957).

[70] J.H. Malmberg and C.F. Driscoll, Phys. Rev. Lett. 44, 654 (1980).

[71] Micro-Coax Components, Inc.; Collegeville, PA 19426.

[72] F.L. Moore, D.L. Farnham, P.B. Schwinberg, and R.S. VanDyck Jr., Nucl. Instr. Meth. Phys. Res. **B43**, 425-430 (1989).

[73] D.L. Morgan and V.W. Hughes, Phys. Rev. D **2**, 1389(1970)

[74] J.W. Müller, Nuc. Instr. Meth., **163**, 241-251 (1979).

[75] Nalorac Cryogenics Corporation; Martinez, CA 94553.

[76] Omega Engineering Inc.; Stamford, CT 06907.

[77] F.M. Penning, Physica (Utrecht) **3**, 873 (1936).

[78] Polygon Co.; Walkerton, IN 46574.

[79] ARRL Handbook for the Radio Amateur, 65*th* ed., (1988).

[80] **Review of Particle Properties**, Physics Letters **B204**, April 1988.

[81] P. Roberson, et. al., Phys. Rev. **C 16**, 1945 (1977).

[82] B.L. Roberts, Phys. Rev. **D 17**, 358 (1978).

[83] S.L. Rolston, G. Gabrielse, X. Fei, L. Haarsma, K. Helmerson, R.L. Tjoelker, T.A. Trainor, H. Kalinowsky, J. Hass, and W. Kells, Bull. Am. Phys. Soc. **32**, 1280 (1987).

[84] S.L. Rolston and G. Gabrielse, Hyperfine Int. **44**, 233 (1988).

[85] G. Savard, St. Becker, G. Bollen, H.-J. Kluge, R.B. Moore, L. Schweikhard, H. Stolzenberg, and U. Wiess; preprint, CERN-EP/90-18 (1990).

[86] P.B. Schwinberg, R.S. VanDyck, Jr., and H.G. Dehmelt, Phys. Lett. **81A**, 119 (1981).

[87] H. Sommer, H.A. Thomas, and J.A. Hipple, Phys. Rev. **82**, 697 (1951).

[88] J. Tan and G. Gabrielse, Appl. Phys. Lett. **55**, 2144 (1989).

[89] J. Tan, C.-H. Tseng, and G. Gabrielse, to be published.

[90] B.N. Taylor, in **Proceedings of the International Conference held at the National Bureau of Standards Gaithersburg, Maryland, August 3-7, 1970**, D.N. Langenberg, B.N. Taylor, eds., Natl. Bur. Stand. (U.S.), Spec. Publ. **343**, 495-498 (1971).

[91] The Team Company; Woburn, MA.

[92] Proposal PSCC/81-84,PSCC/p52, discussed by C. Thibault in **Physics with Antiprotons at LEAR in the ACOL Era**, eds. U. Gastaldi, R. Klapisch, J.M. Richard, and J. Tran Thanh Van, (Editions Frontièrs, Gif-Sur-Yvett, 1985), p.761.

[93] J. Thompson, referenced in [13]

[94] S. van der Meer; CERN/PS/AA 78-17 (unpublished).

[95] R.S. VanDyck, Jr., D.J. Wineland, P.A. Ekstrom, and H.G. Dehmelt, Appl. Phys. Letters **28**, 446 (1976).

[96] R.S. VanDyck, Jr., P.B. Schwinberg, and H.G. Dehmelt in **New Frontiers in High Energy Physics**, B. Kursunoglu, A. Perlmutter, and L. Scott, eds. (Plenum Press, New York, 1978).

[97] R.S. VanDyck, Jr., P.B. Schwinberg, and S.H. Bailey, in **Atomic Masses and Fundamental Constants 6**, J.A. Nolen Jr. and W. Benenson, eds. (Plenum Press, New York, 1980) p. 173.

[98] R.S. VanDyck, Jr. and P.B. Schwinberg, Phys. Rev. Lett. **47**, 395-398 (1981).

[99] R.S VanDyck, Jr., F.L. Moore, D.L. Farnham, P.B. Schwinberg Int. J. Mass Spec. Ion Proc. **66**, 327-337 (1985).

[100] R.S. VanDyck, Jr., F.L. Moore, D.L. Farnham, P.B. Schwinberg, Bull. Am. Phys. Soc., **31**, 244, (1986).

[101] Robert S. VanDyck, Jr., Paul B. Schwinberg, and Hans G. Dehmelt, Phys. Rev. D **34**, 722 (1986).

[102] R.S. VanDyck, Jr., P.B. Schwinberg, and H.G. Dehmelt, Phys. Rev. **D34**, 722 (1986) and Phys. Rev. Lett. **59**, 26 (1987).

[103] R.S. VanDyck, Jr., F.L. Moore, D.L. Farnham, and P.B. Schwinberg, and H. Dehmelt, Phys. Rev. **A 36**, 3455 (1987).

[104] R.S. VanDyck, Jr., F.L. Moore, D.L. Farnham, and P.B. Schwinberg, Phys. Rev. A **40**, 6308 (1989).

[105] R.S. VanDyck, Jr., D.L. Farnham, F.L. Moore, and P.B. Schwinberg, **12^{th} Int. Conf. Atomic Phys.**, (1990).

[106] R.S. VanDyck, Jr., private communication.
W. Jhe and D. Phillips, private communication.

[107] Varian Assoc. Eimac; Salt Lake City, UT 84104.

[108] F. Walls, and H.G. Dehmelt, Phys. Rev. Lett., **21**, 127 (1968).

[109] C.S. Weimer, F.L. Moore, and D.J. Wineland, **12^{th} Int. Conf. Atomic Phys.**, (1990).

[110] R.M. Weisskoff, G.P. Lafyatis, K.R. Boyce, E.A. Cornell, R.W. Flanagan, Jr., and D.E. Pritchard; J. Appl. Phys. **63**, 4599 (1988).

[111] G. Werth; Metrologia **22**, 174 (1986).

[112] J. Wess, Hyper. Int. **44**, 3 (1988).

[113] D. Wineland, P. Ekstrom, and H. Dehmelt; Phys. Rev. Lett. **31**, 1279 (1973).

[114] D.J. Wineland, and H.G. Dehmelt, Int. J. Mass Spec. Ion Phys. **16**, 338 (1975); **19**, 251(E) (1975).

[115] D. Wineland and H. Dehmelt, J. Appl. Phys. **46**, 919 (1975).

[116] D.J. Wineland, in **Precision Measurement and Fundamental Constants II**, B.N. Taylor and W.D. Phillips, Eds., Natl. Bur. Stand. (U.S.), Spec. Publ. **617** (1984).

[117] D. Wineland; in Adv. in At. and Mol. Phys.**19**.

[118] C.S. Wu, et. al.; Phys. Rev. Lett. **104**, 254 (1956).